

Springer Environmental Science and Engineering

Sheng-Qi Yang

# Strength Failure and Crack Evolution Behavior of Rock Materials Containing Pre-existing Fissures



Science Press  
Beijing



Springer

**Springer Environmental Science  
and Engineering**

More information about this series at <http://www.springer.com/series/10177>

Sheng-Qi Yang

# Strength Failure and Crack Evolution Behavior of Rock Materials Containing Pre-existing Fissures

 Science Press  
Beijing

 Springer

Sheng-Qi Yang  
State Key Laboratory for Geomechanics  
and Deep Underground Engineering  
China University of Mining  
and Technology  
Xuzhou, Jiangsu  
China

Sponsored by National Natural Science Foundation of China (51179189, 41272344), Program for New Century Excellent Talents in University (NCET-12-0961), National Basic Research 973 Program of China (2013CB036003), Outstanding Innovation Team Project in China University of Mining and Technology (2014QN002)

ISSN 2194-3214                      ISSN 2194-3222 (electronic)  
Springer Environmental Science and Engineering  
ISBN 978-3-662-47302-3              ISBN 978-3-662-47303-0 (eBook)  
DOI 10.1007/978-3-662-47303-0

Library of Congress Control Number: 2015940417

Springer Heidelberg New York Dordrecht London

© Science Press, Beijing and Springer-Verlag Berlin Heidelberg 2015

This work is subject to copyright. All rights are reserved by the Publishers, whether the whole or part of the material is concerned, specifically the rights of translation, reprinting, reuse of illustrations, recitation, broadcasting, reproduction on microfilms or in any other physical way, and transmission or information storage and retrieval, electronic adaptation, computer software, or by similar or dissimilar methodology now known or hereafter developed.

The use of general descriptive names, registered names, trademarks, service marks, etc. in this publication does not imply, even in the absence of a specific statement, that such names are exempt from the relevant protective laws and regulations and therefore free for general use.

The publishers, the authors and the editors are safe to assume that the advice and information in this book are believed to be true and accurate at the date of publication. Neither the publishers nor the authors or the editors give a warranty, express or implied, with respect to the material contained herein or for any errors or omissions that may have been made.

Printed on acid-free paper

Springer-Verlag GmbH Berlin Heidelberg is part of Springer Science+Business Media  
([www.springer.com](http://www.springer.com))

# Foreword

Fractures in natural rocks have a marked effect on the stability and safety of rock mass. In rock engineering practice, it is often necessary to evaluate strength failure and crack evolution behaviour. Until now, the problem of coming to terms with these features of fissured rock material has had no satisfactory solution, because of the complex role of fissure geometry and confining pressure. But using advanced acoustic emission and photographic monitoring techniques, the author of this book has carried out many valuable experimental investigations to fill the knowledge gap.

By means of a 2014 Endeavour Research Fellowship from Australian government, Professor Sheng-Qi Yang commenced these studies in my group at Monash University as a visiting professor. As his host supervisor, I have been very much impressed with Professor Yang's contributions at Monash. As an exemplary worker, he has pursued his project diligently and has progressed extremely well with his research results. On a close consideration of this book, I am pleased to note its logical organisation and clear presentation, which make for easy and enjoyable reading.

The book is an integration by the authors of research results over the past five years. The project obtained support from National Natural Science Foundation of China, the National Basic Research 973 Program of China and the Program for New Century Excellent Talents in University. Many of the experimental results have been published in major international journals, such as *International Journal of Rock Mechanics and Mining Sciences*, *Rock Mechanics and Rock Engineering*, *Journal of Structural Geology*, *Engineering Geology* and *International Journal of Fracture*. The international peer review process for these English language journals is an additional guarantee of quality.

In comparison with other works on the topic, this book clearly succeeds in at least five aims: (1) to investigate the influence of fissure geometry on strength failure and crack evolution behaviour of real rock material; (2) to analyse the effect of pre-experiment high-temperature treatment on fracture mechanical behaviour of rock material with a single fissure or two parallel fissures; (3) to compare quantitatively simulated results using discrete element modelling and experimental results of fracture mechanical behaviour of rock material with two fissures; (4) to construct the relationship between crack evolution processes and acoustic emission

distribution of pre-fissured rock material under entire deformation; and (5) to discuss the crack evolution mechanism of pre-fissured rock material with respect to different confining pressures.

All things considered, I believe that the publication of this book offers a sound experimental basis for developments in discontinuous rock mechanics. It increases our understanding of the unstable failure mechanism in all kinds of rock engineering (deep underground, dam base, jointed rock slope projects, nuclear waste disposition projects, and more). I am pleased to commend this book to all interested readers.

A handwritten signature in blue ink, reading "Ranjith", with a long horizontal flourish underneath.

May 2015

Prof. P.G. Ranjith  
ARC Future Fellow,  
Director of Deep Earth Energy Research Lab,  
and Professor of Geomechanics  
Monash University, Australia

# Preface

Natural rock is a complicated geological medium that usually contains all kinds of fissures with unequal scales. Under an applied load, new cracks are readily initiated at the tips of nearby pre-existing fissures, and these new cracks propagate along the direction of axial stress in the rock, resulting in an unstable failure due to crack initiation, propagation and coalescence. With the increase of engineering scales and depths, strength failure and crack coalescence behaviour of rock material have become more and more important. In order to understand deeply the fracture mechanism of rock mass containing intermittent structures, in this book, a lot of experimental and numerical investigations are carried out for all kinds of rock materials containing different fissure geometries, such as a single fissure, two fissures and three fissures.

This book includes nine chapters. Chapter 1 summarises the crack evolution behaviour of rocklike materials and real rocks from the experimental and numerical viewpoint. Chapters 2–4 deal with the strength failure and crack coalescence behaviour of brittle sandstone specimen containing a single fissure, two fissures and three fissures, respectively. Chapters 5 and 6 summarise a systematical analysis on fracture coalescence behaviour of red sandstone containing two unparallel fissures under uniaxial compression by the experimental and numerical simulation. Chapters 7 and 8 summarise the experimental analysis of the effect of high-temperature heat treatments and confining pressure on the strength failure and crack evolution behaviour of pre-fissured rock material. Chapter 9 deals with a numerical investigation on the failure mechanical behaviour of red sandstone containing two coplanar fissures under conventional triaxial compression.

This book was supported by the National Natural Science Foundation of China (Grant Nos. 51179189 and 41272344), the National Basic Research 973 Program of China (Grant No. 2013CB036003), the Program for New Century Excellent Talents in University (Grant No. NCET-12-0961) and Outstanding Innovation Team Project in China University of Mining and Technology (Grant No. 2014QN002), which are greatly appreciated. At the same time, I obtained financial support from a 2014 Endeavour Research Fellowship in Australia, which was greatly appreciated. When I stayed in the Department of Civil Engineering, Monash University (Clayton

campus), Melbourne, as a visiting professor, my host supervisor Prof. P.G. Ranjith often discussed with me and brought me a lot of valuable insights, which greatly improved this research. At the same time, Prof. P.G. Ranjith made a foreword for this book, which was also greatly appreciated.

Finally, I would also like to express my sincere thanks to Prof. Hong-Wen Jing from China University of Mining and Technology, Prof. Jian Zhao from Monash University, Dr. Mike Heap from University of Strasbourg and Prof. Tao Xu from Northeastern University for their valuable comments, which have greatly improved this book. I am extremely grateful to my wife Xiao-Qin Chen for many years of personal support and understanding. I would like to thank my daughter Ai-Chen Yang for bringing me a lot of joyfulness and happiness.

June 2015

Sheng-Qi Yang

# Contents

<b>1 Introduction</b> . . . . .	1
1.1 Experimental Studies for Rock-Like Materials . . . . .	1
1.2 Experimental Studies for Real Rock Materials . . . . .	4
1.3 Numerical Studies for Crack Evolution Behavior . . . . .	6
1.4 Study of Fracture Coalescence Behavior by AE Technique . . . . .	7
1.5 Main Contents in This Book . . . . .	8
References . . . . .	11
<b>2 Experimental Investigation on Strength Failure and Crack Evolution Behavior of Brittle Sandstone Containing a Single Fissure</b> . . . . .	15
2.1 Experimental Studies . . . . .	15
2.1.1 Sandstone Material . . . . .	15
2.1.2 Preparation for Specimen with Single Fissure . . . . .	16
2.1.3 Experimental Equipment and Procedure . . . . .	17
2.2 Strength and Deformation Behavior . . . . .	19
2.2.1 Uniaxial Stress–Strain Curves of Sandstone . . . . .	20
2.2.2 Effect of Single Fissure Geometry on Mechanical Parameters of Sandstone . . . . .	21
2.3 Crack Evolution Behavior . . . . .	25
2.3.1 Crack Coalescence Type of Sandstone Specimens Containing a Single Fissure . . . . .	25
2.3.2 AE Behaviors of Intact and Flawed Sandstone Specimens with Single Fissure Geometries . . . . .	30
2.3.3 Real-Time Crack Evolution Process of Sandstone Containing a Single Fissure . . . . .	34
2.4 Conclusions . . . . .	41
References . . . . .	43

<b>3</b>	<b>Experimental Investigation on Crack Evolution Behavior of Brittle Sandstone Containing Two Coplanar Fissures in the Process of Deformation Failure</b> . . . . .	45
3.1	Experimental Material and Procedure . . . . .	46
3.1.1	Physical Behavior of Tested Specimens. . . . .	46
3.1.2	Specimens Containing Two Coplanar Fissures . . . . .	46
3.1.3	Testing Equipment and Procedure . . . . .	48
3.2	Influence of Coplanar Fissure Angle on Strength and Deformation Behavior . . . . .	48
3.2.1	Deformation Failure Behavior of Intact Sandstone Specimen . . . . .	48
3.2.2	Deformation Failure Behavior of Flawed Sandstone with Two Coplanar Fissures . . . . .	50
3.2.3	Relationship Between Coplanar Fissure Angle and Mechanical Parameters . . . . .	52
3.3	Crack Initiation and Coalescence Behavior Analysis. . . . .	54
3.3.1	Crack Coalescence Type of Sandstone Containing Two Coplanar Fissures . . . . .	55
3.3.2	Crack Initiation and Coalescence Behavior of Pre-fissured Sandstone . . . . .	65
3.4	Conclusions . . . . .	74
	References . . . . .	74
<b>4</b>	<b>Experimental Investigation on Fracture Evolution Behavior of Brittle Sandstone Containing Three Fissures</b> . . . . .	77
4.1	Specimen Preparation and Testing Procedure . . . . .	77
4.1.1	Sandstone Material and Specimen Preparation . . . . .	77
4.1.2	Testing Procedure . . . . .	79
4.2	Analysis of Experimental Results . . . . .	79
4.2.1	Axial Stress–Strain Curve of Intact Specimen. . . . .	79
4.2.2	Axial Stress–Strain Curve of Flawed Specimens Containing Three Fissures . . . . .	81
4.3	Crack Initiation Mode and Analysis of the Coalescence Process . . . . .	84
4.3.1	Crack Initiation Mode and Stress Analysis . . . . .	84
4.3.2	Real-Time Crack Coalescence Process of Specimens for $\beta_2 = 75^\circ$ and $90^\circ$ . . . . .	86
4.3.3	Real-Time Crack Coalescence Process of Sandstone Specimens Containing Three Fissures ( $\beta_2 = 105^\circ$ and $120^\circ$ ) . . . . .	91
4.4	Crack Coalescence Type and Strain Evolution Analysis . . . . .	96
4.4.1	Crack Coalescence Type Analysis . . . . .	96
4.4.2	Strain Evolution Analysis. . . . .	98
4.5	Conclusions . . . . .	100
	References . . . . .	102

- 5 Experimental Investigation on Fracture Coalescence Behavior of Red Sandstone Containing Two Unparallel Fissures. . . . .** 103
  - 5.1 Experimental Material and Loading Procedure . . . . . 104
    - 5.1.1 Experimental Material and Specimen Preparation. . . . . 104
    - 5.1.2 Loading Procedure and AE Monitoring . . . . . 106
  - 5.2 Strength and Deformation Behavior. . . . . 106
    - 5.2.1 Axial Stress–Axial Strain Behavior . . . . . 106
    - 5.2.2 Strength and Deformation Parameters . . . . . 110
  - 5.3 Cracking Mode and Characteristics . . . . . 112
  - 5.4 Crack Coalescence Process and AE Behavior . . . . . 116
  - 5.5 Conclusions . . . . . 122
  - References . . . . . 124
  
- 6 Discrete Element Modeling on Fracture Coalescence Behavior of Red Sandstone Containing Two Unparallel Fissures. . . . .** 125
  - 6.1 Discrete Element Modeling Method . . . . . 125
    - 6.1.1 Micro-Bond Model. . . . . 125
    - 6.1.2 Numerical Specimen . . . . . 126
    - 6.1.3 Simulation Procedure. . . . . 128
  - 6.2 Confirmation for Micro-Parameters of Red Sandstone . . . . . 128
    - 6.2.1 Confirming Method for Micro-Parameters of Red Sandstone . . . . . 128
    - 6.2.2 Calibrating Micro-parameters by Experimental Results of Intact Specimen. . . . . 130
  - 6.3 Numerical Results of Red Sandstone Containing Two Unparallel Fissures. . . . . 131
    - 6.3.1 Strength and Deformation Behavior. . . . . 131
    - 6.3.2 Cracking Characteristics. . . . . 135
  - 6.4 Stress Field in Red Sandstone Containing Two Unparallel Fissures. . . . . 146
  - 6.5 Conclusions . . . . . 154
  - References. . . . . 156
  
- 7 Fracture Mechanical Behavior of Red Sandstone Containing a Single Fissure and Two Parallel Fissures After Exposure to Different High-Temperature Treatments . . . . .** 157
  - 7.1 Rock Material and Testing Procedure . . . . . 158
    - 7.1.1 The Experimental Material and Heating Procedure. . . . . 158
    - 7.1.2 Specimen Preparation and Fissure Geometry . . . . . 158
    - 7.1.3 Testing Procedure and AE Monitoring. . . . . 160
  - 7.2 Strength and Deformation Behavior. . . . . 161
  - 7.3 Fracture Evolution Behavior . . . . . 167
  - 7.4 Interpretation and Discussion. . . . . 179
  - 7.5 Conclusions . . . . . 181
  - References. . . . . 182

- 8 Experimental Investigation on Strength and Failure Behavior of Pre-cracked Marble Under Conventional Triaxial Compression. . .** 185
  - 8.1 Experimental Methodology . . . . . 185
    - 8.1.1 Marble Material . . . . . 185
    - 8.1.2 Pre-cracked Sample Preparation . . . . . 186
    - 8.1.3 Experimental Procedure . . . . . 188
  - 8.2 Triaxial Experimental Results of Pre-cracked Marble . . . . . 189
    - 8.2.1 Brittle-Ductile Transition Mechanism of Intact Marble. . . . . 189
    - 8.2.2 Triaxial Stress–Strain Curves of Pre-cracked Marble . . . . . 191
  - 8.3 Strength Behavior of Pre-cracked Marble . . . . . 195
    - 8.3.1 Strength Behavior in Accordance with Mohr-Coulomb Criterion . . . . . 195
    - 8.3.2 Strength Behavior in Accordance with Hoek-Brown Criterion . . . . . 199
    - 8.3.3 A New Evaluation Criterion Based on Optimal Approximation Polynomial Theory . . . . . 204
  - 8.4 Failure Mode of Pre-cracked Marble . . . . . 207
  - 8.5 Conclusions . . . . . 214
  - References . . . . . 215
  
- 9 Numerical Investigation on the Failure Mechanical Behavior of Red Sandstone Containing Two Coplanar Fissures Under Conventional Triaxial Compression . . . . .** 217
  - 9.1 Discrete Element Model and Micro-Parameters . . . . . 217
    - 9.1.1 Intact Red Sandstone Material and Micro-Parameters. . . . . 218
    - 9.1.2 Comparison of Triaxial Experimental and Numerical Results of Intact Specimen. . . . . 219
  - 9.2 Macroscopic Strength and Deformation Behavior. . . . . 223
    - 9.2.1 Triaxial Deformation Behavior of Red Sandstone Containing Two Coplanar Fissures . . . . . 224
    - 9.2.2 Triaxial Strength Behavior of Red Sandstone Containing Two Coplanar Fissures . . . . . 228
  - 9.3 Fracture Evolution Behavior . . . . . 231
    - 9.3.1 Fracture Evolution Process of Intact Specimen . . . . . 232
    - 9.3.2 Fracture Evolution Process of Flawed Specimen. . . . . 234
    - 9.3.3 Effect of Confining Pressure and Coplanar Fissure Angle. . . . . 238
    - 9.3.4 Stress and Displacement Field . . . . . 240
  - 9.4 Conclusions . . . . . 244
  - References . . . . . 246

## About the Author



**Dr. Sheng-Qi Yang** was born in December 1978. In 2003, he started his Ph.D. research, in Hohai University, Nanjing, PR China, and got Geotechnical Engineering of Doctor's degree in April 2006. In 2007–2008, he continued his postdoctoral work in Ecole Polytechnique de Paris, France. In 2014–2015, he obtained an Endeavour Research Fellowship in Australia and commenced his research in the Department of Civil Engineering, Monash University, as a visiting professor. From 2012, he has been promoted as a full-time professor and a Ph.D. supervisor in China University of Mining and Technology. In March, 2014, he was elected as

an assistant director of State Key Laboratory for Geomechanics and Deep Underground Engineering.

In 2013, he was awarded the Program for New Century Excellent Talents in University from Ministry of Education. He obtained the Youth Science and Technology Award from Chinese Society for Rock Mechanics and Engineering and Sunyueqi Foundation Council. In 2011, he also obtained the Second Prize of Science and Technology Progress from Ministry of Education. In the past 5 years, he took charge of more than ten key scientific projects including three projects from National Natural Science Foundation of China (NSFC). His research interests focus mainly on deep-fissured and jointed rock mechanics; rock creep (time-dependent) experimental and model mechanics; and deep underground rock mass engineering and reinforced technique.

To date, Professor Sheng-Qi Yang has published one Chinese book with the title *Study on the Mechanical Behaviour of Fissured Rock and Its Time-dependent Effect Analysis* (Beijing: Science Press, 2011). He has also published about 80 papers, in which more than 20 English papers (indexed by SCI) were published in International Journal of Rock Mechanics and Mining Sciences, Rock Mechanics and Rock Engineering, Tunneling and Underground Space Technology, Journal of Structural Geology, Engineering Geology, International Journal of Fracture,

Engineering Fracture Mechanics, Canadian Geotechnical Journal, etc. He has applied for 10 national invented patents, among which three patents have been awarded. He is the editorial board of two journals *The Scientific World Journal* and *Journal of Basic Science and Engineering*. He has also made six lectures in some important academic conferences, e.g. 2014 International Symposium on Soft Rock.

# Chapter 1

## Introduction

Rock is a complicated geological medium that usually contains all kinds of fissures with unequal scales. Under an applied load, new cracks are readily initiated at the tips of nearby pre-existing fissures, and these new cracks propagate along the direction of axial stress in the rock (Li et al. 2005; Wong and Einstein 2009a, b; Park and Bobet 2009; Yang and Jing 2011), resulting in an unstable failure due to crack initiation, propagation, and coalescence. With the increase of engineering scales, rock masses transform from an intact state to a heavily fractured rock mass (Fig. 1.1) (Hoek 1998). As a result, the mechanical behavior of intact rock can rarely be used to characterize the strength and deformation characteristics of fractured rock masses. Therefore, in order to understand and explore the fracture mechanism of various rock engineering, such as dam-base rock engineering, jointed rock slope project, nuclear waste disposition project, etc., extensive studies (Nemat-Nasser and Horii 1982; Bobet 1997; Shen and Stephansson 1993; Shen 1995; Zhu et al. 1998; Wong et al. 2001) have been conducted for the mechanical behaviors of pre-existing fissured materials (artificial material and real rock material). The results have shown that the geometries of fissures in the rocks have an important influence on the strength, deformation, and failure behaviors.

### 1.1 Experimental Studies for Rock-Like Materials

A number of experimental studies have been carried out for rock-like materials (model specimens) because rock-like material is easy to fabricate. Rock-like material is fabricated by a mixture of gypsum, cement, barite, and water with a different mass ratio to simulate and reflect the mechanical behavior of real rock material. By inserting mica, paper, or thin steel disk, etc., open or closed fissures

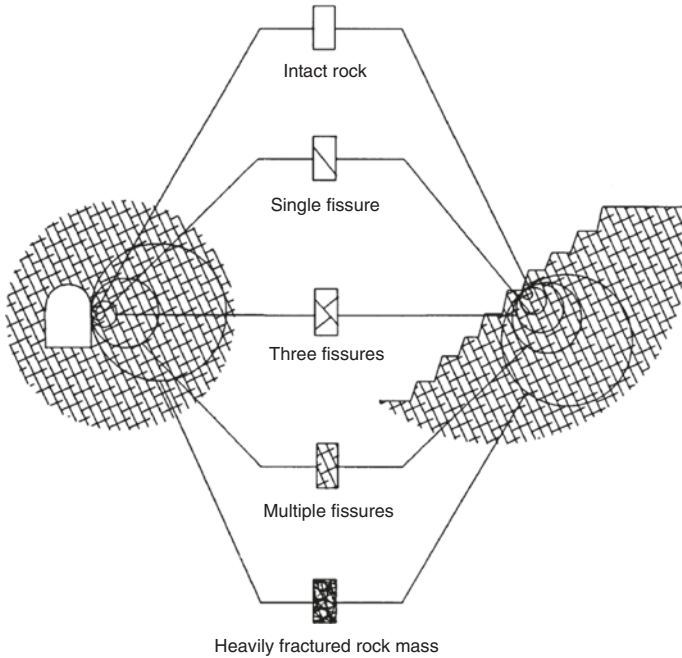


**Fig. 1.1** Idealized diagram showing the transition from an intact state to a heavily fractured rock mass, with increasing specimen scale (after Hoek 1998)

are pre-fabricated to investigate the initiation, propagation, and coalescence behavior of cracks in model materials in two-dimensional (2-D) conditions.

Nemat-Nasser and Horii (1982) investigated the mechanisms of crack interactions and failure modes in flaw plates (model material) under uniaxial and biaxial compression, which showed that flaw length is one of the parameters controlling the failure mode of specimen. Bobet (1997), Bobet and Einstein (1998), Zhu et al. (1998), Wong and Chau (1998), Vásárhelyi and Bobet (2000) investigated the 2-D cracks propagation and coalescence on rock-like materials containing two inclined open or closed fissures. Figure 1.2 shows typically three main modes of 2-D crack coalescence in two fissured specimens under uniaxial compression by Wong et al. 2001. Under uniaxial and biaxial conditions, the experimental investigation of coalescence of two nonoverlapping fissures confirmed the well-established behavior. It also revealed many important new physical phenomena (Bobet and Einstein 1998). Wing cracks occurred at fissure tips as is well known. But these wing cracks shifted toward the middle of the fissures and did not occur as confining stresses increased. Wong et al. (2001) investigated experimentally crack coalescence and peak strength of model materials containing three parallel frictional fissures. The results showed that the mechanisms of 2-D crack coalescence depended on fissure arrangement and frictional coefficient on the fissure surface. Prudencio and Van Sint (2007) presented the results of biaxial tests on

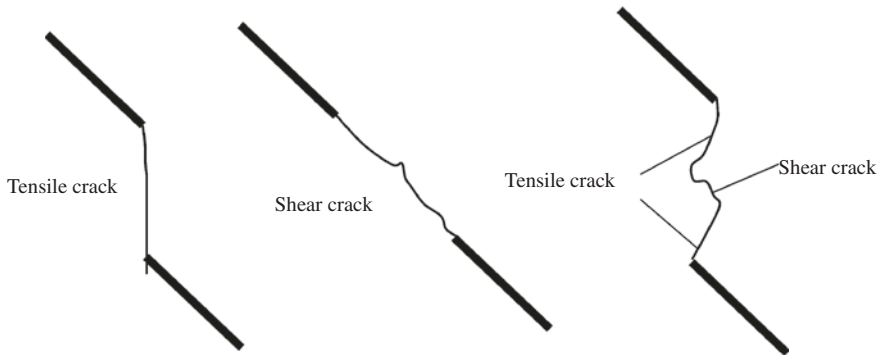


**Fig. 1.2** Three main modes of 2-D crack coalescence in 2-fissure specimens under uniaxial compression (after Wong et al. 2001)

physical models of rock with nonpersistent joints. Tests showed three basic failure modes: failure through a planar surface, stepped failure, and failure by rotation of new blocks. Planar failure and stepped failure were associated with high strength and small failure strains, whereas rotational failure was associated with very low strength, ductile behavior, and large deformation. In reality, pre-existing fissures are usually three-dimensional (3-D) in nature. Therefore, the growth mechanisms of 3-D crack is nearer to rock engineering practice, but the mechanism of 3-D crack growth is more complicated (Germanovich and Dyskin 2000) than that of 2-D crack growth. Huang and Wong (2007) performed a series of uniaxial compressive tests on frozen Polymethyl Methacrylate (PMMA) with pre-existing 3-D cracks. Based on the test results, the mechanisms of crack propagation and coalescence in brittle materials were investigated. It was found that for 3-D surface cracks, the interactions of cracks affected crack growth and extension in two aspects, i.e., the interaction either prompting crack extension or restraining it. The mechanism of crack interaction depends mainly on the location of cracks in spatial domain. Sagong and Bobet (2002) tested a number of specimens (the dimension of the rectangular specimen was  $101.6 \times 203.2 \times 30$  mm) made of gypsum with 3 and 16 fissures under uniaxial compression, which obtained the influence of continuity and ligament length on the crack coalescence stress. Chen et al. (2012) investigated the combined influence of joint inclination angle and joint continuity factor on deformation behavior of jointed rock mass for gypsum specimens (the dimension of the rectangular specimen was  $150 \times 150 \times 50$  mm) with a set of nonpersistent open flaws in uniaxial compression. Zhou et al. (2014) carried out uniaxial compressive tests for rock-like specimens containing four fissures with dimensions of  $90 \times 150 \times 70$  mm, which observed five types of cracks at or near the tips of pre-existing fissures, including wing crack, quasi-coplanar secondary crack, oblique secondary crack, out-of-plane tensile crack, and out-of-plane shear crack.

## 1.2 Experimental Studies for Real Rock Materials

Although rock-like materials can simulate well some behaviors of real rock, such as brittleness and shear-dilatancy (Li et al. 2005), it is difficult to simulate all behaviors of real rock materials with abundant meso-structures. Therefore, some real rock specimens have also been carried out with physical tests to investigate the behaviors of pre-fissured rock materials (Fujii and Ishijima 2004; Hall et al. 2006; Lee and Jeon 2011; Li et al. 2005; Yang and Jing 2011; Yang 2011; Yang et al. 2012, 2013).

The real rock specimens were usually made into thin slices with some slots for the purpose of scanning electron microscope (SEM) study. Zhao and Liang (2004), Zhao and Yang (2005) investigated the initiation, coalescence, and recovery of micro-cracks in plate marble and limestone specimens (of size about  $12 \times 25 \times 2$  mm) subjected to uniaxial compression by real-time SEM observation. But fewer experiments were performed for real macroscopic rock specimens with pre-existing fissures. Li et al. (2005) carried out the uniaxial compression experiment on pre-cracked marble (of size about  $62 \times 110 \times 25$  mm), to investigate the propagation and coalescence of pre-existing cracks in marble specimens, and the characters of acoustic emission (AE) of pre-cracked marble specimens. Two types of newborn cracks are observed: wing (tensile) cracks and secondary (shear) cracks. Both types of cracks initiate from the tips of the fractures and propagate in a stable manner. Wong and Einstein (2009a) investigated the cracking behaviors in modeled gypsum and Carrara Marble specimens ( $76 \times 152 \times 32$  mm) containing a single open fissure (12.5 mm long and 1.3 mm width) under uniaxial compression. Seven different crack types were identified based on their geometry and propagation mechanism (tensile/shear) by a high-speed video observation.

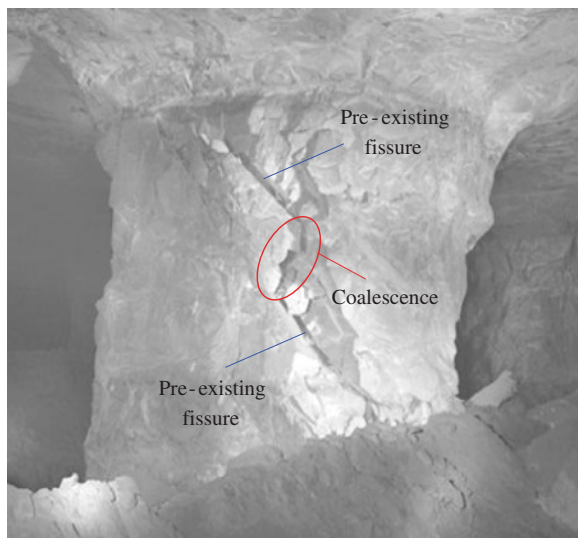
Sandstone is a kind of typical sedimentary rock, which is formed by accumulation of thousands of years of sand grain deposits on the riverbed through water erosion. The microscopic behavior of sandstone material is distinctly different from that of marble material, which leads to the strength failure and crack coalescence in sandstone specimens being distinctly different from that in marble specimen. Of course, sandstone can be divided into less porous sandstone and porous sandstone, which is usually a function of porosity. Therefore, porosity has a key effect on strength failure and crack coalescence behavior.

Khan et al. (1991) conducted numerous triaxial compression experiments for Berea sandstone under a large range of confining pressure, determined the initial yield and failure surfaces, and proposed a yield and failure criteria. Khan et al. (1992) further put forward an elastic-plastic constitutive model, which was in good agreement with the experimental results on Berea sandstone. Heap et al. (2009) investigated the time-dependent behavior of Darley Dale sandstone under triaxial conditions. They demonstrated that the brittle creep strain rate in sandstone was highly dependent on the applied differential stress. Baud et al. (2000) found that the presence of water reduced the strength of Berea, Boise, Darley Dale, and

Gosford sandstones in the cataclastic flow regime. Wong et al. (1997) studied the transition from brittle faulting and cataclastic flow in six different sandstones. At high confining pressures, shear-enhanced compaction and cataclastic flow was observed. However, at lower confining pressures, shear-induced dilation and brittle faulting was observed. Song et al. (2013) studied the damage evolution process and crack development of sandstone by cyclic uniaxial test and digital image correlation. Wasantha and Ranjith (2014) investigated the effect of water on the short-term mechanical behavior of intact Hawkesbury sandstone, which showed that water could reduce the peak strength of sandstone. Yang et al. (2014b) analyzed quantitatively the influence of pore pressure and axial deviatoric stress on the creep mechanical behavior of saturated red sandstone. The results showed that the steady-state creep rate of saturated red sandstone increased nonlinearly but the viscosity coefficient decreased gradually with increasing axial deviatoric stress and pore pressure. An exponential function was suggested to characterize the relationship between the creep parameters (including creep strain, steady-state creep rate, and viscosity coefficient), the axial deviatoric stress, and pore pressure.

However, all of the above studies report on experiments performed on intact sandstone specimens (i.e., they did not contain any macroscopic fissures or joints). In nature, natural rock masses are not usually flawless, and generally contain faults, joints, fissures, etc. Vorobiev (2008) presented a new nonlinear thermomechanical model for heavily jointed rock masses, which can better describe poroelasticity, shear-enhanced compaction, and brittle-ductile transition in dry porous rocks. Figure 1.3 shows a partially benched pillar (with a width-to-height ratio of 0.58) containing a macroscopic fracture that resulted from the coalescence of two inclined discontinuities (Esterhuizen et al. 2011). From Fig. 1.3, it is clear that pre-existing fissures in natural rock masses have great influence on their strength,

**Fig. 1.3** Partially benched pillar with width-to-height ratio of 0.58 that coalesced along two angular discontinuities (after Esterhuizen et al. 2011)



deformation, and fracture coalescence behavior (Hall et al. 2006; Lee and Jeon 2011; Li et al. 2005; Yang et al. 2008, 2014c).

Recently, experimental studies have focused on sandstone specimens that contain pre-existing fissures, in order to better understand the fracturing of engineering rock masses (Fujii and Ishijima 2004; Yang 2011; Yang et al. 2013). For example, Fujii and Ishijima (2004) performed uniaxial compression tests on sandstone specimens ( $60 \times 120 \times 60$  mm) with an inclined slit or an inclined initial fracture on the specimen surface. Their experimental results showed that the crack that formed from the inclined slit grew at a small angle to its initial orientation and curved slightly toward the free surface in all cases. However, no clear relation was observed between the load at which the main fracture initiated and the inclination of the slit. Yang (2011) performed an experimental study on the influence of two coplanar fissures on the strength, deformation, and failure mode of sandstone. They investigated the real-time crack coalescence process in sandstone deforming under uniaxial compression using photographic monitoring. Besides, pre-existing fissures have been the focus of numerous theoretical studies (e.g., Spicak and Locajicek 1986; Wong and Chau 1998). Yang et al. (2013) conducted uniaxial compression tests for red sandstone specimens containing two unparallel fissures, which investigated the effects of the fissure angle on the strength and deformation behaviors of red sandstone material and analyzed the real-time crack coalescence process in red sandstone material using photographic monitoring and AE monitoring techniques.

### 1.3 Numerical Studies for Crack Evolution Behavior

With the innovation of numerical methods, numerous softwares were developed to analyze the fracture coalescence behavior of rock material, such as SAP2000 (Mughieda and Omar 2008), FROCK (Vásárhelyi and Bobet 2000), Discrete Element Method (DEM) (Camborde et al. 2000; Lee and Jeon 2011; Scholtes and Donze 2013; Shimizu et al. 2010; Yoon et al. 2012; Zhang and Wong 2012; Yang et al. 2014a), RFPA<sup>2D</sup> (Tang et al. 2001; Tang and Kou 1998; Tang et al. 2000), boundary element method (BEM) (Chen et al. 1998; Shen and Stephansson 1993; Shen 1995), cellular automata (CA) (Feng et al. 2006; Pan et al. 2009) and X-FEM (Colombo and Massin 2011; Gregoire et al. 2007; Rozycki et al. 2008), etc.

By RFPA<sup>2D</sup> code, Tang et al. (2001) conducted numerical investigations on specimens of rock-like material containing three fissures in uniaxial compression to investigate failure mechanism and crack coalescence modes. The numerical results replicated most of the phenomena observed in actual experiments, such as initiation and growth of wing and secondary cracks, crack coalescence, and the macro-failure of the specimen. The results obtained in the simulations are in good agreement with experiments presented by Wong et al. (2001). Although RFPA<sup>2D</sup> leads to realistic simulations of the breakdown process, it has some limitations (Yuan and Harrison 2006). The main limitation is difficulty to reflect the transition

of stress–strain response from softening to hardening, different failure mechanisms, the form of the ultimate fracture pattern, and dilatancy deformation response. Using the Displacement Discontinuity Method, FROCK, Vásárhelyi and Bobet (2000) modeled the crack initiation, propagation, and coalescence between two bridged flaws in gypsum under uniaxial compression. Results reproduced the types of coalescence observed in the physical experiments, and predicted an increase in coalescence stresses with ligament length. Although the above-mentioned numerical results by software can better reproduce some phenomena of 2-D crack coalescence observed in physical tests, the numerical specimen with pre-cracked model still belongs to the plane strain or plane stress (i.e., 2-D problems), which has been proved many differences with real rock materials containing initial defects such as grain boundaries, micro-cracks, pores, etc.

Recently, DEM is often used to simulate the mechanical behavior of some rock materials. Based on the principle of DEM, PFC<sup>2D</sup> (particle flow code) is greatly developed. Although PFC<sup>2D</sup> is only two-dimensional, it can be used to simulate many problems in mining and geotechnical engineering, such as laboratory uniaxial and triaxial compression experiments on brittle rock material (Potyondy and Cundall 1998; Schopfer and Childs 2013; Yoon 2007), crack propagation and coalescence in the rock specimen containing pre-existing flaws (Ghazvinian et al. 2012; Zhang and Wong 2012), etc. Lee and Jeon (2011) carried out a numerical simulation for the coalescence characteristics of Hwangdeung granite containing two unparallel fissures using PFC<sup>2D</sup>, and the simulated peak strength, crack initiation stress, and ultimate failure mode of Hwangdeung granite were compared with the experimental results. But the fracture coalescence process and the failure mechanism were not analyzed. Manouchehrian and Marji (2012) investigated numerically the influence of confining pressure on the crack propagation behavior in rock-like materials using PFC<sup>2D</sup>, which showed that wing cracks initiated perpendicular to the flaw and propagated toward the direction of major stress; however, when the confining pressures increase, this initiation angle got wider. Manouchehrian et al. (2014) studied the effect of fissure orientation on the crack propagation mechanism in brittle materials such as rocks under various compressive loads using PFC<sup>2D</sup>. Yang et al. (2014a) carried out a particle flow simulation for the fracture coalescence behavior of red sandstone containing two unparallel fissures under uniaxial compression. The simulated results were in good agreement with the experiment results (Yang et al. 2013).

## 1.4 Study of Fracture Coalescence Behavior by AE Technique

As is well known, the AE technique is an efficient measuring tool to reflect the evolution and propagation of defects in materials, which has been widely applied to investigate the damage and fracture behavior internal to the rock material in many past studies (Li et al. 2005; Labuz et al. 2001; Chang and Lee 2004;

Moradian et al. 2010; Pestman and Van Munster 1996; Debecker and Vervoort 2009; Ganne and Vervoort 2007; Eberhardt et al. 1999; Tham et al. 2005; Jouniaux et al. 2001).

Debecker and Vervoort (2009) carried out a series of Brazilian tensile tests and uniaxial compression tests for layered slate by visual recordings and AE technique, which investigated in detail the fracture sequence and growth direction in anisotropic slate specimens. The obtained experimental results provided deep insight into the different parameters that influenced the strength and deformation behavior of slate. Ganne and Vervoort (2007) studied the effect of stress path on pre-peak damage in rock material induced by macro-compressive and tensile stress fields. The results show that previously induced (by compressive stresses) intragranular cracks influence the occurrence and growth of the intergranular cracks caused by tensile stresses, while previously induced (by tensile stresses) intergranular cracks influence the occurrence and growth of the intragranular cracks caused by compressive stresses. Eberhardt et al. (1999) analyzed the influence of grain size on the initiation and propagation thresholds of stress-induced brittle fractures by AE monitoring. Tham et al. (2005) characterized the micro- and macro-failure behaviors of granite and marble plate specimens under uniaxial tension by using the AE technique. The results reveal clearly the failure processes of rock including initiation, nucleation, and propagation of micro-fractures when the axial stress is close to the peak strength of rock. But up to now, AE technique has been less used to explore the initiation, propagation, and coalescence of brittle rock containing fissures (Jouniaux et al. 2001; Wassermann et al. 2009; Van De Steen et al. 2005; Lei et al. 2004). Van De Steen et al. (2005) investigated the effect of a tensile stress gradient on fracture initiation and growth in Brazilian disk rock specimen containing a hole by AE technique, which showed that the maximum local tensile stresses the material was able to withstand increase as the stress gradient increases. The Brazilian disk with a hole split along the loaded diameter or macro-fracturing starts at the hole (Fig. 1.4). Lei et al. (2004) obtained the detailed time-space distribution of AE events during the catastrophic fracture of rock specimens containing a pre-existing joint or potential fracture plane under triaxial compression using a high-speed 32-channel waveform recording system (Fig. 1.5).

## 1.5 Main Contents in This Book

In this book, by a rock mechanicals servo-controlled testing system, compression experimental was first carried out for rock material containing all kinds of pre-existing fissures, which analyzed the influences of fissure number, fissure angle, fissure length, and ligament angle on the strength and deformation parameters of pre-fissured rock specimens. Second, in accordance with AE and photographic monitoring techniques, the crack initiation, propagation, and coalescence process were analyzed in detail during the entire loading. At the same time, high

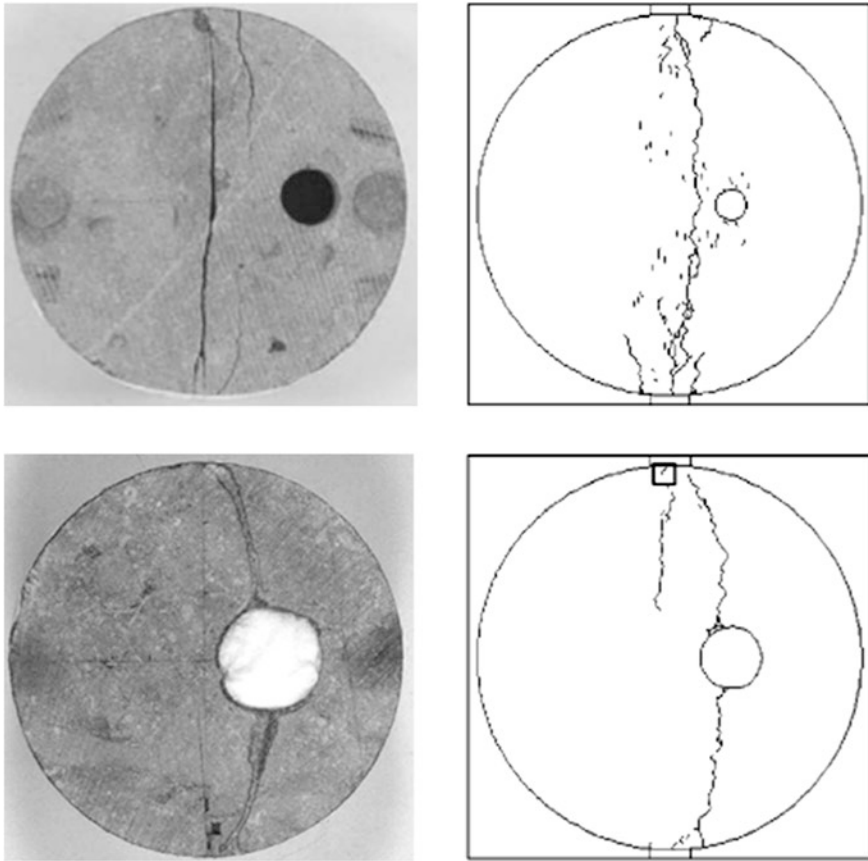


**Fig. 1.4** Two typical failure modes in Brazilian disk rock samples containing a hole (after Van De Steen et al. 2005)

temperature heat treatments and confining pressure were also used to investigate the strength failure and crack coalescence behavior of pre-fissured rock material, which was expected to improve the understanding of fracture mechanism and used in rock engineering with intermittent structures, such as deep underground excavation tunnels and nuclear waste disposition engineering. In this chapter, a lot of experimental and numerical studies on crack coalescence behavior of rock-like materials and real rock materials were summarized. In Chap. 2, the influence of the geometry of single fissures (fissure length and fissure angle) on the strength failure and crack coalescence behavior of brittle sandstone material is investigated. In Chap. 3, the influence of coplanar fissure angle on the strength failure and crack coalescence behavior of brittle sandstone material containing two coplanar fissures is analyzed. Chapter 4 investigates the effects of the ligament angle on the strength and deformation failure behaviors of a brittle sandstone material containing three fissures and analyzes the real-time crack coalescence process in

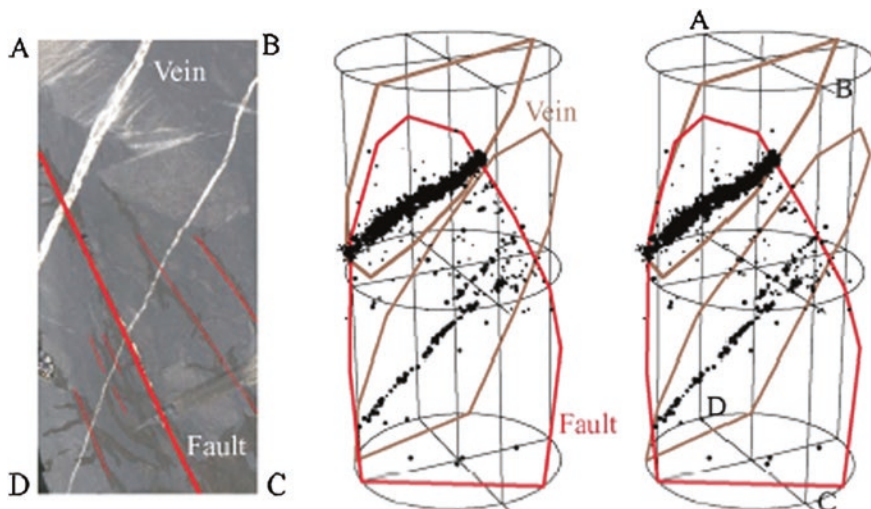


**Fig. 1.5** Typical space AE distribution of cylindrical rock sample containing pre-existing joints (Lei et al. 2004)

a sandstone material under uniaxial compression, using photographic monitoring technique. In Chap. 5, uniaxial compression tests were carried out for red sandstone specimens containing two unparallel fissures, which investigated the strength failure and crack coalescence behavior of red sandstone under uniaxial compression by photographic monitoring and AE monitoring techniques. In Chap. 6, PFC<sup>2D</sup> was used to carry out the numerical simulation for red sandstone containing two unparallel fissures under uniaxial compression, which not only compares quantitatively the numerical results with the experimental results, but also reveals the crack coalescence mechanism of red sandstone containing two unparallel fissures. In Chap. 7, a systematic study analyzing the strength, deformation behavior, crack initiation, and crack coalescence stress of red sandstone containing either a single fissure or two parallel fissures after exposure to different high temperatures was carried out. The emphasis of Chap. 8 is focused on investigation of the influence of the geometry of fissure on strength parameters of marble material, to put forward a new evaluation criterion of confirming the cohesion and internal friction angle of pre-cracked marble, to analyze the crack initiation, propagation, and coalescence in real marble material under different confining pressures. In Chap. 9, the failure mechanical behavior of red sandstone containing two coplanar fissures under conventional triaxial compression is carried out in a detailed numerical simulation by PFC<sup>2D</sup>, which analyzes the effect of the coplanar fissure angle on the strength failure and crack evolution behavior of red sandstone under conventional triaxial compression.

## References

- Baud P, Zhu W, Wong TF (2000) Failure mode and weakening effect of water on sandstone. *J Geophys Res* 105:16371–16389
- Bobet A (1997) Fracture coalescence in rock materials: experimental observations and numerical predictions. Sc.D. Thesis, MIT, Cambridge, USA
- Bobet A, Einstein HH (1998) Fracture coalescence in rock-type materials under uniaxial and biaxial compression. *Int J Rock Mech Min Sci* 35:863–889
- Camborde F, Mariotti C, Donze FV (2000) Numerical study of rock and concrete behavior by discrete element modelling. *Comput Geotech* 27:225–247
- Chen Xin, Liao Zhihong, Peng Xi (2012) Deformability characteristics of jointed rock masses under uniaxial compression. *Int J Min Sci Technol* 22:213–221
- Chen CS, Pan E, Amadei B (1998) Fracture mechanics analysis of cracked discs of anisotropic rock using the boundary element method. *Int J Rock Mech Min Sci* 35(2):195–218
- Colombo D, Massin P (2011) Fast and robust level set update for 3D non-planar X-FEM crack propagation modeling. *Comput Methods Appl Mech Eng* 200(25–28):2160–2180
- Chang SH, Lee CI (2004) Estimation of cracking and damage mechanisms in rock under triaxial compression by moment tensor analysis of acoustic emission. *Int J Rock Mech Min Sci* 41:1069–1086
- Debecker B, Vervoort A (2009) Experimental observation of fracture patterns in layered slate. *Int J Fract* 159:51–62
- Eberhardt E, Stimpson B, Stead D (1999) Effects of grain size on the initiation and propagation thresholds of stress-induced brittle fractures. *Rock Mech Rock Eng* 32(2):81–99
- Esterhuizen GS, Dolinar DR, Ellenberger JL (2011) Pillar strength in underground stone mines in the United States. *Int J Rock Mech Min Sci* 48:42–50
- Feng XT, Pan PZ, Zhou H (2006) Simulation of the rock microfracturing process under uniaxial compression using an elasto-plastic cellular automaton. *Int J Rock Mech Min Sci* 43(7):1091–1108
- Fujii Y, Ishijima Y (2004) Consideration of fracture growth from an inclined slit and inclined initial fracture at the surface of rock and mortar in compression. *Int J Rock Mech Min Sci* 41:1035–1041
- Ganne P, Vervoort A (2007) Effect of stress path on pre-peak damage in rock induced by macro-compressive and—tensile stress fields. *Int J Fract* 144(2):77–89
- Germanovich LN, Dyskin AV (2000) Fracture mechanisms and instability of openings in compression. *Int J Rock Mech Min Sci* 37:263–284
- Gregoire D, Maigre H, Rethore J, Combescure A (2007) Dynamic crack propagation under mixed-mode loading—comparison between experiments and X-FEM simulations. *Int J Solids Struct* 44(20):6517–6534
- Ghazvinian A, Sarfarazi V, Schubert W (2012) A study of the failure mechanism of planar non-persistent open joints using PFC2D. *Rock Mech Rock Eng* 45:677–693
- Hall SA, Sanctis F, Viggiani G (2006) Monitoring fracture propagation in a soft rock (Neapolitan Tuff) using acoustic emissions and digital images. *Pure appl Geophys* 163:2171–2204
- Huang ML, Wong RHC (2007) Experimental study on propagation and coalescence mechanisms of 3D surface cracks. *Chin J Rock Mech Eng* 26:1794–1799
- Heap MJ, Baud P, Meredith PG, Bell AF, Main IG (2009) Time-dependent brittle creep in Darley Dale sandstone. *J Geophys Res* 114:B07203. doi:[10.1029/2008JB006212](https://doi.org/10.1029/2008JB006212)
- Hoek E (1998) Practical rock engineering. Department of Civil Engineering, University of Toronto, Rocscience Inc., Toronto
- Jouinaux L, Masuda K, Lei X et al (2001) Comparison of themicrofracture localization in granite between fracturation and slip of a preexisting macroscopic healed joint by acoustic emission measurements. *J Geophys Res* 106(B5):8687–8698
- Khan AS, Xiang Y, Huang SJ (1991) Behavior of Berea sandstone under confining pressure part I: yield and failure surfaces, and nonlinear elastic response. *Int J Plast* 7:607–624

- Khan AS, Xiang Y, Huang SJ (1992) Behavior of Berea sandstone under confining pressure part II: elastic-plastic response. *Int J Plast* 8:209–220
- Labuz JF, Cattaneo S, Chen L-H (2001) Acoustic emission at failure in quasi-brittle materials. *Constr Build Mater* 15:225–233
- Lee H, Jeon S (2011) An experimental and numerical study of fracture coalescence in pre-cracked specimens under uniaxial compression. *Int J Solids Struct* 48(6):979–999
- Lei XL, Masuda K, Nishizawa O et al (2004) Detailed analysis of acoustic emission activity during catastrophic fracture of faults in rock. *J Struct Geol* 26:247–258
- Li YP, Chen LZ, Wang YH (2005) Experimental research on pre-cracked marble under compression. *Int J Solids Struct* 42:2505–2516
- Mughieda O, Omar MT (2008) Stress analysis for rock mass failure with offset joints. *Geotech Geol Eng* 2008(26):543–552
- Manouchehrian A, Marji MF (2012) Numerical analysis of confinement effect on crack propagation mechanism from a flaw in a pre-cracked rock under compression. *Acta Mech. Sinica* 28(5):1389–1397
- Manouchehrian A, Sharifzadeh M, Marji MF, Gholamnejad J (2014) A bonded particle model for analysis of the flaw orientation effect on crack propagation mechanism in brittle materials under compression. *Arch Civ Mech Eng* 14(1):40–52
- Moradian ZA, Ballivy G, Rivard P, Gravel C, Rousseau B (2010) Evaluating damage during shear tests of rock joints using acoustic emissions. *Int J Rock Mech Min Sci* 47(4):590–598
- Nemat-Nasser S, Horii H (1982) Compression-induced nonlinear crack extension with application to splitting, exfoliation, and rockburst. *J Geophys Res* 87(B8):6805–6821
- Prudencio M, Van Sint Jan M (2007) Strength and failure modes of rock mass models with non-persistent joints. *Int J Rock Mech Min Sci* 34:1165–1186
- Park CH, Bobet A (2009) Crack coalescence in specimens with open and closed flaws: a comparison. *Int J Rock Mech Min Sci* 46(5):819–829
- Pan PZ, Feng XT, Hudson JA (2009) Study of failure and scale effects in rocks under uniaxial compression using 3D cellular automata. *Int J Rock Mech Min Sci* 46(4):674–685
- Potyondy DO, Cundall PA (1998) Modeling notch-formation mechanisms in the URL mine-by test tunnel using bonded assemblies of circular particles. *Int J Rock Mech Min Sci Geomech Abstr* 35:510–511
- Pestman BJ, Van Munster JG (1996) An acoustic emission study of damage development and stress-memory effects in sandstone. *Int J RockMech Min Sci Geomech Abstr* 33(6):585–593
- Rozycki P, Moes N, Bechet E, Dubois C (2008) X-FEM explicit dynamics for constant strain elements to alleviate mesh constraints on internal or external boundaries. *Comput Methods Appl Mech Eng* 197(5):349–363
- Sagong M, Bobet A (2002) Coalescence of multiple flaws in a rock-model material in uniaxial compression. *Int J Rock Mech Min Sci* 39:229–241
- Song HP, Zhang H, Kang YL, Huang GY, Fu DH, Qu CY (2013) Damage evolution study of sandstone by cyclic uniaxial test and digital image correlation. *Tectonophysics* 608:1343–1348
- Spicak A, Locajicek T (1986) Fault interaction and seismicity: laboratory investigation and its seismotectonic interpretation. *Pure appl Geophys* 124:857–874
- Shen B, Stephansson O (1993) Numerical analysis of mixed mode I and Mode II fracture propagation. *Int J Rock Mech Min Sci Geomech Abstr* 30(7):861–867
- Shen B (1995) The mechanism of fracture coalescence in compression—experimental study and numerical simulation. *Eng Fract Mech* 51(1):73–85
- Scholtes L, Donze FV (2013) A DEM model for soft and hard rocks: role of grain interlocking on strength. *J Mech Phys Solids* 61(2):352–369
- Schopfer MPJ, Childs C (2013) The orientation and dilatancy of shear bands in a bonded particle model for rock. *Int J Rock Mech Min Sci* 57:75–88
- Shimizu H, Koyama T, Ishida T, Chijimatsu M, Fujita T, Nakama S (2010) Distinct element analysis for class II behavior of rocks under uniaxial compression. *Int J Rock Mech Min Sci* 47:323–333

- Tang CA, Kou SQ (1998) Crack propagation and coalescence in brittle materials under compression. *Eng Fract Mech* 61:311–324
- Tang CA, Liu H, Lee PKK, Tsui Y, Tham LG (2000) Numerical studies of the influence of microstructure on rock failure in uniaxial compression part II: constraint, slenderness and size effect. *Int J Rock Mech Min Sci* 37(4):571–583
- Tang CA, Lin P, Wong RHC, Chau KT (2001) Analysis of crack coalescence in rock-like materials containing three flaws—part II: numerical approach. *Int J Rock Mech Min Sci* 38:925–939
- Tham LG, Liu H, Tang CA et al (2005) On tension failure of 2-D rock specimens and associated acoustic emission. *Rock Mech Rock Eng* 38(1):1–19
- Vásárhelyi B, Bobet A (2000) Modeling of crack initiation, propagation and coalescence in uniaxial compression. *Rock Mech Rock Eng* 33(2):119–139
- Van De Steen B, Vervoort A, Napier JAL (2005) Observed and simulated fracture pattern in diametrically loaded discs of rock material. *Int J Fract* 131:35–52
- Vorobiev O (2008) Generic strength model for dry jointed rock masses. *Int J Plast* 24:2221–2247
- Wassermann J, Senfaute G, Amitrano D et al (2009) Evidence of dilatant and non-dilatant damage processes in oolitic iron ore: P-wave velocity and acoustic emission analyses. *Geophys J Int* 177(3):1343–1356
- Wasantha PLP, Ranjith PG (2014) Water-weakening behavior of hawkesbury sandstone in brittle regime. *Eng Geol* 178:91–101
- Wong LNY, Einstein HH (2009a) Crack coalescence in molded gypsum and Carrara marble: part I. macroscopic observations and interpretation. *Rock Mech Rock Eng* 42(3):475–511
- Wong LNY, Einstein HH (2009b) Systematic evaluation of cracking behavior in specimens containing single flaws under uniaxial compression. *Int J Rock Mech Min Sci* 46(2):239–249
- Wong RHC, Chau KT, Tang CA, Lin P (2001) Analysis of crack coalescence in rock-like materials containing three flaws-part I: experimental approach. *Int J Rock Mech Min Sci* 38:909–924
- Wong RHC, Chau KT (1998) Crack coalescence in a rock-like material containing two cracks. *Int J Rock Mech Min Sci* 35:147–164
- Wong TF, David C, Zhu W (1997) The transition from brittle faulting to cataclastic flow in porous sandstones: mechanical deformation. *J Geophys Res* 102(B2):3009–3025
- Yang SQ, Jing HW (2011) Strength failure and crack coalescence behavior of brittle sandstone samples containing a single fissure under uniaxial compression. *Int J Fract* 168(2):227–250
- Yang SQ (2011) Crack coalescence behavior of brittle sandstone samples containing two coplanar fissures in the process of deformation failure. *Eng Fract Mech* 78:3059–3081
- Yang SQ, Jiang YZ, Xu WY, Chen XQ (2008) Experimental investigation on strength and failure behavior of pre-cracked marble under conventional triaxial compression. *Int J Solids Struct* 45:4796–4819
- Yang SQ, Yang DS, Jing HW, Li YH, Wang SY (2012) An experimental study of the fracture coalescence behaviour of brittle sandstone specimens containing three fissures. *Rock Mech Rock Eng* 45(4):563–582
- Yang SQ, Liu XR, Jing HW (2013) Experimental investigation on fracture coalescence behavior of red sandstone containing two unparallel fissures under uniaxial compression. *Int J Rock Mech Min Sci* 63:82–92
- Yang SQ, Huang YH, Jing HW, Liu XR (2014a) Discrete element modeling on fracture coalescence behavior of red sandstone containing two unparallel fissures under uniaxial compression. *Eng Geol* 178:28–48
- Yang SQ, Jing HW, Cheng L (2014b) Influences of pore pressure on short-term and creep mechanical behavior of red sandstone. *Eng Geol* 179:10–23
- Yang SQ, Jing HW, Huang YH, Ranjith PG, Jiao YY (2014c) Fracture mechanical behavior of red sandstone containing a single fissure and two parallel fissures after exposure to different high temperature treatments. *J Struct Geol* 69(Part A):245–264
- Yuan SC, Harrison JP (2006) A review of the state of the art in modelling progressive mechanical breakdown and associated fluid flow in intact heterogeneous rocks. *Int J Rock Mech Min Sci* 43:1001–1022

- Yoon J (2007) Application of experimental design and optimization to PFC model calibration in uniaxial compression simulation. *Int J Rock Mech Min Sci* 44:871–889
- Yoon JS, Zang A, Stephansson O (2012) Simulating fracture and friction of Aue granite under confined asymmetric compressive test using clumped particle model. *Int J Rock Mech Min Sci* 49:68–83
- Zhang XP, Wong LNY (2012) Cracking processes in rock-like material containing a single flaw under uniaxial compression: a numerical study based on parallel bonded-particle model approach. *Rock Mech Rock Eng* 45:711–737
- Zhao YH, Liang XF (2004) Testing study on crack development in limestone plate specimen under uniaxial compression. *Chin J Rock Mech Eng* 23:1608–1615 (in Chinese)
- Zhao YH, Yang ZT (2005) Research on fracturing around cemented slot in rock specimen. *Chin J Rock Mech Eng* 24:2350–2356 (in Chinese)
- Zhu WS, Chen WZ, Shen J (1998) Simulation experiment and fracture mechanism study on propagation of Echelon pattern cracks. *Acta Mech Solida Sin* 19:355–360 (in Chinese)
- Zhou XP, Chen H, Feng YF (2014) An experimental study of crack coalescence behavior in rock-like materials containing multiple flaws under uniaxial compression. *Rock Mech Rock Eng* 47(6):1961–1986

## Chapter 2

# Experimental Investigation on Strength Failure and Crack Evolution Behavior of Brittle Sandstone Containing a Single Fissure

In this chapter, in order to better understand the strength and fracture coalescence phenomena in brittle rock material, uniaxial compression experiments were conducted for brittle sandstone specimens containing a single fissure by a rock mechanics servo-controlled testing system. Moreover, this experiment relied on photographic monitoring and AE technique to obtain the real-time crack coalescence process in the process of the whole deformation failure, which was not performed for brittle sandstone in previous studies.

The emphasis of this chapter is focused on investigation of the influence of the geometry of single fissures (fissure length and fissure angle) on the strength and deformation failure behavior of brittle sandstone material, to analyze real-time crack coalescence process in real sandstone material under uniaxial compression on the basis of photographic monitoring and AE technique, and to study the effect of crack coalescence on the strength and deformation failure behavior of brittle sandstone specimens (Yang and Jing 2011).

## 2.1 Experimental Studies

### 2.1.1 Sandstone Material

To investigate the strength failure and crack coalescence behavior of rock containing a single fissure under uniaxial compression, sandstone material located in Linyi City, Shandong province of China was chosen for the experimental object in this chapter. The sandstone has a crystalline and blocky structure, which is a fine-grained heterogeneous material with average unit weight of about  $2620 \text{ kg/m}^3$ . Moreover, the tested sandstone is porous. Based on the results of X-ray diffraction (XRD) (Fig. 2.1), the minerals in sandstone specimens are mainly feldspar, quartz, kaolinite, and chlorite; the detail composition of these rocks are given in Fig. 2.2.

**Fig. 2.1** XRD analysis of sandstone material in this chapter (with kind permission of Springer Publisher)

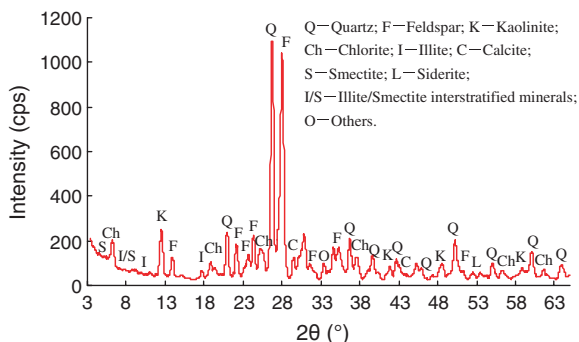
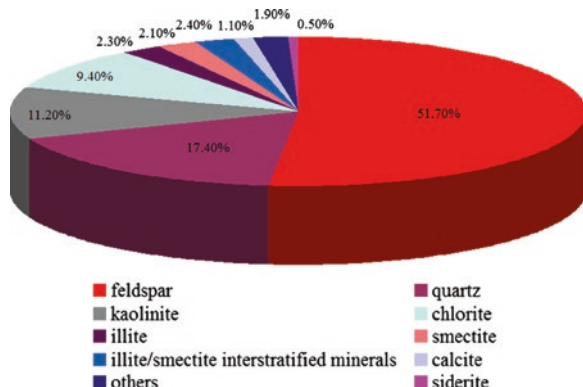


**Fig. 2.2** Composition (wt%) of sandstone. The mineralogical composition is derived from X-ray diffraction (XRD) (with kind permission of Springer Publisher)



### 2.1.2 Preparation for Specimen with Single Fissure

In this chapter, sandstone specimens containing a single fissure were prepared to carry out uniaxial compression tests. The specimens were cut from the same rectangular block. When cutting, the sandstone specimens were machined along the same direction in order to avoid the effect of anisotropy on the experimental results of sandstone. In order to obtain the exact results as well as the best comparison, all the tests were performed in natural and dry conditions.

Following the method suggested by the ISRM (Fairhurst and Hudson 1999), the height-to-width ratio of tested specimen should be in the range of 2.0–3.0 in order to minimize the effect of the end friction effects on the testing results. Therefore, the size of all tested sandstone specimens is rectangular with 120 mm in height, 60 mm in width, and 30 mm in thickness. As a result, all tested specimens with height-to-width ratio of 2.0 ensure a uniform stress state within the central part of the specimens.

The geometry of fissured sandstone is described in Fig. 2.3. Notice in this book, the term “fissure” is used to describe an artificially created flaw or crack; however, the term “crack” is adopted to describe the new fracture or failure in the process of loading. The geometry of single fissure is defined by two geometrical

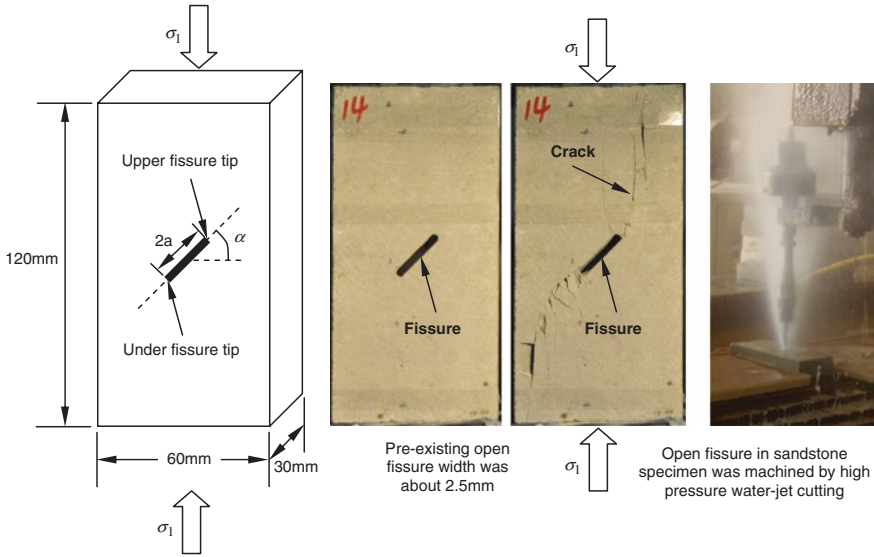


**Fig. 2.3** Geometry of single fissure in the sandstone specimens, in which  $\alpha$  is fissure angle,  $2a$  is fissure length. In this chapter, open fissure in sandstone specimen was machined by high pressure water-jet cutting (with kind permission of Springer Publisher)

parameters—fissure length  $2a$  and fissure angle (the angle of fissure with the direction of the horizontal direction)  $\alpha$  as shown in Fig. 2.3.

Although for rock-like materials, it is easier to make fissures by inserting steel or copper slices during the molding process, it is more difficult to cut fissures in the thick specimens of real rock (Li et al. 2005). High pressure water-jet cutting machine was used to cut open single fissures in the intact sandstone specimens. Machined open fissure width was about 2.5 mm. In order to investigate the effect of pre-existing single fissure geometry on the strength, deformation, and failure behavior of sandstone under uniaxial compression, different geometries of single fissure by varying one of the two parameters ( $2a$  and  $\alpha$ ) while keeping another constant were chosen in this chapter. Detailed description of sandstone specimens with different single fissure geometries is listed in Table 2.1.

### 2.1.3 Experimental Equipment and Procedure

Uniaxial compression experiments for intact and fissured sandstone specimens were carried out on a rock mechanics servo-controlled testing system (MTS815.02) with the maximum loading capacity of 2700 kN and the maximum displacement capacity of 25 mm, as shown in Fig. 2.4. This servo-controlled system can test specimens in load or displacement control while the data are recorded and analyzed in real-time. The axial stress was imposed on the surface

**Table 2.1** Pre-existing single fissure geometries of sandstone specimens under uniaxial compression

Specimen	W (mm)	H (mm)	T (mm)	M (g)	$\rho$ (kg/m <sup>3</sup> )	$\alpha^\circ$	2a (mm)	Note
GS-03 <sup>#</sup>	60.4	120.3	30.0	572.41	2625.9	N/A	0	Intact specimen
GS-04 <sup>#</sup>	60.1	120.4	29.8	559.54	2599.4	45	5	Fissure length
GS-07 <sup>#</sup>	60.2	120.8	29.0	551.09	2622.1	45	10	
GS-10 <sup>#</sup>	60.3	120.0	29.3	549.53	2605.4	45	15	
GS-14 <sup>#</sup>	60.3	120.5	30.1	567.32	2611.9	45	20	
GS-17 <sup>#</sup>	60.1	120.3	29.4	555.72	2637.2	45	25	
GS-19 <sup>#</sup>	60.5	120.0	29.9	571.30	2645.5	15	15	Fissure angle
GS-11 <sup>#</sup>	60.4	120.0	28.3	538.22	2637.6	45	15	
GS-25 <sup>#</sup>	60.5	120.2	29.9	561.64	2596.4	60	15	
GS-28 <sup>#</sup>	60.3	120.2	29.3	552.48	2615.0	75	15	

Note *W* Width; *H* Height; *T* Thickness; *M* Mass



**Fig. 2.4** MTS815.02 rock mechanics servo-controlled testing system and AE21C-06 acoustic emission system, in which the camera and lamp were used to record clearly the crack coalescence process of sandstone (with kind permission of Springer Publisher)

of rock specimen until failure took place. All the tests were conducted under displacement-controlled conditions with a strain rate of  $(1.3\text{--}2.0) \times 10^{-5}$ .

In this chapter, we measured axial force with loading capacity of 600 kN and axial deformation with displacement capacity of 5 mm. During the entire uniaxial compression experiments, loads and deformations of the tested sandstone specimens were recorded simultaneously. Moreover, two rigid steel blocks (63 mm wide, 32 mm thick, and 15 mm high) were placed between the loading frame and rock specimen. At the same time, two antifricition gaskets were placed between two rigid steel blocks and the end face of rock specimen, which decreased distinctly the effect of the end friction effects on the testing results of sandstone specimens of height-to-width ratio  $\sim 2.0$ .

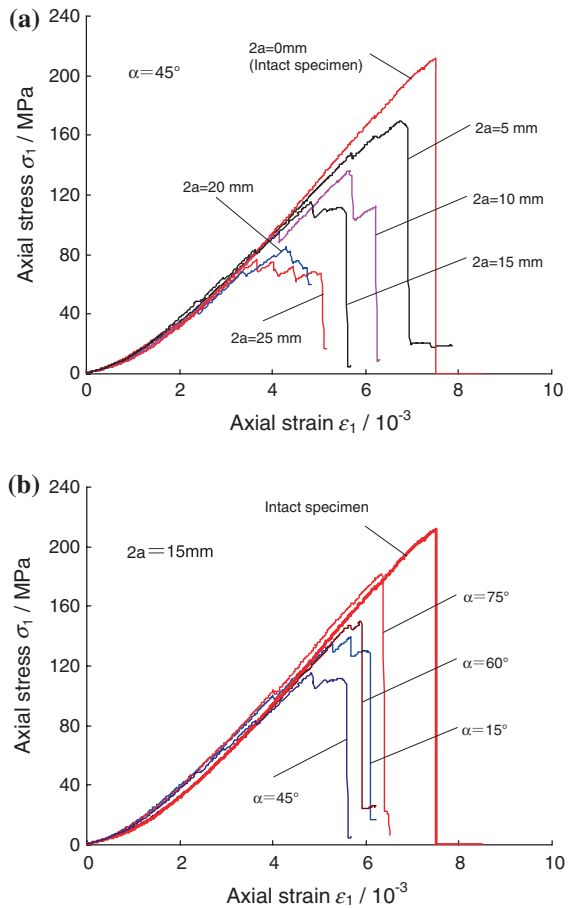
During the uniaxial compression test, in order to investigate the crack coalescence mechanism in the sandstone specimens containing single fissure, the AE technique was adopted. The AE counts and AE energy rate were recorded by AE21C-06 Acoustic Emission System (Fig. 2.4). The frequency of AE system

ranges from 5 kHz to 1 MHz and the recording event rate is 0.1 s. At the same time, the camera was used to trigger manually to capture images when the coalescence cracks developed or specimen failure occurred. When measuring AE signals, it is a pity that only one AE sensor was stuck on the sandstone specimens (Fig. 2.4) using Vaseline as a coupling agent and fixed slightly by cellulose tape, which is approximately similar to that of Li et al. (2005). Notice the AE sensor is near the pre-existing fissure in the specimen.

## 2.2 Strength and Deformation Behavior

Axial stress–axial strain curves for sandstone specimens containing single fissure under uniaxial compression are shown in Fig. 2.5, in which the axial stress–axial strain curve of intact sandstone specimen is also plotted. From Fig. 2.5, it is clear

**Fig. 2.5** Axial stress–axial strain curves of sandstone specimens containing a single fissure under uniaxial compression, in which (a) and (b), respectively, show the effect of fissure length and fissure angle on axial stress–axial strain curves (with kind permission of Springer Publisher)



that the fissure length and fissure angle have a key effect on the strength and deformation behavior of sandstone specimens under uniaxial compression, which will be analyzed in detail as follows.

### 2.2.1 Uniaxial Stress–Strain Curves of Sandstone

In accordance with the axial stress–axial strain curve shown in Fig. 2.5 and the failure mode plotted in Fig. 2.6, we can see that the sandstone in this chapter is a kind of brittle rock and takes on typically axial splitting failure, i.e., the axial stress drops abruptly to zero in 2 s after peak stress and a huge failure sonic can be heard during dropping. Notice the intact specimen was fractured into many small blocks under uniaxial compression. The axial stress–axial strain behavior of sandstone containing a single fissure can be approximately divided into four typical stages, i.e., fissure closure, elastic deformation, crack growth and propagation, and strain-softening.

In the stage of fissure closure, the uniaxial compression stress–strain curve of sandstone specimen containing different single fissure geometries shows the downward concave and the initial nonlinear deformation at low stress levels, which results from the closure of some primary pores and voids in the specimen with increasing compression stress. Moreover, the rigidity of the sandstone specimen at the initial stage of deformation (Fig. 2.5) has better consistency and is not dependent on fissure length and fissure angle, which results from better homogeneity of tested rock material. In the stage of elastic deformation, loading begins with increase in axial stress after the primary fissure closure in intact and flawed sandstone specimen, and elastic deformation dominates the stress–strain curve of

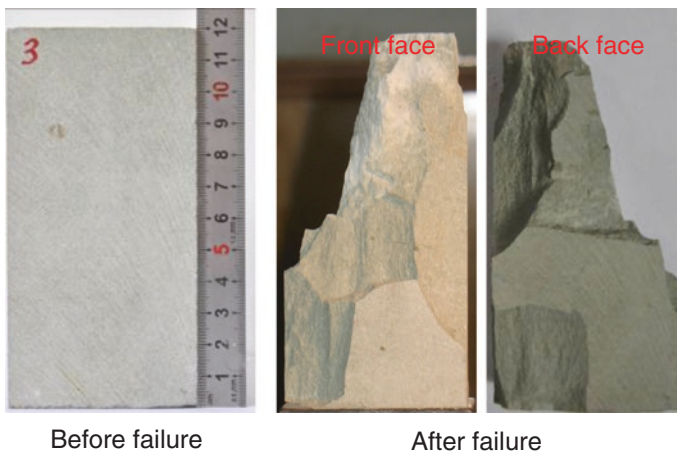


**Fig. 2.6** Typically axial splitting failure of intact sandstone specimen in this chapter (with kind permission of Springer Publisher)

specimen. The linear stress–strain behavior of intact and flawed sandstone specimen does not change although there are some irrecoverable processes such as the fissure closure or crack initiation at this stage. However, it needs to be noted that even at this stage of elastic deformation, some initiated cracks from the tips of fissure in flawed specimen have still been possible to propagate along the direction of axial stress, which is different from intact specimen.

However, at the stage of crack growth and propagation, the sandstone specimen continuously produces stress concentration near the tips of pre-existing single fissure, which result in some new cracks that initiate and propagate from the upper and under tips along the direction of axial stress. Therefore the stress–strain curve departs from the elastic behavior and shows distinct nonlinear deformation. In the stage of strain-softening, the macroscopic crack in intact and flawed sandstone specimen comes out rapidly and the post-peak behavior in the stress–strain curves shows a rapid drop. At this time, the specimen can only support lower axial stress, even though there is no axial stress.

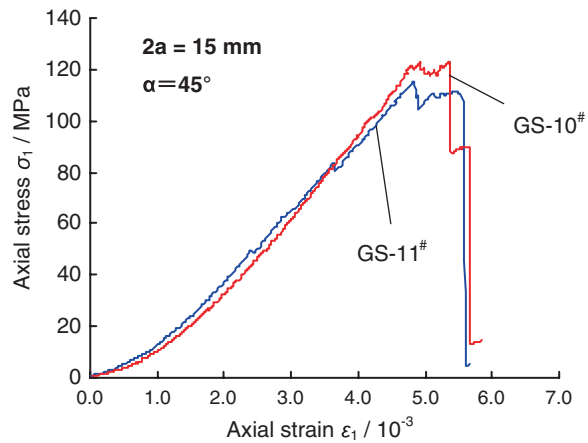
It needs to be noted that the stress–strain curves of sandstone specimen containing single fissure show an abrupt change of slope before peak strength, which is coincident with the propagation of some cracks at the upper and under tips of pre-existing fissures. For the abrupt change in the stress–strain curve, we will make a detailed analysis and explanation in Sect. 2.4. Moreover, compared with intact specimen, specimens containing single fissure take on the localization deformation failure nearby peak strength, which is closely related to the fissure length and fissure angle. For specimens containing longer fissures (keeping  $\alpha = 45^\circ$ ) or larger fissure angles (keeping  $2a = 15$  mm), the localization deformation failure nearby peak strength is more distinct, as shown in Fig. 2.5.

### ***2.2.2 Effect of Single Fissure Geometry on Mechanical Parameters of Sandstone***

In this section, the influence of single fissure geometry is investigated on the strength and deformation parameters of sandstone specimens under uniaxial compression, which are listed in detail in Table 2.2. Before analyzing the effect of single fissure geometry on strength and deformation parameters of sandstone, we first investigate the influence of heterogeneity of sandstone material on axial stress–axial strain curve of specimens containing a single fissure ( $2a = 15$  mm and  $\alpha = 45^\circ$ ) under uniaxial compression, which is presented in Fig. 2.7. From Fig. 2.7, the heterogeneity has nearly no effect on the strength and deformation parameters of two specimens containing the same single fissure, which have good consistency. Therefore, the dispersion of sandstone specimen containing a single fissure in this chapter is very small, and the strength and deformation parameters listed in Table 2.2 can be used to discuss approximately the effect of single fissure geometry on the mechanical parameters of sandstone under uniaxial compression. But due to limited tested specimens from the same block, we cannot repeat the

**Table 2.2** Mechanical parameters of sandstone specimens containing a single fissure under uniaxial compression

Specimen	$\alpha^\circ$	$2a$ (mm)	$\sigma_c$ (MPa)	$E_S$ (GPa)	$E_{50}$ (GPa)	$\varepsilon_{1c}(10^{-3})$	Note
GS-03#	N/A	0	212.08	35.95	24.37	7.500	Intact specimen
GS-04#	45	5	170.04	31.47	22.63	6.768	Fissure length
GS-07#	45	10	136.39	30.74	20.91	5.671	
GS-10#	45	15	122.80	28.61	20.54	5.358	
GS-14#	45	20	85.29	28.21	17.09	4.308	
GS-17#	45	25	77.25	28.56	16.81	3.674	
GS-19#	15	15	139.28	32.86	22.95	5.663	Fissure angle
GS-11#	45	15	115.17	28.11	21.13	4.827	
GS-25#	60	15	149.96	32.25	21.68	5.881	
GS-28#	75	15	181.71	33.97	24.93	6.348	

**Fig. 2.7** Effect of heterogeneity on axial stress–axial strain curve of sandstone specimens containing a single fissure ( $2a = 15$  mm and  $\alpha = 45^\circ$ ) under uniaxial compression (with kind permission of Springer Publisher)

test for other specimens of different fissure lengths and angles. Moreover, because sandstone is a kind of natural geological material; complete axial stress–axial strains of two specimens in Fig. 2.7 have some minor differences, which results from the effect of heterogeneity on the crack coalescence process of rock.

The definition for every mechanical parameter in Table 2.2 is described as follows.  $\sigma_c$  is defined as the uniaxial compressive strength and  $\varepsilon_{1c}$  is defined as peak axial strain value.  $E_S$  represents the elastic modulus; but  $E_{50}$  is defined as deformation modulus. More detailed descriptions of Young's modulus can be found in (Yang and Jiang 2010). In accordance with Table 2.2, the effect of fissure length and fissure angle on the  $\sigma_c$ ,  $\varepsilon_{1c}$ ,  $E_S$ , and  $E_{50}$  of sandstone specimen containing a single fissure are analyzed and discussed in detail (Figs. 2.8 and 2.9). The uniaxial compressive strength, Young's modulus and peak axial strain of sandstone specimens with pre-existing single fissure are all lower than that of intact sandstone specimen, while the reduction extent has a significant relation to the fissure length and fissure angle.

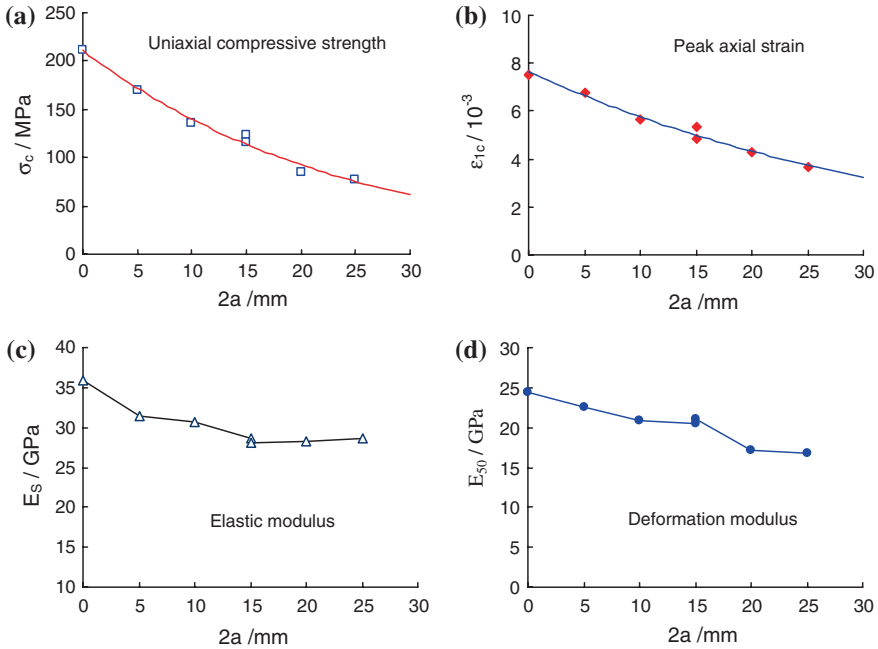


**Fig. 2.8** Effect of fissure length on the strength and deformation parameters of sandstone specimens with the same fissure angle ( $\alpha = 45^\circ$ ) under uniaxial compression (with kind permission of Springer Publisher)

The uniaxial compressive strength of intact specimen was 212.08 MPa, while it could be seen that the UCS of specimens containing single fissure ranged from 77.25 MPa ( $\alpha = 45^\circ$  and  $2a = 25$  mm) to 181.71 MPa ( $\alpha = 75^\circ$  and  $2a = 15$  mm), while the reduction extent of uniaxial compressive strength was between 14.3 and 63.6 %. In accordance with Fig. 2.8a, one can conclude that the uniaxial compressive strength will decrease with increase in fissure length. However, for the relation between uniaxial compressive strength and fissure angle, according to Fig. 2.9a, it can be seen that the uniaxial compressive strength first decreases and then increases with increasing fissure angle.

The intact sandstone specimen failed at a strain of 0.75 % under uniaxial compression, while sandstone specimens containing a single fissure failed at a strain of approximately 0.37–0.68 %, which is less than that of intact specimen. Moreover, the peak axial strain  $\epsilon_{1c}$  of sandstone specimen is dependent distinctly to fissure length and fissure angle. In accordance with Fig. 2.8b, one can conclude that the peak axial strain decreases with increase in fissure length. However, for the relation between peak axial strain and fissure angle, in accordance with Fig. 2.9b, it can be seen that  $\epsilon_{1c}$  has a nonlinear relation with the fissure angle.

The elastic modulus and deformation modulus of intact specimen were 35.95 and 24.37 GPa, respectively. However, the elastic modulus of specimen containing

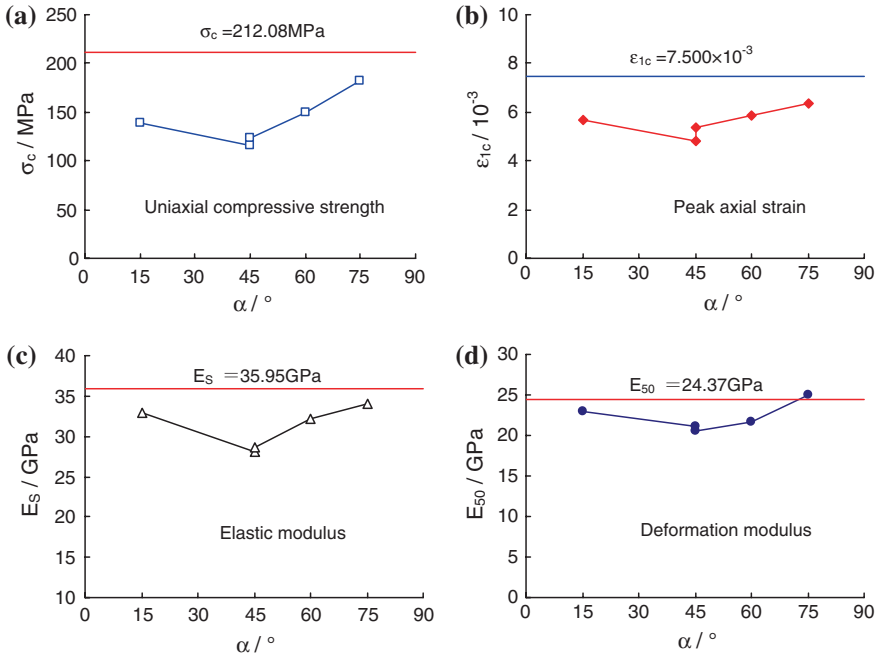


**Fig. 2.9** Effect of fissure angle on the strength and deformation parameters of sandstone specimens with the same fissure length ( $2a = 15$  mm) under uniaxial compression (with kind permission of Springer Publisher)

a single fissure ranged from 28.11 GPa ( $\alpha = 45^\circ$  and  $2a = 15$  mm) to 33.97 GPa ( $\alpha = 75^\circ$  and  $2a = 15$  mm), while the reduction extent of elastic modulus was between 5.5 and 21.8 %. The deformation modulus of specimen containing a single fissure ranged from 16.81 GPa ( $\alpha = 45^\circ$  and  $2a = 25$  mm) to 24.93 GPa ( $\alpha = 75^\circ$  and  $2a = 15$  mm), while the reduction extent of deformation modulus was between -2.3 and 31 %. On the whole, the Young’s modulus of sandstone has a decreasing trend with increase in fissure length, but a nonlinear relation with the fissure angle. Notice, for the fissured specimen with the same angle ( $\alpha = 45^\circ$ ), the elastic modulus of specimen tends to a stable value  $\sim 28$  GPa after the fissure length increases to 15 mm.

Among all the specimens containing single fissure, the deformation moduli of the specimens GS-14<sup>#</sup> ( $\alpha = 45^\circ$  and  $2a = 20$  mm) and GS-17<sup>#</sup> ( $\alpha = 45^\circ$  and  $2a = 25$  mm) are lowest and approximately 17 GPa, which results from the axial stress corresponding to an abrupt change of slope before peak strength is lower than half the peak strength. Except for the specimens GS-14<sup>#</sup> and GS-17<sup>#</sup>, the average deformation modulus of other specimens containing a single fissure is about 22.37 GPa, which reaches 91.8 % of the deformation modulus  $\sim 24.37$  GPa of intact specimen, and the dispersion coefficient (the percentage of the differential value between the maximum and minimum value to the average value) is approximately 18 %.

From the above analysis, one can conclude that, for the specimen with longer fissure or the fissure angle of  $45^\circ$ , the corresponding mechanical parameters are all lower, which shows that the longer fissure and fissure angle of  $45^\circ$  in the specimen have a significant effect on the strength and deformation parameters of sandstone specimen. Moreover, the influence of single fissure geometries on the uniaxial compressive strength and peak axial strain is higher than that on the Young's modulus for such brittle sandstone material.

## 2.3 Crack Evolution Behavior

In this chapter, the intact sandstone specimen leads to typically axial splitting failure (Fig. 2.6), which is a good agreement with many laboratory testing results of brittle rocks. It needs to be explained that we did not observe any crack coalescence for intact specimen before peak strength; moreover, the intact specimen failed in 2 s after peak stress and a huge failure sonic was heard during testing. At the same time, the intact specimen was fractured into many small blocks, see Fig. 2.6. However, for specimens containing a single fissure, under uniaxial compression, different failure modes were observed in comparison with that of intact specimen. The crack coalescence was all observed from upper and under tips of pre-existing fissure in sandstone specimens containing single fissure, and ultimate failure mode is distinctly dependent on the fissure length and fissure angle. Therefore, in this section, systematic evaluation is made on crack coalescence in sandstone specimens by photographic monitoring and AE technique.

### 2.3.1 Crack Coalescence Type of Sandstone Specimens Containing a Single Fissure

Nine different crack types (Fig. 2.10) were identified based on their geometry and crack propagation mechanism (tensile, shear, lateral crack, far-field crack, and surface spalling) by analyzing the ultimate failure modes of sandstone specimens containing a single fissure (Figs. 2.11 and 2.12). In accordance with Fig. 2.10, one can see that five of them (crack types I–VI) are tensile, one of them (crack type VI) is lateral crack, one of them (crack type VII) is shear, one of them (crack type VIII) is far-field, and one of them (crack type IX) is surface spalling. All crack types can be categorized as follows:

- (1) *Crack type I*: Wing crack initiates simultaneously from upper and under tips of single fissure. The tensile wing crack usually initiates along the vertical direction to pre-existing fissure, and then gradually departs toward the direction of axial stress, and finally develops along the direction of axial stress. Moreover, due to very fine grain sizes in sandstone material, this coalescence path of tensile wing crack I is very smooth.

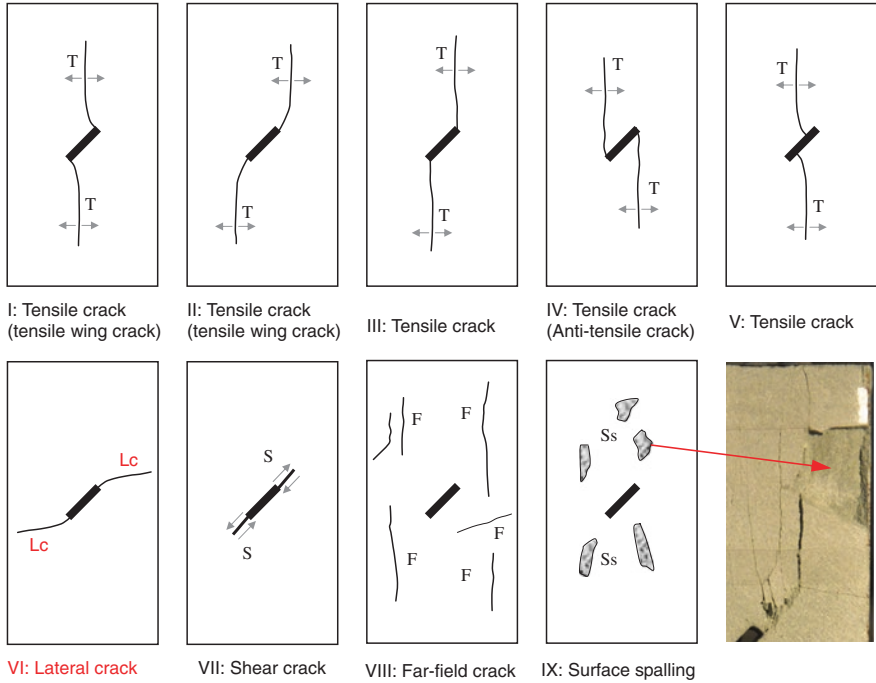


**Fig. 2.10** Various crack types from single fissure identified in this chapter. *T* Tensile crack, *Lc* Lateral crack, *S* Shear crack, *F* Far-field crack, *Ss* Surface spalling (with kind permission of Springer Publisher)

- (2) *Crack type II*: Wing crack often initiates simultaneously from upper and under tips of single fissure. The wing cracks initiate first along the direction of the fissure, and then gradually turn toward the direction of axial stress, and finally develop toward the end face of specimen.
- (3) *Crack type III*: Tensile crack initiates from upper or under tip of single fissure. Usually, the tensile crack III develops along the direction completely parallel to the axial stress, but the crack coalescence path is not very smooth.
- (4) *Crack type IV*: The crack coalescence is reverse to that of crack type III, which is referred to as “anti-tensile crack.” The anti-tensile crack also initiates from upper or under tip of single fissure, and develops along the direction of the axial stress.
- (5) *Crack type V*: The tensile crack usually initiates from this position which is located at a distance away from the tips of single fissure. The tensile crack initiates along the vertical direction to the fissure, and then gradually departs toward the direction of axial stress, and finally develops along the direction of axial stress.
- (6) *Crack type VI*: The crack initiates from upper or under tip of single fissure. The lateral crack initiates first along the direction to the fissure, and then

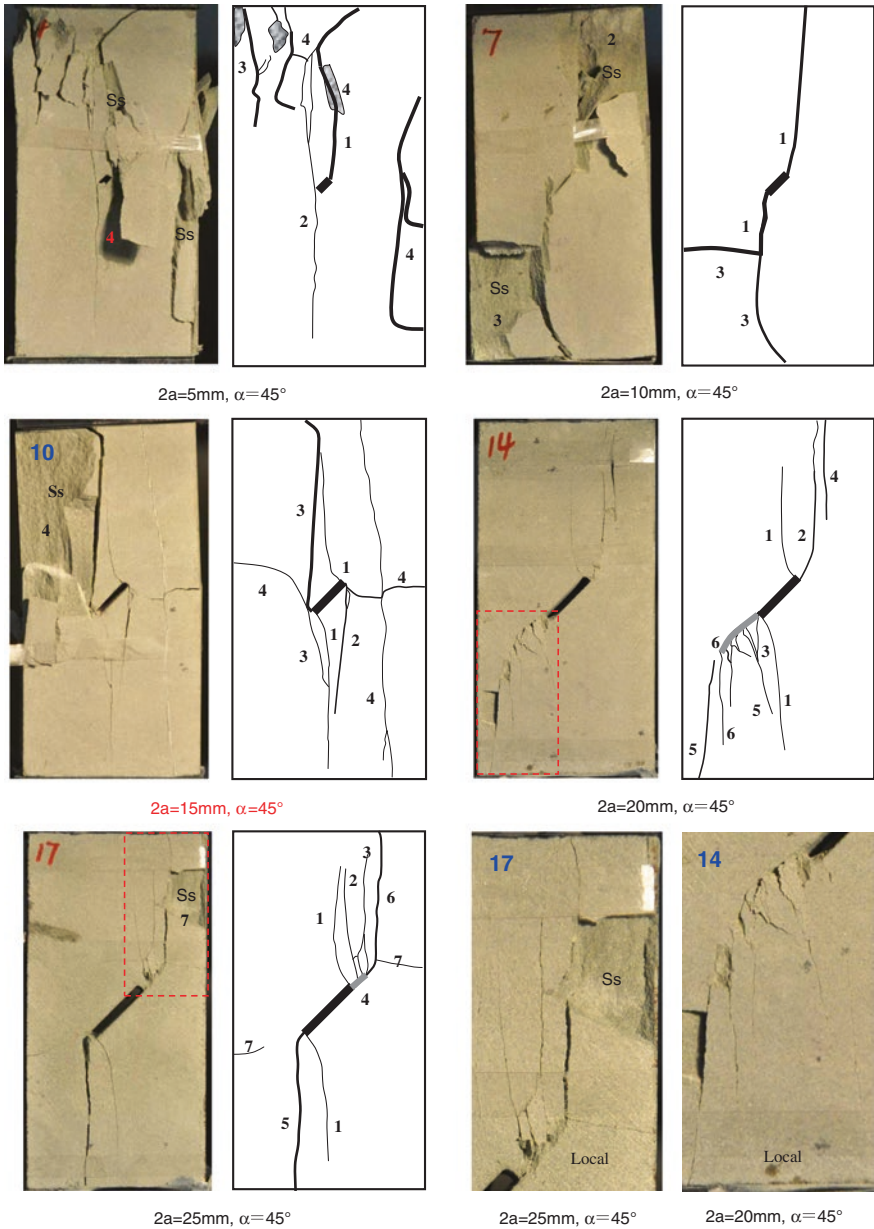


**Fig. 2.11** Effect of fissure length on ultimate failure modes of brittle sandstone specimens containing single fissure under uniaxial compression ( $\alpha = 45^\circ$ ) (with kind permission of Springer Publisher)

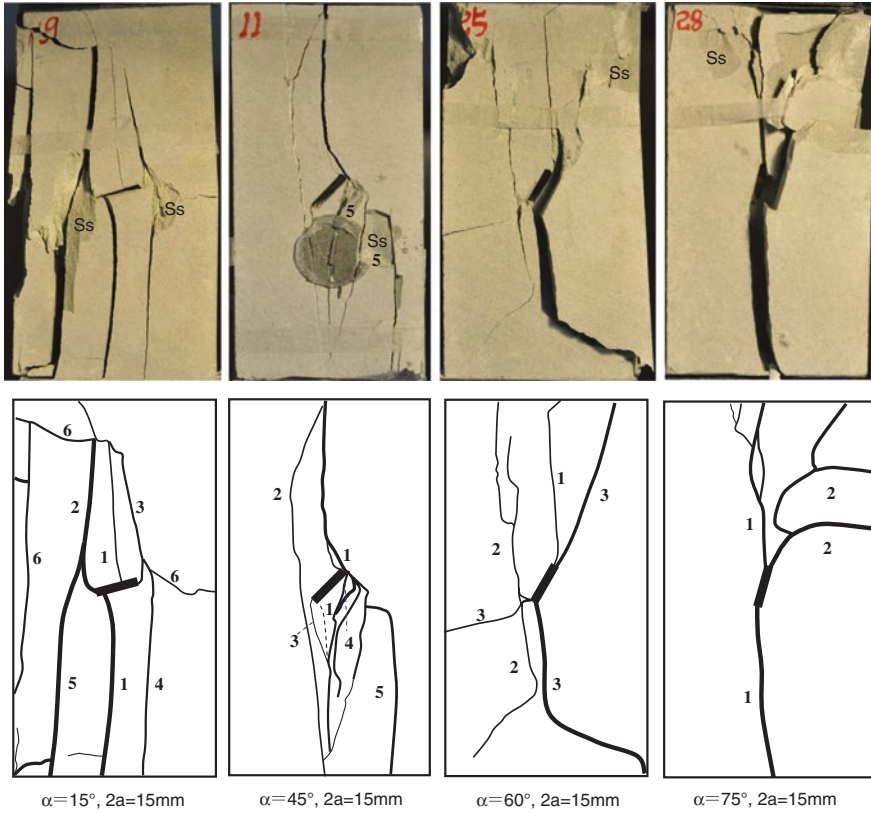


**Fig. 2.12** Effect of fissure angle on ultimate failure modes of brittle sandstone specimens containing single fissure under uniaxial compression ( $2a = 15 \text{ mm}$ ) (with kind permission of Springer Publisher)

gradually turns toward the horizontal direction, and finally develops toward the lateral face of specimen.

- (7) *Crack type VII*: The shear crack initiates from upper or under tip of single fissure, where the crack coalescence path is parallel to the direction of pre-existing fissure. The shear crack and pre-existing fissure are coplanar.
- (8) *Crack type VIII*: The far-field crack does not usually initiate from the tips of single fissure. Moreover, the far-field crack coalescence path is not very smooth, which may be vertical or horizontal in the process of loading.
- (9) *Crack type IX*: The surface spalling shown in Fig. 2.10 is often observed for brittle rock material. The surface spalling usually appears after some tensile cracks (such as crack types I–III) or accompanies with the process of tensile crack (such as crack type IV) propagation.

In accordance with the above nine crack types, one can analyze the ultimate failure mode and cracking process of sandstone specimens containing a single

**Table 2.3** Initiated crack types of sandstone specimens containing single fissure with different lengths and angles

Specimen	Crack types								
	I: Tensile	II: Tensile	III: Tensile	IV: Tensile	V: Tensile	VI: Lateral	VII: Shear	VIII: Far-field	IX: Surface spalling
GS-03 <sup>#</sup>	Intact specimen: typically axial splitting failure (Fig. 2.6)								
GS-04 <sup>#</sup>			√1					√	√ (more)
GS-07 <sup>#</sup>			√1					√	√ (more)
GS-10 <sup>#</sup>	√1		√	√		√		√	√ (more)
GS-14 <sup>#</sup>	√1	√	√				√	√	
GS-17 <sup>#</sup>	√1	√	√				√	√ (small)	√ (small)
GS-19 <sup>#</sup>			√	√	√1	√		√	√ (small)
GS-11 <sup>#</sup>	√1		√	√				√	√ (small)
GS-25 <sup>#</sup>			√1	√		√	√	√	√
GS-28 <sup>#</sup>			√1			√		√	√

Note √1 indicates that the crack is the first crack to initiate from the tips of pre-existing fissure

fissure under uniaxial compression (Figs. 2.11 and 2.12; Table 2.3). It is clear that the macroscopic failure mode of sandstone specimens containing a single fissure (Figs. 2.11 and 2.12) are all a mixture of several cracks among the above nine various crack types. For example, the failure mode of the specimen GS-17<sup>#</sup> ( $2a = 25 \text{ mm}$ ,  $\alpha = 45^\circ$ ) is a mixture of cracks I–III and VII–IX. From Table 2.3, some qualitative conclusions can be summarized as follows.

Table 2.3 summarizes initiated crack types of sandstone specimens containing single fissure with different lengths and angles in response to the applied axial loads. As indicated in Table 2.3, tensile cracks I and III are often the first cracks to initiate from the tips of pre-existing fissure. But sometimes, the tensile crack V located at a distance away from the tips of single fissure is also the first crack, and is only observed in the specimen GS-19<sup>#</sup> ( $2a = 15 \text{ mm}$ ,  $\alpha = 15^\circ$ ), which is possible to result from the heterogeneity of rock material or lower fissure angle. For tensile crack IV, it is clear that anti-tensile crack IV often accompanies with tensile crack III toward the reverse direction, which is usually observed in the specimen with fissure length of 15 mm.

It needs to be noted that tensile wing crack I is usually easier to initiate and nucleate from the tips of the longer fissures, e.g., the fissure length is 20 or 25 mm. Keeping the fissure length of the specimen 15 mm as a constant, only the specimen with fissure angle of  $45^\circ$  initiates tensile wing crack I from the tips of single fissure. Tensile wing crack II is observed only when the fissure length is equal to 20 or 25 mm. But surface spalling IX initiates in all other specimens containing single fissure except for the specimen GS-14<sup>#</sup>. However, the tensile crack III and far-field crack VIII are all observed in all the flawed specimens. The above phenomenon shows that cracks III, VIII–IX are easier to occur during loading for brittle rock material.

In accordance with Table 2.3, tensile crack V is rare, which is only observed in the specimen GS-19<sup>#</sup> ( $2a = 15$  mm,  $\alpha = 15^\circ$ ). Tensile crack IV initiates from the tips of fissure only when the fissure angle is lower than  $60^\circ$ , but lateral crack VI is only observed in specimens with fissure length of 15 mm except for the specimen GS-11<sup>#</sup>. Moreover, it can be concluded that shear crack VII usually occurs in specimens containing longer fissures, such as  $2a = 20$  or 25 mm. But sometimes, the shear crack VII is also observed in the fissured specimen ( $2a = 15$  mm,  $\alpha = 60^\circ$ ), which shows the fissure angle  $\sim 60^\circ$  makes the specimen easier to emanate the crack VII along the direction of pre-existing fissure.

From Figs. 2.11 and 2.12, it can also be seen that some wing cracks appear to be arrested a certain distance from the upper and lower boundaries of the specimen, which is probably related to the confining stress induced by friction between the specimen and the steel platen.

### 2.3.2 AE Behaviors of Intact and Flawed Sandstone Specimens with Single Fissure Geometries

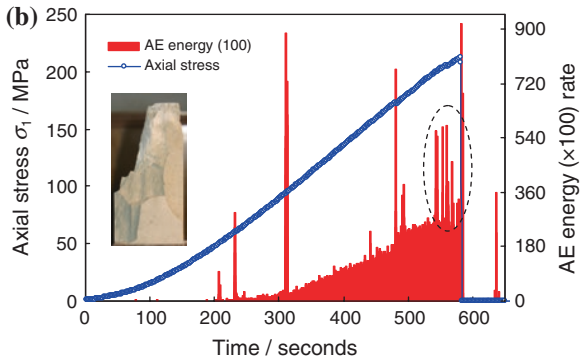
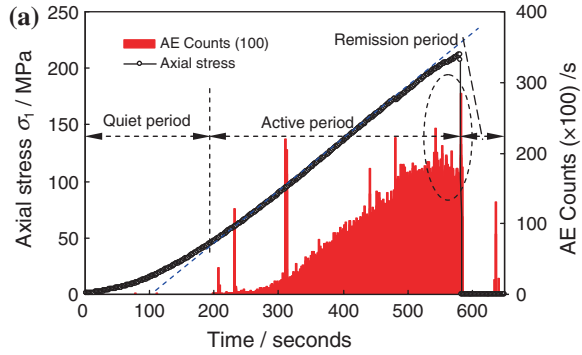
AE monitoring is useful for exploring the failure process and crack coalescence mechanism of brittle rocks, especially for flawed rocks with pre-existing fissures. Therefore, during the uniaxial compression test, the AE technique is adopted for the sandstone specimens in this chapter.

Figure 2.13 shows the AE counts and AE energy of intact sandstone specimen during the whole deformation failure, however, Figs. 2.14, 2.15, 2.16, 2.17, and 2.18 show the AE counts of some typical sandstone specimens containing single fissure in the process of uniaxial compression test. In accordance with the AE results shown in Figs. 2.14, 2.15, 2.16, 2.17, and 2.18, a detailed investigation of the AE characteristics of brittle sandstone specimens with different fissure geometries was carried out. The AE characteristics of intact and flawed sandstone containing single fissure can be approximately divided into three typical periods, i.e., quiet period, active period, and remission period (Fig. 2.13a).

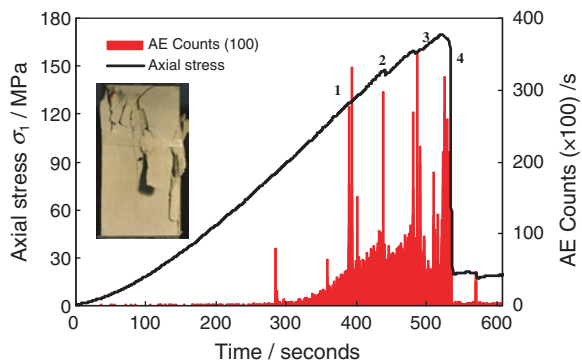
In the quiet period, the uniaxial compression stress–time curve of intact and fissured sandstone specimen all show the downward concave and the initial nonlinear deformation at low stress levels. Notice, the quiet period corresponds to the stage of fissure closure, therefore the AE events are not very active and the AE counts are also very rare compared with the active period, which results from only occurrence of fissure closure at this stage. Moreover, we can see that for hard and brittle sandstone material, the AE behavior at quiet period is not dependent on the fissure geometries, including fissure length and fissure angle.

In the active period, the stress–strain curves of sandstone specimens undergo two different stages, i.e., the stage of elastic deformation, and the stage of crack growth and propagation. With the increase of time, the axial stress increases linearly at the stage of elastic deformation, but when increasing to yielding stress, the axial stress–time curve occurs to depart from the linear curve and shows

**Fig. 2.13** AE counts and AE energy of intact sandstone specimen during the whole deformation failure. The number in *double bracket* in vertical axis labels is the multiplier of coordinates (with kind permission of Springer Publisher)



**Fig. 2.14** Relation between axial stress, AE counts, and time of sandstone specimen containing short fissure ( $2a = 5 \text{ mm}$ ,  $\alpha = 45^\circ$ ) (with kind permission of Springer Publisher)



distinctly nonlinear behavior. For intact specimen (Fig. 2.13), the AE events are quite active, and the AE counts are dense and stable. Moreover, with the increase of axial stress, the AE counts and energy of intact specimen all increase continuously. But after yielding stress, although the AE counts of intact specimen do not increase with increase of time, the AE energy increases rapidly as shown in elliptical zone (Fig. 2.13), which further validates abrupt splitting failure of brittle sandstone (Fig. 2.6).

**Fig. 2.15** Relation between axial stress, AE counts, and time of sandstone specimen containing medium fissure ( $2a = 15 \text{ mm}$ ,  $\alpha = 45^\circ$ ) (with kind permission of Springer Publisher)

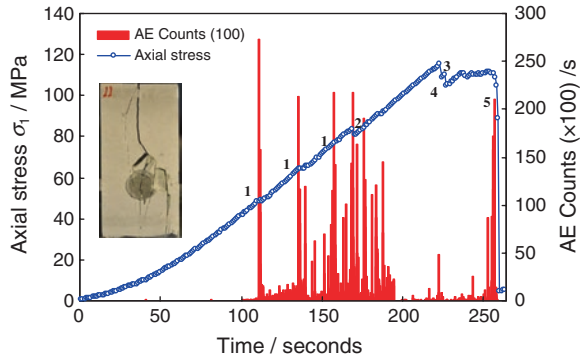
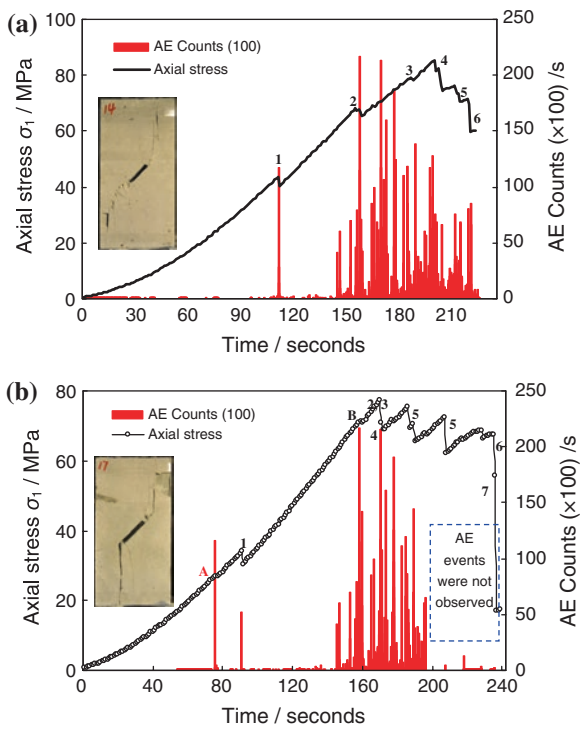


**Fig. 2.16** Relation between axial stress, AE counts, and time of sandstone specimen containing the longer fissure **a**  $2a = 20 \text{ mm}$ ,  $\alpha = 45^\circ$ ; **b**  $2a = 25 \text{ mm}$ ,  $\alpha = 45^\circ$ . Note the AE counts in the square were not observed (with kind permission of Springer Publisher)



However, for flawed specimen with single fissure (Figs. 2.14, 2.15, 2.16, 2.17 and 2.18), the AE behaviors during deformation failure are different from that of intact specimen (Fig. 2.13) in the active period, which is distinctly related to fissure length and fissure angle. The AE counts of flawed specimen with single fissure are more decentralized than that of intact specimen; moreover, the AE counts of all flawed specimens with single fissure have several larger peak values before peak strength, which correspond to the crack initiation and propagation in the specimens. Notice, the quiescence of the AE observed before the failure is probably due to the

**Fig. 2.17** Relation between axial stress, AE counts, and time of sandstone specimen containing lower angles ( $2a = 15 \text{ mm}$ ,  $\alpha = 15^\circ$ ) (with kind permission of Springer Publisher)

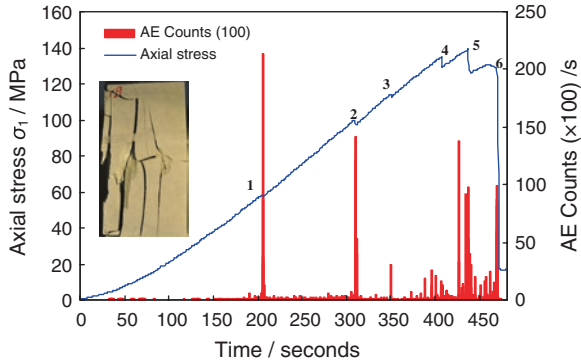
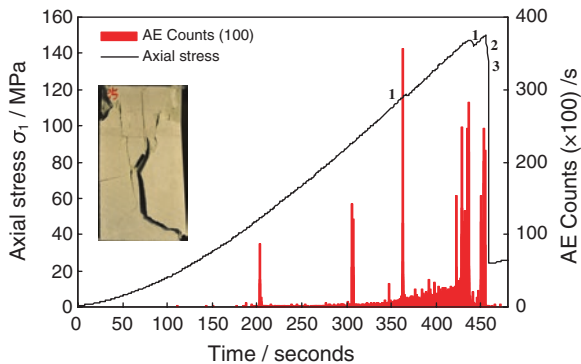


**Fig. 2.18** Relation between axial stress, AE counts and time of sandstone specimen containing higher angles ( $2a = 15 \text{ mm}$ ,  $\alpha = 60^\circ$ ) (with kind permission of Springer Publisher)



increasing attenuation as cracks propagate. This is often observed particularly when spalling occurs near the surface (Wassermann et al. 2009).

In accordance with the AE counts shown in Figs. 2.14, 2.15 and 2.16, one can conclude that the fissure length has great influence on the AE behavior in the active period. When the fissure length is shorter ( $2a = 5 \text{ mm}$ ) in Fig. 2.14, the dense extent of AE counts of flawed specimen is approximately similar to that of intact specimen (Fig. 2.13a), but the flawed specimen has several larger peak values. For the specimens containing medium fissure ( $2a = 15 \text{ mm}$ ) in Fig. 2.15, several larger peak values of AE signals are observed at the stage of elastic deformation, while AE counts are very rare at the stage of crack growth and propagation, which shows that there is no distinct crack coalescence at this stage. However, for specimens containing longer fissures ( $2a = 20, 25 \text{ mm}$ ) as shown in Fig. 2.16, the AE behavior is reverse to that of flawed specimens ( $2a = 15 \text{ mm}$ ), whereby the AE events are not active and AE counts are very rare at the stage of elastic deformation, but very dense at the stage of crack growth and propagation.

From Figs. 2.17 to 2.18, one can also see the effect of fissure angle on the AE behaviors at the active period. For flawed specimens with lower angle ( $\alpha = 15^\circ$ ), the AE events are not very active and AE counts are very rare except for

several larger AE peak values. However, for flawed specimens with larger angle ( $\alpha = 60^\circ$ ), the AE behaviors are approximately the same as that with lower angle ( $\alpha = 15^\circ$ ) at the stage of elastic deformation, while the AE counts at the stage of crack growth and propagation are more and denser than that with lower angle ( $\alpha = 15^\circ$ ).

At the remission period (i.e., the stage of strain-softening), the AE counts and energy of intact specimen are rare. The AE behaviors of flawed specimen with shorter fissure ( $2a = 5$  mm) or higher angle ( $\alpha = 60^\circ$ ) are approximately the same as that of intact specimen, which results from little occurrence of macroscopic cracks after peak strength. But, the AE behaviors of flawed specimen with medium fissure ( $2a = 15$  mm) are not dependent on the fissure angle, which shows that the AE counts undergo first a relative steady phase and then increase abruptly with increasing time, as shown in Figs. 2.15 and 2.17. However, for flawed specimen with longer fissure ( $2a = 20$  and  $25$  mm), it can be seen from Fig. 2.16 that the AE counts are more and relatively denser, which results from gradual crack coalescence in the specimens after peak strength. It needs to be noted that the AE events in the square in Fig. 2.16b were not observed, which is due to the departure between AE sensor and specimen surface.

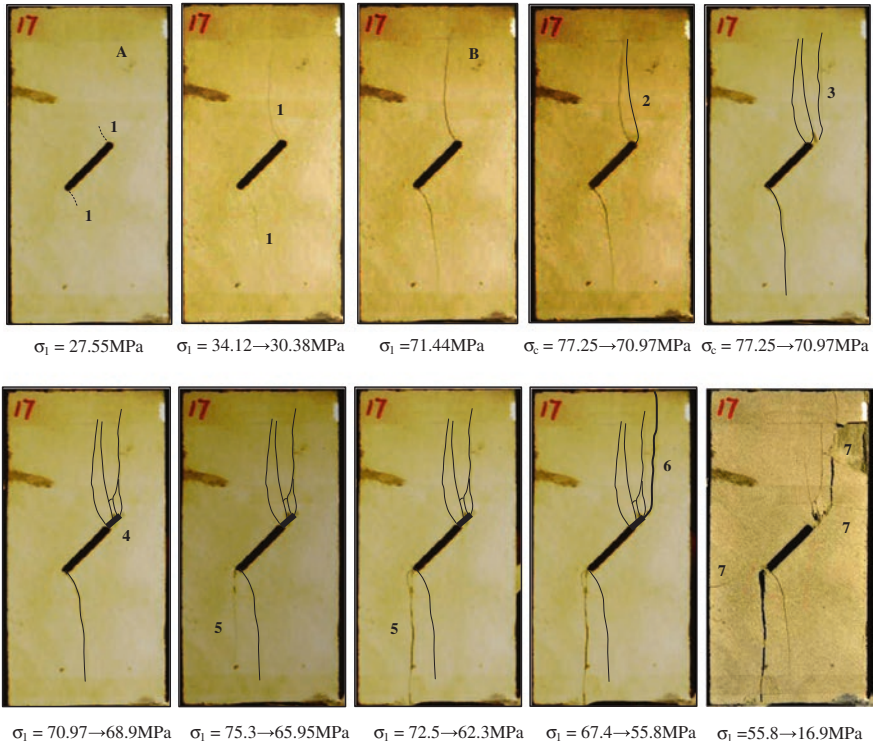
In sum, the above analysis shows clearly that the AE behaviors of specimen are closely dependent on the crack coalescence in the specimen, which will be analyzed and discussed detailed in the following section.

### ***2.3.3 Real-Time Crack Evolution Process of Sandstone Containing a Single Fissure***

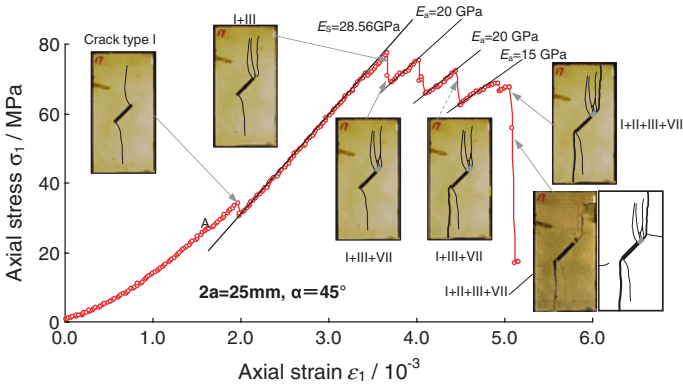
Besides the previous AE technique, photographic monitoring was also adopted during uniaxial compression test to clarify further the precedence relationship of crack coalescence in sandstone specimen. Based on the combined results on AE and photographic monitoring, the real-time crack coalescence process of sandstone containing a single fissure can result in a more detailed analysis as follows.

Figure 2.19 shows typical real-time crack coalescence process of sandstone specimens containing a single fissure ( $2a = 25$  mm,  $\alpha = 45^\circ$ ) using photographic monitoring. From Fig. 2.19, it is clear that photographic monitoring can be used to identify and characterize the crack coalescence process of flawed sandstone. Notice the denoted number and letter shown in Fig. 2.19 are corresponding to Fig. 2.16b. Figure 2.20 shows the influence of real-time crack coalescence on the strength and deformation failure behavior of sandstone specimens containing a single fissure ( $2a = 25$  mm,  $\alpha = 45^\circ$ ) under uniaxial compression.

In accordance with Fig. 2.16b and Figs. 2.19, 2.20, we can analyze real-time crack coalescence process of sandstone specimen containing a single fissure ( $2a = 25$  mm,  $\alpha = 45^\circ$ ). Before point A ( $\sigma_1 = 27.55$  MPa =  $35.7\% \sigma_c$ ) as shown in Fig. 2.16, the stress concentration at the tips of fissure does not reach the material strength nearby the tips, which does not result in a crack initiation. But when



**Fig. 2.19** Typical real-time crack coalescence process of sandstone specimen containing a single fissure ( $2a = 25 \text{ mm}$ ,  $\alpha = 45^\circ$ ). The denoted number and letter shown in the figure are corresponding to Fig. 2.16b (with kind permission of Springer Publisher)



**Fig. 2.20** Effect of real-time crack coalescence on the strength and deformation behavior of sandstone specimens containing a single fissure ( $2a = 25 \text{ mm}$ ,  $\alpha = 45^\circ$ ) under uniaxial compression (with kind permission of Springer Publisher)

the axial stress is loaded to point A, the specimen begins to initiate the wing crack I from the upper and under tips of fissure, but the crack is too fine to be observed with the unaided eyes or in video recordings. Notice the initiated stress of wing crack I is identified by AE counts, as shown in Fig. 2.16b. After point A, with the increase in axial deformation, the wing crack I further lengthens and propagates gradually to the edge of the specimen. When the specimen is loaded to 34.12 MPa ( $44.2\% \sigma_c$ ), the wing crack I undergoes a large and rapid evolution to the edge of the specimen, which leads to the axial supporting capacity dropping to 30.38 MPa in a smaller range of axial strain. Afterwards, with the increase of axial deformation, the wing crack I is difficult to lengthen due to the limitation of specimen boundary, but widens a lot. The continuous increase in deformation leads to the specimen being loaded to 77.25 MPa ( $100\% \sigma_c$ ). At this moment of about 171 s, cracks 2–3 (crack type III) develop rapidly to the edge of specimen in one second, and two subsequent tensile cracks III can only be snapped with photographic monitoring.

However, after the specimen is loaded to peak strength, the axial supporting capacity does not drop to zero. For the moment, the axial stress of this specimen is about 70.97 MPa and corresponding axial strain is  $\sim 3.67 \times 10^{-3}$ . Notice, the specimen still has a supporting structure (Fig. 2.20). Afterwards, with the increase of axial deformation, shear crack VII emanates from the upper tip of fissure and the corresponding axial stress drops rapidly from 70.97 to 68.9 MPa. At this time, the axial supporting capacity begins to increase slowly with increasing deformation. While due to obvious damage of supporting structure, the reloading average modulus  $\sim E_a$  (about 20 GPa) is distinctly lower than the elastic modulus ( $\sim 28.56$  GPa) before peak strength. When the specimen reaches the axial stress  $\sim 75.3$  MPa, crack 5 (crack type III) begins to initiate and propagate from the under tip of fissure along the direction of axial loading, which leads to the axial supporting capacity dropping to 65.95 MPa in a small range of axial strain. Afterwards, with increasing axial deformation, the axial stress begins to increase slowly and the reloading average modulus is approximately equal to 20 GPa, which indicates that the initiation and coalescence of crack 5 does not affect the average modulus, but reduces the axial supporting capacity of fractured rock. With the increase of axial deformation, the axial supporting capacity begins to increase slowly. But due to more obvious damage of supporting structure, the reloading average modulus (15 GPa) is distinctly lower than the previous average modulus (20 GPa) and the axial stress–axial strain begins to depart gradually toward the axial strain. When the specimen was loaded to 67.4 MPa (corresponding axial strain is  $5.06 \times 10^{-3}$ ), crack 6 (crack type II) occurs very fast. The axial stress of the specimen drops to 55.8 MPa and corresponding axial strain is  $5.09 \times 10^{-3}$ . Finally, with the increase of axial deformation, some far-field crack VIII and surface spalling IX are also observed, which results in rapid reduction of axial supporting capacity until 16.9 MPa in an almost constant axial strain.

Using photographic monitoring, Fig. 2.21 also presents the influence of real-time crack coalescence on the strength and deformation failure behavior of sandstone specimens containing a single fissure ( $2a = 15$  mm,  $\alpha = 15^\circ$ ) under uniaxial compression. Notice the denoted number shown in Fig. 2.21 is corresponding to Fig. 2.17.

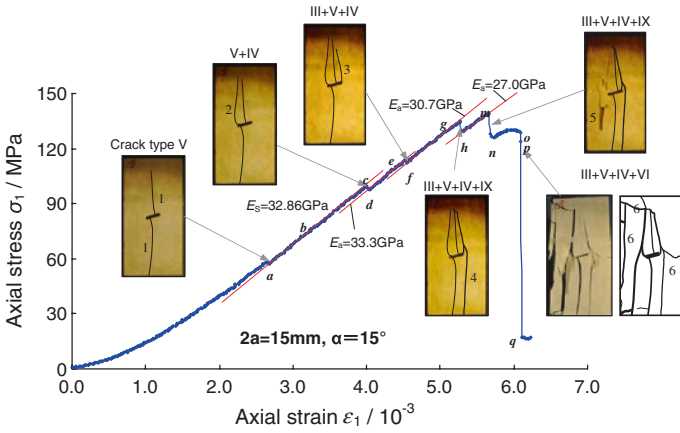


**Fig. 2.21** Effect of real-time crack coalescence on the strength and deformation behavior of sandstone specimens containing a single fissure ( $2a = 15 \text{ mm}$ ,  $\alpha = 15^\circ$ ) under uniaxial compression (with kind permission of Springer Publisher)

Comparing Fig. 2.21 with Fig. 2.20, it can be seen that more main crack coalescences shown in Fig. 2.20 occur after peak strength, while more main crack coalescences in Fig. 2.21 take place before peak strength, which results from the difference of fissure length and angle in the specimen.

In accordance with Fig. 2.21, we can also analyze real-time crack coalescence process of sandstone specimen containing a single fissure ( $2a = 15 \text{ mm}$ ,  $\alpha = 15^\circ$ ). Before point  $a$  ( $\sigma_1 = 58.40 \text{ MPa} = 41.9 \%\sigma_c$ ) as shown in Fig. 2.21, the stress concentration at the tips of fissure does not reach the material strength nearby the tips, which does not result in crack initiation. But when the axial stress is loaded to point  $a$ , the specimen begins to produce rapidly wing crack 1 (crack type V) from the upper and under tips of fissure, which can be observed with the naked eyes. When crack 1 propagates to the edge of the specimen, the axial stress undergoes a minor drop to 57.4 MPa from 58.4 MPa. After point  $a$ , crack 1 is difficult to lengthen due to the limitation of specimen boundary. The axial stress increases linearly with axial deformation as the elastic modulus of 32.86 GPa (Fig. 2.22a). When the specimen is loaded to point  $c$  ( $\sigma_1 = 99.9 \text{ MPa} = 71.7 \%\sigma_c$ ), crack 2 (crack type IV) produces from the under tip of fissure and propagates toward the upper edge of the specimen rapidly, which leads to the corresponding axial stress dropping rapidly from 99.9 to 98.4 MPa. At this time, the specimen has still a good supporting structure. Therefore, with increase of axial deformation, the axial supporting capacity begins to increase with approximately the same average modulus  $\sim 33.3 \text{ GPa}$  (Fig. 2.22b) as elastic modulus  $\sim 32.86 \text{ GPa}$  (Fig. 2.22a), which indicates that the initiation and propagation of cracks 1–2 have no influence on the elastic deformation behavior of the specimen. When the specimen is loaded to point  $e$  ( $\sigma_1 = 114.2 \text{ MPa} = 82 \%\sigma_c$ ), crack 3 (crack type III) emanates from the upper tip of fissure and the corresponding axial stress drops rapidly from 114.2

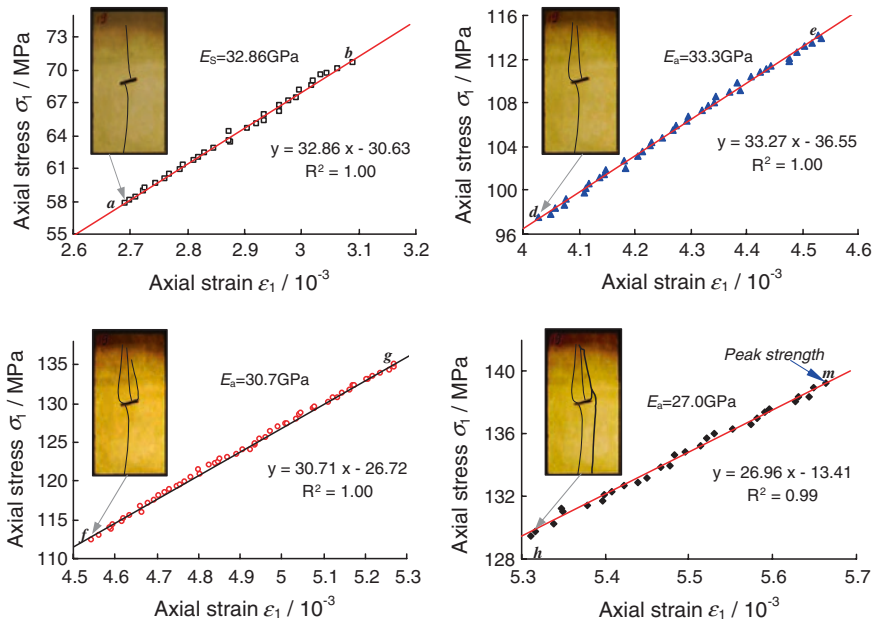


**Fig. 2.22** Relation between axial stress and axial strain after several crack coalescences in brittle sandstone specimen containing a single fissure ( $2a = 15$  mm,  $\alpha = 15^\circ$ ) under uniaxial compression (All the *symbols* represent experimental results and the *lines* represent the regression results) (with kind permission of Springer Publisher)

to 112.4 MPa. Afterwards, the axial supporting capacity begins to increase slowly with increasing deformation; while due to some minor damage of supporting structure, the reloading average modulus  $\sim 30.7$  GPa (Fig. 2.22c) is a little lower than the elastic modulus ( $\sim 32.86$  GPa).

Afterwards, when the specimen is loaded to point *g* ( $\sigma_1 = 135.1$  MPa = 97 % $\sigma_c$ ), crack 4 (crack type IV) emanates from the upper tip of fissure and the corresponding axial stress drops rapidly from 135.1 to 129.4 MPa. For the moment, the axial supporting capacity begins to increase slowly with increasing deformation; while due to obvious damage of supporting structure, the reloading average modulus  $\sim 27.0$  GPa (Fig. 2.22d) is distinctly lower than the elastic modulus ( $\sim 32.86$  GPa). The continuous increase of deformation leads to the specimen being loaded to 139.28 MPa (100 % $\sigma_c$ ), at this moment, crack 5 (crack type III) develops rapidly in 1 s, which leads to the axial supporting capacity dropping to 127.7 MPa in a smaller range of axial strain. From Fig. 2.22, we can see clearly that the axial stress of the specimen has a better linear relation with the axial strain after each larger crack coalescence in the specimen, which results probably from a kind of brittle and hard sandstone material in this chapter. However, after peak strength, the relation between axial stress and axial strain shown in Fig. 2.23 is distinctly different from that shown in Fig. 2.22. After axial stress of the specimen drops to point *n* ( $\sigma_1 = 126.22$  MPa = 90.6 % $\sigma_c$ ) from

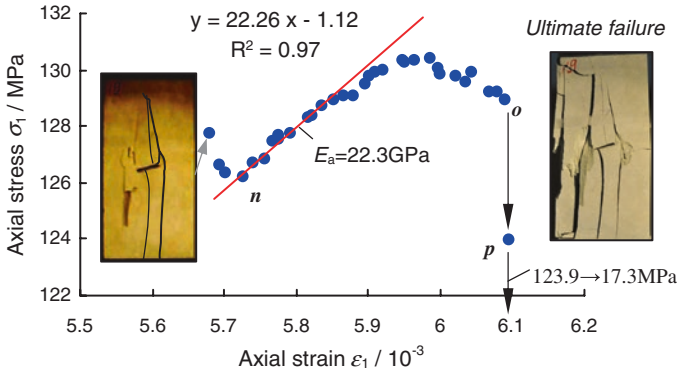


**Fig. 2.23** Relation between axial stress and axial strain in brittle sandstone specimen containing a single fissure ( $2a = 15 \text{ mm}$ ,  $\alpha = 15^\circ$ ) after peak strength under uniaxial compression (with kind permission of Springer Publisher)

127.7 MPa, the axial supporting capacity begins to increase slowly with increase of axial deformation. But due to more obvious damage of supporting structure, the reloading average modulus (22.26 GPa) is distinctly lower than the previous average modulus (27 GPa) and the axial stress–axial strain begins to depart gradually toward the axial strain. When the specimen was loaded to point *o*, crack 6 occurs very fast. The axial stress of the specimen drops to 17.3 MPa and the corresponding axial strain is  $6.10 \times 10^{-3}$ . Moreover, some far-field crack VIII and surface spalling IX are also observed, which results in rapid reduction of axial supporting capacity until 17.3 MPa in an almost constant axial strain.

By adopting the same method as specimen GS-17<sup>#</sup> ( $2a = 25 \text{ mm}$ ,  $\alpha = 45^\circ$ ) and GS-19<sup>#</sup> ( $2a = 15 \text{ mm}$ ,  $\alpha = 15^\circ$ ), the real-time-crack coalescence process of all other specimens with a single fissure can also be identified and characterized on the basis of photographic monitoring and AE technique. Table 2.4 summarizes the successive axial stress values of crack coalescence in the sandstone specimens containing a single fissure. In Table 2.4, numbers 1–7 represent the succession of crack coalescence, which corresponds to that shown in Figs. 2.11 and 2.12. It can be seen that each larger stress drop in the axial stress–axial strain curve indicates a larger crack propagation, which also corresponds to a larger amplifying of AE counts. Notice the initiation, propagation, and coalescence of some cracks occur after peak strength, which shows the re-fracture mechanical behavior of flawed specimen after failing. Moreover, the corresponding axial stress of initiating the first crack is closely dependent on fissure length and fissure angle. With increase of fissure length, the corresponding axial stress of initiating the first crack tends to decrease except for the specimen GS-10<sup>#</sup>, which shows that the initiation of the first crack in the specimen with longer fissure is easier than with shorter fissure. However, the corresponding axial stress of initiating the first crack has a nonlinear relation with the fissure angle, but for specimen GS-11<sup>#</sup> with  $\alpha = 45^\circ$ , the corresponding axial stress is lowest in all the specimens with fissure length of 15 mm

**Table 2.4** Succession of crack coalescence in sandstone specimen containing single fissure

Specimen	Subsequence/corresponding axial stress formed the crack in the specimen (Unit: MPa)						
	1	2	3	4	5	6	7
GS-04#	III (128.2)	VIII (148 → 144.3)	VIII, IX (170.04 = $\sigma_c$ )	VIII, IX (160.9 → 68.3)			
GS-07#	III (95.93 → 88.45)	IX (103.9, 136.39 = $\sigma_c$ , 135.2 → 133)	VIII, IX (112.17 → 8.49)				
GS-10#	I (101.6')	IV (120.8 → 118)	III, IV (122.8 = $\sigma_c$ → 90.8)	VI, VIII, IX (89.8 → 12.9)			
GS-14#	I (43.77 <sup>i</sup> → 40.35)	II (67.73 → 65.5)	III (79.28 → 78.4)	VIII (85.29 = $\sigma_c$ → 81.7)	VIII, III (76.1 → 73.6)	VII, III (69.5 → 59.8)	
GS-17#	I (27.55 <sup>i</sup> , 34.12 → 30.38)	III (77.25 = $\sigma_c$ → 70.97)	III (77.25 = $\sigma_c$ → 70.97)	VII (70.97 → 68.9)	III (75.3 → 65.95, 72.5 → 62.3)	II (67.4 → 55.8)	VIII, IX (55.8 → 16.9)
GS-19#	V (58.4 <sup>i</sup> → 57.4)	IV (99.9 → 98.4)	III (114.2 → 112.4)	IV, IX (135.1 → 129.4)	III, IX (139.28 = $\sigma_c$ → 127.7)	VI, VIII, IX (123.9 → 17.3)	
GS-11#	I (49.2 <sup>i</sup> , 64.3)	VIII (83.9 → 80.7)	III (115.17 = $\sigma_c$ → 108.9)	IV, IX (109.9 → 104.6)	VIII, IX (88.8 → 4.4)		
GS-25#	III (117 <sup>i</sup> , 146.57 → 144.3)	III, IV (149.96 = $\sigma_c$ → 143.6)	III, VI-IX (143.6 → 122.1 → 24)				
GS-28#	III (103.54 <sup>i</sup> → 101.1, 181.71 = $\sigma_c$ → 179.9)	VI, VII, IX (179.9 → 22.8)					

Note The letter *i* indicates the initiated axial stress of the first crack

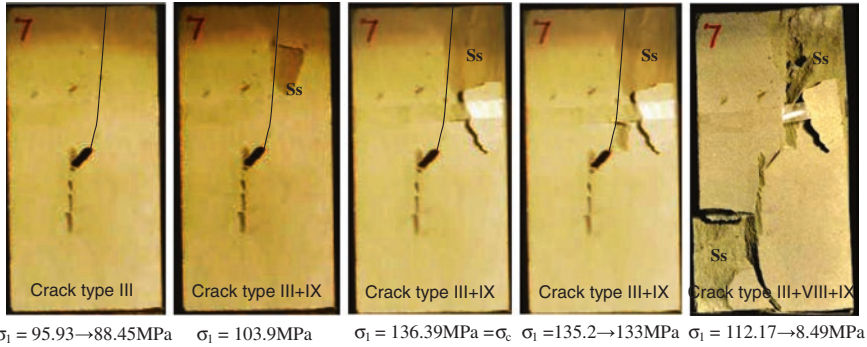


**Fig. 2.24** Typical real-time crack coalescence process of sandstone specimen containing a single fissure ( $2a = 10 \text{ mm}$ ,  $\alpha = 45^\circ$ ) (with kind permission of Springer Publisher)

to initiate the first crack. Moreover, the heterogeneity of sandstone material has a significant effect on the axial stress to initiating the first crack.

In accordance with Table 2.4, one can further conclude that more crack coalescences occur in the specimens with longer fissure or smaller fissure angle, which indicates that the localization deformation failure (Fig. 2.5) is easier to initiate in specimens with longer fissure or smaller fissure angle. For the specimen with shorter fissure (e.g. GS-07<sup>#</sup>) as shown in Fig. 2.24, the surface spalling IX often occurs in brittle rock material but does not complete at once. From Fig. 2.24, it can be seen that surface spalling IX in the specimen GS-07<sup>#</sup> undergoes four processes with increase of axial deformation.

## 2.4 Conclusions

The aim of this chapter is to investigate the strength, deformation failure, and crack coalescence behavior in brittle sandstone material containing a single fissure under uniaxial compression by photographic monitoring and AE technique. On the basis of the experimental results of sandstone specimens containing a single fissure, the following conclusions can be drawn.

The fissure length and fissure angle have a key effect on the strength and deformation behavior of sandstone specimens under uniaxial compression. In this chapter, tested intact sandstone specimen is a kind of typical brittle rock and takes on typically axial splitting failure. Compared with intact specimen, the flawed specimen containing a single fissure fails with lower strengths, smaller Young’s modulus, and smaller peak axial strain, which is closely related to the fissure length and fissure angle. Moreover, the flawed specimen takes on the localization deformation failure behavior. The mechanical parameters of flawed sandstone decrease with increase in fissure length, but first decrease and then increase with

increasing fissure angle. Moreover, the influence of single fissure geometries on the uniaxial compressive strength and peak axial strain is higher than that on the Young's modulus for such brittle sandstone material.

Nine different crack types are identified based on their geometry and crack propagation mechanism (tensile, shear, lateral crack, far-field crack, and surface spalling) for single fissure in response to the applied axial loads. Tensile cracks I and III are often the first cracks to initiate from the tips of pre-existing fissure. But sometimes, tensile crack V is also the first crack, and is only observed in the specimen GS-19<sup>#</sup> ( $2a = 15$  mm,  $\alpha = 15^\circ$ ), which shows that this fissure angle makes the specimen easier to emanate this tensile crack V. Tensile crack IV initiates from the tips of fissure only when the fissure angle is lower than  $60^\circ$ , but lateral crack VI is only observed in the specimens with fissure length of 15 mm except for one specimen GS-11<sup>#</sup>. However, anti-tensile crack IV often accompanies tensile crack III toward the reverse direction. The shear crack VII usually occurs in specimens containing longer fissures, while cracks III, VIII–IX are easier to occur during loading for brittle rock material. In accordance with nine crack types, the failure mode of flawed sandstone specimen containing single fissure under uniaxial compression is analyzed. The failure modes of flawed specimens are all a mixture of several cracks among nine crack types.

According to AE monitoring results in the process of deformation failure, the AE characteristics of intact and flawed sandstone containing single fissure can be approximately divided into three typical periods, i.e., quiet period, active period, and remission period. In quiet period, for hard and brittle sandstone material, the AE events are not very active and the AE counts are very small, which results from the occurrence of fissure closure. Moreover, the AE behavior in quiet period is not dependent on the fissure length and fissure angle. In the active period, the AE counts of intact specimen are very dense and stable, but the AE behaviors of flawed specimens are different from that of intact specimen, which is distinctly related to fissure length and fissure angle. The AE counts of flawed specimen with single fissure are more decentralized than that of intact specimen; moreover, the AE counts of all flawed specimens with single fissure have several larger peak values before peak strength, which correspond to the crack initiation and propagation in the specimens. However, in the remission period, the AE counts and energy of intact specimen are rare, but AE behaviors of flawed specimen with shorter fissure ( $2a = 5$  mm) or higher angle ( $\alpha = 60^\circ$ ) approximate the one of intact specimen, which results from little occurrence of macroscopic cracks after peak strength. While the AE behaviors of flawed specimen with medium fissure ( $2a = 15$  mm) are not dependent on the fissure angle, which shows that the AE counts undergo first a relative steady phase and then increase abruptly with increasing time. For flawed specimen with longer fissure ( $2a = 20$  and  $25$  mm), the AE counts are more and relatively denser, which results from gradual crack coalescence in the specimens after peak strength.

In order to confirm the subsequence of crack coalescence in sandstone specimen, photographic monitoring was adopted during uniaxial compression test. On the basis of the photographic monitoring results, the real-time crack coalescence

process of sandstone containing a single fissure is identified and characterized. Moreover, the corresponding axial stress of crack coalescence in the sandstone specimens containing a single fissure is also obtained. Each larger stress drop in the axial stress–axial strain curve indicates a larger crack propagation, which also corresponds to a larger amount of AE counts. The corresponding axial stress of initiating the first crack is closely dependent on fissure length and fissure angle. With the increase in fissure length, the corresponding axial stress of initiating the first crack tends to decrease except for specimen GS-10<sup>#</sup>, which shows that the initiation of the first crack in the specimen with longer fissure is easier than that with shorter fissure. However, the corresponding axial stress of initiating the first crack has a nonlinear relation with the fissure angle, but for specimen GS-11<sup>#</sup> with  $\alpha = 45^\circ$ , the corresponding axial stress is the lowest in all specimens of fissure length 15 mm to initiate the first crack. Lastly, two typical effects of real-time crack coalescence on the strength and deformation failure behavior of brittle sandstone specimen are analyzed under uniaxial compression.

This chapter investigates only the strength failure and crack coalescence behavior of brittle sandstone containing a single fissure of different lengths and angles under uniaxial compression by photographic monitoring and AE technique. In order to understand in-depth the failure behavior and fracture mechanism of engineering rock mass, more experimental investigations for flawed brittle sandstone specimens with two or three fissures (varying ligament angle, ligament length, fissure angle, fissure length, etc.) will be presented by advanced techniques (such as AE technique, photographic monitoring, etc.) in the following chapters.

## References

- Fairhurst CE, Hudson JA (1999) Draft ISRM suggested method for the complete stress–strain curve for the intact rock in uniaxial compression. *Int J Rock Mech Min Sci* 36(3):279–289
- Li YP, Chen LZ, Wang YH (2005) Experimental research on pre-cracked marble under compression. *Int J Solids Struct* 42:2505–2516
- Wassermann J, Senfaute G, Amitrano D et al (2009) Evidence of dilatant and non-dilatant damage processes in oolitic iron ore: P-wave velocity and acoustic emission analyses. *Geophys J Int* 177(3):1343–1356
- Yang SQ, Jiang YZ (2010) Triaxial mechanical creep behavior of sandstone. *Min Sci Technol* 20(3):339–349
- Yang SQ, Jing HW (2011) Strength failure and crack coalescence behavior of brittle sandstone samples containing a single fissure under uniaxial compression. *Int J Fract* 168(2):227–250

## Chapter 3

# Experimental Investigation on Crack Evolution Behavior of Brittle Sandstone Containing Two Coplanar Fissures in the Process of Deformation Failure

Photographic monitoring is a kind of very effective technique, which can be used to analyze real-time crack coalescence process in the process of deformation failure of rock specimen (Yang and Jing 2011; Ferrero et al. 2008; Ferrero and Migliazza 2009; Roncella et al. 2005). Ferrero et al. (2008) and Ferrero and Migliazza (2009) carried out uniaxial compressive experimental study for two different types of marls, which measured induced 2D or 3D deformations during testing by classical extensometers and by means of photographic monitoring. Moreover, they obtained displacement and deformation maps on the whole specimen surface in accordance with developed image analysis software at the University of Parma (Roncella et al. 2005).

However until now, photographic monitoring technique was less used to explore the crack coalescence of brittle rock material containing two coplanar fissures in the process of whole deformation. Therefore in this chapter, uniaxial compression experiments were conducted for brittle sandstone specimens containing two coplanar fissures by the rock mechanics servo-controlled testing system. Moreover, this investigation relied on photographic monitoring technique to construct the real-time crack coalescence process and axial stress–axial strain curve, which was not preformed for brittle sandstone in previous studies.

The emphasis of this chapter is focused on to investigate the influence of two coplanar fissure angle on the strength and deformation failure behaviors of brittle sandstone material containing two coplanar fissures, and to analyze real-time crack coalescence process in real sandstone material under uniaxial compression on basis of photographic monitoring (Yang 2011).

### 3.1 Experimental Material and Procedure

#### 3.1.1 Physical Behavior of Tested Specimens

To study the crack coalescence behavior of brittle rock containing two coplanar fissures under uniaxial compression, tested sandstone from Linyi City, Shandong province, China, was chosen. The mineral component of sandstone specimen is feldspar, quartz, and debris (Fig. 3.1a). The quartz is mainly granite-type single-crystal with particle size range of 0.05–0.35 mm. The feldspar takes mainly on columnar crystal acid, gather slice pairs of plagioclase, and strong green shade mass with particle size range of 0.05–0.4 mm.

The tested sandstone has a crystalline and blocky structure (Fig. 3.1b) with a porosity of about 4.61 %, which is a fine-grained heterogeneous material with average unit weight about 2650 kg/m<sup>3</sup>. In a word, tested sandstone is characterized by the following particle size, i.e., 0.10–0.25 mm (75 %), 0.25–0.50 mm (10 %), and 0.5–1.0 mm (15 %). The cementation method of particle is pore-type, and the contact method of particle is point-linear contact.

#### 3.1.2 Specimens Containing Two Coplanar Fissures

The tested sandstone specimen was 80 mm in width, 160 mm in height, and 30 mm in thickness. All tested specimens with the height to width ratio of 2.0 ensure a uniform stress state within the central part of the specimens. The geometry of sandstone specimens with two coplanar fissures is described in Fig. 3.2. The geometry of two coplanar fissures is defined by four geometrical parameters—fissure length  $2a$ , ligament length  $2b$ , fissure angle (the angle of fissure with the horizontal direction)  $\alpha$ , and ligament angle  $\beta$  as shown in Fig. 3.2.

In this chapter, high-pressure water-jet cutting machine was used to cut two open coplanar fissures in intact specimens. Machined open fissure width was about 2.5 mm.

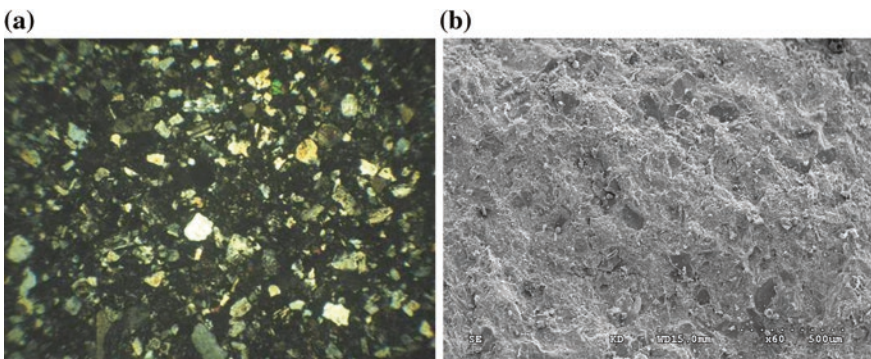


**Fig. 3.1** Microscopic structure of sandstone material in this chapter. **a** Micropolariscope result ( $\times 40$ ). **b** SEM result ( $\times 60$ ) (with kind permission of Elsevier Publisher)

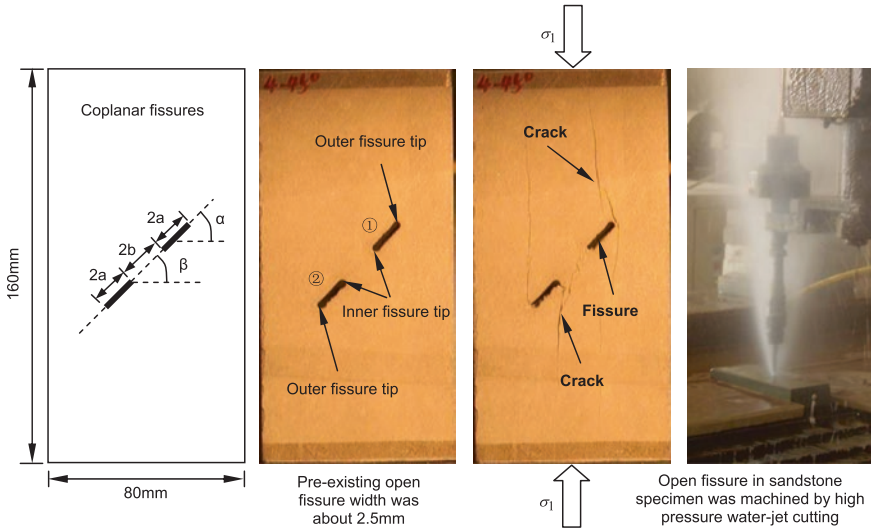


**Fig. 3.2** Geometry of two coplanar fissures in the sandstone specimens, in which  $\alpha$  is fissure angle,  $\beta$  is ligament angle,  $2a$  is fissure length, and  $2b$  is ligament length. In this chapter, two open coplanar fissures in sandstone specimen were machined by high-pressure water-jet cutting (with kind permission of Elsevier Publisher)

To investigate the effect of pre-existing coplanar fissure geometry on the crack coalescence behavior of sandstone subject to uniaxial compression stress, different geometries of two coplanar fissures by varying inclination angle ( $\alpha = \beta$ ) while keeping two constants ( $2a = 15 \text{ mm}$  and  $2b = 18 \text{ mm}$ ) were chosen. Detailed description for sandstone specimens containing two coplanar fissures is listed in Table 3.1.

**Table 3.1** Tested sandstone specimens containing two coplanar fissures under uniaxial compression

Specimen	$W/\text{mm}$	$H/\text{mm}$	$T/\text{mm}$	$\alpha/^\circ$	$\beta/^\circ$	$2a/\text{mm}$	$2b/\text{mm}$	Note
A29 <sup>#</sup>	80.9	157.6	31.0	N/A	N/A	N/A	N/A	Intact specimen
A01 <sup>#</sup>	80.8	159.8	31.4	0	0	15	18	Flawed specimen containing two coplanar fissures
A02 <sup>#</sup>	81.0	159.5	31.0	15	15	15	18	
A10 <sup>#</sup>	80.9	159.9	31.5	15	15	15	18	
A03 <sup>#</sup>	80.9	159.2	31.7	30	30	15	18	
A11 <sup>#</sup>	80.8	159.0	31.8	30	30	15	18	
A04 <sup>#</sup>	80.4	159.5	29.6	45	45	15	18	
A05 <sup>#</sup>	80.8	159.2	31.6	60	60	15	18	
A06 <sup>#</sup>	81.1	158.8	31.4	75	75	15	18	
A08 <sup>#</sup>	81.1	156.5	31.8	90	90	15	18	
A09 <sup>#</sup>	80.6	159.1	31.3	0	0	15	18	Cyclic loading
A13 <sup>#</sup>	80.9	156.5	31.5	75	75	15	18	

Note  $W$  Width,  $H$  Height,  $T$  Thickness

### ***3.1.3 Testing Equipment and Procedure***

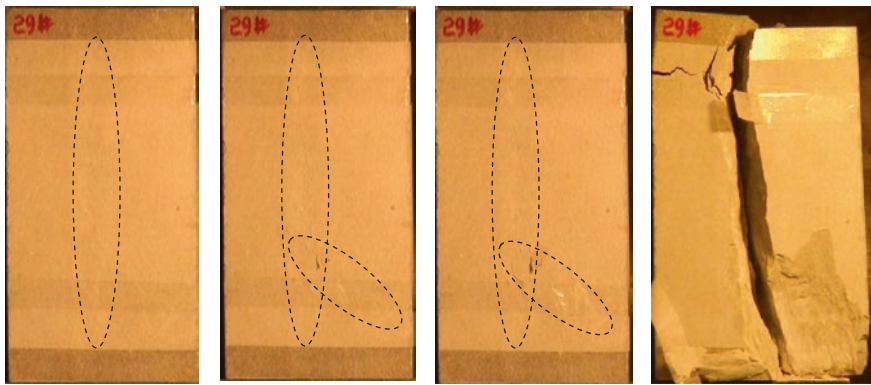
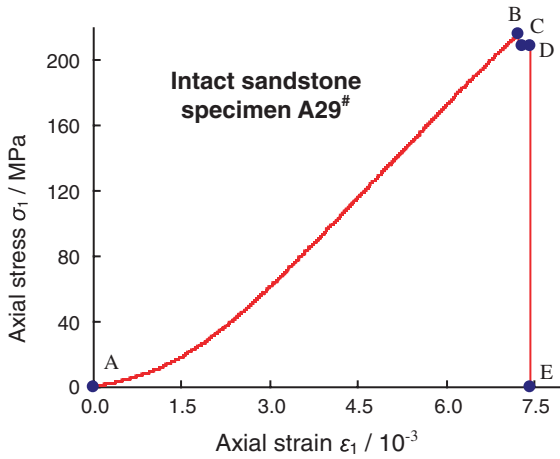
Uniaxial compression experiments for intact and flawed sandstone specimens were carried out on a rock mechanics servo-controlled testing system (MTS815.02) with the maximum loading capacity of 2700 kN and the maximum displacement capacity of 25 mm. This servo-controlled system can test specimens in load or displacement control while the data are recorded and analyzed in real-time. The axial stress was imposed on the surface of rock specimen until the failure took place. All the tests were conducted for sandstone specimen at a strain rate of  $8.125 \times 10^{-6}$ . In this chapter, we measured the axial force with the loading capacity of 600 kN and the axial deformation with displacement capacity of 5 mm. During the whole uniaxial compression experiments, loads and deformations of tested sandstone specimens were recorded simultaneously. Moreover two rigid steel blocks ( $33 \times 83 \times 15$  mm) were placed between the loading frame and rock specimen. At the same time, two antifriction gaskets were placed between two rigid steel blocks and the end face of rock specimen, which decreased distinctly the effect of the end friction effects on the testing results of sandstone specimens with the height to width ratio  $\sim 2.0$ . Moreover, the photographic monitoring was also adopted to obtain real-time crack coalescence process in brittle sandstone specimens subject to different stresses.

## **3.2 Influence of Coplanar Fissure Angle on Strength and Deformation Behavior**

### ***3.2.1 Deformation Failure Behavior of Intact Sandstone Specimen***

To compare the analysis with flawed specimen containing two open coplanar fissures, the axial stress–axial strain curve of intact sandstone specimen is first obtained as shown in Fig. 3.3, in which the crack coalescence process of intact sandstone specimen is also presented. From Fig. 3.3, it can be clearly seen that the sandstone in this chapter is a kind of brittle rock and takes on typically axial splitting tensile failure, i.e., the axial stress drops abruptly to zero in 2 s after peak stress and a huge failure sonic can be heard during the dropping. The phenomenon is in good agreement with many laboratory testing results of brittle rocks.

In accordance with the axial stress–strain curve shown in Fig. 3.3, it can be found that the crack coalescence of intact specimen is very difficult to see by unaided eyes or in video recordings before peak strength. However, after peak strength, the crack coalescence process can be snapped by photographic monitoring even though unclear fracture traces as shown in Fig. 3.3. The unclear fracture traces predict the unstable failure of intact specimen under uniaxial compression. Moreover, the sandstone specimen has a distinct stage of fissure closure, which



B:  $\sigma_1 = \sigma_c = 215.98 \text{ MPa}$     C:  $\sigma_1 = 209.53 \text{ MPa}$     D:  $\sigma_1 = 209.05 \text{ MPa}$     E: After failure

**Fig. 3.3** Uniaxial stress–strain curve and crack coalescence process of intact sandstone specimen under uniaxial compression (with kind permission of Elsevier Publisher)

results from the closure of some primary pores and voids in the specimen with the increasing compression stress. Before peak strength, the elastic deformation dominates the stress–strain curve. After peak strength, the macroscopic crack in intact specimen comes out rapidly and the post-peak behavior in the stress–strain curves shows a rapid drop. At this time, the intact specimen cannot support any axial stress.

The strength and deformation parameters of intact sandstone specimen are listed in Table 3.2. The definition for every mechanical parameter is described as follows. The  $\sigma_c$  is defined as the uniaxial compressive strength and the  $\epsilon_{1c}$  is defined as peak axial strain value.  $E_S$  represents the elastic modulus; but  $E_{50}$  is defined as deformation modulus. More detailed descriptions on Young’s modulus can be found in (Yang and Jiang 2010).

**Table 3.2** Mechanical parameters of intact and flawed sandstone specimens under uniaxial compression

Specimen	$\alpha/^\circ$	$\beta/^\circ$	$2a/\text{mm}$	$2b/\text{mm}$	$\sigma_c/\text{MPa}$	$\varepsilon_{1c}/10^{-3}$	$E_s/\text{GPa}$	$E_{50}/\text{GPa}$	$D_{af}$
A29#	Intact specimen				215.98	7.240	37.41	25.22	0.000
A01#	0	0	15	18	101.62	3.999	31.03	21.94	0.529
A02#	15	15	15	18	91.79	3.390	32.28	23.47	0.575
A10#	15	15	15	18	100.29	3.742	33.36	22.94	0.536
A03#	30	30	15	18	95.50	4.248	31.46	21.50	0.558
A11#	30	30	15	18	111.70	4.551	32.84	22.87	0.483
A04#	45	45	15	18	107.13	3.651	33.29	25.05	0.504
A05#	60	60	15	18	108.56	4.375	32.30	23.53	0.497
A06#	75	75	15	18	145.61	5.494	35.79	23.60	0.326
A08#	90	90	15	18	165.37	6.061	34.39	26.02	0.234
A09#	0	0	15	18	107.42	4.409	Cyclic loading		0.503
A13#	75	75	15	18	154.55	5.584			0.284

### 3.2.2 Deformation Failure Behavior of Flawed Sandstone with Two Coplanar Fissures

To investigate the effect of coplanar fissure angle on mechanical parameters of brittle sandstone, the effect of heterogeneity on axial stress–strain curve of specimens containing two open coplanar fissures under uniaxial compression is first discussed. Figure 3.4 shows the axial stress–strain curves of four sandstone specimens containing two coplanar fissures for  $\alpha = \beta = 15^\circ$  and  $30^\circ$  in uniaxial compression. In accordance with Fig. 3.4, it can be seen that for flawed specimens with the same coplanar fissure angle, the axial stress–strain curves exhibit similar behavior and have a very good consistency. Based

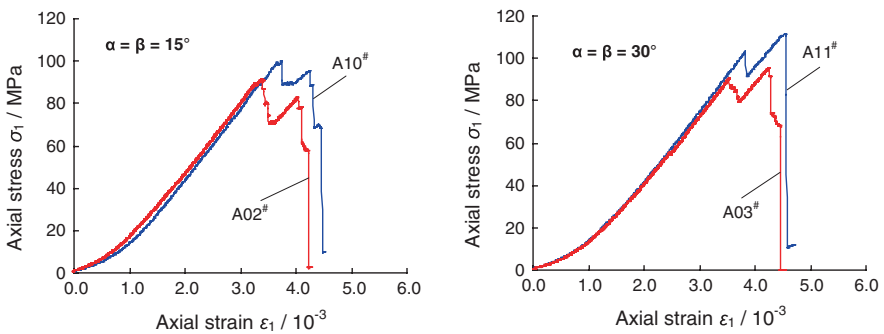


**Fig. 3.4** Effect of heterogeneity on axial stress–strain curves of sandstone specimens containing two coplanar fissures ( $2a = 15 \text{ mm}$  and  $2b = 18 \text{ mm}$ ) under uniaxial compression (with kind permission of Elsevier Publisher)

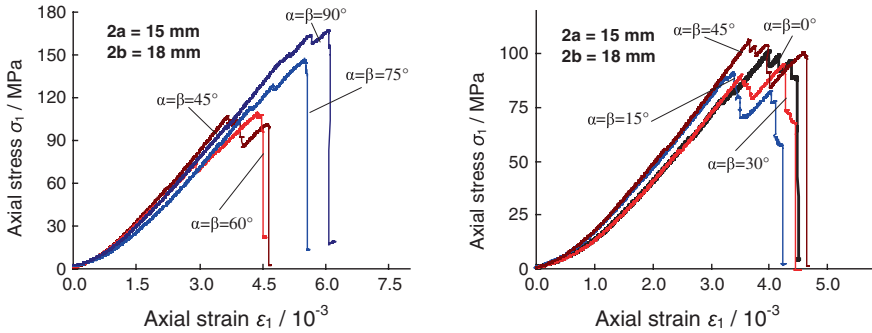


**Fig. 3.5** Axial stress–axial strain curves of sandstone specimens containing two coplanar fissures under uniaxial compression (with kind permission of Elsevier Publisher)

upon the above analysis, it can be concluded that the heterogeneity has no nearly any effect on the deformation failure behavior of flawed specimen containing coplanar fissures with the same inclination angle ( $\alpha = \beta$ ). But it needs to be noted that it is more difficult to reproduce all the flawed specimens containing coplanar fissures due to limited specimens from the same rock block.

The stress–strain curves of sandstone specimen containing two coplanar fissures subject to uniaxial compressive stress are shown in Fig. 3.5, and the corresponding mechanical parameters are listed in Table 3.2. In accordance with Figs. 3.3 and 3.5, it is very clear that coplanar fissure angle has a distinct effect on the strength and deformation behavior of sandstone specimens under uniaxial compression. From Fig. 3.5, the stress–strain curves of sandstone specimen containing two coplanar fissures show several abrupt change of slope (i.e., stress drop) before peak strength compared with that of intact specimen shown in Fig. 3.3. The stress drop in Fig. 3.5 results mainly from the initiation or coalescence of some new cracks at the inner and outer tips of pre-existing fissures. For the abrupt change in the stress–strain curve, we will make a detailed analysis in the fourth section. Moreover, specimens containing two coplanar fissures take on the localization deformation failure nearby peak strength, which is closely related to coplanar fissure angle.

Figure 3.6 shows the comparison between monotonic and cyclic axial stress–strain curves of sandstone specimens containing two coplanar fissures under uniaxial compression. From Fig. 3.6, it is very clear that four cyclic loading–unloading do not increase distinctly peak strength and peak axial strain of sandstone specimens containing two coplanar fissures, while increase the slope of axial stress–strain curve after third cyclic loading–unloading. Moreover, it needs to note that tested sandstone specimens containing two coplanar fissures have a larger plastic hoop with the increase of axial deformation, which results from that the sandstone specimens is porous and induces distinct plastic deformation behavior during loading.

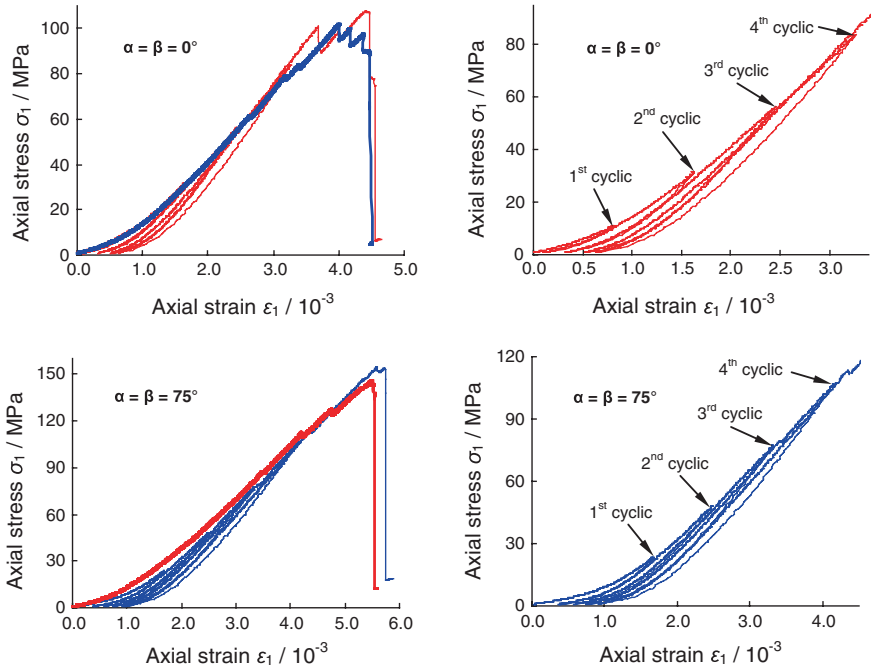


**Fig. 3.6** Comparison between monotonic and cyclic axial stress–strain curves of sandstone specimens containing two coplanar fissures for  $\alpha = \beta = 0^\circ$  and  $75^\circ$  ( $2a = 15$  mm and  $2b = 18$  mm) under uniaxial compression (with kind permission of Elsevier Publisher)

### 3.2.3 Relationship Between Coplanar Fissure Angle and Mechanical Parameters

Table 3.2 lists mechanical parameters of all flawed sandstone specimens containing two coplanar fissures. From Table 3.2, there are some differences between mechanical parameters of two specimens even though with the same coplanar fissure angle due to the heterogeneity of sandstone material (Fig. 3.4). However in a word, the dispersion of sandstone specimen containing two coplanar fissures in this chapter is very small, and the strength and deformation parameters listed in Table 3.2 can be used to discuss approximately the effect of coplanar fissure angle on the strength and deformation parameters of sandstone under uniaxial compression.

In accordance with Table 3.2, two coplanar fissures have distinct influence on the reduction of uniaxial compressive strength of the specimen compared with intact specimen. The uniaxial compressive strength of flawed specimens containing two coplanar fissures is lower than that of intact specimen, while the reduction extent has a significant relation with coplanar fissure angle. Figure 3.7a presents the effect of coplanar fissure angle on the uniaxial compressive strength of flawed sandstone

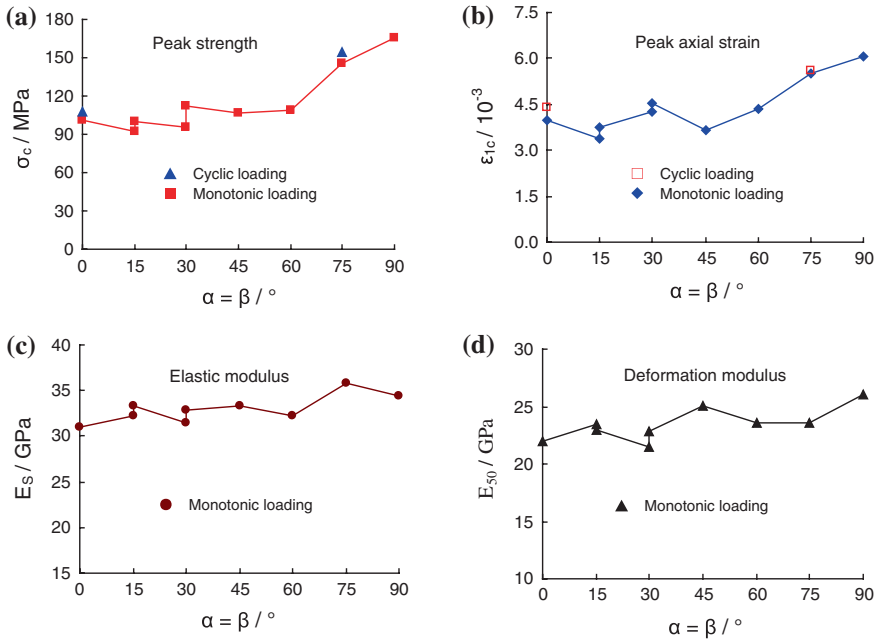


**Fig. 3.7** Effect of coplanar fissure angle on the strength and deformation parameters of sandstone specimens with the same fissure length ( $2a = 15$  mm) and ligament length ( $2b = 18$  mm) under uniaxial compression (with kind permission of Elsevier Publisher)

specimens. The peak strength of intact specimen was 215.98 MPa, while it could be seen that the uniaxial compressive strength of specimens containing two coplanar fissures ranged from 91.79 MPa ( $\alpha = \beta = 15^\circ$ ) to 165.37 MPa ( $\alpha = \beta = 90^\circ$ ).

In order to indicate the attenuation extent of peak strength of flawed specimens compared with intact specimen, an attenuation factor is defined as follows.

$$D_{af} = \frac{\sigma_{ci} - \sigma_{cf}}{\sigma_{ci}} \tag{3.1}$$

where  $\sigma_{ci}$  is the peak strength of intact specimen and  $\sigma_{cf}$  is the peak strength of flawed specimen containing two coplanar fissures. In accordance with Eq. (3.1), calculated  $D_{af}$  of flawed specimens containing two coplanar fissures are also listed in Table 3.2.

From Table 3.2, one can see that  $D_{af}$  of flawed specimens for  $\alpha = \beta$  smaller than  $60^\circ$  has no distinct variance with increasing coplanar fissure angle, which results from the uniaxial compression strength is independent to the coplanar fissure angle. The average  $D_{af}$  of seven flawed specimens for  $\alpha = \beta$  smaller than  $60^\circ$  is about 0.526. However, the  $D_{af}$  of flawed specimen decreases from 0.497 to 0.326 as coplanar fissure angle increases from  $60^\circ$  to  $75^\circ$ , and decreases from 0.326 to 0.234 as coplanar fissure angle increases from  $75^\circ$  to  $90^\circ$ . The above analysis indicates that the uniaxial compression strength of flawed specimen increases

with the coplanar fissure angle for  $\alpha = \beta$  greater than  $60^\circ$ , as shown in Fig. 3.7a. Note, the uniaxial compressive strength of flawed specimen under cyclic loading is approximately equal to that under monotonic loading, and the difference is in the range of normal dispersion.

The intact sandstone specimen failed at a strain of 0.724 % under uniaxial compression, while sandstone specimens containing two coplanar fissures failed at a strain of approximately 0.34~0.61 %, which is less than that of intact specimen. Moreover, the peak axial strain  $\varepsilon_{1c}$  of sandstone specimen is dependent distinctly to coplanar fissure angle. In accordance with Fig. 3.7b, it can be seen that the  $\varepsilon_{1c}$  has a nonlinear relation with coplanar fissure angle. For  $\alpha = \beta$  smaller than  $45^\circ$ , the  $\varepsilon_{1c}$  of sandstone specimen containing two coplanar fissures undergoes a complex variance tendency. The  $\varepsilon_{1c}$  decreases from  $3.999 \times 10^{-3}$  to  $3.566 \times 10^{-3}$  (the average value of two specimens for  $\alpha = \beta = 15^\circ$ ) as  $\alpha = \beta$  increases from  $0^\circ$  to  $15^\circ$ , whereas increases from  $3.566 \times 10^{-3}$  to  $4.4 \times 10^{-3}$  (the average value of two specimens for  $\alpha = \beta = 30^\circ$ ) as  $\alpha = \beta$  increases from  $15^\circ$  to  $30^\circ$ . But when  $\alpha = \beta$  increases from  $30^\circ$  to  $45^\circ$ , the  $\varepsilon_{1c}$  decreases from  $4.4 \times 10^{-3}$  to  $3.651 \times 10^{-3}$ . However, for  $\alpha = \beta$  greater than  $45^\circ$ , the  $\varepsilon_{1c}$  of sandstone specimen containing two coplanar fissures increases with coplanar fissure angle, and the  $\varepsilon_{1c}$  increases from  $3.651 \times 10^{-3}$  to  $6.061 \times 10^{-3}$  when  $\alpha = \beta$  increases from  $45^\circ$  to  $90^\circ$ .

The elastic modulus and deformation modulus of intact specimen were 37.41 GPa and 25.22 GPa, respectively. However, the elastic modulus of specimen containing two coplanar fissures ranged from 31.03 GPa ( $\alpha = \beta = 0^\circ$ ) to 35.79 GPa ( $\alpha = \beta = 75^\circ$ ), while the reduction extent of elastic modulus was between 4.3 and 17.1 %. The deformation modulus of specimen containing two coplanar fissures ranged from 21.50 GPa ( $\alpha = \beta = 30^\circ$ ) to 26.02 GPa ( $\alpha = \beta = 90^\circ$ ), while the reduction extent of deformation modulus was between -3.2 and 14.8 %. On the whole, the Young's modulus of sandstone is not dependent distinctly to coplanar fissure angle. The average elastic modulus of all the specimens containing two coplanar fissures is about 32.97 GPa, which reaches 88.1 % of the deformation modulus ~37.41 GPa of intact specimen, and the dispersion coefficient (the percentage of the differential value between the maximum and minimum value to the average value) is approximately 14.4 %. However, the average deformation modulus of all the specimens containing two coplanar fissures is about 23.44 GPa, which reaches 92.9 % of the deformation modulus ~25.22 GPa of intact specimen, and the dispersion coefficient (the percentage of the differential value between the maximum and minimum value to the average value) is approximately 19.2 %.

### 3.3 Crack Initiation and Coalescence Behavior Analysis

Ultimate failure modes of sandstone specimens containing two coplanar fissures under uniaxial compression are shown in Fig. 3.8, which are different distinctly from that of intact specimen in Fig. 3.3. Figures 3.9 and 3.10 show local magnification of microscopic structure for the regions as shown in Fig. 3.8. From

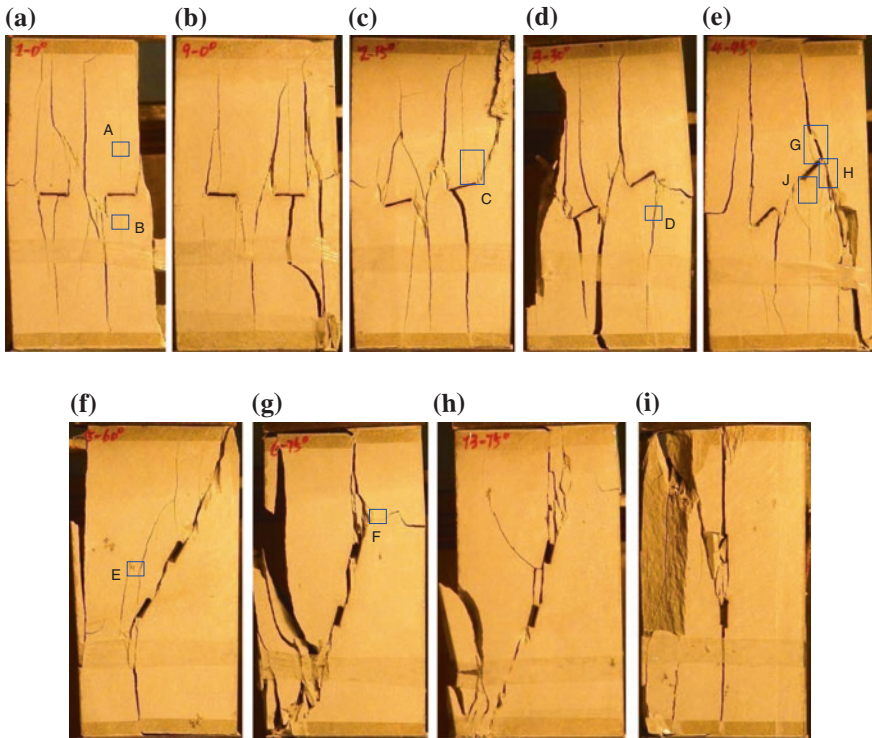


**Fig. 3.8** Ultimate failure modes of sandstone specimens containing two coplanar fissures under uniaxial compression. **b** and **g** represent ultimate failure modes of sandstone specimens under cyclic loading. **a**, **c-f** and **i** denote ultimate failure modes of sandstone specimens under monotonic loading. **a**  $\alpha = \beta = 0^\circ$ . **b**  $\alpha = \beta = 0^\circ$  (cyclic). **c**  $\alpha = \beta = 15^\circ$ . **d**  $\alpha = \beta = 30^\circ$ . **e**  $\alpha = \beta = 45^\circ$ . **f**  $\alpha = \beta = 60^\circ$ . **g**  $\alpha = \beta = 75^\circ$ . **h**  $\alpha = \beta = 75^\circ$  (cyclic). **i**  $\alpha = \beta = 90^\circ$  (with kind permission of Elsevier Publisher)

Figs. 3.8, 3.9 and 3.10, it is very clear that the crack coalescence were observed from the inner and outer tips of pre-existing fissures in sandstone specimens containing two coplanar fissures, and ultimate failure modes are obviously dependent to coplanar fissure angle. Therefore, in this section, a systematic evaluation will be presented on the crack initiation and coalescence in sandstone specimens containing two coplanar fissures by photographic monitoring.

### 3.3.1 Crack Coalescence Type of Sandstone Containing Two Coplanar Fissures

From Fig. 3.8, it is not difficult to see that the cracks in flawed sandstone specimens containing two coplanar fissures under uniaxial compression are not initiated simultaneously from or near the tips of pre-existing fissures. To confirm the

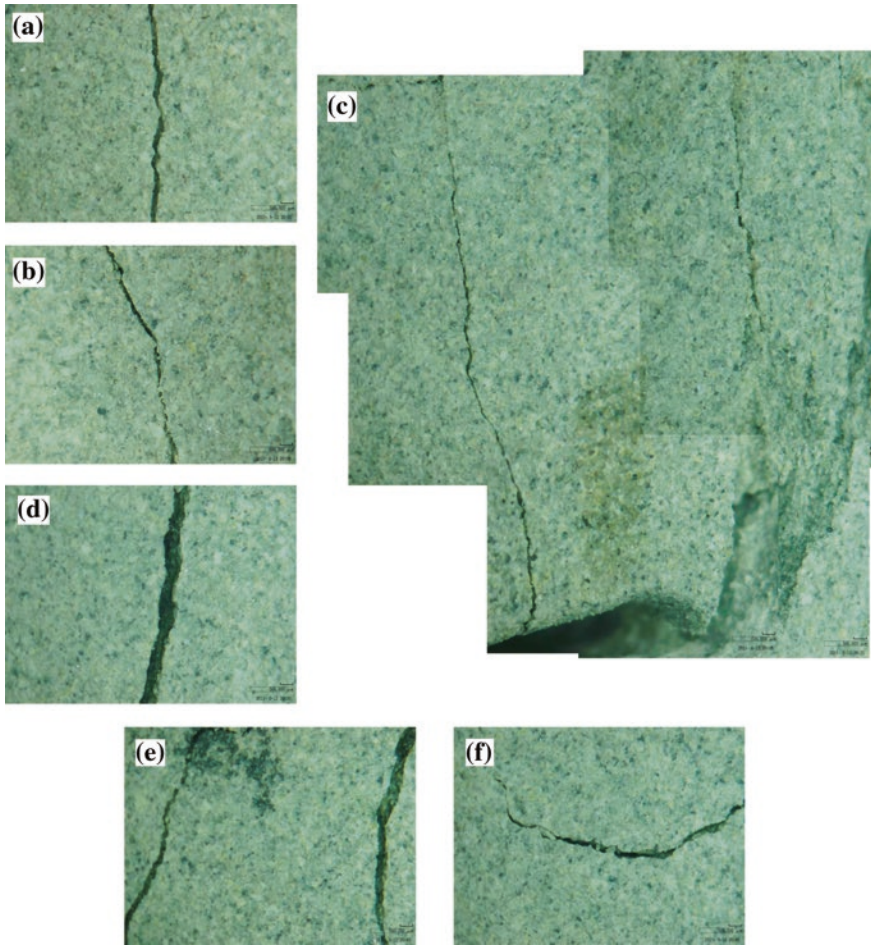


**Fig. 3.9** Local magnification of several crack coalescence of sandstone specimen containing two coplanar fissures for **a–f** as shown in Fig. 3.8 under uniaxial compression (with kind permission of Elsevier Publisher)

sequence of crack coalescence in sandstone specimens containing two coplanar fissures, the photographic monitoring was adopted during the entire experiment. The photographic monitoring results were used to identify the real-time crack coalescence process at the specimen's surface. Moreover, the corresponding axial stress and strain of crack coalescence in the sandstone specimens containing two coplanar fissures were also obtained. In Sect. 3.3.2, we will make a detailed analysis for the crack initiation and coalescence behavior of sandstone specimens containing two coplanar fissures in accordance with the photographic monitoring results (Figs. 3.11, 3.12, 3.13, 3.14, 3.15, 3.16, and 3.17). From Figs. 3.9 and 3.10, we can see that the paths of crack coalescence are not smooth, which is the result of heterogeneity in sandstone material.



**Fig. 3.10** Local magnification of several crack coalescence of sandstone specimen containing two coplanar fissures for **g**, **h** and **j** as shown in Fig. 3.8 under uniaxial compression (with kind permission of Elsevier Publisher)

Based on the geometry and crack propagation mechanism (tensile, shear, lateral crack, far-field crack, and surface spalling), Yang and Jing (2011) identified nine different crack types (Fig. 3.18) for brittle sandstone specimens containing a single fissure. In accordance with the above nine crack types, they analyzed the ultimate failure mode and cracking process of sandstone specimens containing a single fissure under uniaxial compression. Therefore, in this chapter, one can also analyze crack coalescence type in sandstone specimens containing two coplanar fissures on basis of nine different crack types in Fig. 3.18.

Table 3.3 summarizes crack coalescence type in sandstone specimens containing two coplanar fissures with different angles in response to applied axial loads.

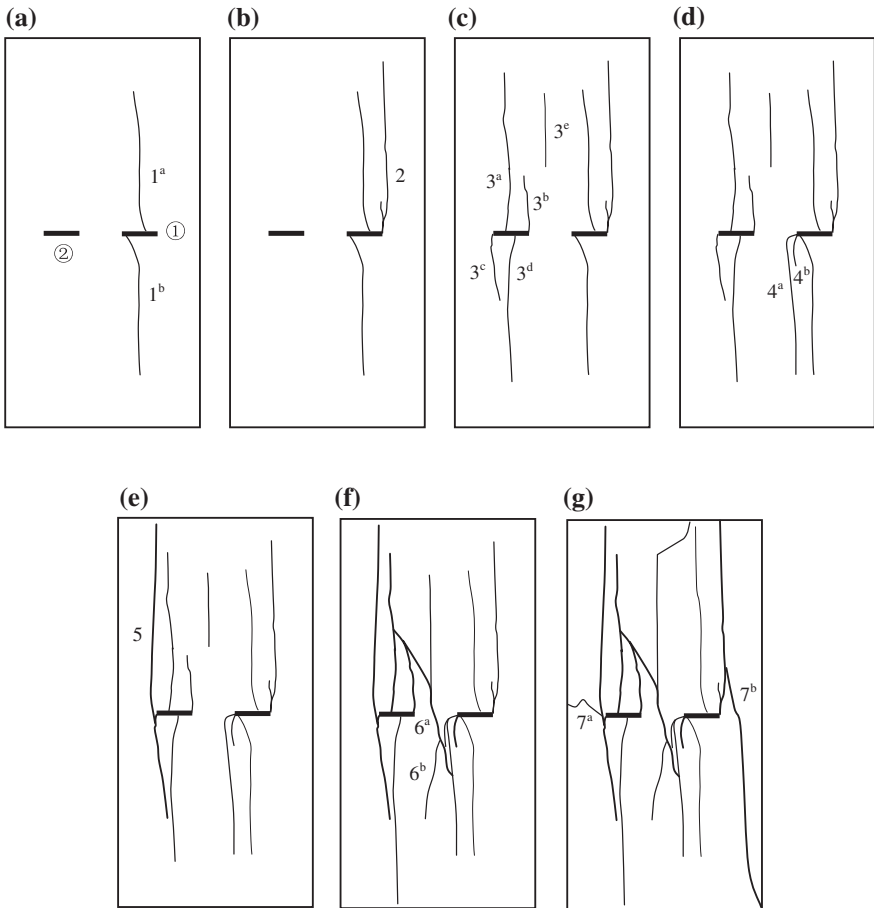


**Fig. 3.11** Crack initiation and coalescence process of sandstone specimens containing two coplanar fissures for  $\alpha = \beta = 0^\circ$ . **a**  $\sigma_1 = 61.28$  MPa,  $\varepsilon_1 = 2.637 \times 10^{-3}$ . **b**  $\sigma_1 = 83.85$  MPa,  $\varepsilon_1 = 3.384 \times 10^{-3}$ . **c**  $\sigma_1 = 101.62$  MPa =  $\sigma_c$ ,  $\varepsilon_1 = 3.999 \times 10^{-3}$ . **e**  $\sigma_1 = 97.08$  MPa,  $\varepsilon_1 = 4.369 \times 10^{-3}$ . **f**  $\sigma_1 = 87.71$  MPa,  $\varepsilon_1 = 4.470 \times 10^{-3}$ . **g** Ultimate failure (with kind permission of Elsevier Publisher)

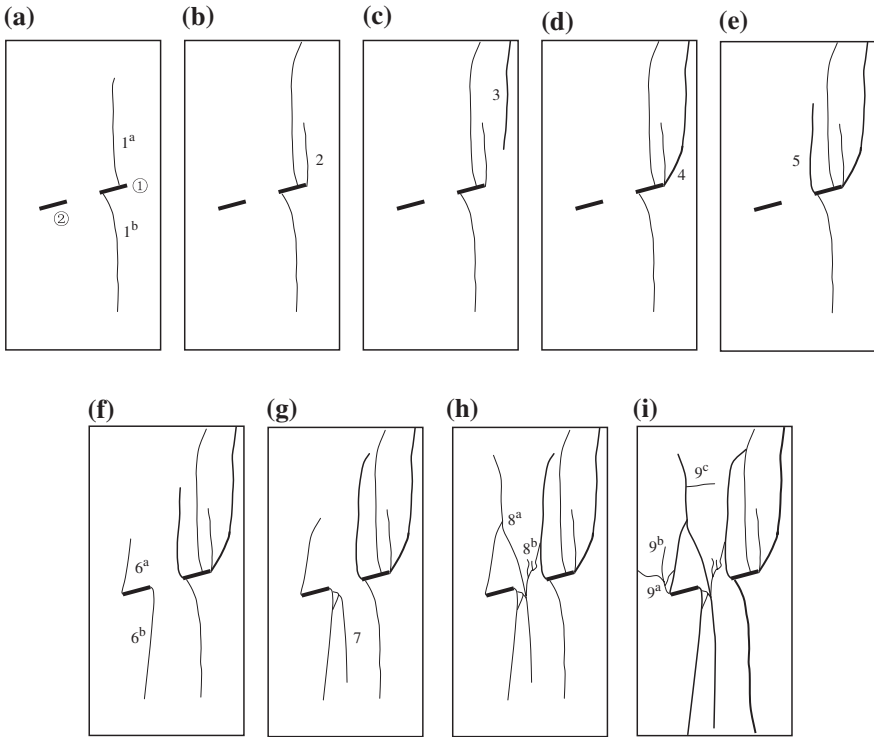


**Fig. 3.12** Crack initiation and coalescence process of sandstone specimens containing two coplanar fissures for  $\alpha = \beta = 15^\circ$ . **a**  $\sigma_1 = 89.51$  MPa,  $\epsilon_1 = 3.267 \times 10^{-3}$ . **b**  $\sigma_1 = 91.79$  MPa =  $\sigma_c$ ,  $\epsilon_1 = 3.390 \times 10^{-3}$ . **c**  $\sigma_1 = 90.89$  MPa,  $\epsilon_1 = 3.409 \times 10^{-3}$ . **d**  $\sigma_1 = 86.72$  MPa,  $\epsilon_1 = 3.425 \times 10^{-3}$ . **e**  $\sigma_1 = 79.64$  MPa,  $\epsilon_1 = 3.489 \times 10^{-3}$ . **f**  $\sigma_1 = 71.81$  MPa,  $\epsilon_1 = 3.571 \times 10^{-3}$ . **g**  $\sigma_1 = 82.70$  MPa,  $\epsilon_1 = 4.028 \times 10^{-3}$ . **h**  $\sigma_1 = 78.02$  MPa,  $\epsilon_1 = 4.104 \times 10^{-3}$ . **i** Ultimate failure (with kind permission of Elsevier Publisher)

Notice, for sandstone specimens containing two coplanar fissures, the shear crack was initiated at the ligament section of two coplanar fissures for  $\alpha = \beta$  smaller than  $30^\circ$  (Fig. 3.19); whereas for  $\alpha = \beta$  in the range of  $45^\circ$ – $75^\circ$ , the shear crack was initiated from the fissure tips along the direction of pre-existing fissures. However, for  $\alpha = \beta = 90^\circ$ , the shear crack was initiated from the inner tip of fissure ② to the left top corner of the specimen, which is different from that as shown in Fig. 3.18.

According to Table 3.3, it is very clear that the macroscopic failure modes of sandstone specimens containing two coplanar fissures are a mixture of several cracks among nine various crack types. For example, the failure mode of the specimen for  $\alpha = \beta = 45^\circ$ , is a mixture of cracks I, III–IV, and VII–IX. From Table 3.3, some qualitative conclusions can be summarized as follows.

As indicated in Table 3.3, tensile cracks I and III are often the first crack to initiate from the inner or outer tip of pre-existing fissure, which is the same behavior

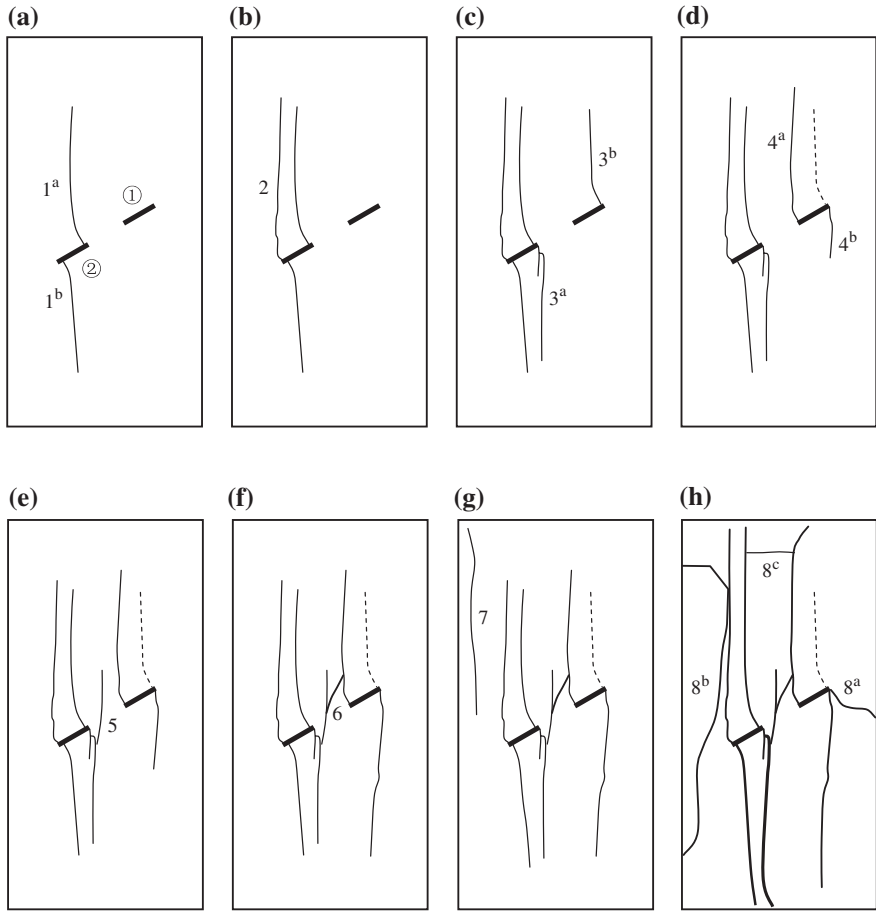


**Fig. 3.13** Crack initiation and coalescence process of sandstone specimens containing two coplanar fissures for  $\alpha = \beta = 30^\circ$ . **a**  $\sigma_1 = 55.41$  MPa,  $\varepsilon_1 = 2$ . **b**  $\sigma_1 = 90.56$  MPa,  $\varepsilon_1 = 3.528 \times 10^{-3}$ . **c**  $\sigma_1 = 86.45$  MPa,  $\varepsilon_1 = 3$ . **d**  $\sigma_1 = 81.92$  MPa,  $\varepsilon_1 = 3.695 \times 10^{-3}$ . **e**  $\sigma_1 = 95.50$  MPa =  $\sigma_c$ ,  $\varepsilon_1 = 4.248 \times 10^{-3}$ . **f**  $\sigma_1 = 90.93$  MPa,  $\varepsilon_1 = 4.273 \times 10^{-3}$ . **g**  $\sigma_1 = 74.07$  MPa,  $\varepsilon_1 = 4.308 \times 10^{-3}$ . **h** Ultimate failure (with kind permission of Elsevier Publisher)

as that observed for flawed specimens containing a single fissure with different fissure angle (Yang and Jing 2011). But sometimes, the tensile crack V located at a distance away from the outer tip of fissure ① is also the first crack, and is only observed for  $\alpha = \beta$  smaller than and equal to  $15^\circ$ , which is possible to result from lower coplanar fissure angle. For tensile crack IV, it is very clear that anti-tensile crack IV often accompanies with tensile crack I or III toward the reverse direction, which is usually observed in the specimen for  $\alpha = \beta$  smaller than and equal to  $60^\circ$ . However, anti-tensile crack IV is not observed in the specimen for  $\alpha = \beta = 75^\circ$

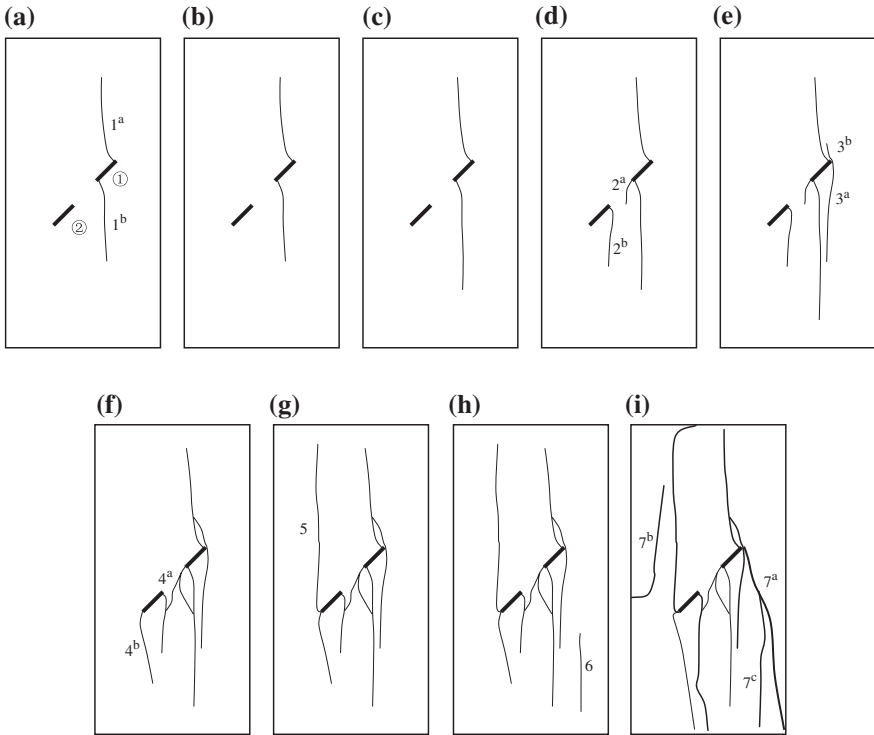


**Fig. 3.14** Crack initiation and coalescence process of sandstone specimens containing two coplanar fissures for  $\alpha = \beta = 45^\circ$ . **a**  $\sigma_1 = 60.67$  MPa,  $\epsilon_1 = 2.377 \times 10^{-3}$ . **b**  $\sigma_1 = 94.72$  MPa,  $\epsilon_1 = 3.329 \times 10^{-3}$ . **c**  $\sigma_1 = 103.61$  MPa,  $\epsilon_1 = 3.581 \times 10^{-3}$ . **d**  $\sigma_1 = 107.13$  MPa =  $\sigma_c$ ,  $\epsilon_1 = 3.651 \times 10^{-3}$ . **e**  $\sigma_1 = 104.03$  MPa,  $\epsilon_1 = 3.767 \times 10^{-3}$ . **f**  $\sigma_1 = 104.07$  MPa,  $\epsilon_1 = 3.979 \times 10^{-3}$ . **g**  $\sigma_1 = 92.37$  MPa,  $\epsilon_1 = 4.008 \times 10^{-3}$ . **h**  $\sigma_1 = 101.48$  MPa,  $\epsilon_1 = 4.60 \times 10^{-3}$ . **i** Ultimate failure (with kind permission of Elsevier Publisher)

and  $90^\circ$ , which indicates that anti-tensile crack is very difficult to induce for the direction of pre-existing fissure with smaller angles to axial stress.

It needs to be noted that tensile wing crack I is usually easier to initiate and nucleate at the fissure tips for  $\alpha = \beta$  smaller than and equal to  $45^\circ$ , while difficult to initiate from the fissure tips for  $\alpha = \beta$  greater than  $45^\circ$ . Tensile crack III initiates in all other specimens containing two coplanar fissures except for  $\alpha = \beta = 30^\circ$ . Tensile crack II is very rare, which is only observed in the specimen with  $\alpha = \beta = 15^\circ$ , but lateral crack VI is only observed in the specimen with  $\alpha = \beta$  smaller than and equal to  $30^\circ$ , and  $\alpha = \beta = 75^\circ$ . Shear crack VII, far-field crack VIII and surface spalling IX are observed in all the flawed sandstone containing two coplanar fissures, which results from that tested sandstone is a kind of typical brittle rock material.

In order to analyze the influence of coplanar fissure angle on each crack coalescence stress, the relationship between coplanar fissure angle and crack coalescence stress is presented in Fig. 3.20. In Fig. 3.20a, the initiation stress is defined as the

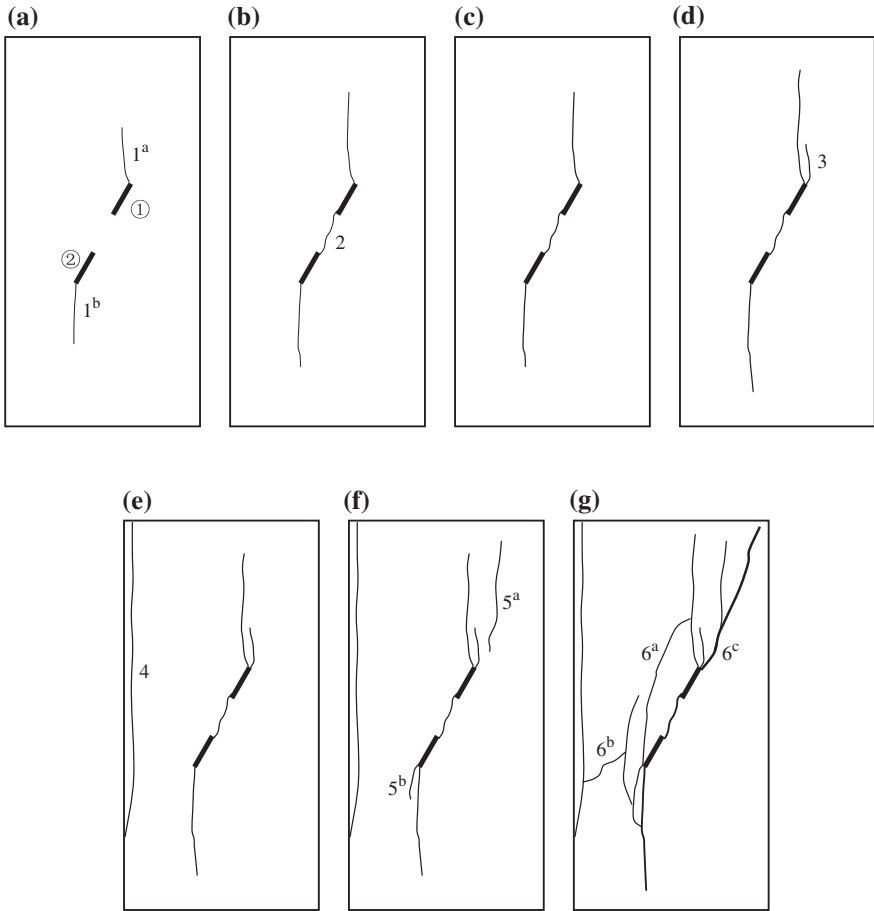


**Fig. 3.15** Crack initiation and coalescence process of sandstone specimens containing two coplanar fissures for  $\alpha = \beta = 60^\circ$ . **a**  $\sigma_1 = 64.21$  MPa,  $\varepsilon_1 = 2.625 \times 10^{-3}$ . **b**  $\sigma_1 = 73.35$  MPa,  $\varepsilon_1 = 2.914 \times 10^{-3}$ . **c**  $\sigma_1 = 78.93$  MPa,  $\varepsilon_1 = 3.313 \times 10^{-3}$ . **d**  $\sigma_1 = 100.67$  MPa,  $\varepsilon_1 = 4.090 \times 10^{-3}$ . **e**  $\sigma_1 = 108.56$  MPa =  $\sigma_c$ ,  $\varepsilon_1 = 4.375 \times 10^{-3}$ . **f**  $\sigma_1 = 107.49$  MPa,  $\varepsilon_1 = 4.478 \times 10^{-3}$ . **g** Ultimate failure (with kind permission of Elsevier Publisher)

axial stress initiated the first crack (i.e., crack 1) in flawed specimens. To compare the analysis, the variance of peak strength with coplanar fissure angle is also plotted in Fig. 3.20a.

From Fig. 3.20a, it can be seen that the crack initiation stress in flawed specimens containing two coplanar fissures is obviously lower than that peak strength except for one specimen with  $\alpha = \beta = 15^\circ$ , which is about 60.3 % of corresponding peak strength. The crack initiation stress of this specimen with  $\alpha = \beta = 15^\circ$  reaches about 98 % of corresponding peak strength. When  $\alpha = \beta$  is in the range of  $30^\circ$ – $60^\circ$ , the crack imitation stress of sandstone specimen has no obvious variance

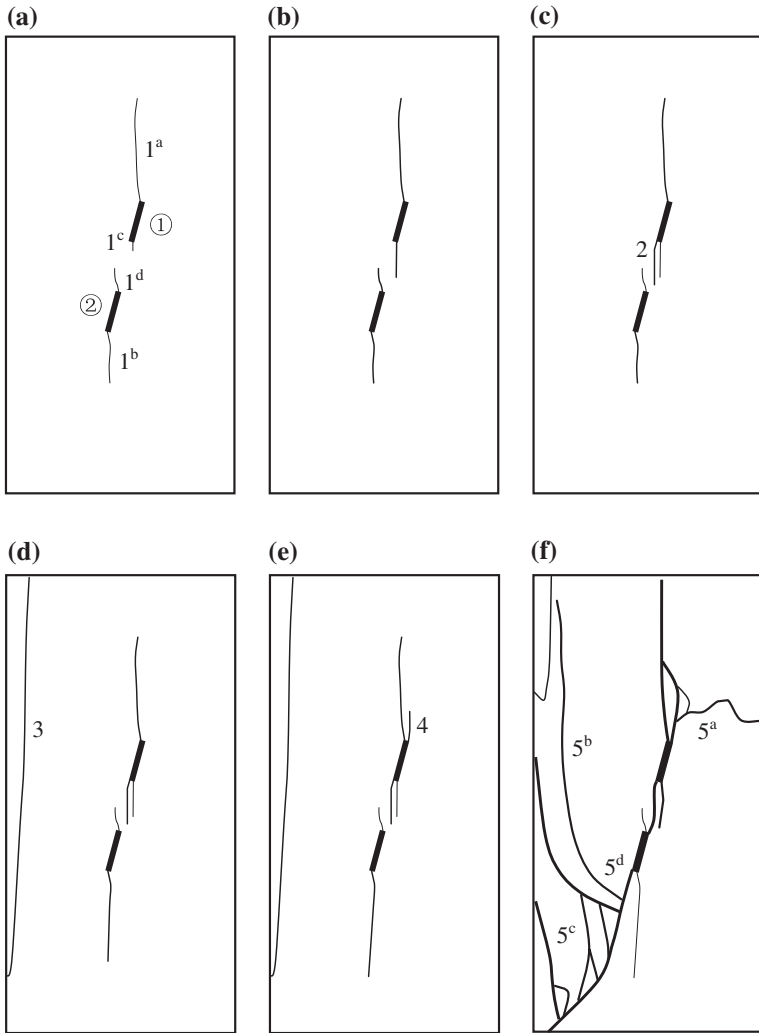


**Fig. 3.16** Crack initiation and coalescence process of sandstone specimens containing two coplanar fissures for  $\alpha = \beta = 75^\circ$ . **a**  $\sigma_1 = 86.22$  MPa,  $\epsilon_1 = 3.485 \times 10^{-3}$ . **b**  $\sigma_1 = 109.06$  MPa,  $\epsilon_1 = 4.129 \times 10^{-3}$ . **c**  $\sigma_1 = 112.46$  MPa,  $\epsilon_1 = 4.202 \times 10^{-3}$ . **d**  $\sigma_1 = 127.75$  MPa,  $\epsilon_1 = 4.758 \times 10^{-3}$ . **e**  $\sigma_1 = 145.61$  MPa =  $\sigma_c$ ,  $\epsilon_1 = 5.494 \times 10^{-3}$ . **f** Ultimate failure (with kind permission of Elsevier Publisher)

with the increase of coplanar fissure angle. However for  $\alpha = \beta$  greater than  $60^\circ$ , the crack initiation stress of sandstone specimen increases distinctly with coplanar fissure angle.

In accordance with Fig. 3.20b, the corresponding axial stress of four cracks (i.e., cracks 1–4) initiated in flawed sandstone specimens is obtained for different coplanar fissure angles. Notice crack coalescence type is different for various

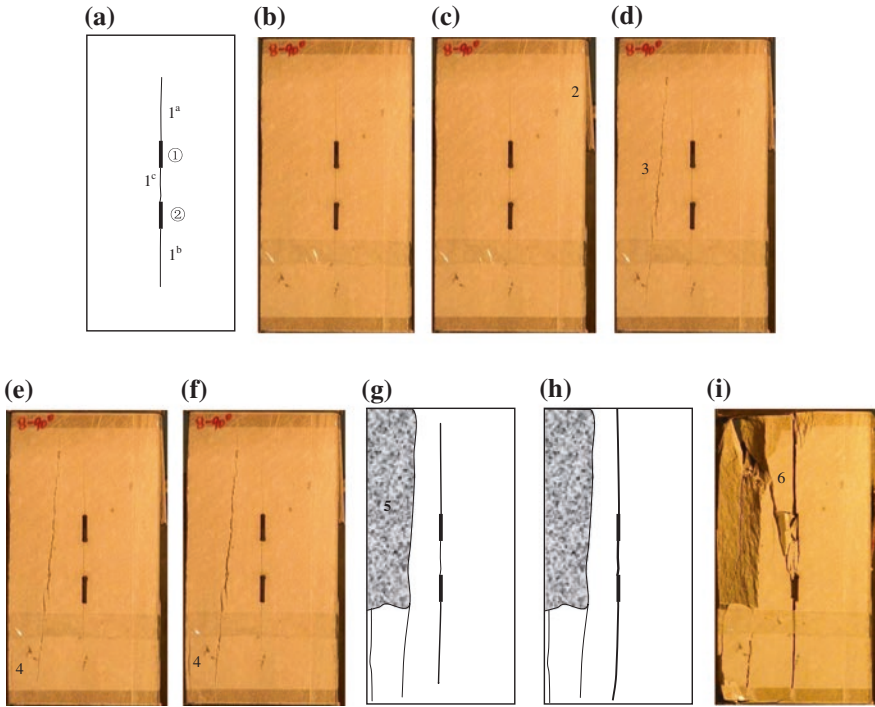


**Fig. 3.17** Crack initiation and coalescence process of sandstone specimens containing two coplanar fissures for  $\alpha = \beta = 90^\circ$ . **a**  $\sigma_1 = 97.55$  MPa,  $\epsilon_1 = 3.633 \times 10^{-3}$ . **b**  $\sigma_1 = 135.60$  MPa,  $\epsilon_1 = 4.692 \times 10^{-3}$ . **c**  $\sigma_1 = 144.38$  MPa,  $\epsilon_1 = 4.945 \times 10^{-3}$ . **d**  $\sigma_1 = 148.87$  MPa,  $\epsilon_1 = 5.13 \times 10^{-3}$ . **e**  $\sigma_1 = 149.01$  MPa,  $\epsilon_1 = 5.211 \times 10^{-3}$ . **f**  $\sigma_1 = 160.89$  MPa,  $\epsilon_1 = 5.559 \times 10^{-3}$ . **g**  $\sigma_1 = 162.03$  MPa,  $\epsilon_1 = 5.635 \times 10^{-3}$ . **h**  $\sigma_1 = 165.37$  MPa =  $\sigma_c$ ,  $\epsilon_1 = 6.061 \times 10^{-3}$ . **i** Ultimate failure (with kind permission of Elsevier Publisher)

**Table 3.3** Initiated crack types of sandstone specimens containing two coplanar fissures with different angles

$\alpha = \beta$	Crack types								
	I: Tensile	II: Tensile	III: Tensile	IV: Tensile	V: Tensile	VI: Lateral	VII: Shear	VIII: Far-field	IX: Surface spalling
Intact	Typically axial splitting tensile failure (Fig. 3.3)								
0°	√1		√	√	√1	√	√c	√	√
15°	√1	√	√	√	√1	√	√c	√	√
30°	√1			√		√	√c	√	√
45°	√1		√	√			√	√	√
60°			√1	√			√	√	√
75°			√1			√	√	√	√
90°			√1				√c	√	√

*Note* √c indicates the shear crack initiated in sandstone specimens containing two coplanar fissures (Fig. 3.19), which is different from that as shown in Fig. 3.18. √1 indicates that the crack is the first crack to initiate at or near the tips of pre-existing fissures

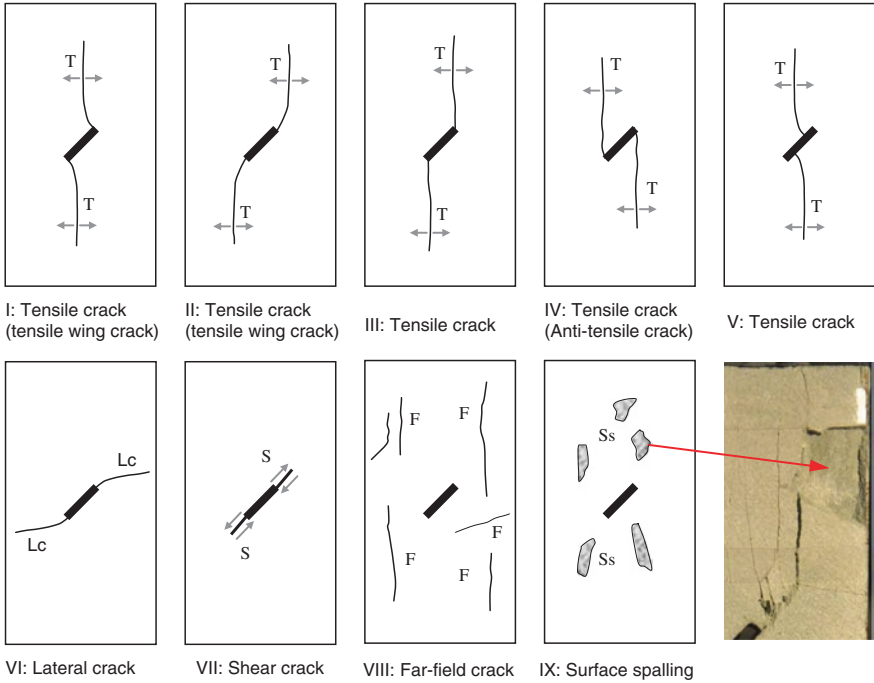


**Fig. 3.18** Various crack types from single fissure identified. *T* Tensile crack, *Lc* Lateral crack, *S* Shear crack *F* Far-field crack *Ss* Surface spalling. (Yang and Jing 2011) (with kind permission of Elsevier Publisher)

coplanar fissure angles. For example, when  $\alpha = \beta$  is  $60^\circ$ , the type of the second crack (i.e., crack 2) is shear crack VII, when  $\alpha = \beta$  is  $30^\circ$ , that is anti-tensile crack IV. The corresponding axial stress of initiating crack 4 is approximate to the peak stress of the specimen, moreover has a similar relation with coplanar fissure angle as the peak stress of sandstone specimen.

### 3.3.2 Crack Initiation and Coalescence Behavior of Pre-fissured Sandstone

Table 3.4 presents the crack initiation and coalescence behavior of sandstone specimen containing two coplanar fissures for  $\alpha = \beta$  smaller than and equal to  $45^\circ$  in the process of deformation as shown in Fig. 3.21. In Fig. 3.21, the denoted letter corresponds to the crack coalescence process as shown in Figs. 3.11, 3.12, 3.13, and 3.14. In accordance with Table 3.4 and Fig. 3.21, we can analyze real-time crack coalescence process of sandstone specimens containing two coplanar fissures for  $\alpha = \beta$  smaller than and equal to  $45^\circ$ .

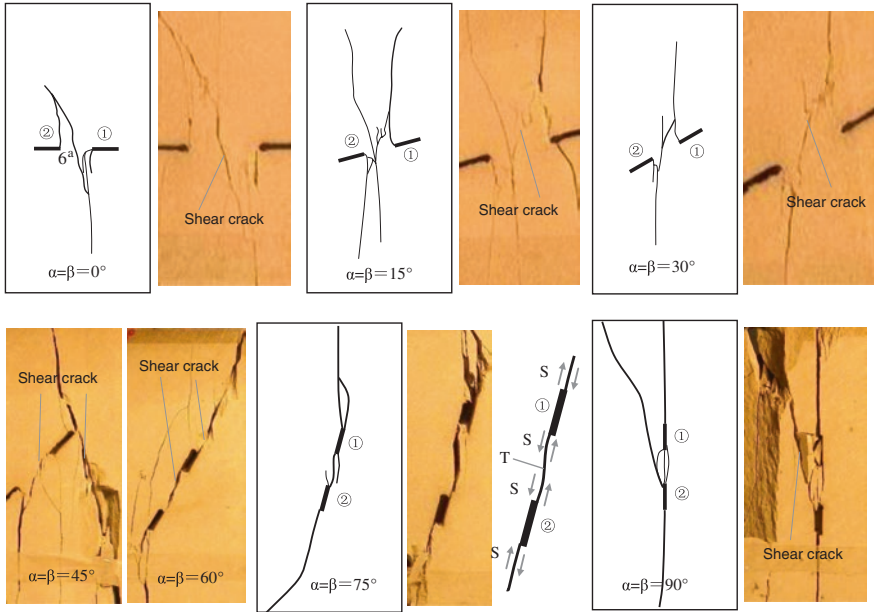


**Fig. 3.19** Shear crack in sandstone specimens containing two coplanar fissures with different angles in this chapter (with kind permission of Elsevier Publisher)

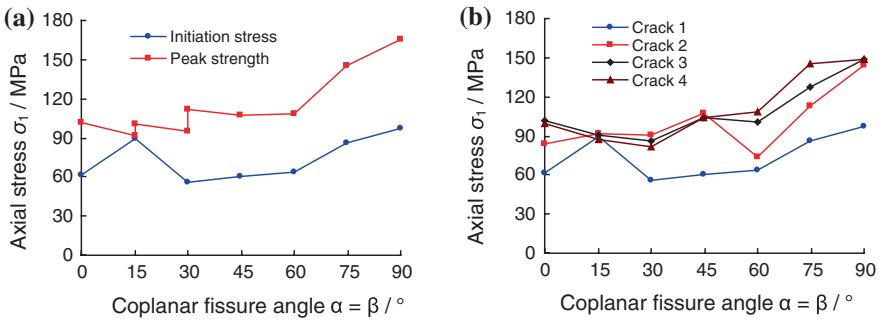


**Fig. 3.20** Crack coalescence stress versus coplanar fissure angle in sandstone specimens containing two coplanar fissures (with kind permission of Elsevier Publisher)

For  $\alpha = \beta = 0^\circ$ , before point a ( $\sigma_1 = 61.28 \text{ MPa} = 60.3 \% \sigma_c$ ) as shown in Fig. 3.21a, the stress concentration at the inner and outer tips of two coplanar fissures does not reach the material strength close to the tips, and consequently does not result in a crack initiation. But when the axial stress is loaded up to 61.28 MPa (point a in Fig. 3.21a), tensile wing cracks (cracks 1<sup>a</sup> and 1<sup>b</sup>) are initiated simultaneously from the inner tip and near the outer tip of fissure ①. It should be noted that the first crack is initiated at the angle of about 70° with fissure ①, and then gradually

**Table 3.4** Crack initiation and coalescence behavior of sandstone specimen containing two coplanar fissures ( $\alpha = \beta = 0^\circ, 15^\circ, 30^\circ, 45^\circ$ )

Coplanar fissure angle	Crack initiation and coalescence behavior
$\alpha = \beta = 0^\circ$	<ul style="list-style-type: none"> <li>• The first tensile cracks were initiated from the inner tip and near the outer tip of fissure ① and propagated along the direction of major principal stress</li> <li>• Four larger tensile cracks 2–5 occurred before coalescing</li> <li>• Mixed tensile and shear crack coalescence occurred between crack 3<sup>b</sup> and 4</li> <li>• No crack coalescence at the inner tips of two fissures ① and ②</li> <li>• Decrease in the width of both the fissure ① and ② with increasing axial deformation</li> <li>• Anti-tensile cracks were observed at the outer tip of fissure ②</li> <li>• Lateral tensile and far-field cracks often accompanied with unstable failure of specimen</li> <li>• Crack coalescence path was very clean and smooth</li> </ul>
$\alpha = \beta = 15^\circ$	<ul style="list-style-type: none"> <li>• The first tensile cracks were initiated from the inner tip and near the outer tip of fissure ① and propagated along the direction of major principal stress</li> <li>• Mixed tensile and shear crack coalescence occurred between crack 5 and 7</li> <li>• No crack coalescence at the inner tips of two fissures ① and ②</li> <li>• Decrease in the width of both the fissure ① and ② with increasing axial deformation</li> <li>• Anti-tensile crack were observed at the inner and outer tips of fissure ②</li> <li>• Anti-tensile crack were observed at the inner tip of fissure ①</li> <li>• Lateral tensile and far-field cracks often accompanied with unstable failure of specimen</li> </ul>
$\alpha = \beta = 30^\circ$	<ul style="list-style-type: none"> <li>• The first tensile cracks were initiated from the inner and outer tips of fissure ② and propagated along the direction of major principal stress</li> <li>• Four larger tensile cracks 2–5 occurred before coalescing</li> <li>• Shear crack coalescence occurred between crack 4<sup>a</sup> and 5</li> <li>• No crack coalescence at the inner tips of two fissures ① and ②</li> <li>• Decrease in the width of both the fissure ① and ② with increasing axial deformation</li> <li>• Anti-tensile cracks were observed at the inner and outer tips of both fissure ① and ②</li> <li>• Open tensile crack 3<sup>b</sup> occurred to close with the increase of axial deformation</li> <li>• Lateral tensile and far-field cracks often accompanied with unstable failure of specimen</li> </ul>
$\alpha = \beta = 45^\circ$	<ul style="list-style-type: none"> <li>• The first tensile cracks were initiated from the inner and outer tips of fissure ① and propagated along the direction of major principal stress</li> <li>• Crack coalescence occurred from the inner tip of fissure ① to crack 2<sup>b</sup></li> <li>• No variance in the width of the fissure ① with increasing axial deformation</li> <li>• Decrease in the width of the fissure ② with increasing axial deformation</li> <li>• Anti-tensile cracks were observed at the inner and outer tips of fissure ②</li> <li>• Anti-tensile crack was observed at the outer tip of the fissure ①</li> <li>• Shear crack was observed between two fissures ① and ②</li> <li>• Far-field cracks often accompanied with unstable failure of specimen</li> </ul>

departs toward the direction of major principal stress, and finally propagated along the direction of major principal stress. But after point a, with an increase in the axial deformation, crack 2 (crack type III) is initiated from the outer tip of fissure ①, and propagated along the direction of axial stress toward the top edge of the specimen.

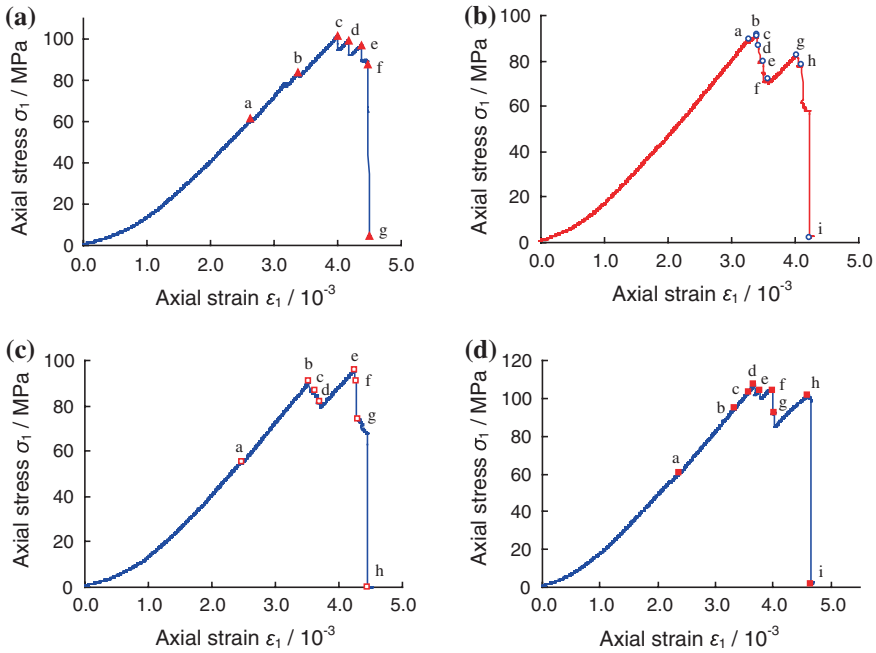


**Fig. 3.21** Relation between axial stress–strain curve and crack coalescence process in flawed specimens for  $\alpha = \beta = 0^\circ, 15^\circ, 30^\circ, 45^\circ$ . **a**  $\alpha = \beta = 0^\circ$ , **b**  $\alpha = \beta = 15^\circ$ , **c**  $\alpha = \beta = 30^\circ$ , **d**  $\alpha = \beta = 45^\circ$  (with kind permission of Elsevier Publisher)

The continuous increase of axial deformation leads to the specimen being loaded to peak strength (point c in Fig. 3.21a), at this moment, crack 3 ( $3^a$ – $3^e$ ) emanates rapidly and leads to a large stress drop in axial stress–strain curve. Notice, cracks  $3^b$  and  $3^c$  (crack type III) are initiated from the inner and outer tip of the fissure  $\textcircled{2}$ , respectively, whereas cracks  $3^a$  and  $3^d$  (crack type V) are initiated from the middle point of the fissure  $\textcircled{2}$ . Besides, crack  $3^d$  is far-field crack VIII. The crack 3 propagates along the direction of axial stress toward the top and bottom edges of the specimen, while cracks  $3^b$  and  $3^c$  do not evolve the boundary of the specimen as cracks  $3^a$  and  $3^d$ . However, after peak strength, the axial stress of the specimen does not drop to zero but to 94.39 MPa due to a good supporting structure (Fig. 3.11c). Afterward, with continuous increasing of the displacement, the axial stress increases to the point d ( $\sigma_1 = 99.40$  MPa) and corresponding axial strain is  $\sim 4.164 \times 10^{-3}$ . At this time, crack 4 is initiated from the inner tip of fissure  $\textcircled{1}$  and propagated along the direction of major principal stress toward the bottom edge of the specimen. Notice, crack  $4^b$  does not evolve to the edge of the specimen like crack  $4^a$ . The coalescence of crack 4 also leads to a big stress drop to 91.97 MPa in 0.2 s. Afterward, with the increase of deformation, the specimen is loaded to point e, crack 5 emanates from the outer tip of fissure  $\textcircled{2}$ , which is an anti-tensile crack IV compared with crack  $3^c$ . Notice, the axial stress also undergoes a big stress drop from point e to 90.14 MPa

in one second. With further increase of axial deformation, the specimen cannot reach a higher axial stress due to serious damage of supporting structure. When the peak strain of the specimen is  $4.470 \times 10^{-3}$ , the axial stress is 87.71 MPa, and the specimen occurs to the crack coalescence by a mixture of tensile and shear crack (Fig. 3.19) in the ligament region. Finally, with the increase of axial deformation, the specimen fails completely and the axial supporting capacity drops to 4.2 MPa in an almost constant axial strain. During the final failure, lateral tensile and far-field cracks often occur, which can be seen from Fig. 3.11. The width of both fissure ① and ② decreases with increasing axial deformation, which is because two coplanar fissures are perpendicular to the axial stress. Moreover, the crack coalescence path was very clean and smooth, and the crack coalescence does not occur at the inner tips of two fissures ① and ②.

For  $\alpha = \beta = 15^\circ$ , tensile wing crack (cracks 1<sup>a</sup> and 1<sup>b</sup>) is initiated simultaneously from the inner tip and near the outer tip of fissure ①, which is the same as the specimen for  $\alpha = \beta = 0^\circ$ , whereas the axial stress ( $\sigma_1 = 89.51 \text{ MPa} = 98 \% \sigma_c$ ) initiating crack 1 is distinctly higher than that of the specimen for  $\alpha = \beta = 0^\circ$ . It needs to be noted that the first crack is initiated in the direction perpendicular to fissure ①, and then gradually departs toward the direction of axial stress, and finally propagated along the direction of axial stress. But after the point a, the continuous increase of axial deformation leads to the specimen being loaded to peak strength (point b in Fig. 3.21b). At this moment, crack 2 (crack type III) is initiated from the outer tip of fissure ① and develops rapidly to the top edge of specimen. After the peak strength, the axial stress drops to 90.89 MPa (point c in Fig. 3.21b), and crack 3 (far-field crack VIII) emanates at the top right area of the specimen. Afterward, with continuous increase of axial displacement, the axial stress drops further from 90.89 to 71.81 MPa (point f in Fig. 3.21b), and the corresponding axial strain is  $3.571 \times 10^{-3}$ . In this deformation process, cracks 4–5 emanates from the outer and inner tip of fissure ①, respectively, and crack 6 (anti-tensile crack IV) is initiated at the inner and outer tip of fissure ②, and consequently results in a continuous stress drop. After the point f, the axial supporting capacity begins to increase slowly with the increase of axial deformation. But due to obvious damage of supporting structure, the reloading average modulus (28.62 GPa) is distinctly lower than elastic modulus (32.28 GPa). When the specimen is loaded to the point g, crack 7 (anti-tensile crack IV) occurs very fast from the inner tip of fissure ②. The axial stress of the specimen drops to 78.02 MPa (point h in Fig. 3.21b) and the corresponding axial strain is  $4.104 \times 10^{-3}$ . At this moment, mixed tensile and shear crack coalescence occur between crack 5 and 7 as shown in Fig. 3.19. Finally with the increase of axial deformation, the axial supporting capacity of the specimen reduces rapidly until 2.3 MPa in an almost constant axial strain. In the process of ultimate failure, some lateral crack VI, far-field crack VIII, and surface spalling IX are also observed. The width of both fissure ① and ② decreases with increasing axial deformation, which is similar to the specimen for  $\alpha = \beta = 0^\circ$ , but it should be noted that the crack coalescence does not occur at the inner tips of two fissures ① and ②.

For  $\alpha = \beta = 30^\circ$ , tensile wing crack (cracks 1<sup>a</sup> and 1<sup>b</sup>) emanates simultaneously from the inner and outer tips of fissure ②, which is different from the specimen for

$\alpha = \beta = 0^\circ$  and  $15^\circ$ , whereas the axial stress (point a,  $\sigma_1 = 55.41 \text{ MPa} = 58 \% \sigma_c$ ) initiating crack 1 is distinctly lower than that of the specimen for  $\alpha = \beta = 15^\circ$ . But, the coalescence direction of crack 1 (tensile crack I) is approximate as the specimen for  $\alpha = \beta = 15^\circ$ . After the point a as shown in Fig. 3.21c, crack 1 is very difficult to lengthen due to the limitation of specimen boundary. The axial stress increases linearly as the elastic modulus of 31.46 GPa, which is the same as that before the point a. When the specimen is loaded to the point b ( $\sigma_1 = 90.56 \text{ MPa} = 94.8 \% \sigma_c$ ), crack 2 (anti-tensile crack IV) induces from the outer tip of fissure ② and propagates toward the top edge of the specimen rapidly, which leads to the axial stress drops to 85.51 MPa. Afterward, the axial stress of the specimen reaches the point c ( $\sigma_1 = 86.45 \text{ MPa} = 90.5 \% \sigma_c$ ), at the moment, cracks 3<sup>a</sup> and 3<sup>b</sup> are initiated from the inner tip of fissure ② and the outer tip of fissure ①, respectively, which leads to a small stress drop in the axial stress–axial strain curve. With continuous loading displacement, the axial stress continues dropping to 79.3 MPa from the point d ( $\sigma_1 = 81.92 \text{ MPa} = 85.8 \% \sigma_c$ ) due to the coalescence of crack 4 (anti-tensile crack IV) at the inner and outer tips of fissure ①. It should be noted that open crack 3<sup>b</sup> (tensile crack I) occurred to close in the above deformation process as the dotted line shown in Fig. 3.13d. At this time, the specimen has still a good supporting structure. Therefore, with the increase of axial deformation, the axial stress begins to increase as the average modulus  $\sim 31.05 \text{ GPa}$  (Fig. 3.21c), approximately equal to elastic modulus  $\sim 31.46 \text{ GPa}$ , which indicates that the initiation and propagation of cracks 2–4 have no any influence on the deformation behavior of the specimen. When the specimen is loaded to the peak strength (point e), crack 5 emanates at the ligament area of the specimen, which leads to the axial stress drops rapidly from 95.5 to 91.5 MPa. Afterward, with continuous displacement, the axial stress continues to drop from 90.93 MPa (point f) to zero (point h) in a smaller range of axial strain and the specimen undergoes the coalescence of cracks 6–8. Crack 6 is shear crack as shown in Fig. 3.19, and crack 7 is far-field crack VIII. During the final failure, the far-field crack, lateral crack, and small surface spalling are observed.

For  $\alpha = \beta = 45^\circ$ , tensile wing crack (cracks 1<sup>a</sup> and 1<sup>b</sup>) is initiated simultaneously from the inner and outer tips of fissure ①, which is different from the specimen for  $\alpha = \beta$  smaller than  $30^\circ$ ; whereas the axial stress (point a,  $\sigma_1 = 60.67 \text{ MPa} = 56.6 \% \sigma_c$ ) initiating crack 1 is approximately equal to that of the specimen for  $\alpha = \beta = 30^\circ$ . Moreover, the coalescence direction of crack 1 (tensile crack I) is approximate as the specimen for  $\alpha = \beta = 30^\circ$ . After the point a (Fig. 3.21d), with the increase of axial deformation, crack 1 widens and lengthens a little. The axial stress increases linearly as the elastic modulus of 33.29 GPa. When the specimen is loaded to the point d ( $\sigma_1 = 107.13 \text{ MPa} = 100 \% \sigma_c$ ), crack 2 emanates from the inner tips of two fissures, which leads to the axial stress drops to 101.7 MPa. Notice, crack 2<sup>b</sup> is anti-tensile crack IV. With continuous displacement, the axial stress begins to increase slowly due to a good supporting structure, but which is very difficult to reach the peak stress of the specimen. When the specimen is loaded to the point e, crack 3 induces rapidly from the outer tip of fissure ①, which leads to that the axial stress drops to 99.5 MPa. At this time, due to some minor damage of supporting structure, the reloading average modulus  $\sim 30.5 \text{ GPa}$  is a little lower than the elastic modulus

(~33.29 GPa). Afterward, when the specimen is loaded to the point f, crack 4 emanates from the outer tip of fissure ② and the inner tip of fissure ①. The corresponding axial stress drops rapidly from 104.07 to 91.8 MPa. The continuous increase of axial deformation leads the axial stress drops further to 85 MPa from the point g in an almost constant axial strain due to rapidly developing of crack 5 (anti-tensile crack IV). For the moment, the axial supporting capacity begins to increase slowly with axial deformation, and the axial stress–strain begins to depart gradually toward the axial strain, which indicates some damage of the specimen. When the specimen is loaded to the point h, crack 6 (Far-field crack VIII) is initiated and the axial stress drops to 98 MPa. The continuous loading displacement leads to the ultimate failure of the specimen and crack 7 emanates very fast. For the moment, the axial stress drops to 2.0 MPa rapidly in an almost constant strain.

Table 3.5 summarizes the crack initiation and coalescence behavior of sandstone specimen containing two coplanar fissures for  $\alpha = \beta$  greater than  $60^\circ$  in the

**Table 3.5** Crack initiation and coalescence behavior of sandstone specimen containing two coplanar fissures ( $\alpha = \beta = 60^\circ, 75^\circ$  and  $90^\circ$ )

Coplanar fissure angle	Crack initiation and coalescence behavior
$\alpha = \beta = 60^\circ$	<ul style="list-style-type: none"> <li>• The first tensile cracks were initiated from the outer tips of both fissure ① and ②</li> <li>• The first tensile cracks propagated along the direction of major principal stress</li> <li>• Shear crack coalescence occurred between the inner tips of two fissures</li> <li>• Shear crack was observed from the outer tip of fissure ① to the upper right corner of the specimen</li> <li>• Small surface spalling was observed after peak strength</li> <li>• Far-field crack (vertical splitting) occurred at the peak strength</li> <li>• Anti-tensile cracks were observed at the outer tip of fissure ②</li> <li>• No variance in the width of both fissures ① and ② with increasing axial deformation</li> </ul>
$\alpha = \beta = 75^\circ$	<ul style="list-style-type: none"> <li>• The first tensile cracks were initiated from the inner and outer tips of two fissures and propagated along the direction of major principal stress</li> <li>• Mixed tensile-shear crack coalescence occurred between the inner tips of two fissures</li> <li>• Shear crack was observed from the outer tip of fissure ② to the lower left corner of the specimen</li> <li>• No variance in the width of both fissures ① and ② with increasing axial deformation</li> <li>• Far-field crack (vertical splitting) occurred at 87.7 % of peak strength</li> <li>• Small surface spalling was observed after peak strength</li> <li>• Lateral tensile and far-field cracks often accompanied with unstable failure of specimen</li> </ul>
$\alpha = \beta = 90^\circ$	<ul style="list-style-type: none"> <li>• The first tensile cracks were initiated from the inner and outer tips of two fissures and propagated along the direction of major principal stress</li> <li>• Tensile crack coalescence occurred between the inner tips of two fissures</li> <li>• Shear crack was observed from the inner tip of fissure ② to the upper left corner of the specimen</li> <li>• No variance in the width of fissure ② with increasing axial deformation</li> <li>• Far-field crack (vertical splitting) occurred at 90 % of peak strength</li> <li>• Collapse in the width of fissure ① with increasing axial deformation</li> <li>• More surface spalling was observed in left part of the specimen</li> </ul>

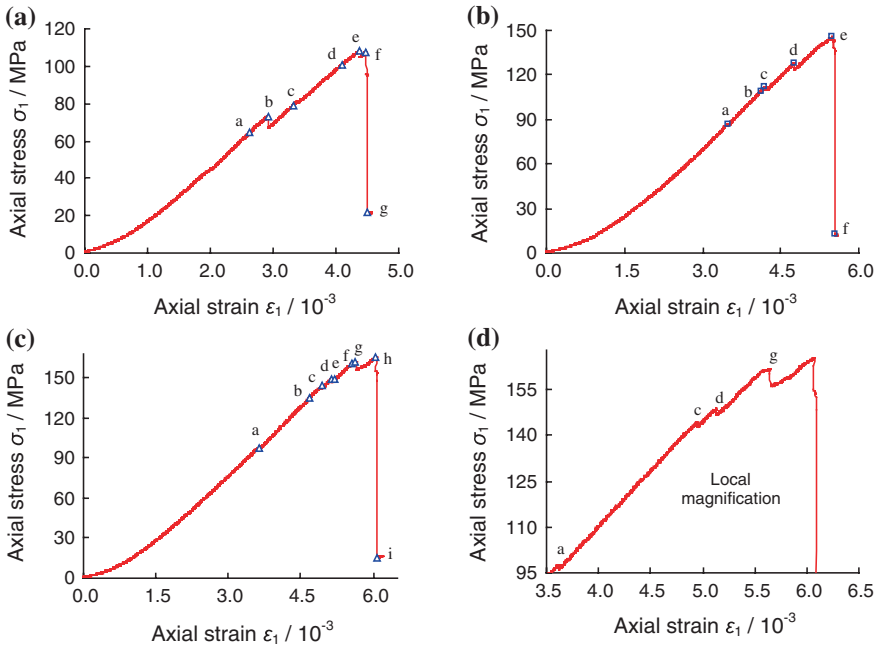


**Fig. 3.22** Relation between axial stress–strain curve and crack coalescence process in flawed specimens for  $\alpha = \beta = 60^\circ, 75^\circ, 90^\circ$ . **a**  $\alpha = \beta = 60^\circ$ , **b**  $\alpha = \beta = 75^\circ$ , **c**  $\alpha = \beta = 90^\circ$ , **d**  $\alpha = \beta = 90^\circ$  (with kind permission of Elsevier Publisher)

process of deformation as shown in Fig. 3.22. In Fig. 3.22, the denoted letter is corresponding to the crack coalescence process as shown in Figs. 3.15, 3.16, and 3.17. In accordance with Table 3.5 and Fig. 3.22, it can be seen that the real-time crack coalescence process of sandstone specimens containing two coplanar fissures for  $\alpha = \beta$  greater than  $60^\circ$  is different obviously from that for  $\alpha = \beta$  smaller than and equal to  $45^\circ$ . Compared with the axial stress–strain curves in Figs. 3.21 and 3.22, it can be seen that the real-time crack coalescence processes occur mainly after peak strength for the specimens with  $\alpha = \beta$  smaller than and equal to  $45^\circ$ , while before peak strength for the specimens with  $\alpha = \beta$  greater than and equal to  $60^\circ$ . Here, we do not analyze the real-time crack coalescence process of each specimen any longer. Only some difference between Tables 3.4 and 3.5 are analyzed as follows.

For  $\alpha = \beta = 60^\circ$ , tensile crack 1 (crack type III) is initiated from the outer tips of two fissures at the stress level of 64.21 MPa. In Fig. 3.22, there is a larger stress drop in the specimen when crack 2 (shear crack VII) coalesced as shown in Fig. 3.15b. But the widening of cracks 1–2 does not lead to a stress drop. Moreover, the coalescence of shorter crack (crack 3) from the outer tip of fissure ① does not lead to an obvious stress drop. However, the far-field crack 4 (vertical splitting) coalesced as shown in Fig. 3.15d; there was a smaller stress drop in the specimen, which can be seen from the point e in Fig. 3.22a. Anti-tensile crack 6<sup>a</sup>

occurs at the outer tip of fissure ② and propagates toward crack 1<sup>a</sup> in a curve form during ultimate failure as shown in Fig. 3.15g.

For  $\alpha = \beta = 75^\circ$ , these tensile cracks (1<sup>a</sup>–1<sup>d</sup>) were initiated simultaneously from the inner and outer tips of two fissures at the stress level of 86.22 MPa in a stable manner, which did not lead to a obvious stress drop in axial stress–strain curve. But there was a stress drop when crack 2 (Mixed tensile-shear crack) propagated from the inner tip of fissure ① at the stress level of 112.46 MPa as shown in Fig. 3.16c. Afterward, there was a bigger stress drop in the specimen when far-field crack 3 (vertical splitting) coalesced as shown in Fig. 3.16d. In the process of ultimate failure, shear crack, lateral crack, and far-field crack are observed due to obvious brittleness of tested sandstone.

For  $\alpha = \beta = 90^\circ$ , three tensile cracks (1<sup>a</sup>–1<sup>c</sup>) were initiated simultaneously from the inner and outer tips of two fissures very fast at the stress level of 97.55 MPa (point a), which results in a smaller stress drop as shown in Fig. 3.22d. With the increase of axial deformation, there is a minor stress drop when far-field crack 2 occurs at the stress level of 144.38 MPa as shown in Fig. 3.17c. However, when far-field crack 3 (vertical splitting) coalesced as shown in Fig. 3.17d; there was a stress drop in the specimen. Notice the coalescence of crack 4 (far-field crack VIII) as shown in Fig. 3.17e does not result in a stress drop. The continuous increase of axial displacement leads to the coalescence of crack 5 (Surface spalling IX) at the stress level of 162.03 MPa; therefore there is a bigger stress drop in the specimen. During ultimate failure, shear crack VII was also observed from the inner tip of fissure ② to the upper left corner of the specimen as shown in Fig. 3.19.

In the specimens for  $\alpha = \beta$  greater than and equal to  $60^\circ$ , there are no variance in the width of both fissure ① and ② with increasing axial deformation except for the collapse in the width of fissure ① of the specimen for  $\alpha = \beta = 90^\circ$ , while in the specimens for  $\alpha = \beta$  smaller than and equal to  $45^\circ$ , the width of both fissures ① and ② decreases except for no variance in the width of fissure ① of the specimen for  $\alpha = \beta = 45^\circ$ .

It should be more interesting to make a qualitative comparison of the results in this chapter with existing results containing a single fissure (Yang and Jing 2011). There are some common laws for brittle sandstone containing two coplanar fissures and a single fissure, which can be summarized as follows. Tensile cracks I and III are often the first crack, and tensile crack V is only observed for  $\alpha = \beta$  smaller than and equal to  $15^\circ$ . Anti-tensile crack IV often accompanies with tensile crack I or III toward the reverse direction, which is usually observed in the specimen for  $\alpha = \beta$  smaller than and equal to  $60^\circ$ . Moreover, far-field crack VIII and surface spalling IX are usually observed for flawed sandstone specimens. However, shear crack VII (Fig. 3.19) in brittle sandstone containing two coplanar fissures is different from existing results containing a single fissure (Yang and Jing 2011). More difference in sandstone specimen containing two coplanar fissures and a single fissure should be further reinforced in the future.

### 3.4 Conclusions

Uniaxial compression tests were carried out for brittle sandstone specimens (80 mm in width, 160 mm in height, and 30 mm in thickness) containing two coplanar fissures ( $2a = 15$  mm,  $2b = 18$  mm) by photographic monitoring. The following conclusions can be drawn.

In this chapter, tested intact sandstone specimen is a kind of typical brittle rock and takes on typically axial splitting failure. The peak strength and peak axial strain of sandstone specimens containing two coplanar fissures are lower than that of intact specimen, but the reduction extent is distinctly related to coplanar fissure angle. The Young's moduli of flawed specimens are not obviously related to coplanar fissure angle although a little lower than that of intact specimen. Four cyclic loading–unloading do not increase the peak strength and peak axial strain of sandstone specimens containing two coplanar fissures, but increase the slope of axial stress–strain curve after third cyclic loading–unloading.

The crack initiation and coalescence are observed and characterized from the inner and outer tips of pre-existing coplanar fissures in brittle sandstone specimen by adopting photographic monitoring. Crack coalescence type in brittle sandstone specimens containing two coplanar fissures are analyzed in detail on basis of the crack propagation mechanism (tensile, shear, lateral crack, far-field crack, and surface spalling) for a single fissure in response to the applied axial loads. The macroscopic failure modes of sandstone specimens containing two coplanar fissures are a mixture of several cracks among nine various crack types.

In accordance with photographic monitoring results, the real-time crack coalescence process of sandstone containing two coplanar fissures is characterized. Moreover, the relationship between coplanar fissure angle and crack coalescence stress is constructed. The crack initiation stress in flawed specimens containing two coplanar fissures is obviously lower than that peak strength except for one specimen with  $\alpha = \beta = 15^\circ$ . The corresponding axial stress of initiating crack 4 is approximate to the peak stress of the specimen, moreover has a similar relation with coplanar fissure angle as peak stress. The influence of real-time crack coalescence process on axial stress–strain curve of sandstone containing two coplanar fissures is further discussed.

Finally, it should be noted that this chapter only investigates the crack coalescence behavior of brittle sandstone containing two coplanar fissures with different angles under uniaxial compression by photographic monitoring. In order to understand deeply the fracture coalescence and mechanism of engineering rock mass, more experimental results for flawed brittle sandstone specimens with three fissures will be presented in the Chap. 4.

### References

- Ferrero AM, Migliazza M, Roncella R, Tebaldi G (2008) Analysis of the failure mechanisms of a weak rock through photogrammetrical measurements by 2D and 3D visions. *Eng Fract Mech* 75:652–663

- Ferrero AM, Migliazza M (2009) Theoretical and numerical study on uniaxial compressive behavior of marl. *Mech Mater* 41:561–572
- Roncella R, Romeo E, Forlani G (2005) Image based microstructural analysis in fracture mechanics. *Optical 3-D Measurement Techniques II*:51–60
- Yang SQ (2011) Crack coalescence behavior of brittle sandstone samples containing two coplanar fissures in the process of deformation failure. *Eng Fract Mech* 78:3059–3081
- Yang SQ, Jiang YZ (2010) Triaxial mechanical creep behavior of sandstone. *Min Sci Technol* 20(3):339–349
- Yang SQ, Jing HW (2011) Strength failure and crack coalescence behavior of brittle sandstone samples containing a single fissure under uniaxial compression. *Int J Fract* 168(2):227–250

# Chapter 4

## Experimental Investigation on Fracture Evolution Behavior of Brittle Sandstone Containing Three Fissures

In the past, the relationship between real-time crack coalescence process using photographic monitoring and the axial stress–strain curve of rock material has so far not been investigated for brittle sandstone specimens containing three pre-existing fissures. Therefore in this chapter, a rock mechanics servo-controlled testing system was used to conduct uniaxial compression tests with brittle sandstone specimens containing three fissures. Moreover, photographic monitoring technique was used to obtain the relationship between the real-time crack coalescence process and the axial stress–strain behavior for brittle sandstone containing three fissures. The emphasis of this chapter was to investigate the effects of the ligament angle on the strength and deformation failure behaviors of a brittle sandstone material containing three fissures and to analyze the real-time crack coalescence process in a sandstone material under uniaxial compression, using photographic monitoring technique (Yang et al. 2012).

### 4.1 Specimen Preparation and Testing Procedure

#### 4.1.1 Sandstone Material and Specimen Preparation

Sandstone specimens from Linyi City, Shandong province, China, were used in the experiments. The mineral components of the sandstone material were feldspar, quartz, and detritus (Fig. 4.1). The sandstone, a fine-grained heterogeneous material, had a crystalline and blocky feature and an average unit weight of about 2650 kg/m<sup>3</sup>.

Rectangular prismatic specimens of sandstone, with dimensions of 80 × 160 × 30 mm, were prepared. All specimens had a height-to-width ratio of 2.0 to ensure a uniform stress state within the central part of the specimens. The geometry of the specimens containing three fissures is described in Fig. 4.2. The

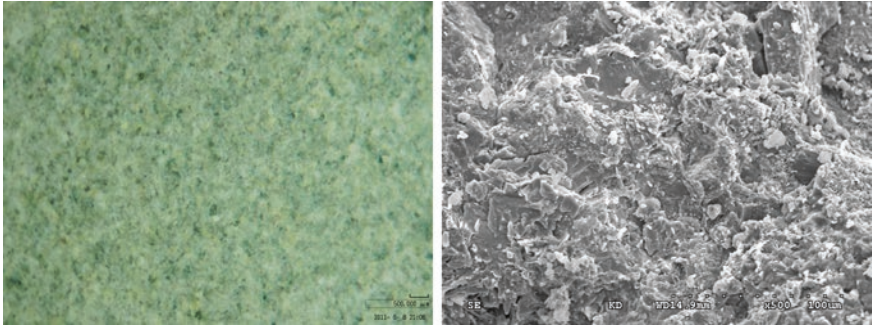


**Fig. 4.1** Microscopic feature of sandstone material used in this chapter (with kind permission of Springer Publisher)

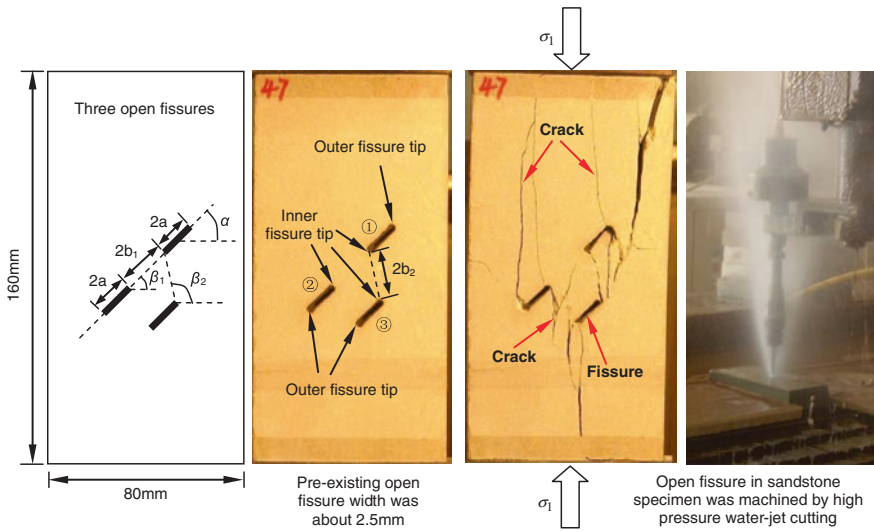


**Fig. 4.2** Geometry of the three fissures in the sandstone specimens.  $\alpha$  is the fissure angle;  $\beta_1$  is the ligament angle between fissures ①②;  $\beta_2$  is the ligament angle between fissures ①③;  $2a$  is the fissure length;  $2b_1$  is the ligament length between fissures ①②; and  $2b_2$  is the ligament length between fissures ①③. In this chapter, three open fissures were machined in sandstone specimens by high-pressure water-jet cutting (with kind permission of Springer Publisher)

geometry of the three fissures is defined by six geometrical parameters: fissure length  $2a$ , ligament length  $2b_1$  between fissures ①②, ligament length  $2b_2$  between fissures ①③, fissure angle  $\alpha$  (the angle of the fissure with the horizontal direction), ligament angle  $\beta_1$  between fissures ①②, and ligament angle  $\beta_2$  between fissures ①③, as shown in Fig. 4.2. Fissures ① and ② are coplanar, and fissures ①②③ are parallel, as shown in Fig. 4.2.

A high-pressure water-jet cutting machine (Yang and Jing 2011) was used to cut three fissures in intact specimens. The machined open fissure widths are

**Table 4.1** Sandstone specimens containing three fissures under uniaxial compression

Specimen	W/mm	H/mm	T/mm	$\alpha/^\circ$	$\beta_1/^\circ$	$\beta_2/^\circ$	2a/mm	2b <sub>1</sub> /mm	2b <sub>2</sub> /mm	Note
B0r <sup>#</sup>	80.8	158.9	31.4	N/A	N/A	N/A	N/A	N/A	N/A	Intact specimen
B45 <sup>#</sup>	80.6	159.5	29.8	45	45	75	15	20	20	Flawed specimen containing three open fissures
B46 <sup>#</sup>	81.0	160.0	31.2	45	45	90	15	20	20	
B47 <sup>#</sup>	80.5	159.1	29.8	45	45	105	15	20	20	
B48 <sup>#</sup>	80.1	159.2	29.8	45	45	120	15	20	20	
B56 <sup>#</sup>	80.9	156.5	31.2	45	45	120	15	20	20	

Note W Width, H Height, T Thickness

approximately 2.5 mm. To investigate the effects of the geometry of three pre-existing fissures on the fracture coalescence behavior of sandstone under uniaxial compression, different fissure geometries are designed by varying  $\beta_2$  while holding other five parameters as constant values ( $2a = 15$  mm,  $2b_1 = 2b_2 = 20$  mm, and  $\alpha = \beta_1 = 45^\circ$ ). A detailed description of the sandstone specimens containing three fissures is listed in Table 4.1.

### 4.1.2 Testing Procedure

Uniaxial compression tests for intact and flawed sandstone specimens containing three fissures were conducted using a rock mechanics servo-controlled testing system. The axial stress was imposed on the surface of the rock specimen until the failure. All tests were conducted under displacement-controlled conditions with a strain rate of  $8.125 \times 10^{-6}$ /s. During the uniaxial compression experiment, the loads and deformations of the specimens were recorded simultaneously. Moreover, two rigid steel blocks, with dimensions of  $33 \times 83 \times 15$  mm, were placed between the loading frame and the rock specimen. Two antifricition gaskets were placed between two rigid steel blocks and the end faces of the rock specimens to reduce the end friction effects for specimens with a height-to-width ratio of approximately 2.0.

## 4.2 Analysis of Experimental Results

### 4.2.1 Axial Stress–Strain Curve of Intact Specimen

Figure 4.3 presents the axial stress–strain curve of intact sandstone specimens under uniaxial compression. The corresponding cracking process is also captured by photographic monitoring, as shown in Fig. 4.4. The letters in Fig. 4.3 correspond to those shown in Fig. 4.4. Table 4.2 lists the peak strength  $\sigma_c$  and the peak axial strain  $\varepsilon_{1c}$  for intact specimen under uniaxial compression.

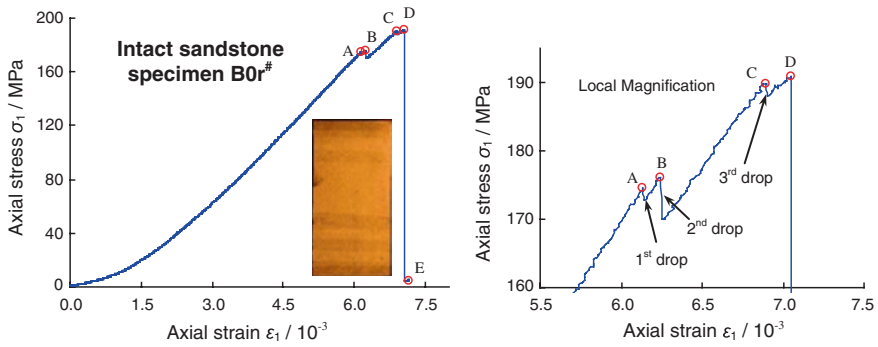


**Fig. 4.3** Axial stress–strain curve of intact sandstone specimen under uniaxial compression (with kind permission of Springer Publisher)

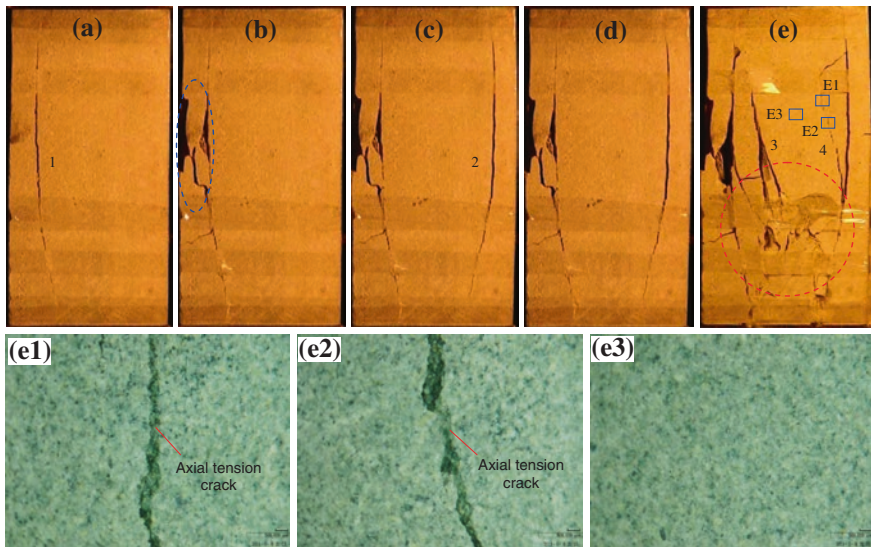


**Fig. 4.4** Crack coalescence process of intact sandstone specimen under uniaxial compression (with kind permission of Springer Publisher)

**Table 4.2** Mechanical parameters of intact and flawed sandstone specimens containing three fissures under uniaxial compression

Specimen	$\alpha/^\circ$	$\beta_1/^\circ$	$\beta_2/^\circ$	$2a/\text{mm}$	$2b_1/\text{mm}$	$2b_2/\text{mm}$	$\epsilon_{1c}/10^{-3}$	$\sigma_c/\text{MPa}$	$D_a$
B0r#	Intact sandstone specimen						7.051	190.8	0.000
B45#	45	45	75	15	20	20	4.568	87.17	0.543
B46#	45	45	90	15	20	20	4.464	73.87	0.613
B47#	45	45	105	15	20	20	3.387	79.71	0.582
B48#	45	45	120	15	20	20	4.254	101.86	0.466
B56#	45	45	120	15	20	20	4.100	101.36	0.469

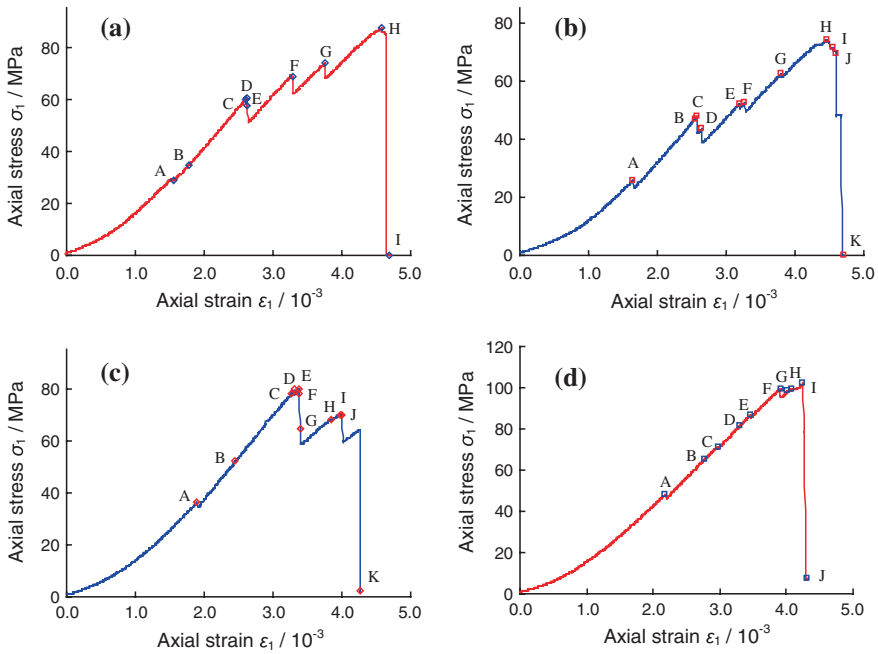
In accordance with Figs. 4.3 and 4.4, crack coalescence in the intact specimen cannot be observed by unaided eyes before point A ( $\sigma_1 = 174.46 \text{ MPa} = 91.4 \% \sigma_c$ ). However, when the axial stress is loaded to point A, the first crack (vertical splitting tensile failure) rapidly propagates along the direction of axial loading, which causes the axial stress to drop to 172.8 MPa in an approximately constant axial strain. After the first stress drop and with increasing deformation, the axial stress is loaded to point B ( $\sigma_1 = 176.06 \text{ MPa} = 92.3 \% \sigma_c$ ); some surface failures and short cracks occur near crack 1, as shown in the elliptical region of Fig. 4.5b. At this moment, the second stress drop occurs, falling from 176.06 to 170 MPa in an approximately constant axial strain. Afterwards, the axial supporting capacity slowly increases with the increasing deformation because the specimen still had a good supporting structure. When the specimen reaches an axial stress of approximately 189.8 MPa (Point C, 99.5 %  $\sigma_c$ ), crack 2 (vertical splitting tensile failure) forms quickly along the direction of axial stress, which leads to the third stress drop, from 189.8 to 188.1 MPa, as shown in Fig. 4.3. Continuously increasing the axial displacement causes the specimen to reach point D ( $\sigma_1 = 190.8 \text{ MPa} = 100 \% \sigma_c$ ) quickly. During this process, the axial stress–strain curve departs notably toward the strain axis because of obvious damage of the supporting structure, but no new cracks are observed. However, after peak stress, the specimen undergoes brittle failure, and the axial stress drops abruptly to 4.4 MPa in additional cracks (e.g., cracks 3–4), as shown in Fig. 4.4e. During the ultimate drop, a large failure sound can be heard.

In accordance with the above description, the axial stress–strain behavior of rock materials is an external response and has a notable relation with the real-time crack coalescence process. However, for some hard and brittle rocks, real-time crack coalescence process, similar to that shown in Fig. 4.4, is usually difficult to be captured because of abruptly brittle failure of rock specimen.

### 4.2.2 Axial Stress–Strain Curve of Flawed Specimens Containing Three Fissures

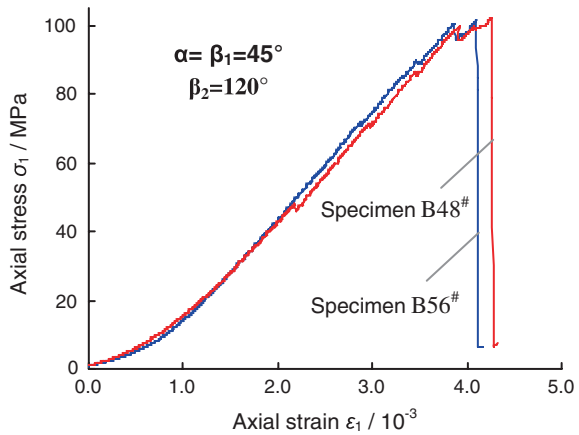
Figure 4.5 shows the complete axial stress–strain curves for sandstone specimens containing three fissures ( $\alpha = \beta_1 = 45^\circ$ ) under uniaxial compression. These curves are different from those of intact specimens, as shown in Fig. 4.3. Compared with intact specimens, more stress drops are observed in the axial stress–strain curves as a result of the coalescence of new cracks in flawed specimens with the increasing deformation. The relationship between the real-time crack coalescence process and the axial stress–strain curve of brittle sandstone specimens containing three fissures will be depicted in the fourth section of this article. Here, only the axial stress–strain curve behavior of flawed specimens containing three fissures is discussed.

Figure 4.6 shows the effect of heterogeneity on axial stress–strain curves of sandstone specimens containing three fissures ( $\alpha = \beta_1 = 45^\circ$ ,  $\beta_2 = 120^\circ$ ) under uniaxial compression. From Fig. 4.6, it can be seen that for flawed specimens containing three fissures with the same geometry, the axial stress–strain curves exhibit



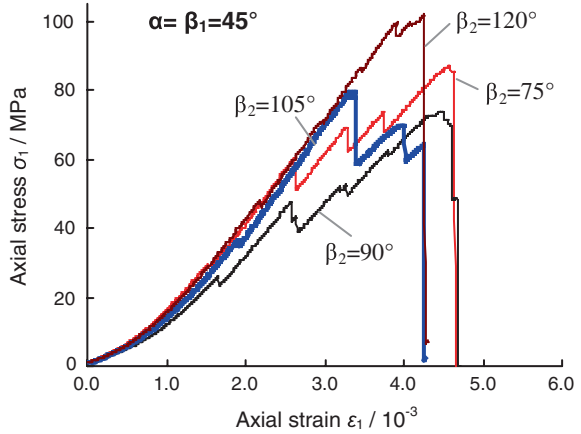
**Fig. 4.5** Complete axial stress–strain curves of sandstone specimens containing three fissures ( $\alpha = \beta_1 = 45^\circ$ ) under uniaxial compression . **a**  $\alpha = \beta_1 = 45^\circ \beta_2 = 75^\circ$ , **b**  $\alpha = \beta_1 = 45^\circ \beta_2 = 90^\circ$ , **c**  $\alpha = \beta_1 = 45^\circ \beta_2 = 105^\circ$  and **d**  $\alpha = \beta_1 = 45^\circ \beta_2 = 120^\circ$  (with kind permission of Springer Publisher)

**Fig. 4.6** Effect of heterogeneity on axial stress–strain curves of sandstone specimens containing three fissures under uniaxial compression (with kind permission of Springer Publisher)



very good consistency. Peak strengths of two specimens B48# and B56# are 101.86 and 101.36 MPa, respectively, while the corresponding peak axial strain of the two specimens are  $4.254 \times 10^{-3}$  and  $4.100 \times 10^{-3}$ . Based on the above analysis, we can see that the heterogeneity has nearly no effect on the axial stress–strain curve of

**Fig. 4.7** Effect of ligament angle  $\beta_2$  on axial stress–strain curves of sandstone specimens containing three fissures under uniaxial compression (with kind permission of Springer Publisher)



flawed specimen containing three fissures with the same geometry. Therefore in this research, the experimental results in Fig. 4.6 can be used to discuss the effects of the ligament angle  $\beta_2$  on strength and deformation parameters of the specimen.

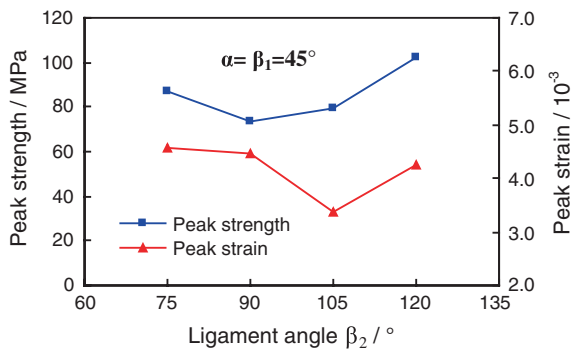
To show clearly the effect of the ligament angle  $\beta_2$  on the axial stress–strain curves of the specimen, four axial stress–strain curves (Fig. 4.5) were plotted together in Fig. 4.7. The corresponding peak strength and peak axial strain of the specimens are also listed in Table 4.2.

From Table 4.2, peak strength and peak axial strain of flawed specimens are lower than those of the intact specimen, and the extent of this reduction is significantly related to the ligament angle  $\beta_2$ . Figure 4.8 shows the influence of  $\beta_2$  on the peak strength and peak strain of the specimens. Note that in Fig. 4.8, only the mechanical parameter of specimen B48# as shown in Fig. 4.6 is used.

To indicate the reduction extent of the peak strength of flawed specimens containing three fissures in relation to intact specimens, reduction factor was defined as follows:

$$D_{at} = \frac{\sigma_{cm} - \sigma_{cn}}{\sigma_{cm}} \tag{4.1}$$

**Fig. 4.8** Influence of ligament angle  $\beta_2$  on peak strength and peak strain of sandstone specimens containing three fissures under uniaxial compression (with kind permission of Springer Publisher)



where  $\sigma_{cm}$  is the peak strength of an intact specimen, equal to 190.8 MPa in the present study, and  $\sigma_{cn}$  is the peak strength of a flawed specimen containing three fissures. In accordance with Eq. (4.1), the calculated  $D_{at}$  values of flawed specimens containing three fissures are also listed in Table 4.2.

As indicated in Table 4.2, the  $D_{at}$  value of the specimen with three fissures of  $\beta_2 = 90^\circ$  is the highest of the four specimens containing three fissures (with  $\alpha = \beta_1 = 45^\circ$ ), indicating that the peak strength of the specimen with three fissures of  $\beta_2 = 90^\circ$  is the lowest ( $\sim 73.87$  MPa) under uniaxial compression. As  $\beta_2$  decreases from  $90^\circ$  to  $75^\circ$ , the  $D_{at}$  value of the flawed specimens decreases from 0.613 to 0.543. However, the  $D_{at}$  value of the flawed specimens also decreases from 0.613 to 0.466 as  $\beta_2$  increases from  $90^\circ$  to  $120^\circ$ . The above analysis reveals that uniaxial compressive strength first decreases and then increases as the ligament angle  $\beta_2$  is increased in the range from  $75^\circ$  to  $120^\circ$ , as shown in Fig. 4.8.

The intact sandstone specimen fails at a strain of 0.705 % under uniaxial compression, while the sandstone specimens containing three fissures fail at a strain of approximately 0.34–0.46 %, which is less than that of the intact specimen. Moreover, the peak axial strain  $\varepsilon_{1c}$  of the sandstone specimens depends on the ligament angle  $\beta_2$ . As shown in Fig. 4.8,  $\varepsilon_{1c}$  is nonlinearly related to  $\beta_2$ . As  $\beta_2$  increased from  $75^\circ$  to  $90^\circ$ ,  $\varepsilon_{1c}$  decreases slightly from  $4.568 \times 10^{-3}$  to  $4.464 \times 10^{-3}$ , whereas it decreases substantially from  $4.464 \times 10^{-3}$  to  $3.387 \times 10^{-3}$  as  $\beta_2$  increases from  $90^\circ$  to  $105^\circ$ . However,  $\varepsilon_{1c}$  increases from  $3.387 \times 10^{-3}$  to  $4.254 \times 10^{-3}$  as  $\beta_2$  increases from  $105^\circ$  to  $120^\circ$ . But, the effect of  $\beta_2$  on peak strain is not synchronous to the effect on peak strength, as shown in Fig. 4.8.

### 4.3 Crack Initiation Mode and Analysis of the Coalescence Process

#### 4.3.1 Crack Initiation Mode and Stress Analysis

During deformation, the crack initiation mode and coalescence process of brittle sandstone specimens containing three fissures ( $\alpha = \beta_1 = 45^\circ$ ) are observed using a photographic monitoring technique.

Figure 4.9 shows the crack initiation mode of the sandstone specimens containing three fissures ( $\alpha = \beta_1 = 45^\circ$ ) under uniaxial compression. From this figure, the effect of ligament angle  $\beta_2$  on the crack initiation mode can be analyzed. Here, the mode initiated the first crack (crack 1) is defined as the crack initiation mode. The corresponding axial stress (i.e., the crack initiation stress) is also given in Fig. 4.9. The axial stress listed in Fig. 4.9 corresponds to point A in Fig. 4.5.

As shown in Fig. 4.9, the crack initiation mode of sandstone specimens containing three fissures ( $\alpha = \beta_1 = 45^\circ$ ) depends on the ligament angle  $\beta_2$ . For  $\beta_2 = 75^\circ$ , crack 1 is initiated from the inner and outer tips of fissures ②③, while no crack is initiated from the inner and outer tips of fissure ①. Notably, crack 1<sup>a</sup> is initiated at the inner tip of fissure ②, and crack 1<sup>b</sup> is initiated at the outer tip of fissure

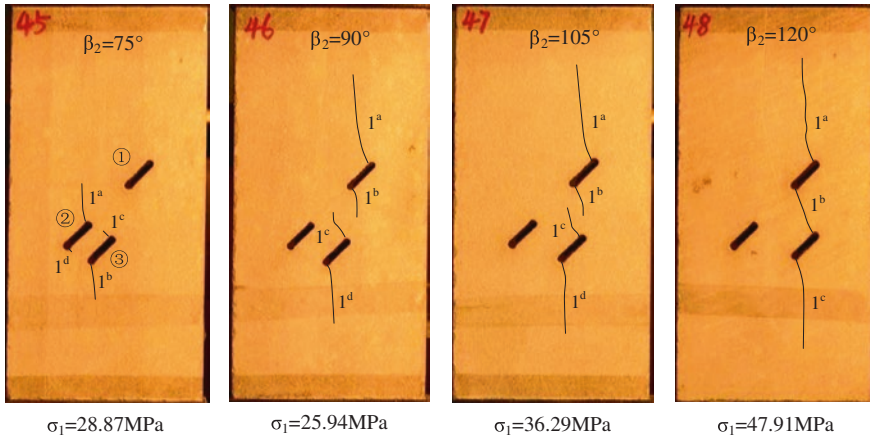


**Fig. 4.9** Crack initiation mode of sandstone specimens containing three fissures ( $\alpha = \beta_1 = 45^\circ$ ) under uniaxial compression (with kind permission of Springer Publisher)

③ and propagates along the direction of major principal stress. However, crack  $1^c$  is initiated from the inner tip of fissure ③ and evolves toward the inner tip of fissure ②. Crack  $1^d$  is initiated from the outer tip of fissure ② and evolves toward the outer tip of fissure ③ along the vertical direction of the pre-existing fissure. Moreover, the coalescence speed of cracks  $1^c$  and  $1^d$  are lower than those of cracks  $1^a$  and  $1^b$ . This result is likely due to stress field interactions between fissures ②③, and it limits the propagation of cracks  $1^c$  and  $1^d$ .

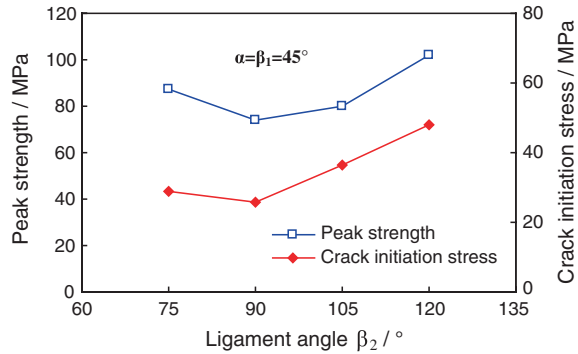
For  $\beta_2 = 90^\circ$  and  $\beta_2 = 105^\circ$ , the crack initiation modes are approximately similar. In these two specimens, the crack initiation mode is different from that of the other two specimens. Crack 1 is initiated from the inner and outer tips of fissures ①③, while no crack is initiated from the inner and outer tips of fissure ②. Cracks  $1^a$  and  $1^b$  are initiated from the outer and inner tips of fissure ①, respectively, while cracks  $1^c$  and  $1^d$  are initiated from the inner and outer tips of fissure ③, respectively. Four cracks  $1^a-1^d$  are initiated in the direction vertical to pre-existing fissure ① or ③ and then evolves along the direction of axial stress.

For  $\beta_2 = 120^\circ$ , crack  $1^a$  is initiated from the outer tip of fissure ①, and crack  $1^c$  is initiated from the outer tip of fissure ③. Crack  $1^b$  quickly coalesces between the inner tips of fissures ①③. Note, cracks  $1^a$  and  $1^c$  propagate toward the edge of the specimen along the direction of axial stress.

The crack initiation mode in Fig. 4.9 appears very fast, which leads to an obvious stress drop in the axial stress–strain curve except for  $\beta_2 = 75^\circ$ . For example, the axial stress drops to 23.22 from 25.94 MPa for  $\beta_2 = 90^\circ$  and from 36.29 to 34.61 MPa for  $\beta_2 = 105^\circ$ . However, for  $\beta_2 = 75^\circ$ , although no distinct axial stress drop is observed, there is an obvious turning point (see point A of Fig. 4.5a) in the axial stress–strain curve.

Figure 4.10 depicts the effect of the ligament angle  $\beta_2$  on the crack initiation stress of sandstone specimens containing three fissures ( $\alpha = \beta_1 = 45^\circ$ ) under uniaxial compression. The peak strength is also given in this figure for comparison.

**Fig. 4.10** Effect of ligament angle  $\beta_2$  on crack initiation stress of sandstone specimens containing three fissures (with kind permission of Springer Publisher)



From Fig. 4.10, the crack initiation stress is distinctly lower than the peak strength for sandstone specimens containing three fissures. It is approximately 34 % of the corresponding peak strength for  $\beta_2 = 75^\circ$  and  $90^\circ$  and 46 % of the corresponding peak strength for  $\beta_2 = 105^\circ$  and  $120^\circ$ . The crack initiation stress is nonlinearly related to  $\beta_2$ , and the effect of  $\beta_2$  on peak strength is approximately similar. As  $\beta_2$  increases from  $75^\circ$  to  $90^\circ$ , the crack initiation stress decreases by 10 % from 28.87 to 25.94 MPa, whereas it increases linearly from 25.94 to 47.91 MPa as  $\beta_2$  increases from  $90^\circ$  to  $120^\circ$ .

### 4.3.2 Real-Time Crack Coalescence Process of Specimens for $\beta_2 = 75^\circ$ and $90^\circ$

Figures 4.11 and 4.12 present real-time crack coalescence process for sandstone specimens containing three fissures with  $\beta_2 = 75^\circ$  and  $90^\circ$ , respectively. As seen in Figs. 4.11 and 4.12, photographic monitoring can be used to identify and characterize the crack coalescence process. The letters denoted in Figs. 4.11 and 4.12 correspond to Figs. 4.5a, b and the numbers represent the crack coalescence sequence during deformation (see Tables 4.3 and 4.4). Results for the flawed specimen containing three fissures ( $\alpha = \beta_1 = 45^\circ$ ,  $\beta_2 = 90^\circ$ ) are presented below to provide an example of the relationship between real-time crack coalescence process and axial stress–strain curve.

In accordance with Fig. 4.12 and Table 4.4, the real-time crack coalescence behavior of sandstone specimen containing three fissures ( $\alpha = \beta_1 = 45^\circ$ ,  $\beta_2 = 90^\circ$ ) is analyzed for the entire deformation process, as shown in Fig. 4.5b. Before point A ( $\sigma_1 = 25.94 \text{ MPa} = 35.1 \% \sigma_c$ ), the stress concentration at the inner and outer tips of three fissures do not reach the material strength, and no crack is initiated. However, when the axial stress is loaded to point A, crack 1 induces rapidly from the inner and outer tips of fissures ① and ③, as shown in Fig. 4.9. The corresponding axial stress drops slightly from 25.94 to 23.22 MPa. After point A, the axial stress increases linearly with the strain as the elastic modulus

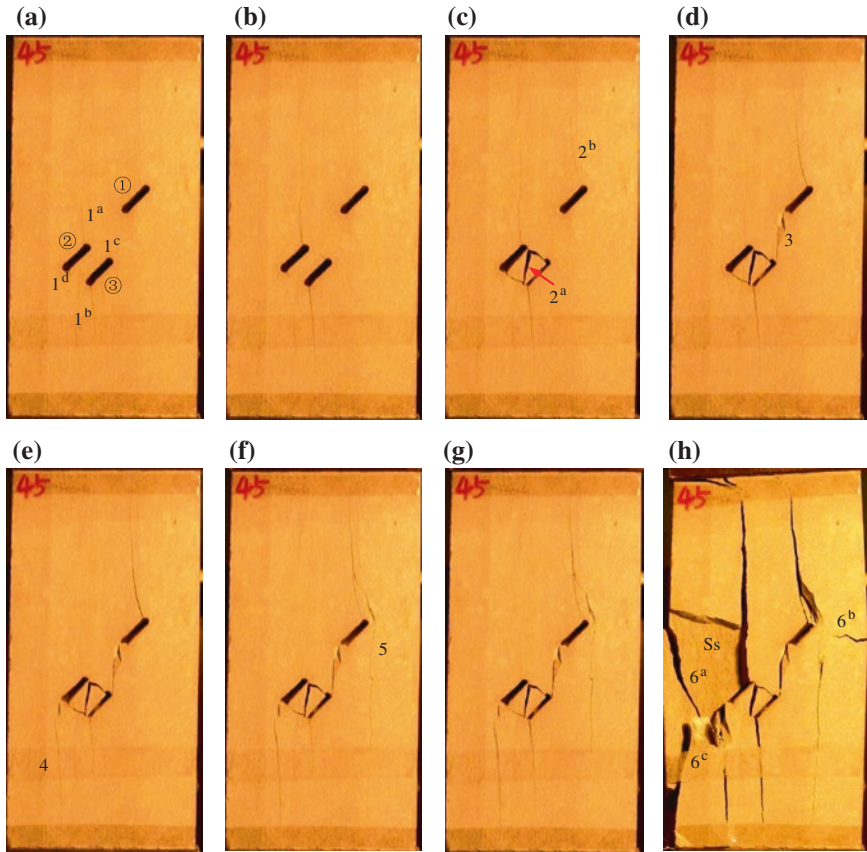


**Fig. 4.11** Crack coalescence process of sandstone specimen containing three fissures ( $\alpha = \beta_1 = 45^\circ$ ,  $\beta_2 = 75^\circ$ ) under uniaxial compression. The letters correspond to those shown in Fig. 4.5a (with kind permission of Springer Publisher)

of 27.11 GPa. For this moment, the length and width of crack 1 increases with the increasing axial deformation, and this occurrence can be inferred from point B ( $\sigma_1 = 46.89 \text{ MPa} = 63.5 \% \sigma_c$ ) in Fig. 4.12. When the specimen is loaded to point C ( $\sigma_1 = 47.54 \text{ MPa} = 64.4 \% \sigma_c$ ), crack  $2^a$  quickly coalesces between the inner tip of fissure ② and the outer tip of fissure ③, and crack  $2^b$  is initiated from the inner tip of fissure ② and evolves rapidly toward the top edge of the specimen along the direction of axial stress. This occurrence rapidly leads to a corresponding axial stress drop from 47.54 to 41.89 MPa. The continuous axial deformation increase (point D,  $\sigma_1 = 43.46 \text{ MPa}$ ) leads to the third stress drop from 43.46 to 38.87 MPa as a result of the coalescence of crack 3 between the inner tips of fissures ①③. The specimen still has a better supporting structure (Fig. 4.12c). Thus, with increasing deformation, the axial supporting capacity also increases as an average modulus of approximately 25.15 GPa, which is slightly lower than the elastic modulus of

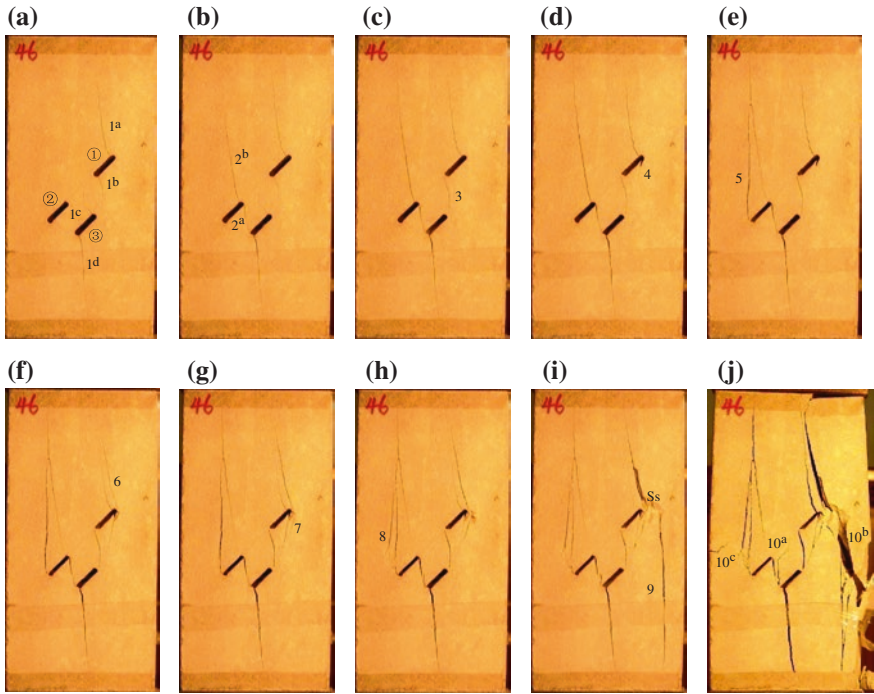


**Fig. 4.12** Crack coalescence process of sandstone specimen containing three fissures ( $\alpha = \beta_1 = 45^\circ$ ,  $\beta_2 = 90^\circ$ ) under uniaxial compression. The letters correspond to those shown in Fig. 4.5b (with kind permission of Springer Publisher)

**Table 4.3** Crack coalescence behavior of sandstone specimen containing three fissures ( $\alpha = \beta_1 = 45^\circ$ ,  $\beta_2 = 75^\circ$ )

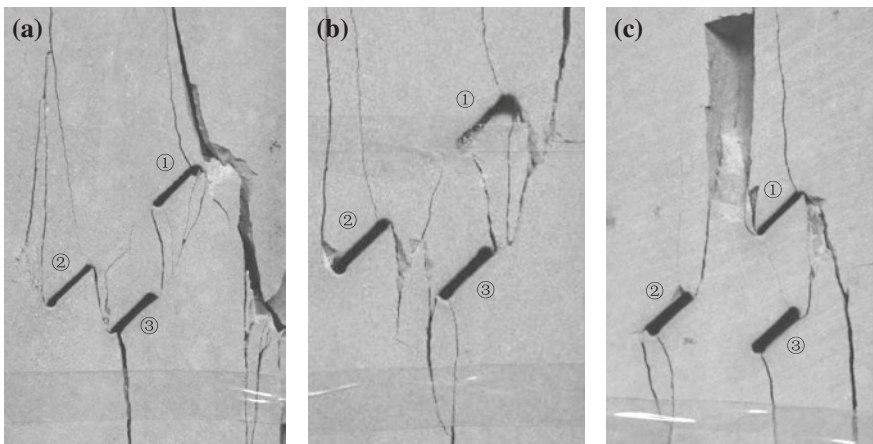
Coalescence point	Initiated cracks	$\epsilon_1 / \times 10^{-3}$	$\sigma_1 / \text{MPa}$	Stress drop/MPa
B	No new crack	1.774	34.50	No
C	No new crack	2.592	59.76	No
D	Crack 2	2.618	60.48	57.19
E	Crack 3	2.625	57.52	51.30
F	Crack 4	3.292	68.82	62.31
G	Crack 5	3.757	73.61	67.92
H (Peak strength)	No new crack	4.568	87.17	86.97
I	Crack 6	4.690	0.168	Ultimate failure

27.11 GPa. Because of the opening of crack 3, cracks 1<sup>b</sup> and 1<sup>c</sup> close but can still be seen by local magnification, as shown in Figs. 4.13a and Fig. 4.14.

Afterwards, when the specimen is loaded to point E ( $\sigma_1 = 51.98 \text{ MPa} = 70.4 \% \sigma_c$ ), crack 4 is initiated from the outer tip of fissure ① and propagates toward the inner tip of fissure ③. However, it does not nucleate with the inner tip of fissure ③. The

**Table 4.4** Crack coalescence behavior of sandstone specimen containing three fissures ( $\alpha = \beta_1 = 45^\circ, \beta_2 = 90^\circ$ )

Coalescence point	Initiated cracks	$\varepsilon_1/\times 10^{-3}$	$\sigma_1/\text{MPa}$	Stress drop/MPa
B	No new crack	2.548	46.89	No
C	Crack 2	2.572	47.54	41.89
D	Crack 3	2.637	43.46	38.87
E	Crack 4	3.191	51.98	50.50
F	Crack 5	3.273	52.57	49.49
G	Crack 6	3.804	62.44	61.14
H (Peak strength)	Crack 7	4.464	73.87	73.74
I	Crack 8	4.549	71.25	70.57
J	Crack 9	4.601	69.42	47.99
K	Crack 10	4.708	0.148	Ultimate failure

**Fig. 4.13** Local magnification of ultimate failure mode of sandstone specimens containing three fissures ( $\alpha = \beta_1 = 45^\circ, \beta_2 = 90^\circ, 105^\circ$  and  $120^\circ$ ) under uniaxial compression (with kind permission of Springer Publisher). **a**  $\beta_2 = 90^\circ$ , **b**  $\beta_2 = 105^\circ$ , **c**  $\beta_2 = 120^\circ$ 

corresponding axial stress drops rapidly from 51.98 to 50.50 MPa, a minor drop compared with the previous two stress drops. The increasing displacement leads to the specimen being loaded to point F ( $\sigma_1 = 52.57 \text{ MPa} = 71.2 \% \sigma_c$ ). Crack 5 is initiated at the outer tip of fissure ② and propagates toward the top edge of the specimen along the direction of axial stress, resulting in a rapid axial stress drop from 52.57 to 49.49 MPa. At this time, the specimen still has a good supporting structure (Fig. 4.12e). Therefore, with increase of axial deformation, the axial supporting capacity begins to increase with an approximately equal modulus of 25.39 GPa as the previous average modulus of 25.15 GPa, revealing that the initiation and coalescence of cracks 4 and 5 do not affect the deformation behavior of the specimen. When the specimen is loaded to point G ( $\sigma_1 = 62.44 \text{ MPa} = 84.5 \% \sigma_c$ ), crack 6 emanates toward the top edge of the specimen



**Fig. 4.14** Microscopic observation of crack coalescence between fissures ①②③ of sandstone specimen containing three fissures ( $\alpha = \beta_1 = 45^\circ, \beta_2 = 90^\circ$ ) after failing under uniaxial compression (with kind permission of Springer Publisher)

from the outer tip of fissure ① along the direction of axial stress, leading to a minor axial stress drop from 62.44 to 61.14 MPa. For the moment, the axial stress begins to increase slowly as the axial deformation increases. As a result of obvious damage to the supporting structure (Fig. 4.12f), the reloading average modulus of 22.8 GPa is distinctly lower than the elastic modulus of 27.11 GPa. Moreover, the axial stress–strain curve of the specimen departs toward the strain axis when the deformation approaches the peak strain. The continuous deformation increase leads to the specimen being loaded to peak point H ( $\sigma_1 = 73.87 \text{ MPa} = 100 \% \sigma_c$ ). At this moment, crack 7 is initiated at the outer tip of fissure ① and evolves toward the inner tip of fissure ③. The corresponding axial stress of the specimen begins to decrease slowly as the deformation increases. When the axial stress of the specimen decreases to point I ( $\sigma_1 = 71.25 \text{ MPa}$ ), crack 8 emanates from the outer tip of fissure ② and propagates toward the top edge of the specimen along the direction of axial stress, and the corresponding axial stress drops to 70.57 MPa. It should be noted that Fig. 4.16 shows local magnification of several cracks, from Fig. 4.15 it is clear that nearby the outer tip of fissure ②, a lot of minor microscopic cracks are observed, which results probably from local compressive stress concentration. The continuous deformation increase leads to the axial stress being dropped to point J ( $\sigma_1 = 69.42 \text{ MPa}$ ). At this time, crack 9 forms rapidly in the right bottom region of the specimen near the outer tip of fissure ①, and the coalescence direction is approximately parallel to axial stress. Therefore, the axial supporting capacity drops rapidly to 47.99 MPa in an approximately constant axial strain. During the coalescence of crack 9, some surface failures are observed. Ultimate brittle failure then occurs quickly and crack 10 emanates, resulting in a rapid reduction of axial stress to 0.15 MPa. At this point, the specimen can no longer support axial stress.

In accordance with microscopic observation after failure of the specimen shown in Figs. 4.14 and 4.15, we can see that the crack coalescence path is zig-zag with local magnification, e.g., cracks  $1^b$  and  $1^c$ , which results mainly from the effect of grain scale in tested sandstone material on the crack coalescence path. The width of cracks  $1^b$  and  $1^c$  is very small at about 40–50  $\mu\text{m}$ . The width of crack 3 reaches about 500–600  $\mu\text{m}$ , which is distinctly higher than that of cracks  $1^b$  and  $1^c$ . However, the width of crack 2 is up to 800–1000  $\mu\text{m}$ . Therefore different cracks have unequal width. Although the same crack, the width of the crack is different along the direction of crack length during loading.

### 4.3.3 Real-Time Crack Coalescence Process of Sandstone Specimens Containing Three Fissures ( $\beta_2 = 105^\circ$ and $120^\circ$ )

Figures 4.16 and 4.17 presents the real-time crack coalescence process of sandstone specimens containing three fissures with  $\beta_2 = 105^\circ$  and  $120^\circ$ , respectively. Figure 4.13b, c shows the corresponding, locally magnified images of the ultimate

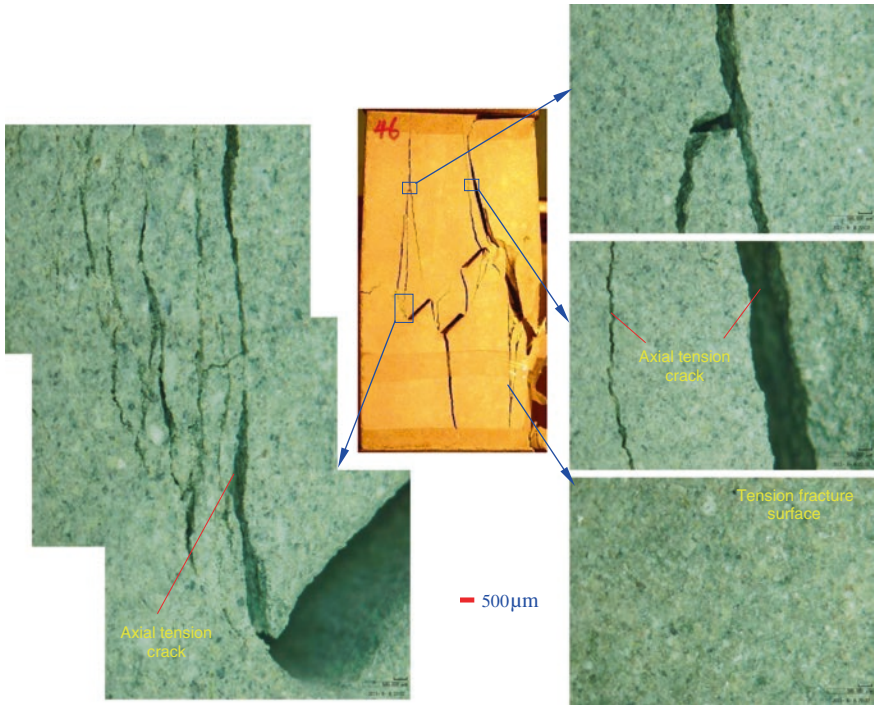


**Fig. 4.15** Microscopic observation of several crack coalescence of sandstone specimen containing three fissures ( $\alpha = \beta_1 = 45^\circ$ ,  $\beta_2 = 90^\circ$ ) under uniaxial compression (with kind permission of Springer Publisher)

failure mode of the specimens. The letters denoted in Figs. 4.16 and 4.17 correspond to Fig. 4.5c, d, and the numbers represent the crack coalescence sequence during the entire deformation (see Tables 4.5 and 4.6). Here, results from the flawed specimen containing three fissures ( $\alpha = \beta_1 = 45^\circ$ ,  $\beta_2 = 120^\circ$ ) are presented to provide an example of the relationship between the real-time crack coalescence process and the axial stress–strain curve for specimens with overlapping fissure geometry ①③.

Compared with the real-time crack coalescence process of the flawed specimen containing three fissures ( $\alpha = \beta_1 = 45^\circ$ ,  $\beta_2 = 90^\circ$ ), the process of the flawed specimen containing three fissures ( $\alpha = \beta_1 = 45^\circ$ ,  $\beta_2 = 120^\circ$ ) was distinctly different. Therefore, the difference between the effects of real-time crack coalescence process on the axial stress–strain curve was also larger.

In accordance with Fig. 4.17 and Table 4.6, the real-time crack coalescence behaviors of sandstone specimens containing three fissures ( $\alpha = \beta_1 = 45^\circ$ ,  $\beta_2 = 120^\circ$ ) are analyzed during the entire deformation, as shown in Fig. 4.5d. Before point A ( $\sigma_1 = 47.91 \text{ MPa} = 47 \% \sigma_c$ ), the stress concentration at the inner and outer tips of the three fissures does not reach the material strength, and no crack is induced. However, when the axial stress is loaded to point A, crack

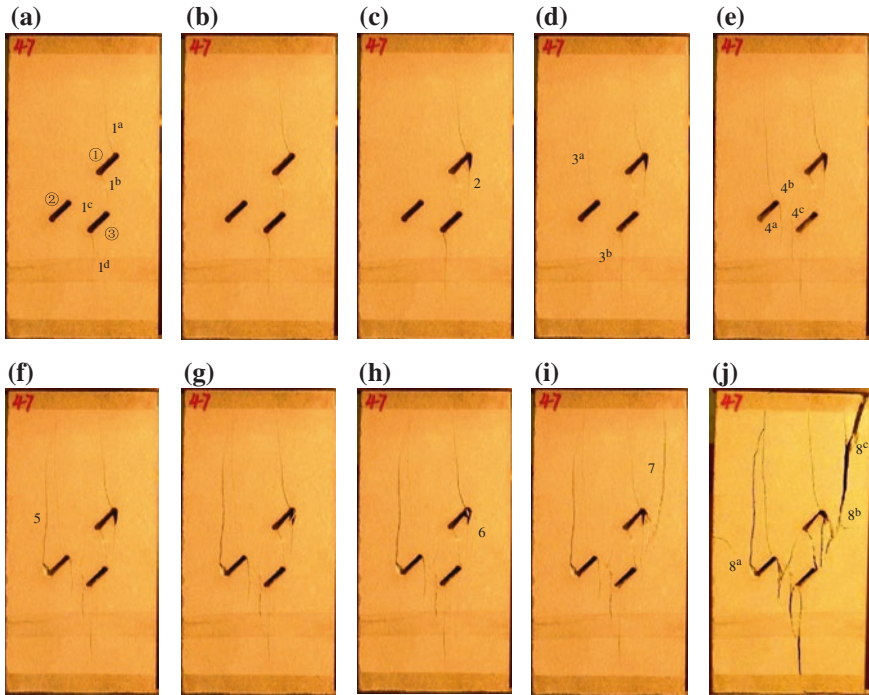


**Fig. 4.16** Crack coalescence process of sandstone specimen containing three fissures ( $\alpha = \beta_1 = 45^\circ$ ,  $\beta_2 = 105^\circ$ ) under uniaxial compression. The denoted letters correspond to those shown in Fig. 4.5c (with kind permission of Springer Publisher)

1 rapidly forms from the inner and outer tips of fissures ① and ③, as shown in Fig. 4.9. The corresponding axial stress slightly drops from 47.91 to 46.12 MPa. After point A, the axial stress increases linearly with the increasing axial deformation as the elastic modulus of 32.21 GPa. The width of crack 1 also increases, while the length of crack 1 does not increase because of the boundary limitations of the specimen, as shown by point B ( $\sigma_1 = 65.10 \text{ MPa} = 63.9 \% \sigma_c$ ) in Fig. 4.17. When the specimen is loaded to point C ( $\sigma_1 = 71.14 \text{ MPa} = 69.8 \% \sigma_c$ ), crack 2 is initiated from the outer tip of fissure ① and propagates toward the inner tip of fissure ③ along the direction of axial stress. This occurrence does not lead to an obvious axial stress drop and the stress changes from 71.14 to 70.45 MPa. The continuous axial deformation increase (point D,  $\sigma_1 = 81.47 \text{ MPa}$ ) does not result in new cracks, but the width of cracks 1 and 2 slightly increases. Crack 2 does not coalesce to the inner tip of fissure ③. The specimen still has a better supporting structure (Fig. 4.17c). Thus, with increase in axial deformation, the axial stress of the specimen increases at an approximate average modulus of 31.73 GPa, similar to the elastic modulus of 32.21 GPa. When the specimen is loaded to point E ( $\sigma_1 = 86.37 \text{ MPa} = 84.8 \% \sigma_c$ ), crack 2 coalesces rapidly to the inner tip of fissure ③, and its width increases substantially, while crack 1<sup>b</sup> closes. In the above

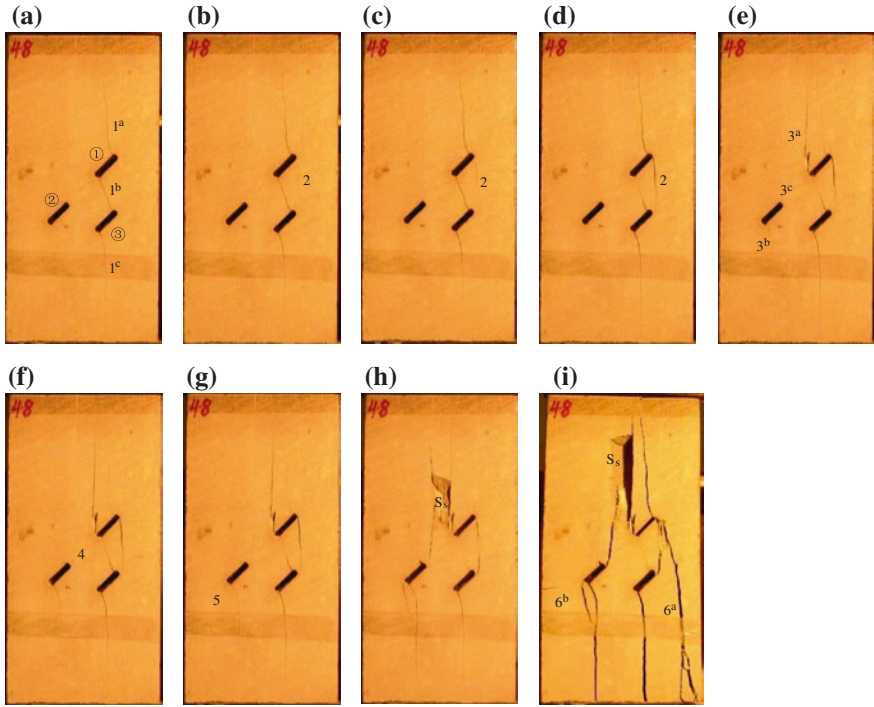


**Fig. 4.17** Crack coalescence process of sandstone specimen containing three fissures ( $\alpha = \beta_1 = 45^\circ, \beta_2 = 120^\circ$ ) under uniaxial compression. The denoted letters correspond to those shown in Fig. 4.5d (with kind permission of Springer Publisher)

**Table 4.5** Crack coalescence behavior of sandstone specimen containing three fissures ( $\alpha = \beta_1 = 45^\circ, \beta_2 = 105^\circ$ )

Coalescence point	Initiated cracks	$\epsilon_1/\times 10^{-3}$	$\sigma_1/\text{MPa}$	Stress drop/MPa
B	No new crack	2.449	51.98	No
C	No new crack	3.272	78.22	No
D	Crack 2	3.308	79.46	77.66
E (Peak strength)	Crack 3	3.387	79.71	77.88
F	Crack 4	3.387	77.88	64.64
G	Crack 5	3.404	64.64	58.54
H	No new crack	3.845	67.89	No
I	Crack 6	3.967	69.58	No
J	Crack 7	3.996	69.82	59.36
K	Crack 8	4.277	2.1	Ultimate failure

**Table 4.6** Crack coalescence behavior of sandstone specimen containing three fissures ( $\alpha = \beta_1 = 45^\circ$ ,  $\beta_2 = 120^\circ$ )

Coalescence point	Initiated cracks	$\epsilon_1/\times 10^{-3}$	$\sigma_1/\text{MPa}$	Stress drop/MPa
B	No new crack	2.776	65.10	No
C	Crack 2	2.978	71.14	70.45
D	No new crack	3.303	81.47	No
E	No new crack	3.457	86.37	85.49
F	Crack 3	3.915	99.59	95.58
G	Crack 4	4.022	98.66	98.36
H	Crack 5	4.079	99.56	98.74
I (Peak strength)	No new crack	4.254	101.86	78.76
J	Crack 6	4.315	7.26	Ultimate failure

process, the axial stress drops from 86.37 to 85.49 MPa. Afterwards, the axial stress increases linearly with increasing deformation as the average modulus of 32.56 GPa, which is approximately equal to the elastic modulus of 32.21 GPa.

When the specimen is loaded to point F ( $\sigma_1 = 99.59 \text{ MPa} = 97.8 \% \sigma_c$ ), crack 3<sup>a</sup> emanates from the inner tip of fissure ① and propagates toward the top edge of the specimen along the direction of axial stress. However, cracks 3<sup>b</sup> and 3<sup>c</sup> are initiated from the outer and inner tips of fissure ②, respectively, and propagate along the direction of axial stress. Notably, the width of crack 3<sup>a</sup> is greater than that of cracks 3<sup>b</sup> and 3<sup>c</sup>. The corresponding axial stress drops rapidly from 99.59 to 95.58 MPa. Afterwards, with increasing deformation, the specimen experiences two minor stress drops as a result of the emanation of cracks 4–5 in the specimen. The axial stress–strain curve departs toward the strain axis during the coalescence process of cracks 4–5. The continuous increase in deformation results in the specimen being loaded to peak point I ( $\sigma_1 = 101.86 \text{ MPa} = 100 \% \sigma_c$ ). At this moment, the width and length of cracks 3–5 increase with increasing axial deformation, and crack 1<sup>a</sup> closes. Moreover, some surface failures are observed between cracks 3<sup>a</sup> and 4. Although no new crack is observed, there is an obvious stress drop from 101.86 to 78.76 MPa in an approximately constant axial strain. Ultimate brittle failure is then quickly induced, and crack 6 is initiated as a result of the rapid reduction of axial stress to 7.2 MPa.

Figures 4.18 and 4.19 show some microscopic observations of crack coalescence in the flawed sandstone specimen containing three fissures ( $\alpha = \beta_1 = 45^\circ$ ,  $\beta_2 = 105^\circ$ ) under uniaxial compression. Open tensile cracks are very clear and the path of crack coalescence is very zigzag on the basis of local magnification. Tensile cracks can also be further testified by tensile fracture surface shown in Fig. 4.18. From Fig. 4.19, the maximum width of crack 1<sup>b</sup> reaches about 1500  $\mu\text{m}$ , whereas crack 1<sup>c</sup> is very fine compared with crack 1<sup>b</sup>.

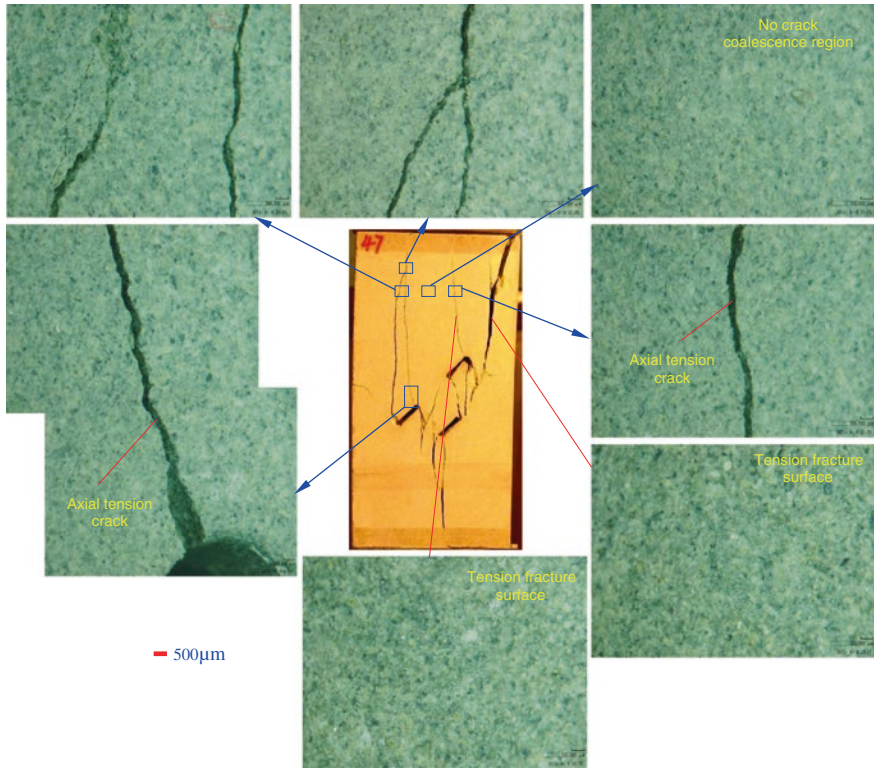


**Fig. 4.18** Microscopic observation of several crack coalescence of sandstone specimen containing three fissures ( $\alpha = \beta_1 = 45^\circ$ ,  $\beta_2 = 105^\circ$ ) under uniaxial compression (with kind permission of Springer Publisher)

## 4.4 Crack Coalescence Type and Strain Evolution Analysis

### 4.4.1 Crack Coalescence Type Analysis

Figure 4.20 depicts a sketch of the initiated crack coalescence types for sandstone specimens containing three fissures. Although the crack coalescence types for the specimens in this study were the same as those observed in the previous study (Yang and Jing 2011), each flawed specimen with three fissures had different crack coalescence types as a result of the different flaw geometries. Table 4.7 summarizes the initiated crack coalescence types of sandstone specimens containing three fissures ( $\alpha = \beta_1 = 45^\circ$ ). The crack coalescence modes are also plotted in Table 4.7.

In accordance with Table 4.7, no crack coalescence occurs between fissures ①② in the flawed specimens containing three fissures ( $\alpha = \beta_1 = 45^\circ$ ). Whereas crack coalescence occurs between fissures ①③ and ②③ but not between fissures ②③ for one specimen with  $\beta_2 = 120^\circ$ . Tensile wing crack, secondary tensile crack,

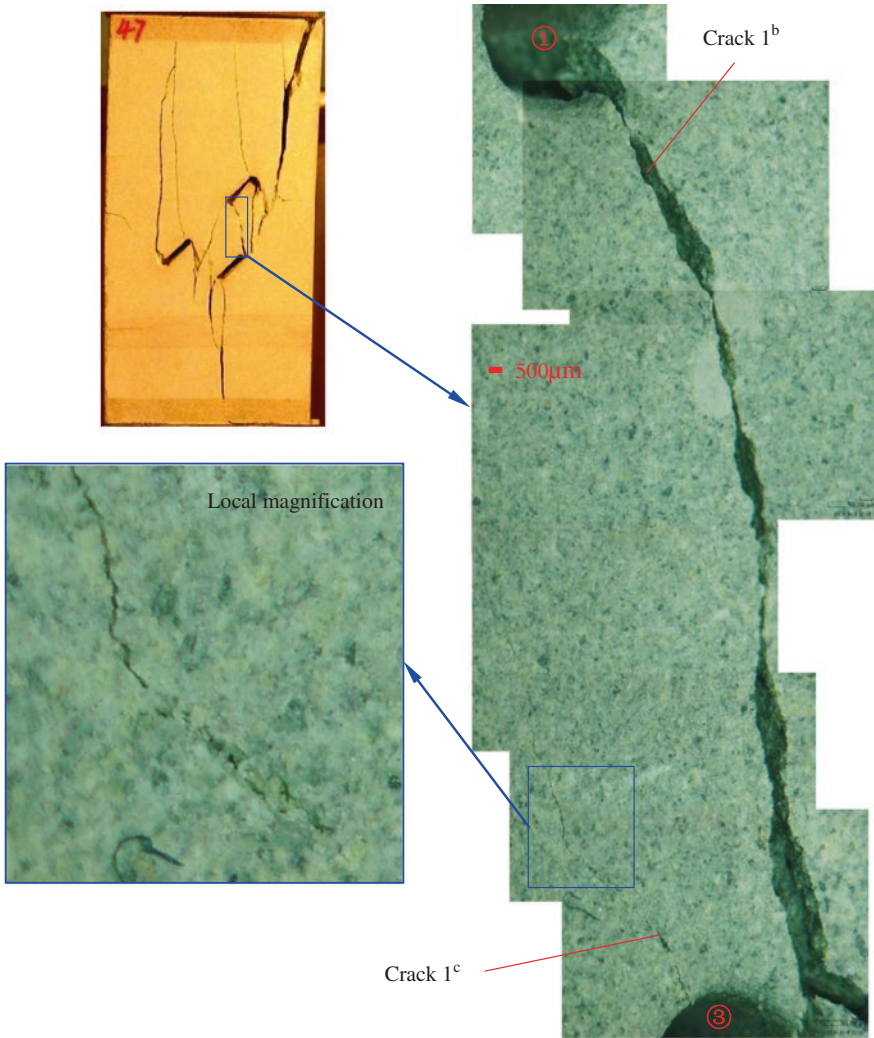


**Fig. 4.19** Microscopic observation of crack coalescence between fissures ①③ of sandstone specimen containing three fissures ( $\alpha = \beta_1 = 45^\circ$ ,  $\beta_2 = 105^\circ$ ) after failing under uniaxial compression (with kind permission of Springer Publisher)

and far-field crack are observed in all flawed specimens containing three fissures ( $\alpha = \beta_1 = 45^\circ$ ). Shear crack and lateral crack are only observed between fissures ①③ in flawed specimens with  $\beta_2 = 75^\circ$ , while compressive crack is observed between fissures ②③ in flawed specimens with  $\beta_2 = 75^\circ$  and  $90^\circ$ . However, an anti-tensile crack is observed in flawed specimens with  $\beta_2 = 90^\circ$ ,  $105^\circ$  and  $120^\circ$ . Surface spalling is observed in all flawed specimens as a result of the brittleness of the sandstone material and the local concentration of compression.

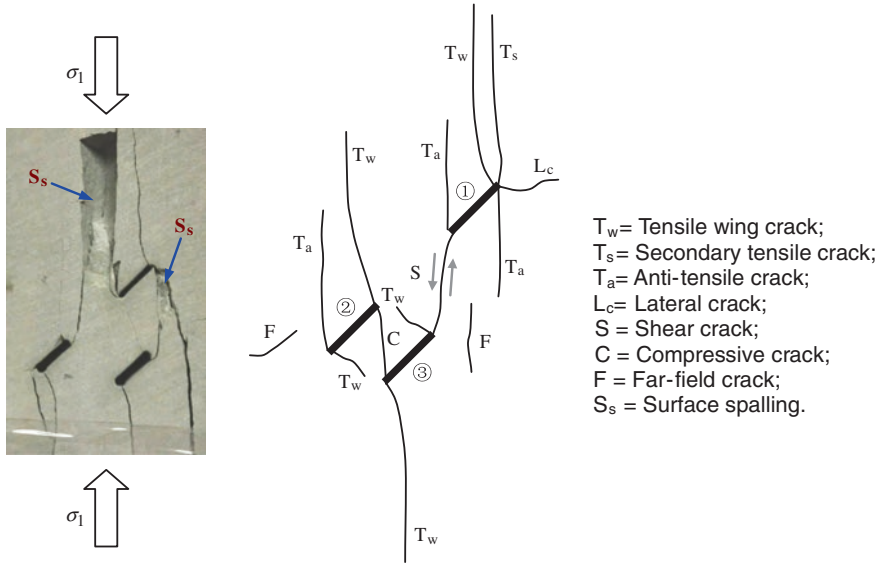


**Fig. 4.20** A sketch of initiated crack coalescence type of sandstone specimens containing three fissures (with kind permission of Springer Publisher)

### 4.4.2 Strain Evolution Analysis

Using the Digital Image Correlation technique and analyzing the images captured during loading, the full-field strain of the specimen surface is obtained. In this research, the images are analyzed with the software CMV, developed at the Ecole Polytechnique of Paris in France (Yang et al. 2011). The transformation gradients are averaged over the domain of interest ( $4.4 \times 4.4$  mm) to determine the strains.

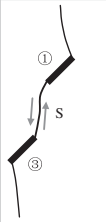
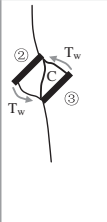
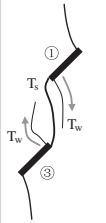
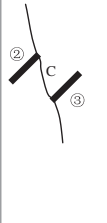
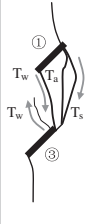
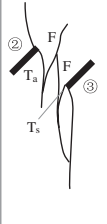
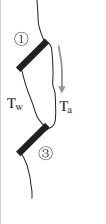
The following equation for equivalent strain is used to study the mechanical behavior:

$$\text{Equivalent strain} = \sqrt{2/3 e_{ij} e_{ij}} \tag{4.2}$$

where  $e_{ij}$  is the deviatory strain. Here, results for the specimen containing three fissures ( $\alpha = \beta_1 = 45^\circ$ ,  $\beta_2 = 90^\circ$ ) are presented to demonstrate the strain evolution analysis for pre-cracked brittle sandstone. Because several large cracks are created during loading and because these zones become new subsets that cannot be identified in the undeformed image, reference images are taken at different states (stress at 0, 51.98, 63.08 MPa). The equivalent strain evolution under mechanical loading is illustrated in Figs. 4.21 and 4.22.

The full-field strain clearly shows that the strain at the intact zone is relatively homogeneous (e.g., zone A in Fig. 4.21a) and that strain localization mainly

**Table 4.7** Crack coalescence mode and type of sandstone specimen containing three fissures ( $\alpha = \beta_1 = 45^\circ$ )

$\beta_2$	Fissures ①③	Fissures ②③	Fissures ①②	Fissures ①②③	Crack coalescence type description
75°			No coalescence	 	$T_w$ Crack 1 <sup>a-1<sup>d</sup></sup> , 2 <sup>b</sup> $T_s$ Crack 4 $S$ Crack 3 $C$ Crack 2 <sup>a</sup> $L_c$ Crack 6 <sup>b</sup> $F$ Crack 5, 6 <sup>a</sup> , 6 <sup>c</sup> $S_s \checkmark$ more
90°			No coalescence	 	$T_w$ Crack 1 <sup>a-1<sup>d</sup></sup> , 2 <sup>b</sup> $T_s$ Crack 3, 6-8, 9, 10 <sup>a</sup> , 10 <sup>b</sup> $T_a$ Crack 4-5. $C$ Crack 2 <sup>a</sup> $F$ Crack 10 <sup>c</sup> $S_s \checkmark$ small
105°			No coalescence	 	$T_w$ Crack 1 <sup>a-1<sup>d</sup></sup> , 3 <sup>a</sup> $T_s$ Crack 3 <sup>b</sup> , 6 $T_a$ Crack 2, 4 <sup>a</sup> , 5 $F$ Crack 4 <sup>b</sup> , 4 <sup>c</sup> , 7, 8 <sup>a-8<sup>c</sup></sup> $S_s \checkmark$ small
120°		No coalescence	No coalescence	 	$T_w$ Crack 1 <sup>a-1<sup>c</sup></sup> , 3 <sup>b-3<sup>c</sup></sup> $T_s$ Crack 4-5, 6 <sup>a</sup> $T_a$ Crack 2, 3 <sup>a</sup> $F$ Crack 6 <sup>b</sup> $S_s \checkmark$ more

Note The numbers correspond to those shown in Figs. 4.11–4.12 and 4.16–4.17

occurs around the pre-created fissures (e.g., zone B in Fig. 4.21b) and develops along the new cracks (e.g., zone C in Figs. 4.21 and 4.22). While the axial stress increases to 25.94 MPa, several new micro-cracks appear, and this level of stress is regarded to be the threshold for damage. The direction of the new crack around the pre-existing fissures is approximately perpendicular to the latter and is probably related to the maximal tension in this direction.

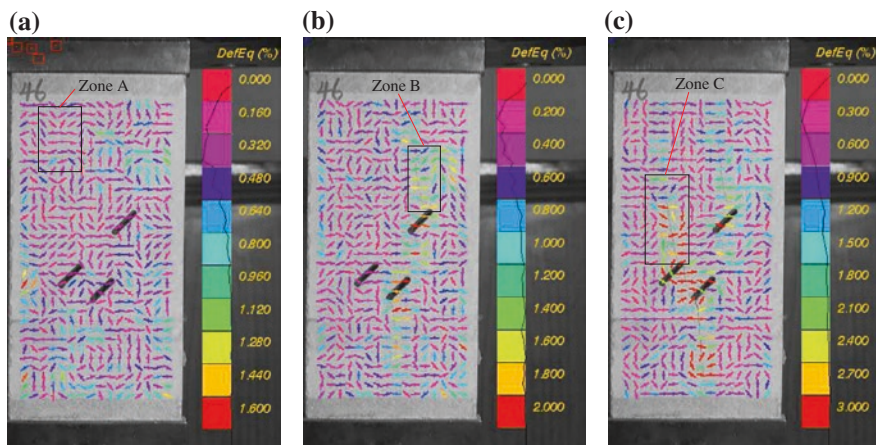


**Fig. 4.21** Equivalent strain evolution with increasing axial stress: **a** from 0 MPa to 25.94 MPa; **b** from 0 MPa to 32.44 MPa; **c** from 0 MPa to 47.54 MPa (with kind permission of Springer Publisher)

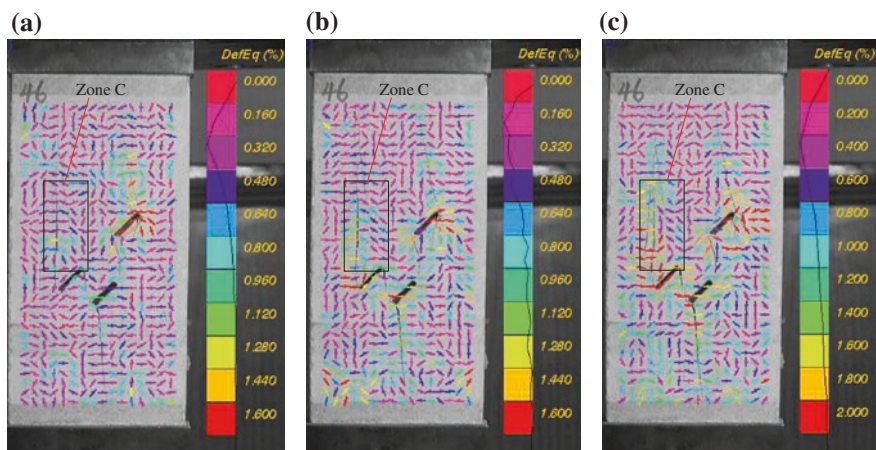


**Fig. 4.22** Equivalent strain evolution with increasing axial stress: **a** from 51.98 MPa to 63.08 MPa; **b** from 63.08 MPa to 73.87 MPa; **c** from 63.08 MPa to rupture (with kind permission of Springer Publisher)

### 4.5 Conclusions

In this chapter, we conducted uniaxial compression tests on brittle sandstone specimens, of dimensions  $80 \times 160 \times 30$  mm, containing three pre-existing open fissures to investigate the effect of the ligament angle  $\beta_2$  on the fracture coalescence behavior of sandstone specimens.

The influence of the ligament angle  $\beta_2$  on the crack initiation stress, peak strength, and peak strain of sandstone specimen containing three fissures is

determined. The peak strength and peak strain of flawed specimen containing three fissures are lower than those of intact specimen. To indicate the reduction extent of the peak strength of flawed specimen containing three fissures compared with intact specimen, a reduction factor is proposed. The crack initiation stress is nonlinearly related to  $\beta_2$ , and the effect of  $\beta_2$  on peak strength is approximately the same. The crack initiation stress and peak strength first decrease and then increase as  $\beta_2$  increases in the range from  $75^\circ$  to  $120^\circ$ . The crack initiation stress is distinctly lower than the peak strength for the sandstone specimen containing three fissures; the peak strength is approximately 34 % lower for  $\beta_2 = 75^\circ$  and  $90^\circ$ , while it is 46 % of the corresponding peak strength for  $\beta_2 = 105^\circ$  and  $120^\circ$ .

The crack initiation mode of brittle sandstone specimen containing three fissures ( $\alpha = \beta_1 = 45^\circ$ ) under uniaxial compression is analyzed and determined to be dependent on  $\beta_2$ . For  $\beta_2 = 75^\circ$ , crack 1 is initiated from the inner and outer tips of fissures ②③, while no crack is initiated from the inner and outer tips of fissure ①. For  $\beta_2 = 90^\circ$  and  $105^\circ$ , the crack initiation mode is different from that of the other three specimens. Crack 1 initiates from the inner and outer tips of fissures ①③, while no crack is initiated from the inner and outer tips of fissure ②. For  $\beta_2 = 120^\circ$ , crack 1<sup>a</sup> initiates from the outer tip of fissure ①, and crack 1<sup>c</sup> is initiated from the outer tip of fissure ③. However, crack 1<sup>b</sup> quickly coalesces between the inner tips of fissures ①③.

To confirm the sequence of crack coalescence in brittle sandstone specimens containing three fissures ( $\alpha = \beta_1 = 45^\circ$ ), photographic monitoring technique is used throughout the entire process of deformation failure. According to monitored results, the relationship between the real-time crack coalescence process and the axial stress–strain curve of the specimens is also obtained, which can be used to evaluate the macroscopic deformation failure characteristics of pre-cracked rock materials.

The crack coalescence modes of sandstone specimens containing three fissures ( $\alpha = \beta_1 = 45^\circ$ ) are analyzed using initiated crack coalescence types from previous study, including tensile wing crack, anti-tensile crack, lateral crack, shear crack, compressive crack, far-field crack, surface spalling, and secondary tensile crack. No crack coalescence occurs between fissures ①② in the flawed specimens. However, crack coalescence occurs between fissures ①③ and ②③ but not between fissures ②③ for one specimen with  $\beta_2 = 120^\circ$ . Tensile wing crack, secondary tensile crack, far-field crack, and surface spalling are observed in all flawed specimens. Shear crack and lateral crack are only observed between fissures ①③ in the flawed specimen with  $\beta_2 = 75^\circ$ , while compressive crack is observed between fissures ②③ in flawed specimens with  $\beta_2 = 75^\circ$  and  $90^\circ$ . Anti-tensile crack is observed in flawed specimens with  $\beta_2 = 90^\circ$ ,  $105^\circ$  and  $120^\circ$ .

The equivalent strain evolution fields of specimens with  $\alpha = \beta_1 = 45^\circ$ ,  $\beta_2 = 90^\circ$  are obtained using the Digital Image Correlation technique, and the results agree with the experimental results for pre-cracked brittle sandstone. The full-field strain clearly shows that the strain at the intact zone is relatively homogeneous and that strain localization mainly occurs around the pre-created fissures and develops along the new cracks. The direction of the new crack around the

pre-existing fissures is nearly perpendicular to the latter and is probably related to the maximal tension in this direction.

## References

- Yang DS, Bornert M, Chanchole S, Wang LL, Pierre Valli, Gatmiri B (2011) Experimental investigation of the delayed behavior of unsaturated argillaceous rocks by means of digital image correlation techniques. *Appl Clay Sci* 53(1):53–62
- Yang SQ, Jing HW (2011) Strength failure and crack coalescence behavior of brittle sandstone samples containing a single fissure under uniaxial compression. *Int J Fract* 168(2):227–250
- Yang SQ, Yang DS, Jing HW, Li YH, Wang SY (2012) An experimental study of the fracture coalescence behaviour of brittle sandstone specimens containing three fissures. *Rock Mech Rock Eng* 45(4):563–582

# Chapter 5

## Experimental Investigation on Fracture Coalescence Behavior of Red Sandstone Containing Two Unparallel Fissures

In nature, engineering rock masses do not always contain parallel fissures and are generally composed of unparallel fissures (Lajitai et al. 1994; Lee and Jeon 2011). Lee and Jeon (2011) carried out uniaxial compression experiment for Diastone (types of molded gypsum) and Hwangdeung granite containing two unparallel fissures (a horizontal fissure and an inclined fissure underneath). The results showed that crack initiation and propagation had similar and different patterns depending on the material. For Diastone and Hwangdeung granite, tensile cracks were observed followed by the initiation of shear cracks and coalescence occurred mainly through the tensile cracks or tensile and shear cracks. But up to now, no laboratory experiments have been carried out on red sandstone specimens containing two unparallel fissures with different fissure angles. Besides, in the previous investigation for rock specimens containing two unparallel fissures, AE monitoring technique had not been adopted and the relationship between macroscopic deformation and fracture coalescence process was not constructed.

Therefore in this chapter, a rock mechanics servo-controlled testing system was used to conduct uniaxial compression tests for red sandstone specimens containing two unparallel fissures. Moreover, photographic monitoring and AE monitoring techniques were all used to obtain the relationship between the real-time crack coalescence process and axial stress–time behavior for red sandstone containing two unparallel fissures. The emphasis of this chapter was to investigate the effects of the fissure angle on the strength and deformation behaviors of red sandstone material containing two unparallel fissures and to analyze the real-time crack coalescence process in red sandstone material under uniaxial compression, using photographic monitoring and AE monitoring techniques (Yang et al. 2013).

## 5.1 Experimental Material and Loading Procedure

### 5.1.1 Experimental Material and Specimen Preparation

In this chapter, red sandstone specimens from Linyi City, Shandong province, China, were used. The tested red sandstone has a crystalline and blocky structure, which is a medium-grained heterogeneous material with average unit weight about  $2400 \text{ kg/m}^3$ . Moreover, tested red sandstone is more porous. According to the result of X-ray diffraction (XRD) (Fig. 5.1), the minerals in the red sandstone specimens are mainly feldspar and quartz, with some smectite and zeolite, and very minor quantities of hematite.

Rectangular prismatic specimens of red sandstone, with dimensions of  $80 \times 160 \times 30 \text{ mm}$ , were prepared from the same set of blocks. All specimens had a height-to-width ratio of 2.0 to ensure a uniform stress state within the central part of the specimens. The geometry of the specimens containing two unparallel fissures is described in detail in Fig. 5.2. Geometry of fissure in tested red sandstone specimens is defined as follows:  $\alpha_1$  is the angle of fissure ①,  $\alpha_2$  is the angle of fissure ②,  $\beta$  is ligament angle (the angle between segment B and C with the horizontal direction),  $2a$  is fissure length,  $2b$  is ligament length (i.e., the distance from point B to C). In this chapter, open fissure in red sandstone specimen was machined by high-pressure water jet cutting and the width of the preexisting fissures was about 2.0 mm.

In order to accurately investigate the effect of the angle of fissure ② (i.e.  $\alpha_2$ ) on the strength, deformability and fracture coalescence behavior of red sandstone containing two unparallel fissures under uniaxial compression, the same fissure

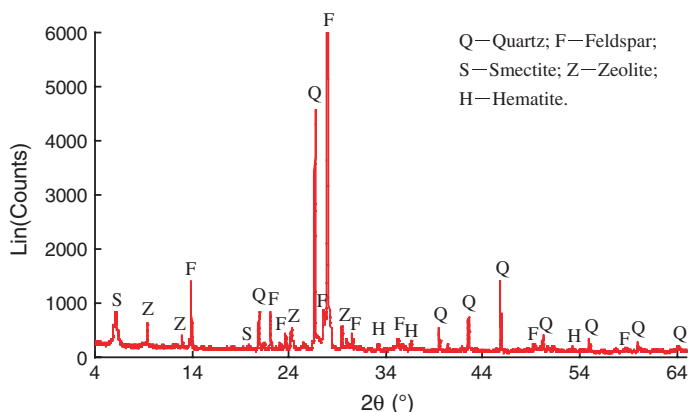


**Fig. 5.1** XRD analysis of tested red sandstone material in this chapter (with kind permission of Elsevier Publisher)

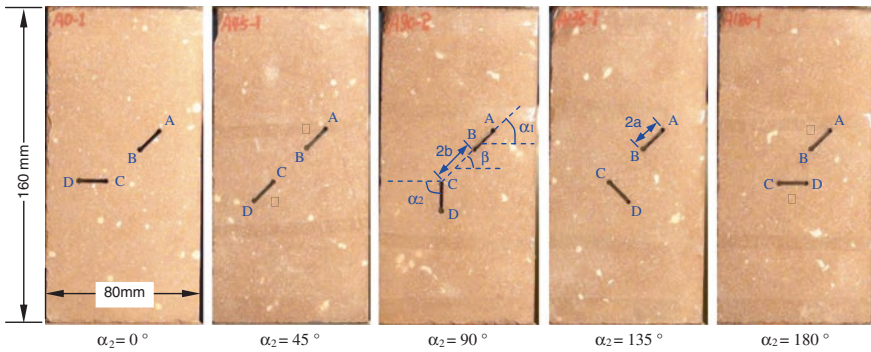


**Fig. 5.2** Five different fissure geometries of tested red sandstone in this chapter, where,  $\alpha_1$  is the angle of fissure ①,  $\alpha_2$  is the angle of fissure ②,  $\beta$  is ligament angle,  $2a$  is fissure length,  $2b$  is ligament length (with kind permission of Elsevier Publisher)

geometries are designed by varying  $\alpha_2$  while keeping other fissure parameters as constant. In this chapter,  $\alpha_1$  and  $\beta$  were all fixed to  $45^\circ$ ; whereas  $2a$  and  $2b$  were fixed to 16 and 22 mm, respectively. A detailed description of the specimens containing two unparallel fissures is given in Table 5.1.

**Table 5.1** Tested red sandstone specimens containing two unparallel fissures in this chapter

Specimen	$W$ (mm)	$H$ (mm)	$T$ (mm)	$\alpha_1$	$\alpha_2$	$\beta$	$2a$ (mm)	$2b$ (mm)
WZ-2	80.9	160.7	29.9	Intact specimen				
WZ-3	80.4	160.7	29.9	Intact specimen				
A0-1	80.8	161.0	29.3	45	0	45	16	22
A0-2	80.8	160.4	29.7	45	0	45	16	22
A0-3	80.6	161.0	29.5	45	0	45	16	22
A0-4	80.5	160.9	29.4	45	0	45	16	22
A45-1	81.1	161.0	29.8	45	45	45	16	22
A45-2	80.7	160.2	29.6	45	45	45	16	22
A45-3	80.8	160.0	29.9	45	45	45	16	22
A90-2	80.7	161.0	29.2	45	90	45	16	22
A90-3	80.6	161.1	29.6	45	90	45	16	22
A90-4	80.7	160.9	29.4	45	90	45	16	22
A135-1	80.5	160.4	29.5	45	135	45	16	22
A135-2	80.7	161.1	29.6	45	135	45	16	22
A135-3	80.7	161.0	29.5	45	135	45	16	22
A135-4	80.8	160.4	29.5	45	135	45	16	22
A180-1	80.8	161.0	29.6	45	180	45	16	22
A180-2	80.7	161.2	29.4	45	180	45	16	22
A180-3	80.7	160.3	29.8	45	180	45	16	22
A180-4	81.2	161.1	28.0	45	180	45	16	22

Note  $W$  Width;  $H$  Height;  $T$  Thickness

### 5.1.2 Loading Procedure and AE Monitoring

All of the uniaxial compression tests for tested red sandstone specimens containing two unparallel fissures were carried out using a rock mechanics servo-controlled testing system. The axial stress was imposed on the surface of the rock specimen until the failure. Tests were conducted under displacement-controlled conditions, with a strain rate of  $1.059 \times 10^{-5}/s$ . During the uniaxial compression experiment, the loads and deformations of the specimens were recorded simultaneously and continuously. Two rigid steel blocks, with dimensions of  $33 \times 83 \times 15$  mm, were placed between the loading frame and the rock specimen.

During testing, in order to investigate the fracture coalescence characteristics of the deforming specimens containing two unparallel fissures, the AE technique was adopted. The AE counts were recorded by a DS2 full-information AE measuring system. The frequency of AE system was fixed to 3 MHz. At the same time, the photographic monitoring technique was used to trigger manually to capture images when the cracks propagated or specimen failure coalesced. When measuring AE signals, we stuck two AE sensors on the back face of red sandstone specimens using hot bar as a coupling agent and fixed slightly by cellulose tape.

## 5.2 Strength and Deformation Behavior

### 5.2.1 Axial Stress–Axial Strain Behavior

In accordance with the axial stress–time curve and the ultimate failure mode of two intact red sandstone specimens shown in Fig. 5.3, we can obtain that tested red sandstone is a kind of brittle rock, i.e., the axial stress drops abruptly to zero after the peak strength. Moreover from Fig. 5.3, we can conclude that the heterogeneity has no nearly any effect on the mechanical parameters of two intact specimens, which have a good consistency. The two intact red sandstone specimens all lead to axial splitting failure mode as shown in Fig. 5.3. However, we did not observe any crack coalescence for intact specimen prior to the peak stress and a huge failure sonic was heard due to rapid failure in two seconds after the peak stress, which was also be testified by the general absence of AE counts.

Figures 5.4, 5.5, 5.6, 5.7, and 5.8 show the axial stress–axial strain curves of red sandstone specimens containing two unparallel fissures with various fissure angle  $\alpha_2$  (from  $0^\circ$  to  $180^\circ$ ) under uniaxial compression. To obtain the best possible results, we repeated several specimens for each fissure angle  $\alpha_2$ . In general, the effect of specimen variability on the mechanical parameters (e.g., the uniaxial compressive strength) is smaller. But it should be noted that for each same  $\alpha_2$ , e.g.  $\alpha_2 = 180^\circ$  shown in Fig. 5.8, due to the difference of crack coalescence

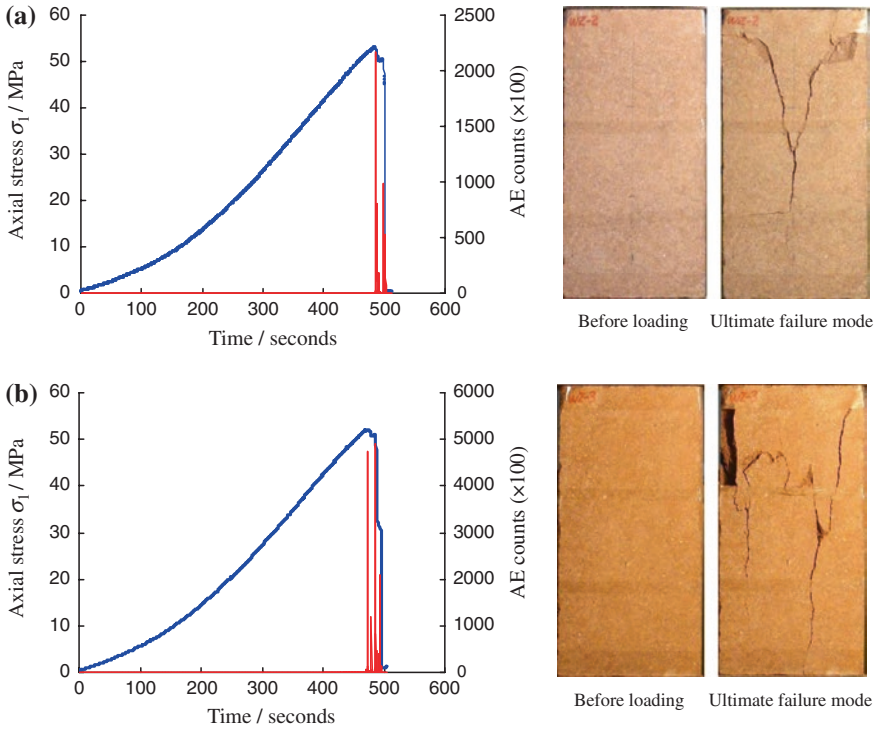


**Fig. 5.3** Experimental results of intact red sandstone specimens under uniaxial compression. The number in double bracket in *vertical axis* labels is the multiplier of coordinates. **a** Intact red sandstone specimen WZ-2<sup>#</sup>. **b** Intact red sandstone specimen WZ-3<sup>#</sup> (with kind permission of Elsevier Publisher)

process in the rock, the axial stress–strain curves of specimens are also various, especially those nearby the peak stress.

From Figs. 5.4, 5.5, 5.6, 5.7 and 5.8, we can also see that red sandstone specimens containing two unparallel fissures all have an initial nonlinear deformation, which results mainly from the closure of original fissures or pores in the rock material. After that, the elastic deformation begins to dominate the axial stress–strain curve, and the axial stress has an approximately linear relation with the axial strain. However, when tensile cracks are initiated from the tips of two preexisting unparallel fissures, distinct stress drops are observed in the axial stress–strain curves of specimens. Note, each stress drop corresponds to one crack coalescence in the specimen. For their relationship, we will make a detailed analysis in the fourth section. After several stress drops, the specimen will reach rapidly the peak strength and occur brittle unstable failure with the increase of axial deformation.

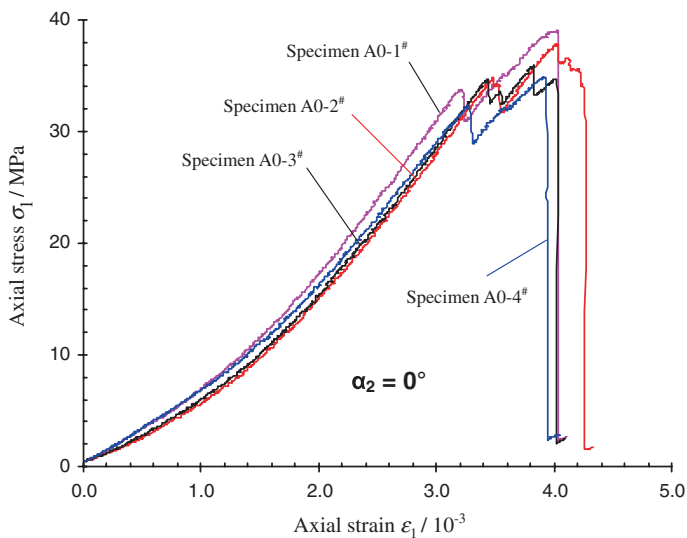


**Fig. 5.4** Axial stress–axial strain curves of red sandstone specimens containing two unparallel fissures ( $\alpha_2 = 0^\circ$ )

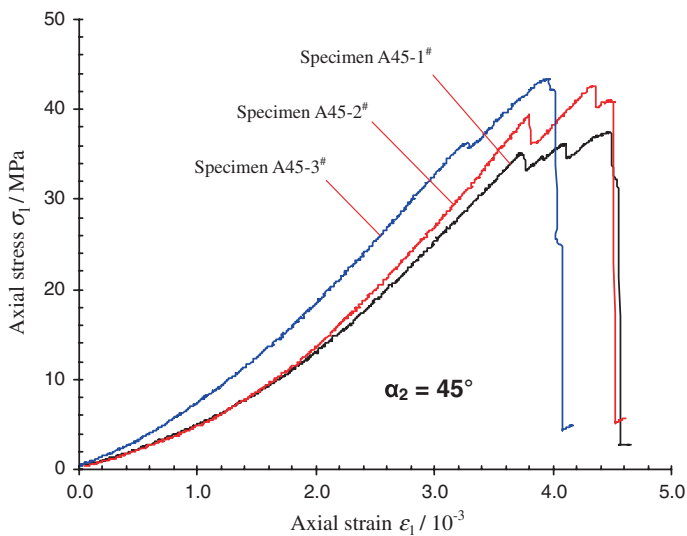


**Fig. 5.5** Axial stress–axial strain curves of red sandstone specimens containing two unparallel fissures ( $\alpha_2 = 45^\circ$ )

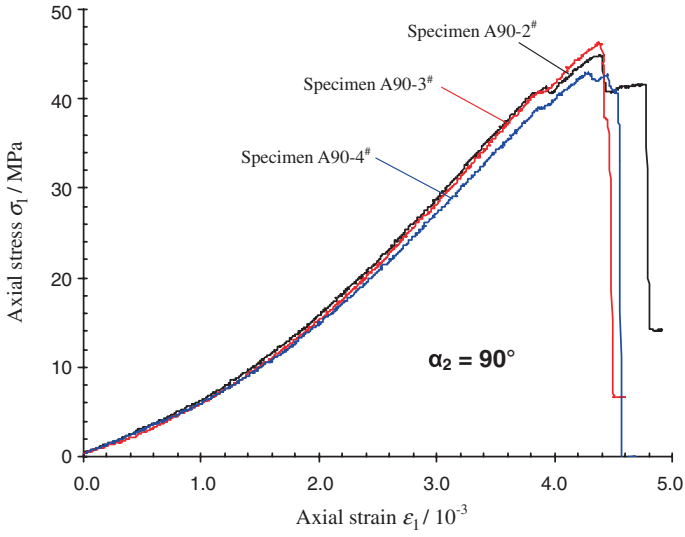


**Fig. 5.6** Axial stress–axial strain curves of red sandstone specimens containing two unparallel fissures ( $\alpha_2 = 90^\circ$ )

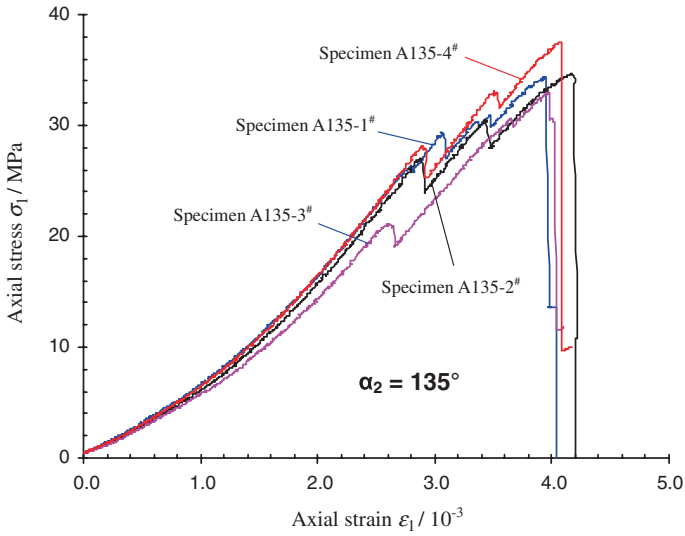


**Fig. 5.7** Axial stress–axial strain curves of red sandstone specimens containing two unparallel fissures ( $\alpha_2 = 135^\circ$ )

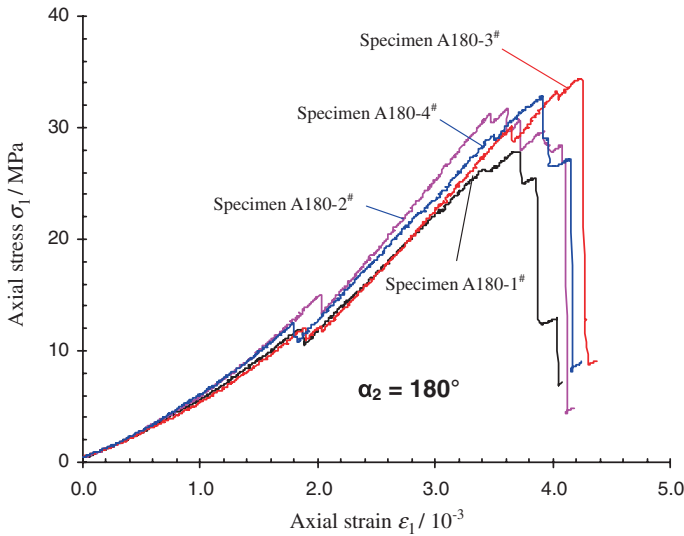


**Fig. 5.8** Axial stress–axial strain curves of red sandstone specimens containing two unparallel fissures ( $\alpha_2 = 180^\circ$ ) (with kind permission of Elsevier Publisher)

### 5.2.2 Strength and Deformation Parameters

Figure 5.9 depicts the influence of fissure angle  $\alpha_2$  on the strength and deformation parameters of red sandstone containing two unparallel fissures. In Fig. 5.9, the  $\sigma_c$  and  $\varepsilon_{1c}$  are the uniaxial compressive strength and peak axial strain of red sandstone, respectively. The  $E_{50}$  is defined as the tangent Young's modulus at the stress level of 50 % of its uniaxial compressive strength, and the  $E_T$  as the secant Young's modulus from zero stress to its uniaxial compressive strength. From Fig. 5.9, it can be seen that the  $\sigma_c$  and  $\varepsilon_{1c}$  for specimens containing two unparallel fissures are all less than those for the intact specimens shown in Fig. 5.3.

The effect of  $\alpha_2$  on the uniaxial compressive strength of red sandstone specimen containing two unparallel fissures is shown in Fig. 5.9a. The  $\sigma_c$  first increased and then decreased, and reached the maximum value at  $\alpha_2 = 90^\circ$ . The average  $\sigma_c$  of four specimens at  $\alpha_2 = 0^\circ$  was 36.89 MPa. When  $\alpha_2 = 45^\circ$ , the two fissures in the specimens were both parallel and coplanar, and the average  $\sigma_c$  of three specimens was increased to 42.14 MPa. As  $\alpha_2$  increased from  $45^\circ$  to  $90^\circ$ , the average  $\sigma_c$  of red sandstone specimen containing two unparallel fissures increased from 42.14 to 44.74 MPa. Whereas when the  $\alpha_2$  was increased from  $90^\circ$  to  $180^\circ$ , the average  $\sigma_c$  of specimen decreased rapidly from 44.74 to 31.73 MPa (marginally lower than that for  $\alpha_2 = 0^\circ$ ).

Figure 5.9b shows the effect of  $\alpha_2$  on the peak axial strain of red sandstone specimen containing two unparallel fissures, which is similar to the variance on the peak strength (see Fig. 5.9a). The average peak axial strain of specimen

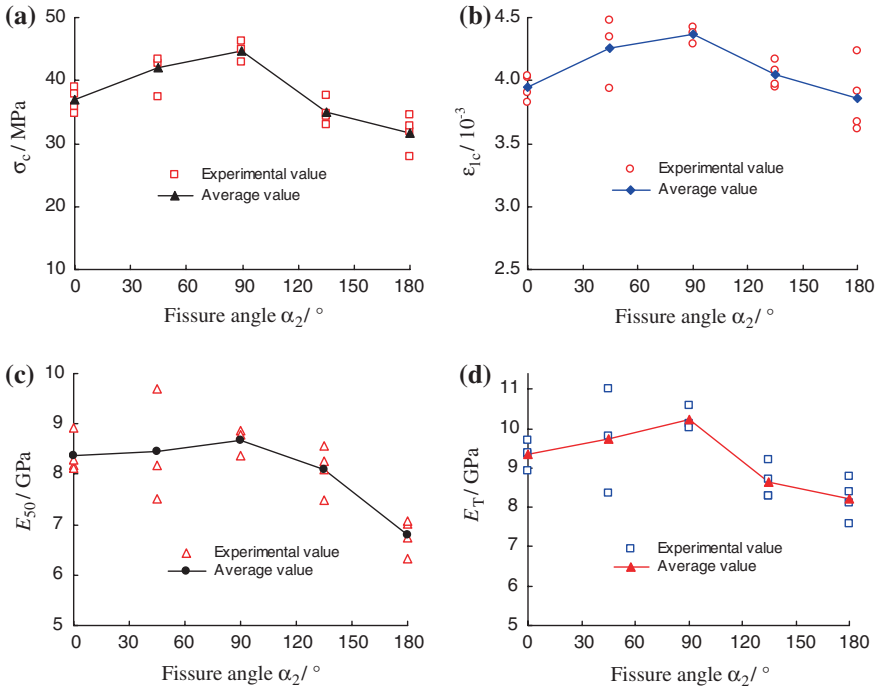


**Fig. 5.9** Influence of fissure angle  $\alpha_2$  on strength and deformation parameters of red sandstone containing two unparallel fissures (with kind permission of Elsevier Publisher)

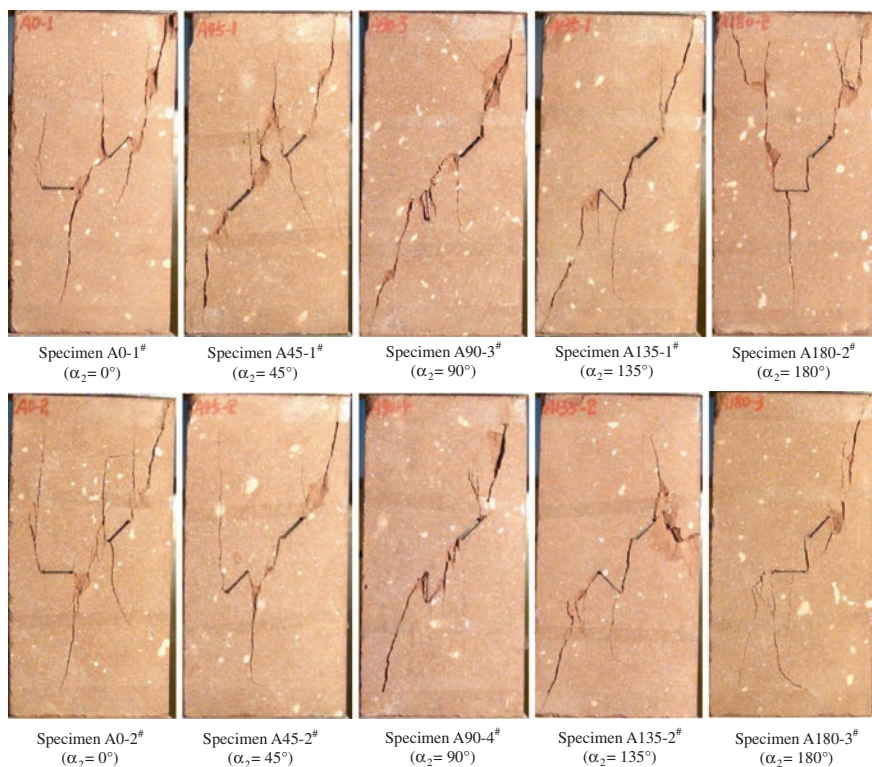
containing two unparallel fissures at  $\alpha_2 = 0^\circ$  was approximately  $3.950 \times 10^{-3}$ , but the average peak axial strain value at  $\alpha_2 = 45^\circ$  increased to  $4.253 \times 10^{-3}$ . In general, the peak axial strain of specimen containing two unparallel fissures had a little increasing from  $4.253 \times 10^{-3}$  to  $4.363 \times 10^{-3}$  with the increase of  $\alpha_2$  from  $45^\circ$  to  $90^\circ$ . However, when the  $\alpha_2$  increased from  $90^\circ$  to  $180^\circ$ , the average  $\epsilon_{1c}$  of specimen decreased rapidly from  $4.363 \times 10^{-3}$  to  $3.862 \times 10^{-3}$  (a little lower than that for  $\alpha_2 = 0^\circ$ ).

Figure 5.9c, d depicts the fissure angle on the influence of tangent and secant Young's modulus of red sandstone containing two unparallel fissures under uniaxial compression, respectively. From Fig. 5.9c, d, it is very clear that both Young's moduli of red sandstone containing two unparallel fissures all depend on the fissure angle  $\alpha_2$ . The relationship is qualitatively similar to that for the uniaxial compressive strength and the peak axial strain: both Young's moduli increased in the range of  $\alpha_2$  from  $0^\circ$  to  $90^\circ$  and then decreased up to  $180^\circ$ . For example, when the  $\alpha_2$  was increased from  $0^\circ$  to  $90^\circ$ , the average secant modulus increased from 9.34 to 10.25 GPa. However, when the  $\alpha_2$  was increased from  $90^\circ$  to  $180^\circ$ , the average secant modulus decreased from 10.25 to 8.22 GPa. Compared Fig. 5.9c, d with Fig. 5.9a, b, we can see that the influence of specimen variability on the Young's moduli was higher than that on the uniaxial compression strength and the peak axial strain.

### 5.3 Cracking Mode and Characteristics

Compared with the crack mode of intact red sandstone presented in Fig. 5.3, the cracking modes in red sandstone specimens containing two unparallel fissures are obviously different (see Figs. 5.10 and 5.11). Moreover, in red sandstone specimens containing two unparallel fissures, the crack coalescence modes were different with respect to fissure angle  $\alpha_2$ .

For  $\alpha_2 = 0^\circ$ , the cracks in two specimens were very similar, even though with some minor differences. One tensile crack was initiated from the C tip of fissure  $\textcircled{2}$  and propagated toward the bottom edge of the specimen; another tensile crack from the D tip of fissure  $\textcircled{2}$  evolved toward the top edge of the specimen. However, for the cracks emanated from the tips of fissure  $\textcircled{1}$ , the cracking mode differed with specimen variability. In specimen A0-1<sup>#</sup>, only two anti-tensile cracks were observed from the A and B tips of fissure  $\textcircled{1}$ , respectively; whereas in specimen A0-2<sup>#</sup>, two tensile wing cracks were, respectively, initiated from the A and B



**Fig. 5.10** Ultimate failure mode of red sandstone specimens containing two unparallel fissures under uniaxial compression with respect to different fissure angle  $\alpha_2$  (with kind permission of Elsevier Publisher)

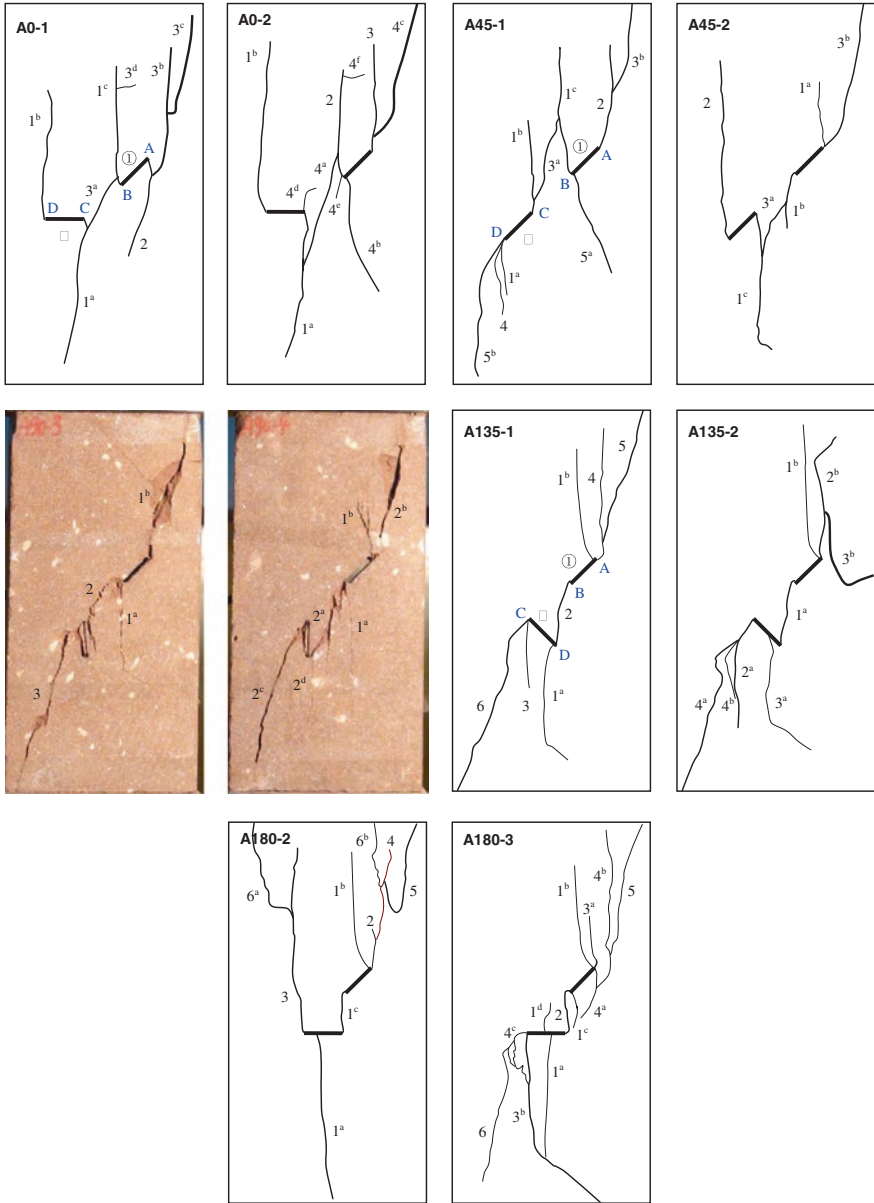


**Fig. 5.11** Cracking mode in red sandstone specimens containing two unparallel fissures under uniaxial compression with respect to different fissure angle  $\alpha_2$  (with kind permission of Elsevier Publisher)

tips of fissure ① except for one anti-tensile crack at the B tip of fissure ①. In most cases, these tensile cracks all propagated in either upward or downward direction along the direction of major principal stress toward the boundary of the specimen. It should be noted that some cracks were not perfectly straight, but followed a tortuous path through the specimens, which resulted from that the cracks always propagated along the boundaries of large quartz grains within the matrix of the red sandstone.

In two specimens containing two unparallel fissures for  $\alpha_2 = 0^\circ$ , no any cracks were coalesced between the B tip of fissure ① and the C tip of fissure ②. But, one inclined crack was all observed in the middle ligament region of the specimen. Besides, some far-field cracks (not emanating from the fissure tips) were also observed in the right top region of each specimen and some surface spalling failures were also found in both specimens A0-1<sup>#</sup> and A0-2<sup>#</sup> due to obvious brittle characteristics. Note, in specimen A0-2<sup>#</sup>, one small tensile crack 4<sup>d</sup> was also initiated from the C tip of fissure ②. By comparing the aperture thickness of preexisting fissures before and after the specimen failed, we could see that the aperture thickness of the fissures all decreased with increasing deformation in both specimens.

When  $\alpha_2$  was  $45^\circ$ , the two fissures were actually coplanar as shown in Fig. 5.6, therefore the cracking mode was various with that for  $\alpha_2 = 0^\circ$ . In both specimens A45-1<sup>#</sup> and A45-2<sup>#</sup>, one tensile wing crack was observed emanating from the B tip of fissure ①, and propagated in downward direction. But in both specimens, the cracks from the A tip of fissure ① were different. In specimen A45-1<sup>#</sup>, only one tensile wing crack was initiated at the A tip, whereas in specimen A45-2<sup>#</sup>, two tensile cracks were observed from the same position. Except for the above difference, in specimen A45-1<sup>#</sup>, one anti-tensile wing crack was also observed from the B tip of fissure ① and propagated toward the top edge of the specimen. Note, the starting point emanating tensile cracks 1<sup>c</sup> and 5<sup>a</sup> in specimen A45-1<sup>#</sup> were the same but the propagating direction was opposite.

However, for the cracks emanated from the tips of fissure ②, the propagating mode in specimen A45-1<sup>#</sup> was obviously different from that in specimen A45-2<sup>#</sup>. In specimen A45-1<sup>#</sup>, one tensile wing crack was initiated from the C tip of fissure ②, whereas one tensile wing crack and two secondary tensile cracks were observed from the D tip of fissure ②. The length and width of these cracks were all different and the cracking order was also various in the process of deformation, which would be analyzed in the next section. But in specimen A45-2<sup>#</sup>, two anti-tensile wing cracks emanated from the C and D tips of fissure ②, respectively. The anti-tensile crack 1<sup>c</sup> propagated toward the bottom edge of the specimen, but anti-tensile crack 2 toward the top edge of the specimen. Note, no any crack coalescence in specimens for  $\alpha_2 = 45^\circ$  occurred between the B tip of fissure ① and the C tip of fissure ②, which was similar to that for  $\alpha_2 = 0^\circ$ . The inclined crack emanated in the middle ligament region of the specimen for  $\alpha_2 = 45^\circ$  was in the top or bottom of the pre-existing two fissures, which was different from those for  $\alpha_2 = 0^\circ$ , while some far-field cracks in the right top region of specimen A45-1<sup>#</sup> were all similar to those for  $\alpha_2 = 0^\circ$ . In both specimens, the aperture thickness of two fissures did not decrease a lot with the increasing deformation.

In the specimens for  $\alpha_2 = 90^\circ$ , the preexisting fissure ② was parallel to the major principal stress. From Fig. 5.11, we can see that the cracking mode in two red sandstone specimens containing two unparallel fissures for  $\alpha_2 = 90^\circ$  were different from those for  $\alpha_2 = 0^\circ$  and  $45^\circ$ . For the inclined fissure ①, in specimen A90-3<sup>#</sup>, one tensile wing crack was initiated at the A tip and propagated toward the top edge of the specimen until the boundary, but in specimen A90-4<sup>#</sup>, two tensile cracks were observed at the A tip. But at the B tip, one tensile wing crack was observed and propagated toward the bottom edge in both specimens. There was all one coalesced crack, which occurred in the ligament region. The specimen A90-3<sup>#</sup> coalesced between the B and C tips, but the specimen A90-4<sup>#</sup> coalesced between the B and D tips. For the vertical fissure ②, in both specimens, one inclined crack all emanated from the C tip of fissure ② to the left bottom corner of the specimen, furthermore some splitting failures were also observed near to the fissure ②, which resulted in the decrease in the aperture thickness of fissure ②. In both specimens, the aperture thickness of fissure ① kept basically constant.

When  $\alpha_2$  was  $135^\circ$  and  $180^\circ$ , each tested specimen all occurred to coalesce, i.e., crack coalesced between the B tip of fissure ① and the D tip of fissure ② (see Fig. 5.11), which was different to that for  $\alpha_2$  smaller than or equal to  $90^\circ$ . The coalesced reason can be explained as follows. The segment BD was approximately parallel to the major principal stress, and the tensile stress field in the ligament region led to coalesce easily between the B and D tips.

For  $\alpha_2 = 135^\circ$ , the cracking mode of both specimens A135-1<sup>#</sup> and A135-2<sup>#</sup> was very approximate. At the A tip of fissure ①, one tensile wing crack was initiated, and at the same time, one secondary crack was also observed in both specimens. These cracks all propagated in the direction of axial stress toward the top edge of the specimen. Note, the propagating path of tensile wing crack 1<sup>b</sup> is not perfectly straight, but very tortuous through the specimens, which was also due to that the cracks always propagated along the boundaries of large quartz grains within the matrix of the red sandstone. However below fissure ②, the cracks from the tips of fissure ② were different in specimens A135-1<sup>#</sup> and A135-2<sup>#</sup>. In specimen A135-1<sup>#</sup>, one tensile wing crack was observed from the D tip and two anti-tensile cracks from the C tip, but in specimen A135-2<sup>#</sup>, tensile crack was initiated from a certain distance away the D tip and three cracks (one anti-tensile crack and two far-field cracks) from the C tip. Even though in all cases, the tensile cracks all propagated in the direction of axial stress toward the bottom edge of the specimen, but the cracks initiated from the D tip occurred to shield due to the limitation of boundary of the specimen.

For  $\alpha_2 = 180^\circ$ , the cracking mode of two specimens can be separated into two types, i.e., the first type for specimen A180-2<sup>#</sup>, and the second type for specimen A180-3<sup>#</sup>. The main difference of two types can be described as follows. In the first type, specimen A180-2<sup>#</sup> all coalesced between the B and D tips when emanating crack 1, whereas in the second type, specimen A180-3<sup>#</sup> occurred to coalesce between the B and D tips when emanating crack 2. It should be noted that in the second type, one tensile wing crack 1<sup>c</sup> emanated from the B tip of fissure ① and evolved in the downward direction, at the same time, one small tensile

crack 1<sup>d</sup> emanated in the middle part of fissure ② and evolved in the upward direction. Moreover, one anti-tensile crack was initiated from the A tip of fissure ① in the second type, which was not observed in the first type. In both specimens for  $\alpha_2 = 180^\circ$ , tensile wing crack 1<sup>b</sup> was all initiated at the A tip of fissure ① and one tensile crack 1<sup>a</sup> emanated near to the middle position of fissure ②. The two cracks all propagated along the direction of major principal stress toward the edge of the specimen. In both specimens, one secondary tensile crack was also observed from the A tip of fissure ① and evolved in the upward direction, but these cracks did not reach the boundary of the specimen. In specimen A180-2<sup>#</sup>, two secondary cracks were observed at the A tip. At the C tip of fissure ②, one tensile crack was observed in specimen A180-3<sup>#</sup> and propagated in the downward direction toward the bottom edge of the specimen. However in specimen A180-2<sup>#</sup>, one tensile crack (see crack 3) was initiated from the C tip of fissure ② and propagated in the upward direction toward the top edge of the specimen. Note, in specimen A180-3<sup>#</sup>, one secondary tensile crack 4<sup>c</sup> was also observed from the same position. In two specimens for  $\alpha_2 = 180^\circ$ , far-field cracks were all observed, such as crack 6<sup>a</sup> in specimen A180-2<sup>#</sup>, crack 4<sup>b</sup> and 5 in specimen A180-3<sup>#</sup>, etc.

It should be noted that the aperture thickness of fissure ② in specimens for  $\alpha_2 = 135^\circ$  and  $180^\circ$  all decreased with the increase of deformation, whereas the aperture thickness of fissure ① did not decrease a lot except for that in specimen A180-3<sup>#</sup> (a distinct reduction).

## 5.4 Crack Coalescence Process and AE Behavior

In the preceding section, we had analyzed detailed the cracking mode of red sandstone specimens containing two unparallel fissures under uniaxial compression. But as a matter of fact, these cracks in the specimens were not simultaneously initiated with the increase of deformation. Therefore, in order to observe the order of cracking in red sandstone specimens containing two unparallel fissures in detail, we employed both photographic monitoring and acoustic emission monitoring techniques throughout the entire deformation process.

Figures 5.12, 5.13, 5.14, 5.15, and 5.16 presented the axial stress–time curves, the output of AE counts and accumulated AE counts of red sandstone specimens containing two unparallel fissures for different  $\alpha_2$ . Note, the denoted numbers shown in Figs. 5.12, 5.13, 5.14, 5.15, and 5.16 corresponded to the order of cracking shown in Fig. 5.11. The number “1” indicated that the crack was the first crack to initiate from the tips of preexisting fissures, while the superscript letters on the number meant that the cracks from different tips were simultaneously initiated. It should be noted that even though the ultimate failure mode of specimen was very approximate, the order of cracking may also be different.

From Figs. 5.12, 5.13, 5.14, 5.15 and 5.16, some AE characteristics in fissured specimens can be summarized as follows. In a word, the AE characteristics of specimens for  $\alpha_2 = 90^\circ$  were very similar to that of intact specimen, whereas the

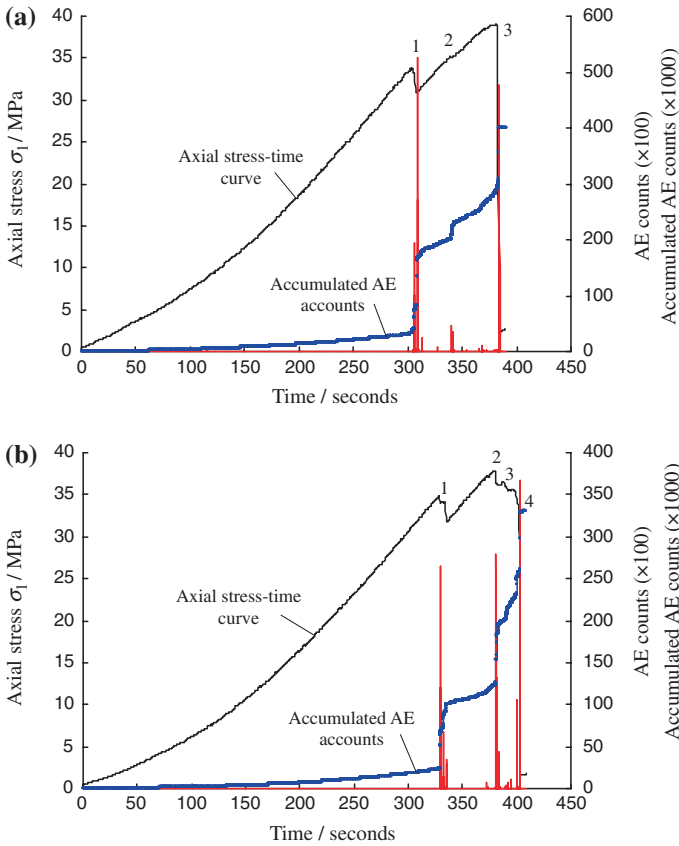


**Fig. 5.12** AE counts and accumulated AE counts of red sandstone specimens containing two unparallel fissures ( $\alpha_2 = 0^\circ$ ) during the whole deformation failure. The number in double bracket in *vertical axis* labels is the multiplier of coordinates. **a** Specimen A0-1<sup>#</sup>. **b** Specimen A0-2<sup>#</sup> (with kind permission of Elsevier Publisher)

AE behavior of specimens with other fissure angles were different to that of intact specimen, which resulted mainly from the variances of the crack initiation and coalescence process. All of the stress–time curves showed an initial nonlinear concave component at low stress levels, which was usually associated with the closure of original fissures or pores in specimens. In the closing stage of microscopic flaws, very few AE events were recorded. Therefore, during the initial stage, the output of AE counts could be regarded independent of fissure angle  $\alpha_2$ .

After this initial stage of nonlinear deformation, the specimens entered a linear elastic stage. Some AE events were observed during this stage, which can also be concluded from a very slow increasing of the accumulated AE counts with the increase of time. When tensile crack 1 emanated from the fissure tips and propagated toward the boundary of the specimen, there was an obvious stress drop in the stress–time curve of the deforming specimen, which was also testified with a

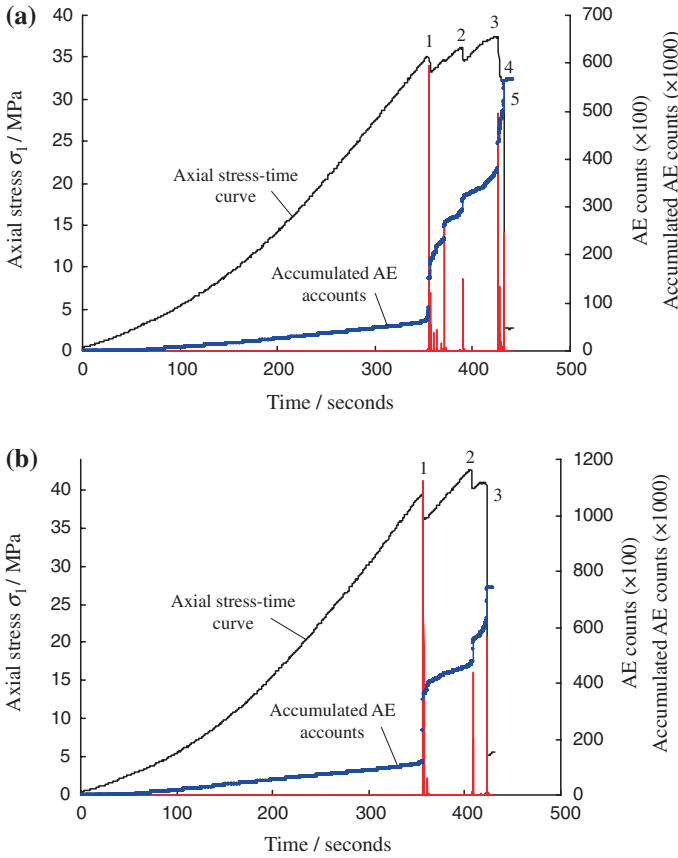


**Fig. 5.13** AE counts and accumulated AE counts of red sandstone specimens containing two unparallel fissures ( $\alpha_2 = 45^\circ$ ) during the whole deformation failure. The number in double bracket in vertical axis labels is the multiplier of coordinates. **a** Specimen A45-1#. **b** Specimen A45-2# (with kind permission of Elsevier Publisher)

bigger AE event and a sudden increasing in the accumulated AE counts curve as the increase of deformation. Note, for  $\alpha_2 = 90^\circ$ , when the specimen was loaded to point A, the crack 1 had not been completely formed, therefore the AE event at point A was not active and only a lower AE count and a smaller accumulated AE burst was observed. The AE count forming crack 1 depended on not only fissure angle  $\alpha_2$  but also specimen variability. For instance, the AE count in the specimens for  $\alpha_2 = 45^\circ$  reached up to 600–1200 events, which were obviously higher than that (only 300–400 events) in the specimens for  $\alpha_2 = 180^\circ$ . Even though for the same  $\alpha_2$  (e.g.  $\alpha_2 = 0^\circ$ ), the AE count in specimen A0-1# was also higher than that in A0-2#, which resulted from the influence of the heterogeneity on the AE behavior of red sandstone material.

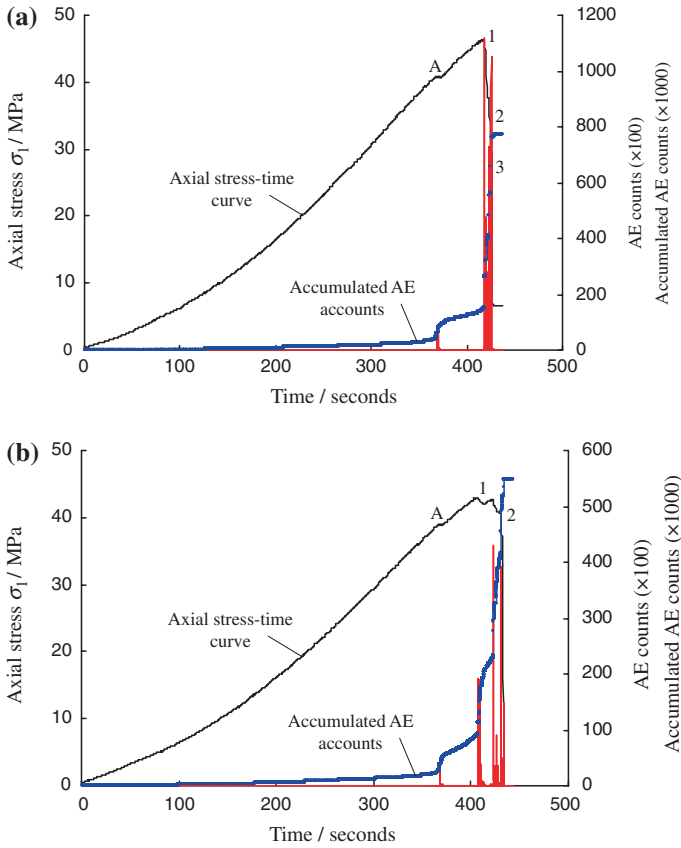


**Fig. 5.14** AE counts and accumulated AE counts of red sandstone specimens containing two unparallel fissures ( $\alpha_2 = 90^\circ$ ) during the whole deformation failure. The number in double bracket in vertical axis labels is the multiplier of coordinates. **a** Specimen A90-3<sup>#</sup>. **b** Specimen A90-4<sup>#</sup> (with kind permission of Elsevier Publisher)

After the first crack propagation, except for  $\alpha_2 = 90^\circ$ , with the increase of deformation, the axial stress also increased further and the corresponded AE events became active, which indicated that the damage internal to the specimen increased. After further loading, crack 2 was observed in the specimen, but the initiated positions of crack 2 were different among different specimens due to the heterogeneity of rock material. Similar to crack 1, the propagation of crack 2 also corresponds to a bigger AE event and a sudden increase in the accumulated AE counts curve, which was also actual, even though for  $\alpha_2 = 90^\circ$ . After the 2nd crack propagation, some specimens (e.g., A0-2<sup>#</sup> and A45-2<sup>#</sup>) began to enter the post-peak strength region, but most of specimens did not reach their peak stress.

For some specimens (e.g., A135-1<sup>#</sup>), crack coalescence process mainly occurred before the peak strength; but for some specimens (e.g., A180-2<sup>#</sup>), a lot of crack

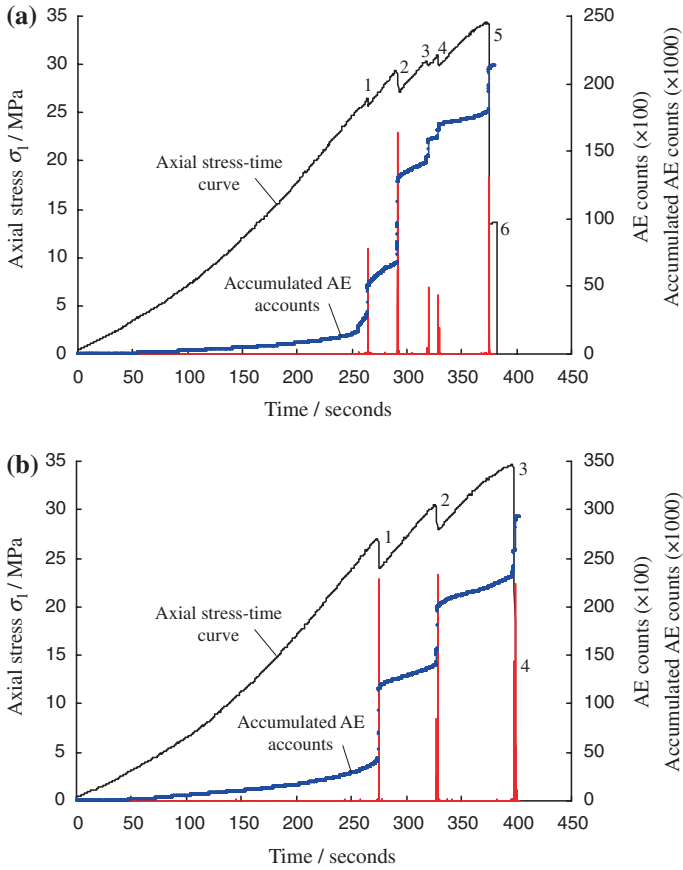


**Fig. 5.15** AE counts and accumulated AE counts of red sandstone specimens containing two unparallel fissures ( $\alpha_2 = 135^\circ$ ) during the whole deformation failure. The number in double bracket in vertical axis labels is the multiplier of coordinates. **a** Specimen A135-1<sup>#</sup>. **b** Specimen A135-2<sup>#</sup> (with kind permission of Elsevier Publisher)

coalescence processes were observed after the peak strength, which also led to the difference on AE characteristics of various specimens. Even though for the same  $\alpha_2$ , when reaching the peak strength, the sequence of crack coalescence in fissured specimens was also different due to specimen variability. However, it should be noted that the stress drops in the stress–time curves all corresponded to the crack initiation or coalescence in the specimen, which was also linked to a bigger AE event and a sudden increase in the accumulated AE counts curve. For instance, in specimen A0-1<sup>#</sup>, the AE event emanating crack 1 (with bigger stress drop) was obviously higher than that forming crack 2 (with smaller stress drop); whereas in specimen A135-1<sup>#</sup>, the AE event emanating crack 1 (with smaller stress drop) was obviously lower than that forming crack 2 (with larger stress drop).

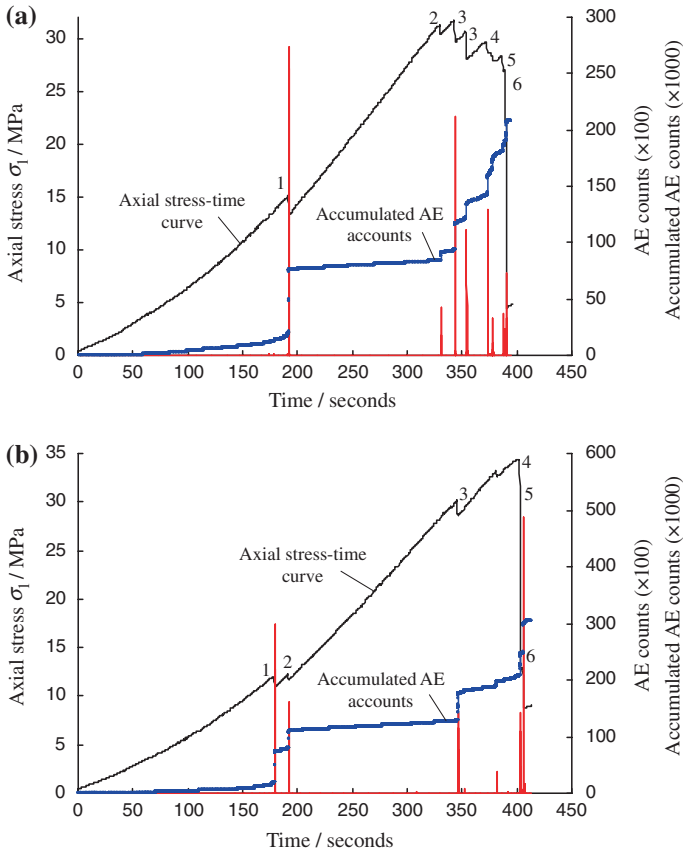


**Fig. 5.16** AE counts and accumulated AE counts of red sandstone specimens containing two unparallel fissures ( $\alpha_2 = 180^\circ$ ) during the whole deformation failure. The number in double bracket in vertical axis labels is the multiplier of coordinates. **a** Specimen A180-2#. **b** Specimen A180-3# (with kind permission of Elsevier Publisher)

However, we found that in a certain specimen, it was not actual that the bigger the axial stress dropped, the larger the corresponding AE event was. In some specimens (e.g. A0-2#), even though smaller stress drop when emanating crack 2, but the AE event was higher than that emanating crack 1, and the reason could be analyzed as follows. The energy dissipated in fracturing the rock can be related with not only the fracture mode but also the fracture mechanism. When emanating crack 1, the elastic energy in the specimen had released a part, but more elastic energy was stored in the specimen. Thus, with the increase of deformation, more gathered energy in the specimen were dissipated to emanate crack 2, therefore the AE event was higher, even though with smaller stress drop. When emanating the same fracture mode, the dissipated energy forming the tensile crack was also higher than that forming the shear crack.

In order to analyze in detail the relationship between the stress–time curve and the fracture coalescence process, AE events of red sandstone specimens containing two unparallel fissures, we will take specimens for  $\alpha_2 = 135^\circ$  as an example. From Fig. 5.15, before emanating crack 1, the stress concentration at the tips of preexisting fissures did not reach the material strength, and no any cracks were initiated. However, with the increase of deformation, crack 1 was observed from the preexisting fissure tips. But the order of cracking in various specimens was different. In specimen A135-1<sup>#</sup>, cracks 1<sup>a</sup> and 1<sup>b</sup> were initiated from the D tip of fissure ② and the A tip of fissure ①, respectively. But in specimen A135-2<sup>#</sup>, crack 1<sup>a</sup> coalesced between the B and D tips, although crack 1<sup>b</sup> was initiated from the A tip of fissure ①. Furthermore, the initiation and coalescence of crack 1 all leads to an obvious stress drop in the stress–time curve of the deforming specimen, which were also testified with a bigger AE event and a sudden increase in the accumulated AE counts curve as the increase of deformation. But, the stress drop initiating crack 1 in specimen A135-2<sup>#</sup> was bigger than that in specimen A135-1<sup>#</sup>.

Afterwards, with the increase of deformation, crack 2 was observed in two specimens for  $\alpha_2 = 135^\circ$ . For specimen A135-1<sup>#</sup>, crack 2 coalesced between the B and D tips, but for specimen A135-2<sup>#</sup>, the crack 2<sup>a</sup> and 2<sup>b</sup> were initiated from the A tip of fissure ① and the C tip of fissure ②, respectively. It should be noted that for specimen A135-1<sup>#</sup>, the AE counts due to crack 2 were higher obviously than that due to crack 1, but for specimen A135-2<sup>#</sup>, the AE counts due to crack 2 were approximately equal to that due to crack 1. After emanating crack 2, as the axial deformation further increased, for specimen A135-1<sup>#</sup>, anti-tensile crack 3 was first initiated from the C tip of fissure ② and then secondary tensile crack 4 from the A tip of fissure ①, which were all linked with bigger AE events and sudden increase in the accumulated AE counts curve (see Fig. 5.11a). After that, the specimen A135-1<sup>#</sup> was loaded to the peak strength with increasing axial deformation. At this moment, crack 5 emanated from the A tip of fissure ①, and a biggest AE event was also observed, which was also linked with a biggest stress drop. Rapidly crack 6 also emanated from the C tip of fissure ②, which also led to an unstable failure of specimen A135-1<sup>#</sup>. However for specimen A135-2<sup>#</sup>, when crack 3 was initiated, the axial stress also reached up to the peak strength. At this time, crack 3<sup>a</sup> was observed in the right top region of specimen and crack 3<sup>b</sup> was initiated from a certain distance away the D tip of fissure ②. When the specimens were loaded to the peak strength, specimen A135-2<sup>#</sup> occurred rapidly to unstable fail, and far-field crack 4 was observed in this specimen. Accompanied with biggest stress drop, the biggest AE events were also emanated.

## 5.5 Conclusions

In this chapter, a systematic experimental investigation was performed to explore the strength, deformation, and fracture coalescence behavior of red sandstone specimens (with the dimension of  $80 \times 160 \times 30$  mm) containing two unparallel

fissures (a kind of new fissure geometry). The fissures were all cut using a high-pressure water jet cutting device and were all approximately 2.0 mm wide. Based on the present study, the following conclusions can be summarized:

1. The mechanical parameters of the red sandstone containing two unparallel fissures were weaker than those of intact specimens, but being dependent to fissure angle  $\alpha_2$ . The average uniaxial compressive strength of red sandstone containing two unparallel fissures was increased from 36.89 to 44.74 MPa as  $\alpha_2$  from  $0^\circ$  to  $90^\circ$ , and then decreased from 44.74 to 31.73 MPa as  $\alpha_2$  from  $90^\circ$  to  $180^\circ$ . The average peak axial strain of red sandstone containing two unparallel fissures was increased from  $3.950 \times 10^{-3}$  to  $4.363 \times 10^{-3}$  as  $\alpha_2$  from  $0^\circ$  to  $90^\circ$ , and then decreased from  $4.363 \times 10^{-3}$  to  $3.862 \times 10^{-3}$  as  $\alpha_2$  from  $90^\circ$  to  $180^\circ$ . Both Young's moduli increased in the range of  $\alpha_2$  from  $0^\circ$  to  $90^\circ$  and then decreased up to  $180^\circ$ . When the  $\alpha_2$  was increased from  $0^\circ$  to  $90^\circ$ , the average secant modulus increased from 9.34 to 10.25 GPa. However, when the  $\alpha_2$  was increased from  $90^\circ$  to  $180^\circ$ , the average secant modulus decreased from 10.25 to 8.22 GPa.
2. No any crack coalescence for intact specimen was observed prior to the peak stress and a huge failure sonic was heard due to axial splitting failure in two seconds after the peak stress. But the cracking process of red sandstone containing two unparallel fissures depended on both the fissure angle  $\alpha_2$  and the heterogeneity of rock material. For  $\alpha_2$  smaller than or equal to  $45^\circ$ , no crack coalescence was occurred between the B tip of fissure ① and the D tip of fissure ②. For  $\alpha_2 = 90^\circ$ , in the ligament region of both specimens, there was all one coalesced crack between the B and C tips or the B and D tips, which resulted from the influence of the heterogeneity of red sandstone material on the cracking process. However, when  $\alpha_2$  was  $135^\circ$  and  $180^\circ$ , each tested specimen all occurred to coalesce, i.e., crack coalesced between the B tip of fissure ① and the D tip of fissure ②, which was different to that for  $\alpha_2$  smaller than or equal to  $90^\circ$ . The coalesced reason can be explained as follows: The segment BD was approximately parallel to the major principal stress, and the tensile stress field in the ligament region led to coalesce easily between the B and D tips.
3. The tested intact red sandstone displayed typical brittle rock behavior, which was also be testified by the general absence of AE counts; whereas the AE behavior of fissured specimens except for  $\alpha_2 = 90^\circ$  were different to that of intact specimen. The AE events of fissured specimens showed more decentralized than that of intact specimen, which resulted mainly from the gradual coalescence of cracks. The stress drops in the stress–time curves all corresponded to the crack initiation or coalescence in the specimen, which was also linked to a bigger AE event and a sudden increase in the accumulated AE counts curve. In the end, the macroscopic deformation characteristics of red sandstone containing two unparallel fissures under uniaxial compression were systematically evaluated by analyzing the relationship between the stress–time curve and the fracture coalescence process.

This chapter investigates only the strength failure and crack coalescence behavior of red sandstone containing two unparallel fissures from the viewpoint of

experiment. In order to understand deeply the fracture mechanism of engineering rock mass with unparallel intermittent structures, we will carry out a numerical simulation for red sandstone containing two unparallel fissures under uniaxial compression in the next chapter.

## References

- Lajitai EZ, Carter BJ, Duncan EJS (1994) En echelon crack-arrays in Postash salt rock. *Rock Mech Rock Eng* 27:89–111
- Lee H, Jeon S (2011) An experimental and numerical study of fracture coalescence in pre-cracked specimens under uniaxial compression. *Int J Solids Struct* 48(6):979–999
- Yang SQ, Liu XR, Jing HW (2013) Experimental investigation on fracture coalescence behavior of red sandstone containing two unparallel fissures under uniaxial compression. *Int J Rock Mech Min Sci* 63:82–92

# Chapter 6

## Discrete Element Modeling on Fracture Coalescence Behavior of Red Sandstone Containing Two Unparallel Fissures

In this chapter, we use PFC<sup>2D</sup> to carry out numerical simulation for red sandstone containing two unparallel fissures under uniaxial compression (Yang et al. 2014). Compared with other numerical softwares (SAP2000 and X-FEM, et al.), PFC<sup>2D</sup> code can better simulate the crack coalescence behavior of rock material by assembly of rigid circular particles bonded together at their contact points. First, the numerical micro-parameters of red sandstone are calibrated from the experimental results of intact specimen by the method of trial and error. Then, a systematic numerical simulation is performed for red sandstone containing two unparallel fissures under uniaxial compression by comparing quantitatively the numerical results with the experimental results. According to the simulated cracking process during the entire deformation, some significant features on the cracking characteristics are summarized. Finally, the stress field in red sandstone containing two unparallel fissures under uniaxial compression is analyzed in detail.

### 6.1 Discrete Element Modeling Method

#### 6.1.1 Micro-Bond Model

In PFC<sup>2D</sup>, there are two kinds of micro-bond models: one is a contact bond model (namely CBM), and another is a parallel bond model (namely PBM), as shown in Fig. 6.1 (Cho et al. 2007). The contact bonds can only transmit forces acting at the contact point, but the parallel bonds can transmit both forces and moments between particles. The parallel bonds may contribute to the resultant force and moment acting on the two bonded particles. In the PBM, the parallel bonds can be envisioned as a set of elastic springs with constant normal and shear stiffnesses, uniformly distributed over either a circular or rectangular cross section lying on the contact plane and centered at the contact point. These springs act in parallel

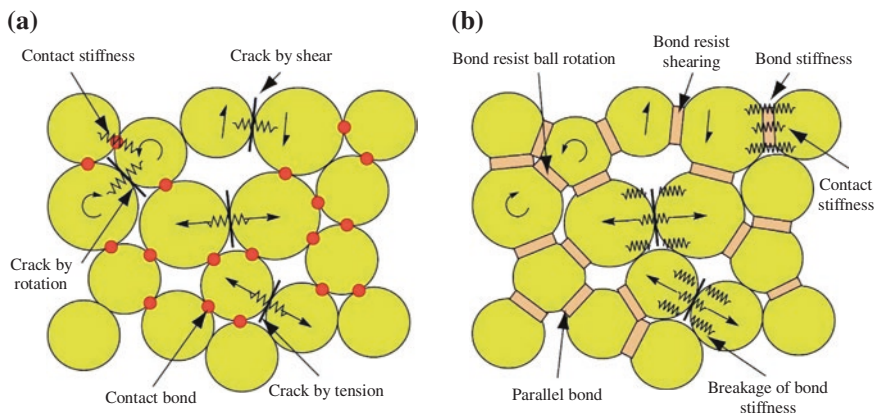


**Fig. 6.1** Illustration of the micro-bond types in PFC<sup>2D</sup> (after Cho et al. 2007). **a** Contact bond model (namely CBM) **b** Parallel bond model (namely PBM) (with kind permission of Elsevier Publisher)

with the point-contact springs that are used to model particle stiffness at a point. Relative motion at the contact (occurring after the parallel bond has been created) causes a force and a moment to develop within the bond material as a result of the parallel-bond stiffnesses. This force and moment act on the two bonded particles, and can be related to maximum normal and shear stresses acting within the bond material at the bond periphery. Moreover, in the PBM, bond breakage can lead to immediate decrease in macro stiffness because the stiffness is contributed by both contact stiffness and bond stiffness. Therefore in this chapter, we chose the PBM to carry out the numerical simulation, because the PBM can be more realistic for rock material modeling in which the bonds may break in either tension or shearing with an associated reduction in stiffness (Cho et al. 2007).

### 6.1.2 Numerical Specimen

Tested red sandstone specimens have a crystalline and blocky structure with a connected porosity of 8.8 %. According to the result of X-ray diffraction (XRD) (Yang et al. 2013), the minerals in the red sandstone specimens are mainly feldspar and quartz, with some smectite and zeolite, and very minor quantities of hematite. Figure 6.2 shows one numerical intact specimen generated by PFC<sup>2D</sup>, and the scale of numerical specimen is similarly equal to that of experimental specimen, i.e., the dimensions of 80 mm in width and 160 mm in height. All specimens had a height-to-width ratio of 2.0 to ensure a uniform stress state within the central part of the specimens. Each numerical intact specimen was discretized into 26,423 particles with 68,684 contacts and 52,435 parallel bonds. The particle size followed a uniform distribution ranging from 0.3 to 0.45 mm. The average unit weight of red sandstone was about 2400 kg/m<sup>3</sup>.

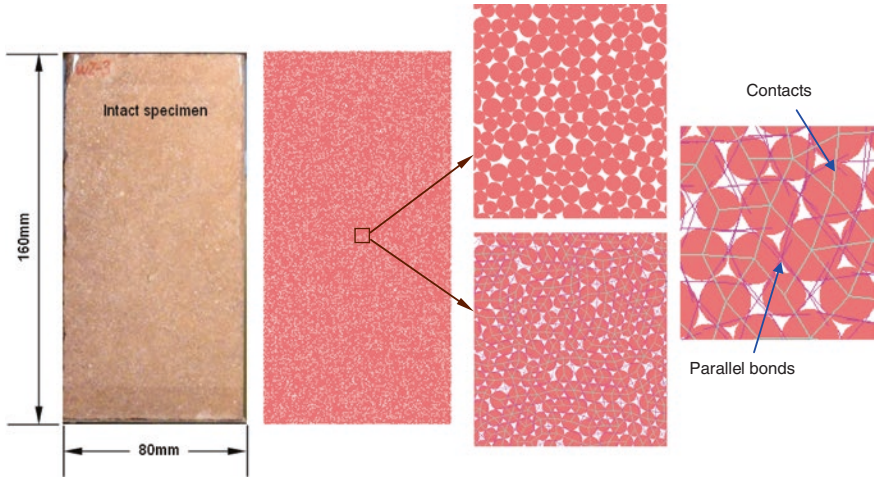


**Fig. 6.2** Numerical intact specimens generated in PFC<sup>2D</sup> in this chapter. Each numerical intact specimen was discretized into 26,423 particles with 68,684 contacts and 52,435 parallel bonds (with kind permission of Elsevier Publisher)

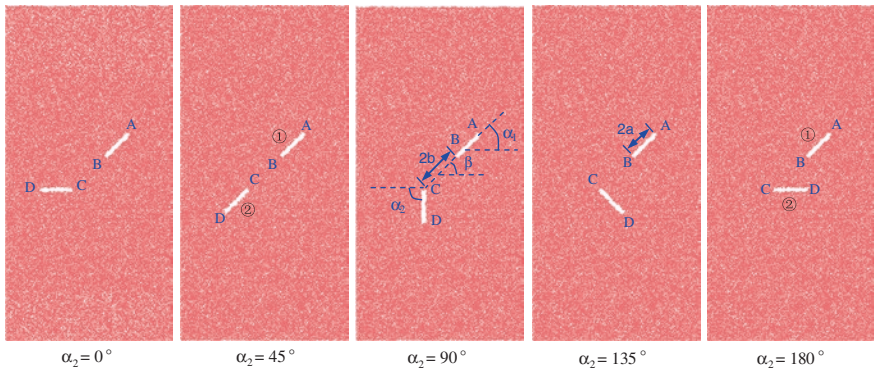


**Fig. 6.3** Numerical specimens containing two unparallel fissures, where,  $\alpha_1$  is the angle of fissure ① ( $\alpha_1 = 45^\circ$ ),  $\alpha_2$  is the angle of fissure ②,  $\beta$  is ligament angle ( $\beta = 45^\circ$ ),  $2a$  is fissure length ( $2a = 16$  mm), and  $2b$  is ligament length ( $2b = 22$  mm) (with kind permission of Elsevier Publisher)

After generating the intact specimen, we created two open and unparallel fissures by deleting ball particles. In order to investigate in detail the influence of fissure geometry on the strength, deformability, and fracture coalescence behavior of red sandstone containing two unparallel fissures, we designed the fissure geometry as shown in Fig. 6.3.  $\alpha_1$  is the angle of fissure ①,  $\alpha_2$  is the angle of fissure ②,  $\beta$  is ligament angle (the angle between segment B and C with the horizontal direction),  $2a$  is fissure length, and  $2b$  is ligament length (i.e., the distance from point B to C). In Fig. 6.3,  $2a$  and  $2b$  were, respectively, fixed to 16 and 22 mm;  $\alpha_1$  and  $\beta$  are all fixed to  $45^\circ$ . The open thickness of the pre-existing fissures was about 2.0 mm, but  $\alpha_2$  is changed in the range from  $0^\circ$  to  $180^\circ$  at an interval of  $45^\circ$ . The above geometry parameters used in numerical simulation are exactly identical to those during the experiment (Yang et al. 2013).

### **6.1.3 Simulation Procedure**

It should be noted that even though PFC has a 3-D version which can be employed for 3-D problems, a 3-D PFC simulation needs a very long time and the loading/boundary conditions are difficult to control. Therefore in this chapter, numerical simulation for red sandstone specimens was carried out on a 2-D plane stress model (Debecker and Vervoort 2013). An external displacement was applied on the top of the rock specimens in the axial direction. To ensure that the specimen remained in a quasi-static equilibrium throughout the simulation, a sufficiently low displacement loading rate must be applied. Zhang and Wong (2013) analyzed in detail the influence of loading rate on the cracking behavior of specimens containing a single fissure and two parallel fissures under uniaxial compression by PFC<sup>2D</sup>, which showed that the crack initiation stress and uniaxial compressive strength remained basically a constant when the loading rate was increased from 0.005 to 0.08 m/s even though for different flaw inclination angles. Therefore, in this chapter, the loading rate of 0.05 m/s was adopted in the numerical simulation, which was also the same as that by Potyondy and Cundall (2004) for uniaxial compression, biaxial compression, and Brazilian numerical simulation. In the simulation, the PFC<sup>2D</sup> will compute the critical time step first and assign a reasonable time step before each cycle. For example, if the time step equals  $1 \times 10^{-8}$  s/step, 0.05 m/s can be translated into  $5 \times 10^{-7}$  mm/step, which means that it requires 2,000,000 steps to move the specimen for 1 mm. Thus, this loading rate of 0.05 m/s is low enough in the PFC simulation.

In the present simulation, when the rock specimen was loaded to post-peak 40 % of the peak strength, less crack evolution (including crack initiation, propagation, and coalescence) could be further observed if continuously increasing the axial deformation. Therefore, loading was continuously applied until failure occurred, which was defined as a drop of post-peak axial stress down to 40 % of the peak strength. Based on the numerical results of red sandstone containing two unparallel fissures under uniaxial compression, we can analyze in detail the crack evolution process and the stress field around the pre-existing fissures in red sandstone.

## **6.2 Confirmation for Micro-Parameters of Red Sandstone**

### **6.2.1 Confirming Method for Micro-Parameters of Red Sandstone**

As it is well known to all of us, it is difficult to determine micro-parameters by experiment. But in order to validate the particle properties used in numerical modeling, it is essential to establish a correlation between the macro-behavior

(i.e., the axial stress–axial strain curve, the peak strength and elastic modulus, the ultimate failure mode, and the crack coalescence process) and micro-parameters. During the calibration process, the micro-parameters were confirmed using the trial and error method. The macroscopic behavior of intact red sandstone obtained by experiment was used in this chapter to calibrate the micro-parameters. The macroscopic results obtained by numerical simulation after each trial were used to check the micro-parameters. This process was repeated until the numerical results achieved good agreement with the experimental results.

Table 6.1 lists the micro-parameters used in the PFC<sup>2D</sup> model for red sandstone specimens in this chapter. The Young’s modulus of the particle and the parallel bond are all 8.6 GPa, and the ratio of normal to shear stiffness of the particle and the parallel bond are all 1.0. The particle friction coefficient is 0.7. The mean value of parallel-bond normal strength ( $\sigma_n$ ) and the mean value of parallel-bond shear strength ( $\tau_n$ ) are, respectively, 32 and 51 MPa, and the ratio of  $\sigma_n/\tau_n$  is about 0.63. In the past, Zhang and Wong (2012) had investigated the influence of the ratio of bond normal strength ( $\sigma_n$ ) to bond shear strength ( $\tau_n$ ) on the failure mode of rock-like material by adopting PFC<sup>2D</sup>, which showed that when the ratio of  $\sigma_n/\tau_n$  was 0.74, the specimen was mainly in tensile failure mode, while when the ratio of  $\sigma_n/\tau_n$  was 1.35, the specimen was mainly in shear failure mode. Therefore, in our numerical research, the ratio of  $\sigma_n/\tau_n$  is designed to 0.63 by taking into account an obviously brittle tensile failure of intact red sandstone (Yang et al. 2013). But the average standard deviation of parallel-bond normal strength is 6 MPa and the average standard deviation of parallel-bond shear strength is 10 MPa. Due to heterogeneity and randomness in PFC<sup>2D</sup> model for the micro-strength values, we repeat the simulation of two specimens with the same fissure geometry to make a more realistic numerical simulation of the natural rock material.

**Table 6.1** The micro-parameters used in the PFC<sup>2D</sup> model for red sandstone specimens in this chapter

Micro-parameters	Values	Remarks
Young’s modulus of the particle, $E_c$ (GPa)	8.6	
Young’s modulus of the parallel bond, $\bar{E}_c$ (GPa)	8.6	
Ratio of normal to shear stiffness of the particle, $k_n/k_s$	1.0	
Ratio of normal to shear stiffness of the parallel bond, $\bar{k}_n/\bar{k}_s$	1.0	
Particle friction coefficient, $\mu$	0.7	
Parallel-bond normal strength, mean (MPa)	32	Normal distribution
Parallel-bond normal strength, standard deviation (MPa)	6	
Parallel-bond shear strength, mean (MPa)	51	Normal distribution
Parallel-bond shear strength, standard deviation (MPa)	10	

## 6.2.2 Calibrating Micro-parameters by Experimental Results of Intact Specimen

Figure 6.4 shows the comparison between experimental and numerical stress-strain curves of intact red sandstone specimen under uniaxial compression. From Fig. 6.4, it can be seen that the numerically simulated curve under uniaxial compression agrees well with the experimental curve, including the stage of elastic deformation, the stage of crack initiation and growth before the peak strength, and the stage of unstable failure after the peak strength. However, due to closure of some primary cracks, pores, and voids in tested sandstone, the experimental specimen shows the downward concave and the initial nonlinear deformation at low stress levels, which however are not observed in the numerical specimen.

Table 6.2 shows the comparison between experimental and numerical mechanical parameters of intact red sandstone specimens. In Table 6.2,  $\sigma_c$  is defined as the uniaxial compressive strength and  $\varepsilon_{1c}$  refers to peak axial strain.  $E_S$  (the elastic modulus) refers to the slope of the linear part of the stress-strain curve. In accordance with Table 6.2, we can conclude that the simulated peak strength and elastic modulus of intact red sandstone specimens are similarly equal to those obtained by experiment (Yang et al. 2013). Besides, from Fig. 6.4, it can be seen that the

**Fig. 6.4** Comparison between experimental and numerical stress-strain curves of intact red sandstone specimen under uniaxial compression. The experimental curves of two intact specimens were obtained from the reference (Yang et al. 2013) (with kind permission of Elsevier Publisher)

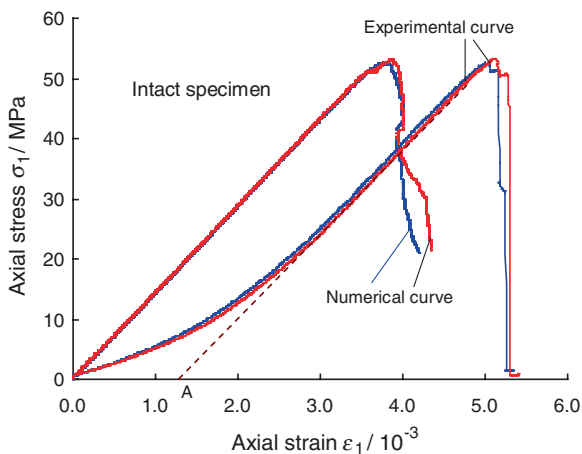


**Table 6.2** Comparison between the experimental and numerical mechanical parameters for intact red sandstone

Mechanical parameters	Experimental results		Numerical simulated results	
	Specimen WZ-2 <sup>#</sup>	Specimen WZ-3 <sup>#</sup>	Specimen NRS-1 <sup>#</sup>	Specimen NRS-2 <sup>#</sup>
$\sigma_c$ /MPa	52.98	52.20	52.41	52.92
$E_S$ /GPa	14.42	14.39	14.35	14.31
$\varepsilon_{1c}/10^{-3}$	5.113	5.005	3.730	3.854

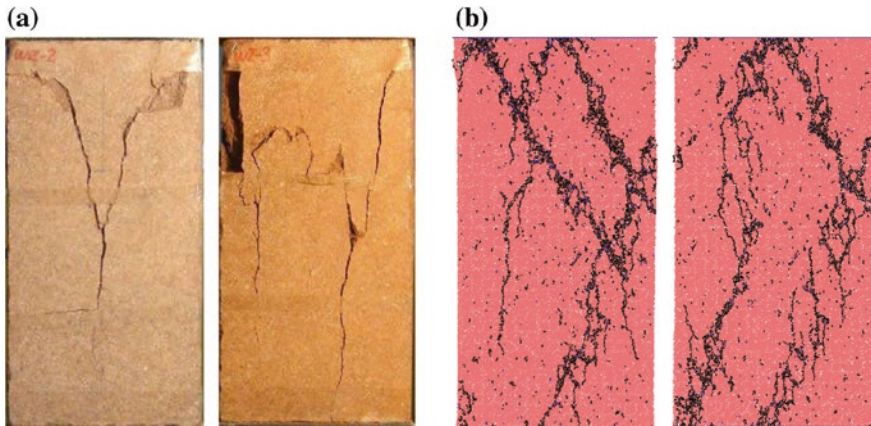


**Fig. 6.5** Comparison between experimental and numerical failure mode of intact red sandstone specimen under uniaxial compression. The experimental failure modes of two intact specimens were obtained from the reference (Yang et al. 2013). **a** Experimental failure mode; **b** numerical failure mode (with kind permission of Elsevier Publisher)

heterogeneity of rock material does not have an obvious effect on the mechanical parameters of intact red sandstone specimen.

Figure 6.5 further depicts the comparison between the experimental and numerical failure mode of intact red sandstone specimen. For numerical failure mode shown in Fig. 6.5, the black and blue dots represent the micro-cracks formed as a result of the tensile and shear contact force exceeding the prescribed parallel-bond normal and shear strength, respectively. The numerical intact red sandstone specimens also lead to axial splitting failure mode, which is similar to those obtained by experiment. The comparisons shown in Figs. 6.4 and 6.5 calibrate the rightness and reasonability of micro-parameters used in Table 6.1.

### 6.3 Numerical Results of Red Sandstone Containing Two Unparallel Fissures

Based on the experimental results of red sandstone containing two unparallel fissures under uniaxial compression (Yang et al. 2013), in this section, we will carry out a systematic simulation for pre-fissured red sandstone specimens and compare quantitatively the numerical results with the experimental results.

#### 6.3.1 Strength and Deformation Behavior

The comparison between experimental and numerical stress–strain curves of red sandstone specimens containing two unparallel fissures under uniaxial compression is illustrated in Fig. 6.6. In accordance with Fig. 6.6, generally, the numerical

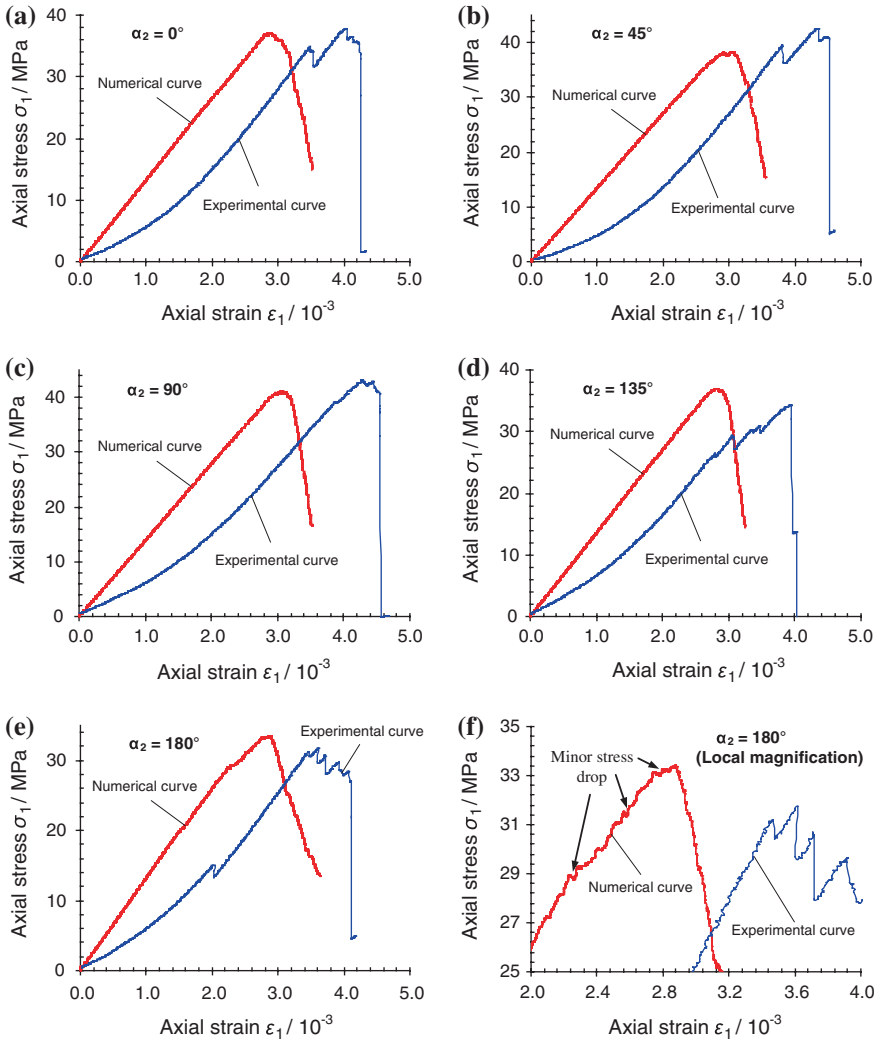


**Fig. 6.6** Comparison between experimental and numerical stress–strain curves of red sandstone specimen containing two unparallel fissures under uniaxial compression. **a**  $\alpha_2 = 0^\circ$ , **b**  $\alpha_2 = 45^\circ$ , **c**  $\alpha_2 = 90^\circ$ , **d**  $\alpha_2 = 135^\circ$ , **e**  $\alpha_2 = 180^\circ$ , **f**  $\alpha_2 = 180^\circ$  (Local magnification) (with kind permission of Elsevier Publisher)

simulated stress–strain curves of red sandstone specimens containing two unparallel fissures are similar to the experimental stress–strain curves before the peak strength if not taking into account the initial nonlinear deformation. It should be noted that the numerically simulated curve of intact specimen under uniaxial compression has agreed well with the experimental curve (see Fig. 6.4), including the post-peak region.

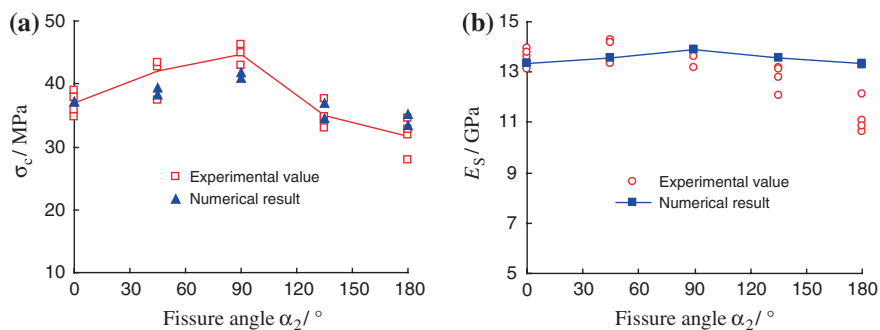
However, when the same micro-parameters (Table 6.1) were used to model the fissured specimens, the experimental and simulated post-peak curves have some minor differences, especially for  $\alpha_2 = 180^\circ$  (Fig. 6.6e). From Fig. 6.6e, it can be seen that the post-peak stress–strain curve obtained numerically is a little more ductile than that obtained experimentally, which is possible to result from the difference in the fracturing mechanisms after the peak strength. Moreover, it should be noted that there are some obvious stress drops in the experimental stress–strain curves of red sandstone specimens, which results mainly from gradual coalescence of the cracks (Yang et al. 2013). But in the numerical stress–strain curves of red sandstone containing two unparallel fissures, greater stress drops are not observed. However, when the numerical stress–strain curves are magnified as shown in Fig. 6.6f, a lot of minor stress drops can also be found.

Table 6.3 lists the strength and deformation parameters of red sandstone specimens containing two unparallel fissures obtained by numerical simulation. In accordance with the data listed in Table 6.3, we can carry out a detailed comparison between experimental and numerical uniaxial compressive strength and the elastic modulus of red sandstone containing two unparallel fissures, as shown in Fig. 6.7. The solid points and hollow points represent the mechanical parameters of the numerical models and the experiment specimens, respectively.

From Fig. 6.7a, it is clear that the uniaxial compressive strength of red sandstone specimens containing two unparallel fissures simulated by PFC<sup>2D</sup> has the similar trend with increase of fissure angle  $\alpha_2$ . Moreover, the simulated uniaxial compressive strength is similarly equal to that obtained by experiment for the same  $\alpha_2$  (see Fig. 6.7a). But from Fig. 6.7b, it can be seen that when  $\alpha_2$  equals to or is smaller than  $135^\circ$ , the simulated elastic modulus is approximately equal to that obtained by experiment for the same  $\alpha_2$ . However, when  $\alpha_2$  was  $180^\circ$  the simulated elastic modulus (13.32 GPa) was 16.1 % higher than the experimental elastic modulus (11.17 GPa for the average value of four specimens), which can be explained as follows. In accordance with Fig. 6.6e, it is clear that there is an obvious stress drop at the lower stress level in the experimental curve for  $\alpha_2 = 180^\circ$ , which is

**Table 6.3** Strength and deformation parameters of red sandstone specimens containing two unparallel fissures (PFC<sup>2D</sup> simulation)

Specimen	$\alpha_1/^\circ$	$\alpha_2/^\circ$	$\beta/^\circ$	$2a/\text{mm}$	$2b/\text{mm}$	$\varepsilon_{1c}/10^{-3}$	$\sigma_c/\text{MPa}$	$E_s/\text{GPa}$	$\nu_s$
N000-1 <sup>#</sup>	45	0	45	16	22	2.831	37.16	13.35	0.198
N000-2 <sup>#</sup>	45	0	45	16	22	2.875	37.13	13.34	0.198
N045-1 <sup>#</sup>	45	45	45	16	22	3.067	38.30	13.57	0.158
N045-2 <sup>#</sup>	45	45	45	16	22	3.037	39.38	13.57	0.157
N090-1 <sup>#</sup>	45	90	45	16	22	3.072	40.96	13.88	0.152
N090-2 <sup>#</sup>	45	90	45	16	22	3.207	41.86	13.88	0.153
N135-1 <sup>#</sup>	45	135	45	16	22	2.801	36.97	13.59	0.182
N135-2 <sup>#</sup>	45	135	45	16	22	2.690	34.42	13.59	0.181
N180-1 <sup>#</sup>	45	180	45	16	22	2.875	33.43	13.32	0.197
N180-2 <sup>#</sup>	45	180	45	16	22	2.990	35.25	13.31	0.197

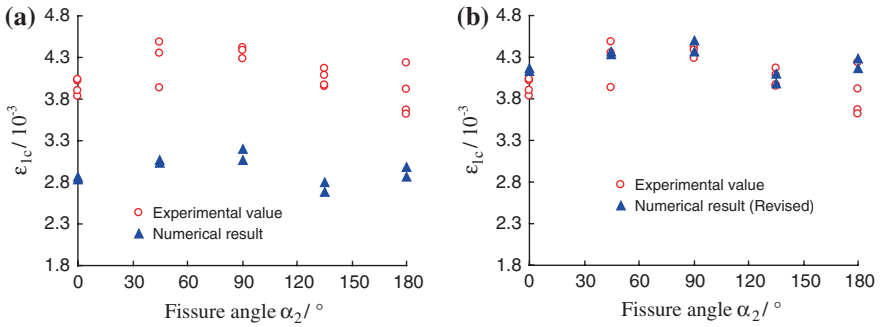


**Fig. 6.7** Comparison between experimental and numerical uniaxial compressive strength of the elastic modulus of red sandstone containing two unparallel fissures. The experimental values were obtained from the reference (Yang et al. 2013) (with kind permission of Elsevier Publisher)

different from the experimental curves of specimen with other fissure angles. The approximately linear part of the stress–strain curve after the first stress drop shown in Fig. 6.6e was used to calculate the elastic modulus, which led to lower experimental elastic modulus due to minor damage of specimen after the first stress drop.

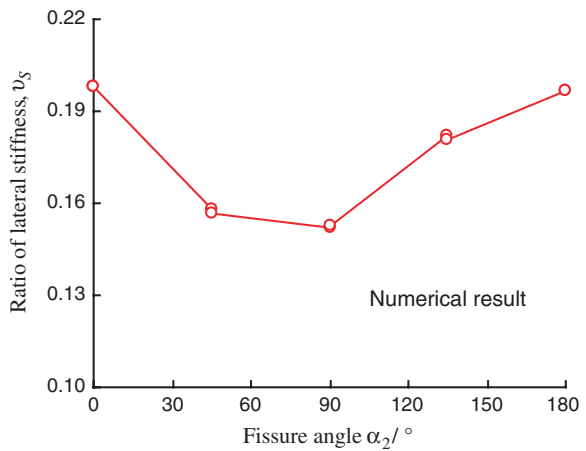
Figure 6.8a shows the comparison between experimental and numerical peak axial strain of red sandstone specimens containing two unparallel fissures under uniaxial compression. In general, the experimental peak axial strain of specimen is higher than that obtained by numerical simulation, which results mainly from the initial nonlinear deformation for experimental specimens. If the initial nonlinear deformation is taken into account, the simulated peak axial strain of specimens containing two unparallel fissures can be revised by adding an initial strain value (about  $1.3 \times 10^{-3}$ , the strain value corresponded to the point A) in accordance with Fig. 6.4. Figure 6.8b shows the comparison between experimental and revised numerical peak axial strain of red sandstone specimens containing two unparallel fissures. From Fig. 6.8b, it is clear that the experimental peak axial strain agrees very well with the revised numerical peak axial strain.

Figure 6.9 illustrates the influence of fissure angle  $\alpha_2$  on the ratio of lateral stiffness ( $\nu_s$ ) of red sandstone containing two unparallel fissures under uniaxial compression. The ratio of lateral stiffness is defined as the ratio of the lateral strain to the axial strain at a half stress of peak strength (Eberhardt et al. 1998). In accordance with the ratio of lateral stiffness listed in Table 6.3, we can see that the ratio of lateral stiffness of red sandstone containing two unparallel fissures ranges from 0.152 to 0.198. It is clear that the ratio of lateral stiffness of red sandstone containing two unparallel fissures under uniaxial compression depends on fissure angle  $\alpha_2$ , and the trend is different from the variance on other mechanical parameters. The  $\nu_s$  value of specimen containing two unparallel fissures at  $\alpha_2 = 0^\circ$  was 0.198, but the  $\nu_s$  value at  $\alpha_2 = 45^\circ$  decreased to 0.158. With increase of fissure angle  $\alpha_2$  from  $45^\circ$  to  $90^\circ$ , the  $\nu_s$  value of specimen containing two unparallel fissures had a slight decrease from 0.158 to 0.153. However, when  $\alpha_2$  increased from  $90^\circ$  to  $180^\circ$ , the  $\nu_s$  value of specimen increased rapidly from 0.153 to 0.197 (similarly equal to that for  $\alpha_2 = 0^\circ$ ).



**Fig. 6.8** Influence of fissure angle  $\alpha_2$  on the peak axial strain of red sandstone containing two unparallel fissures. The experimental values were obtained from the reference (Yang et al. 2013) (with kind permission of Elsevier Publisher)

**Fig. 6.9** Influence of fissure angle  $\alpha_2$  on the ratio of lateral stiffness of red sandstone containing two unparallel fissures (with kind permission of Elsevier Publisher)



### 6.3.2 Cracking Characteristics

Figure 6.10 illustrates the influence of fissure angle  $\alpha_2$  on ultimate failure mode of red sandstone specimens containing two unparallel fissures under uniaxial compression in PFC<sup>2D</sup> numerical simulation. Comparing with the experimental ultimate failure mode shown in Fig. 5.10 in Chap. 5, we can see that PFC<sup>2D</sup> software can be used to simulate the cracking characteristics of red sandstone material. That is to say, the crack initiation and coalescence modes of numerical specimens show good agreement with those of experimental specimens.

Figures 6.11, 6.12, 6.13, 6.14, 6.15, 6.16, 6.17, and 6.18 further summarize the crack coalescence process of red sandstone specimen obtained by PFC<sup>2D</sup> simulation under uniaxial compression. In accordance with Figs. 6.11, 6.12, 6.13, 6.14, 6.15, 6.16, 6.17, and 6.18, we can analyze the detailed effect of fissure angle  $\alpha_2$  on the crack coalescence process of red sandstone specimen containing two

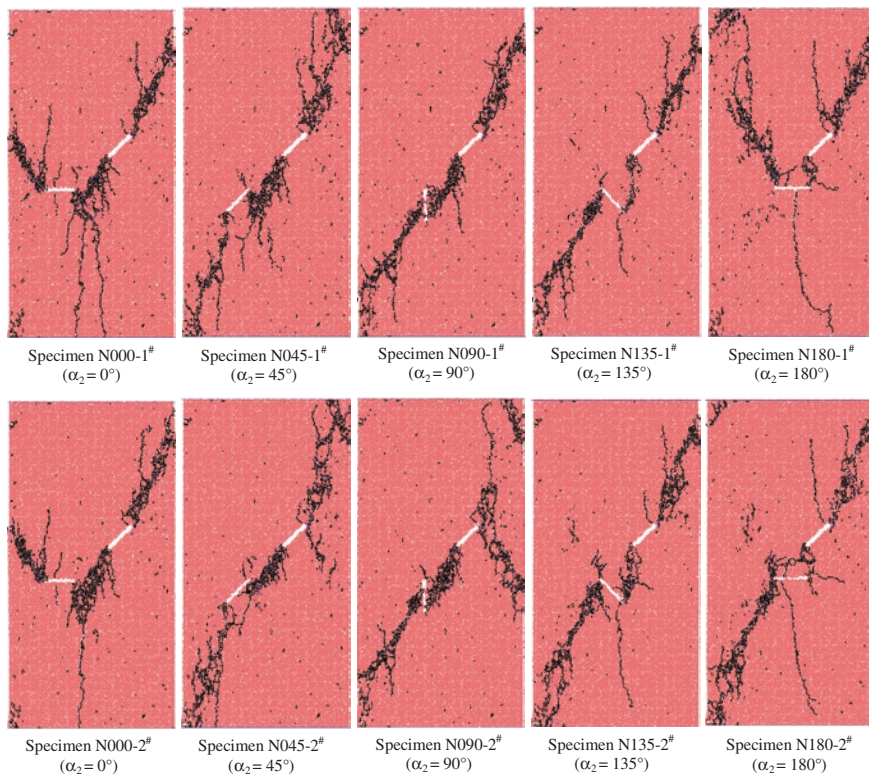


**Fig. 6.10** Numerical ultimate failure mode of red sandstone specimens containing two unparallel fissures under uniaxial compression with respect to different fissure angle  $\alpha_2$  (with kind permission of Elsevier Publisher)

unparallel fissures. From Figs. 6.11, 6.12, 6.13, 6.14, 6.15, 6.16, 6.17, and 6.18, it is clear that these cracks in the specimens are not simultaneously initiated with the increase of deformation, but a gradual evolution process.

The axial stress at point a shown in Figs. 6.11, 6.12, 6.13, 6.14, 6.15, 6.16, 6.17, and 6.18 refers to the crack initiation stress. For the crack initiation stress, it was usually identified by analyzing the relationship between the axial stress and the volumetric strain of rock material (Yang et al. 2012). The crack initiation stress could be defined as the stress where the volumetric strain departs from pseudo-linear elastic behavior. But in PFC<sup>2D</sup> modeling, due to discrete micro-cracks that appear early and scatter within the numerical specimens, it is usually more difficult to define the crack initiation stress, especially for intact specimen by using the crack number. But for fissured specimens, it should be noted that the first macro-crack is usually initiated from nearby pre-existing fissures. Therefore, in this research, we define the first macro-crack as enough micro-cracks have coalesced from nearby pre-existing fissures (Zhang and Wong, 2012). That is, when the crack number in the specimen reaches about 10 % of the total crack number

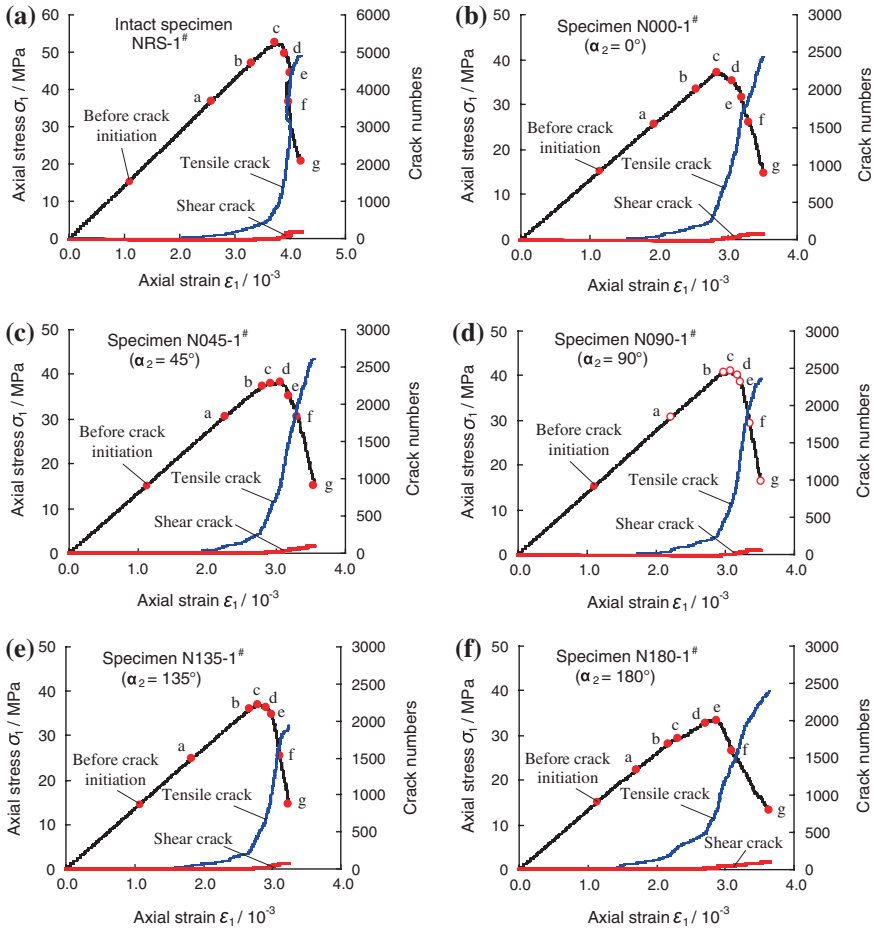


**Fig. 6.11** Relation between axial stress–axial strain curve and crack numbers, crack coalescence process in red sandstone specimens under uniaxial compression. The denoted letters corresponded to those listed in Figs. 6.12, 6.13, 6.14, 6.15, 6.16, and 6.17 (with kind permission of Elsevier Publisher)

(including tensile and shear crack number) (f) at the peak strength, the corresponding stress is defined as the crack initiation stress.

For intact specimen, before the peak strength (see point c in Fig. 6.11a), the tensile and shear crack numbers in the specimen were rare, and they result from small micro-failure occurrences. It should be noted that these micro-cracks in the specimen emanated before the peak strength was invisible to the naked eyes during the experiment. After the peak strength, more micro-cracks were observed with increase of deformation; which increased more rapidly than that before the peak strength. Furthermore, the tensile micro-crack numbers were distinctly

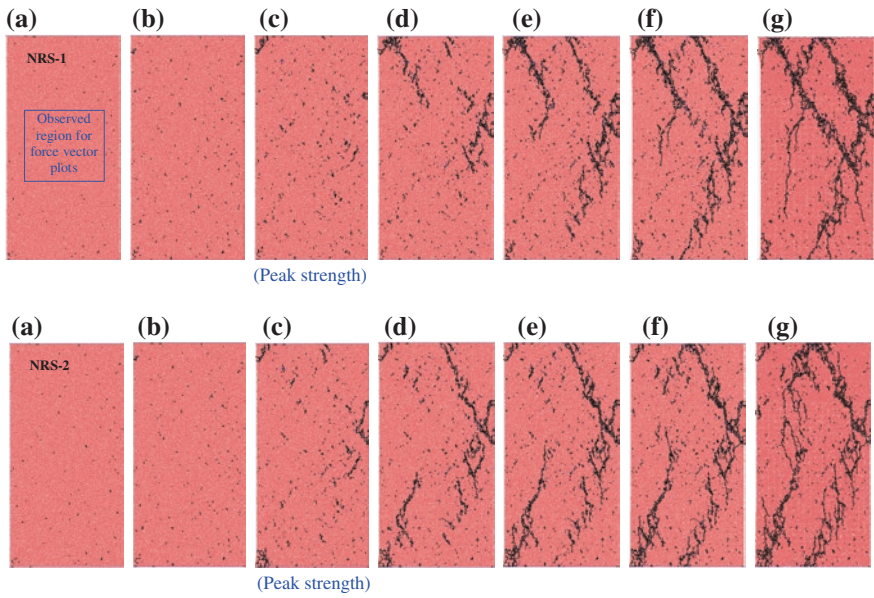


**Fig. 6.12** Crack coalescence process of intact red sandstone specimens under uniaxial compression (with kind permission of Elsevier Publisher)

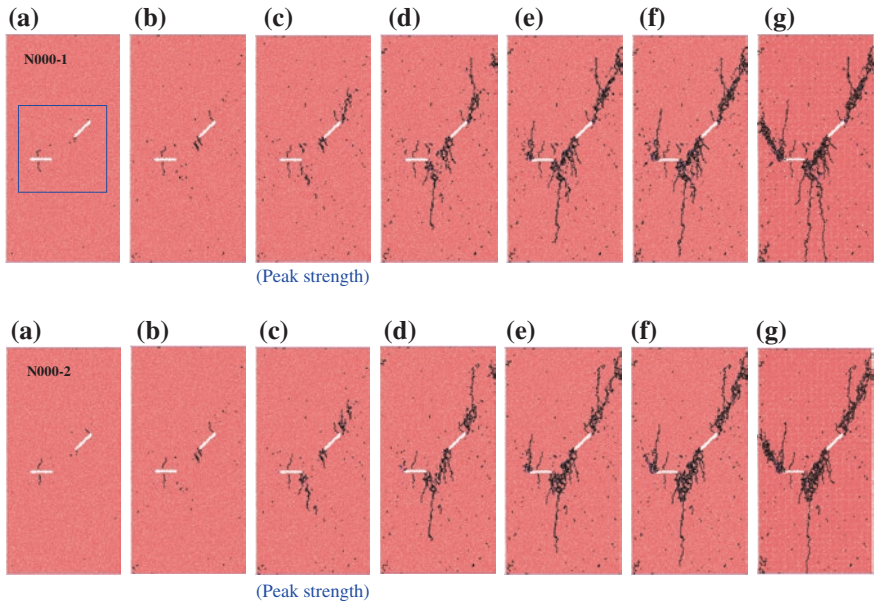


**Fig. 6.13** Crack coalescence process of flawed red sandstone specimens ( $\alpha_2 = 0^\circ$ ) under uniaxial compression (with kind permission of Elsevier Publisher)

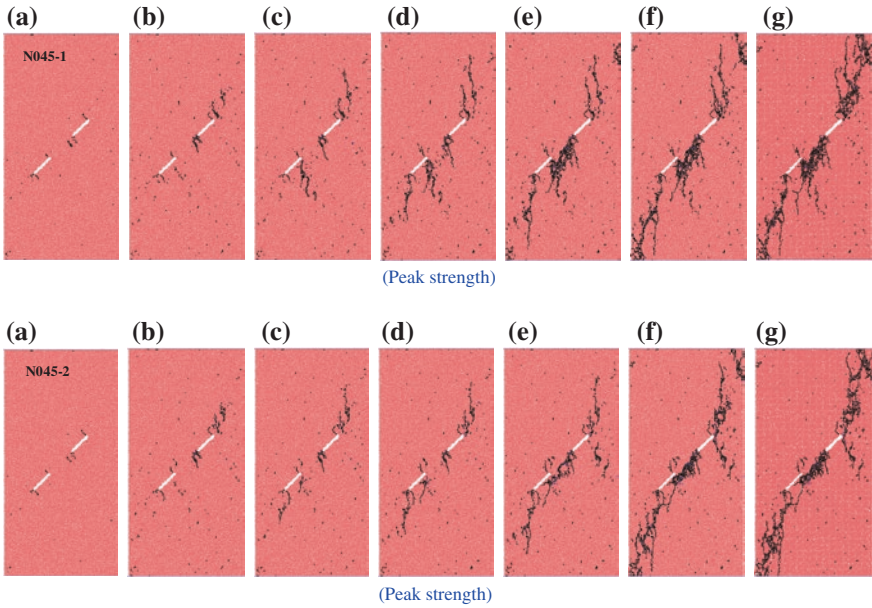


**Fig. 6.14** Crack coalescence process of flawed red sandstone specimens ( $\alpha_2 = 45^\circ$ ) under uniaxial compression (with kind permission of Elsevier Publisher)

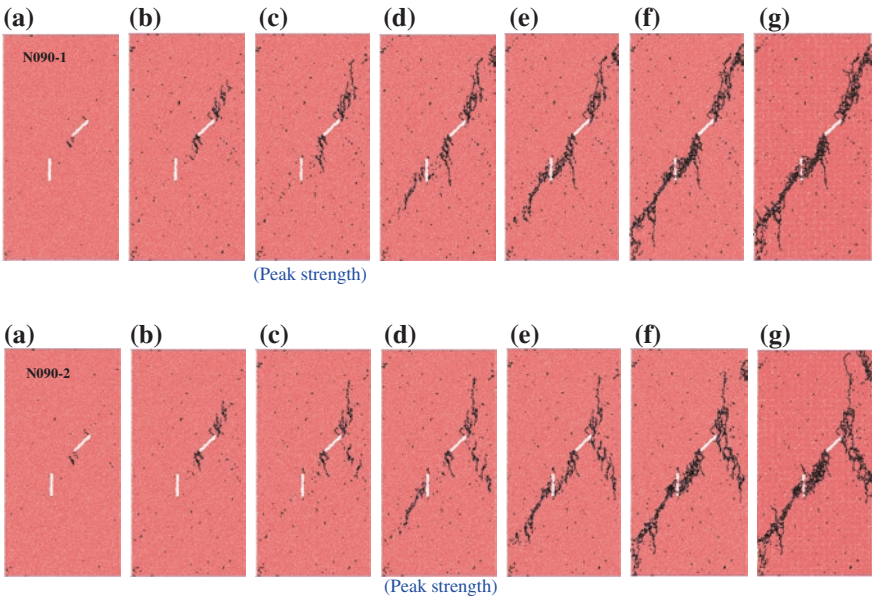


**Fig. 6.15** Crack coalescence process of flawed red sandstone specimens ( $\alpha_2 = 90^\circ$ ) under uniaxial compression (with kind permission of Elsevier Publisher)

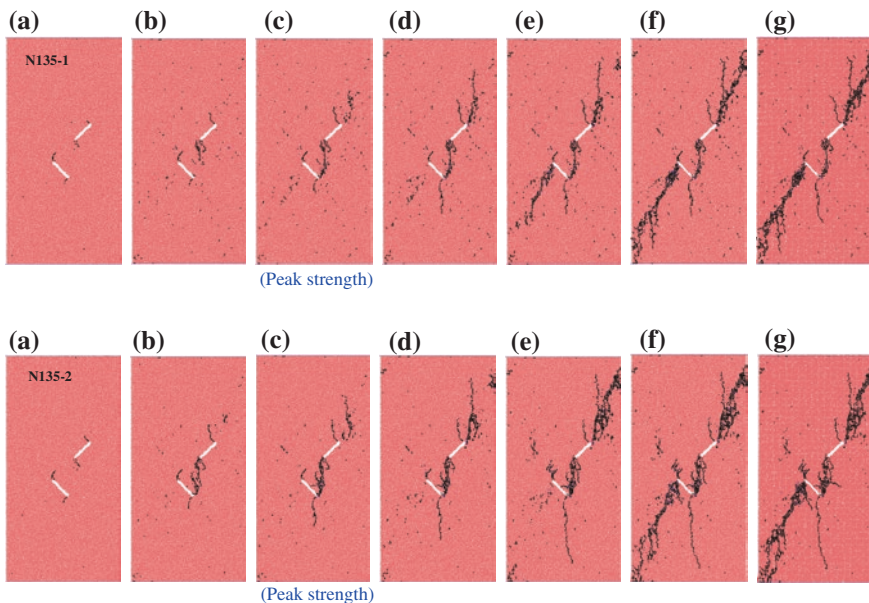


**Fig. 6.16** Crack coalescence process of flawed red sandstone specimens ( $\alpha_2 = 135^\circ$ ) under uniaxial compression (with kind permission of Elsevier Publisher)

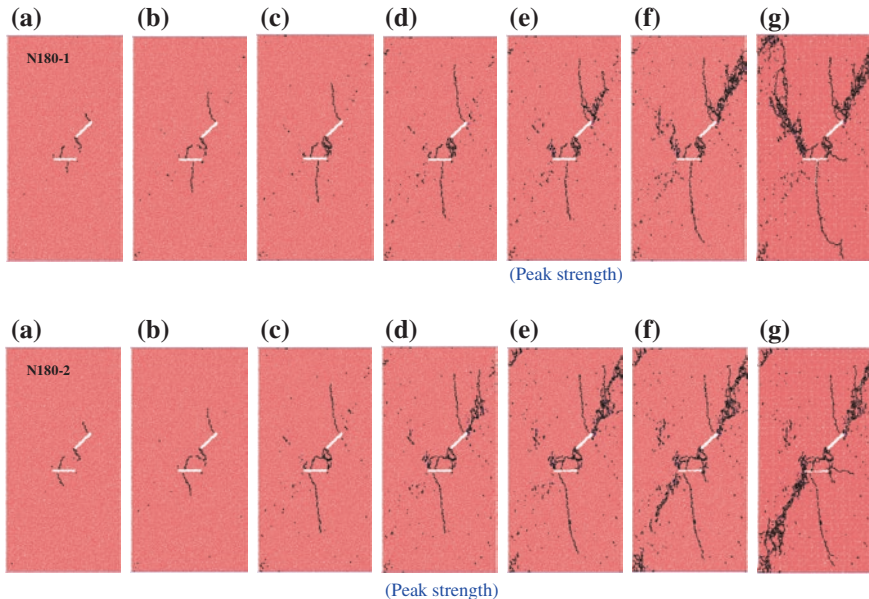


**Fig. 6.17** Crack coalescence process of flawed red sandstone specimens ( $\alpha_2 = 180^\circ$ ) under uniaxial compression (with kind permission of Elsevier Publisher)

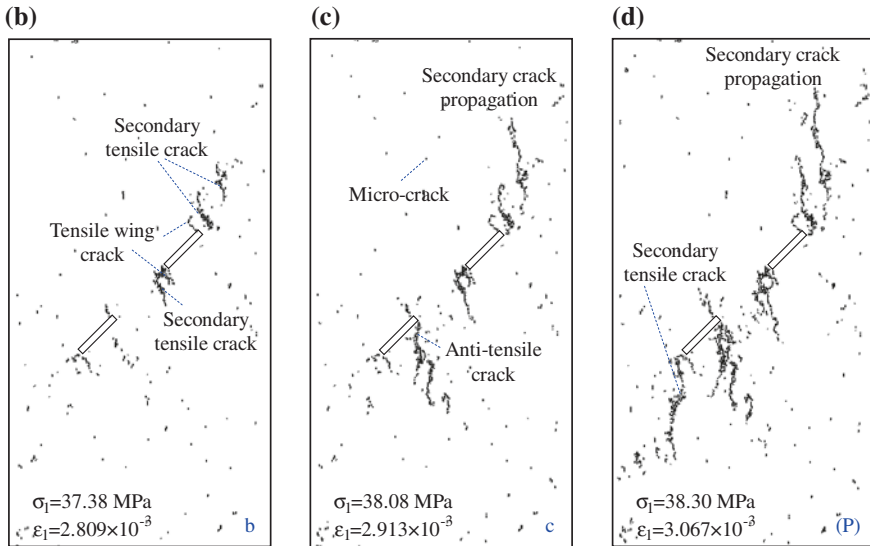


**Fig. 6.18** Local magnification on the crack coalescence process of red sandstone specimen N045-1# containing two parallel fissures under uniaxial compression (with kind permission of Elsevier Publisher)

higher than the shear micro-crack numbers. For example, in Fig. 6.11a, when reaching the peak stress, the tensile and shear crack numbers were, respectively, 831 and 46, whereas at point e after the peak strength, the tensile and shear crack numbers were, respectively, 2965 and 152. Macroscopic cracks were clustered along the direction of axial stress after the peak strength in numerical simulation (see Fig. 6.12), which was also validated in the experiment.

For red sandstone containing two unparallel fissures under uniaxial compression, the crack coalescence process can be analyzed in detail from Figs. 6.11, 6.12, 6.13, 6.14, 6.15, 6.16, 6.17, and 6.18. It should be noted that the denoted letters in Fig. 6.11 corresponded to those listed in Figs. 6.12, 6.12, 6.13, 6.14, 6.15, 6.16, and 6.17. In order to make a good evaluation, we adopted three stages to summarize, i.e., stage I: at the crack initiation stress (point a); stage II: in the deformation process from point a to the peak strength (including the peak strength); stage III: after the peak strength.

**Stage I:** when the specimen was loaded to point a, the crack initiation stress was reached. Two tensile wing cracks were, respectively, initiated from the tips A and B of fissure ①, and the initiating direction was vertical to the pre-existing fissure. Furthermore, in all the specimens, the two tensile wing cracks were observed, which did not depend on fissure angle  $\alpha_2$ . Whereas the tensile wing cracks emanated from the fissure tips of fissure ② were dependent on fissure angle  $\alpha_2$ .

When  $\alpha_2 = 0^\circ$  and  $180^\circ$ , fissure ② was parallel to the horizontal direction, i.e., vertical to the axial stress. Under uniaxial compression, the concentrated tensile

stress along the vertical middle line of fissure is much higher than the tensile stress concentration at the tips of fissure ②. Hence, tensile wing cracks were not initiated from the tips of fissure ②, but a certain distance from the tips of fissure ②. The crack initiation direction was also similarly parallel to the axial stress. It should be noted that, the crack initiation mode of numerical specimen for  $\alpha_2 = 180^\circ$  was similar to that of experimental specimen (Yang et al. 2013), but the crack initiation mode of numerical specimen for  $\alpha_2 = 0^\circ$  was different from that of experimental specimen. In the real experimental specimen for  $\alpha_2 = 0^\circ$ , anti-tensile crack at the B tip of fissure ① was observed and tensile wing cracks were initiated from the tips C and D of fissure ②, which was not observed in the simulation. When  $\alpha_2 = 45^\circ$  and  $135^\circ$ , in the numerical specimen, two tensile wing cracks were, respectively, initiated from the tips C and D of fissure ②, and the initiating direction was vertical to the pre-existing fissure. When  $\alpha_2 = 90^\circ$ , no macro-cracks were initiated from the tips C and D of fissure ②, which was similar to the experimental specimen.

**Stage II:** After the crack initiation stress, the specimen will undergo the deformation stage from point a to the peak strength with increasing axial deformation. In this stage, the crack coalescence characteristic was also dependent on fissure angle  $\alpha_2$ .

For  $\alpha_2 = 0^\circ$ , with the increase of deformation, the tensile wing cracks propagated along the direction of major principal stress (see the crack mode at Fig. 6.13b in specimens N000-1<sup>#</sup> and N000-2<sup>#</sup>), but only propagated a little, which was likely due to the stress field interaction in the ligament region. When the specimen was loaded to the peak stress, some secondary cracks and far-field cracks were observed from the tips of fissure ① and nearby the C tip of fissure ② (see the crack mode at Fig. 6.13c in specimens N000-1<sup>#</sup> and N000-2<sup>#</sup>). It should be noted that the propagating speed of secondary cracks was higher than that of tensile wing cracks. These secondary or far-field cracks are propagated in the upward or downward direction parallel to axial stress.

For  $\alpha_2 = 45^\circ$ , with the increase of deformation, the tensile wing cracks did not propagate further, but when the specimen was loaded to point b, two secondary cracks were observed nearby the A tip of fissure ① and one secondary crack was initiated from the B tip of fissure ①, which can be validated from local magnification shown in Fig. 6.18. From Fig. 6.18, we observe many micro-cracks, which were difficult to be seen during the experiment. When many micro-cracks linked each other together, macroscopic cracks formed, which indicated that the macroscopic cracks were actually a confluence of many microscopic cracks. After the specimen was loaded to point c, one anti-tensile crack was observed from the C tip of fissure ②, and at the same time two far-field cracks beneath the C tip of fissure ② were also observed. The secondary tensile crack and far-field crack nearby the tips of fissure ① propagated similarly in the direction of major principal stress. When the specimen reached the peak strength, no new cracks emanated except for one secondary tensile crack from the D tip of fissure ②. From Fig. 6.18, it could be seen that although the axial stress increased a little, the crack evolution process in the specimens could still be observed with increasing axial deformation.

For  $\alpha_2 = 90^\circ$ , with the increase of deformation, secondary tensile cracks were observed from the tips A and B of fissure ①, respectively. At the same time, several far-field cracks were also initiated nearby the A tip of fissure ①. But in specimen N090-2<sup>#</sup>, several far-field cracks were also observed underfeed the A tip of fissure ①, which indicated the formation of anti-tensile crack. Afterwards, the increased deformation led to the specimen being increased to the peak strength. When reaching the peak strength, several cracks at or near the A tip of fissure ① propagated and clustered toward the top edge of the specimen. For specimen N090-2<sup>#</sup>, another tensile crack was observed near the left middle position of fissure ② and had an angle of  $45^\circ$  with axial stress (see the crack mode at Fig. 6.15d in specimen N090-2<sup>#</sup>), which was not observed for specimen N090-1<sup>#</sup> at peak stress.

For  $\alpha_2 = 135^\circ$ , with the increase of deformation, in both the specimens there was coalescence in this ligament region. For specimen N135-1<sup>#</sup>, the crack started from the B tip of fissure ① and propagated toward the D tip of fissure ② (see the crack mode at Fig. 6.16b–c in specimen N135-1<sup>#</sup>). Whereas for specimen N135-2<sup>#</sup>, the coalescence started from the center of the ligament region and propagated toward the B tip of fissure ① and the D tip of fissure ②, respectively. It was noted that the length of tensile wing cracks initiated from the A tip of fissure ① and the D tip of fissure ② increased a lot but another two tensile wing cracks did not increase, which was likely due to the interaction of stress field in the ligament region. At the same time, the increase of axial deformation also led to the initiation and propagation of two far-field cracks.

But for  $\alpha_2 = 180^\circ$ , with increase of deformation, the lengths of tensile wing cracks emanated from the A tip of fissure ① and from the middle position of fissure ② in the downward direction all increased. For example, for specimen N180-1<sup>#</sup>, the length of tensile wing crack emanating from the A tip of fissure ① was about 21 mm at point b, the length was about 26 mm at point c, and the length reached about 40 mm at point d, but the length was only 44 mm at point e (peak strength). In general, the propagating speeds of the above two tensile wing cracks were obviously higher than that in the specimens with other fissure angles. But it should be noted that when the axial stress was up to the peak strength, the propagating speed of the above two tensile wing cracks was very small, which resulted mainly from the limitation of the specimen boundary. Similar to the specimens for  $\alpha_2 = 135^\circ$ , the specimen for  $\alpha_2 = 180^\circ$  also coalesced in the ligament region. The coalescence started from the center of the ligament region and propagated toward the B tip of fissure ① and the D tip of fissure ②, respectively. Moreover, the coalesced crack was clustered as shown at point d. At the same time, one tensile crack emanated from the C tip of fissure ② and propagated in the upward direction. One secondary tensile crack was also observed from the A tip of fissure ① and evolved toward the top edge of the specimen along the direction of axial stress.

**Stage III:** When the axial stress was loaded after peak strength, the specimen entered the final stage. At this stage, although the axial deformation still increased, the axial stress began to decrease gradually. The initiation, propagation, and coalescence of some cracks were all observed in specimens with different fissure angles.

For  $\alpha_2 = 0^\circ$ , the crack coalescence clustered in the ligament region. The tensile cracks emanated from the A tip of fissure ① and the C tip of fissure ② propagated until the boundary of the specimen with increasing deformation. In two specimens, one primary tensile crack was first initiated from the C tip of fissure ② and then one secondary tensile crack was also observed from the same position. Furthermore, in the right upper part of the specimen, one far-field crack was also observed accompanied with the ultimate failure of the specimen.

For  $\alpha_2 = 45^\circ$ , in the two numerical specimens there occurred crack coalescence between the B tip of fissure ① and anti-tensile crack from the C tip of fissure ②. Some far-field cracks were also observed in the right top region and left bottom region of the specimen. For specimen N045-2<sup>#</sup>, one anti-tensile crack emanated from the A tip of fissure ① in the downward direction, but was not observed in specimen N045-1<sup>#</sup>, which was due to the effect of nonuniform force field.

For  $\alpha_2 = 90^\circ$ , the specimen had coalescence between the B tip of fissure ① and the D tip of fissure ②, at the same time, one inclined crack was also observed close to the middle part on the right side of fissure ②. For specimen N090-2<sup>#</sup>, one anti-tensile crack was also observed from the A tip of fissure ①, which was similar to that in specimen N045-2<sup>#</sup> for  $\alpha_2 = 45^\circ$ . Some far-field cracks were observed in the right top region of the specimen. It also should be noted that the coalesced crack in the ligament region was clustered more and more with multiple micro-cracks (see point e to f in specimen for  $\alpha_2 = 90^\circ$  shown in Fig. 6.15).

For  $\alpha_2 = 135^\circ$ , because the crack coalescence in the ligament region occurs at the peak strength, we cannot observe any further coalescence in the bridge region after the peak strength. One far-field crack was found in the right top region of the specimen. Another anti-tensile crack (about inclined angle  $50^\circ$  with the horizontal direction) was observed from the C tip of fissure ②.

For  $\alpha_2 = 180^\circ$ , similar to that for  $\alpha_2 = 135^\circ$ , the crack coalescence in the ligament region occurred before the peak strength; we cannot observe any further coalescence in the bridge region after the peak strength. However, in both N180-1<sup>#</sup> and N180-2<sup>#</sup>, the cracking characteristics were different. In specimen N180-1<sup>#</sup>, one large tensile crack was observed from the C tip of fissure ② and developed along the direction of major principal stress until the top edge of the specimen. Whereas in specimen N180-2<sup>#</sup>, one large tensile crack was also observed from the C tip of fissure ②, but the propagating direction was reverse to that in specimen N180-1<sup>#</sup>, i.e., developed toward the bottom edge of the specimen. At the same time, in both specimens, far-field cracks were all clustered in the right top region of the specimen.

In general, the ultimate failure mode obtained from numerical simulation was similar to that from the experiment. Some differences between the numerical simulation and experiment (e.g., for  $\alpha_2 = 45^\circ$ ) may result from the following several reasons.

The first reason is because numerical simulation was 2-D analysis by materials composed of many circular particles, it cannot exactly simulate the 3-D experimental specimen (Lee and Jeon 2011). The second reason is possible due to the influence of the heterogeneity of tested rock material or inherent randomness of

the numerical simulation, which can be seen from the difference in the cracking modes of two specimens with the same  $\alpha_2$  as shown in Fig. 6.10. The third reason may be the representativeness of the micro-parameters used in the numerical simulation. In the past study, only one or two in four key factors (i.e., the axial stress–axial strain curve, the peak strength and elastic modulus, the ultimate failure mode, and the crack coalescence process) were used to calibrate the micro-parameters in the numerical simulation (Lee and Jeon 2011; Zhang and Wong 2012), which led to a big difference in cracking characteristics between the numerical simulation and experiment. Therefore, in the present research, the above four key factors are put forward to discriminate the rightness and reasonability of numerical simulated results, which distinctly decreases the difference between the numerical simulation and experiment.

In accordance with the above analysis of the simulated cracking process during the entire deformation, some significant features on the cracking characteristics can be summarized as follows.

- The tensile cracks in the intact specimen and fissured specimen were considerably greater in number than the shear cracks, and the differences were more obvious with the increase of axial deformation. For each numerical specimen, more crack numbers occurred after the peak strength and tensile cracks increased exponentially with the increase of axial deformation. Moreover, the increasing rate of tensile crack numbers after the peak strength was obviously higher than that before the peak strength.
- In all the specimens, for fissure ① ( $\alpha_1 = 45^\circ$ ), two tensile wing cracks (first crack) were observed from the tips A and B; whereas for fissure ②, the tensile wing cracks emanated from the fissure tips depending on fissure angle  $\alpha_2$ . For  $\alpha_2 = 0^\circ$  and  $180^\circ$ , tensile wing cracks were initiated close to a certain distance away from the tips of fissure ②. For  $\alpha_2 = 90^\circ$ , no macroscopic cracks were observed at the tips of fissure ②, which can be explained as follows: even though the specimen reached the peak stress, it was also not enough to break in the bonds at the tips of pre-existing fissures parallel to the axial stress. But for  $\alpha_2 = 45^\circ$  and  $135^\circ$ , two tensile wing cracks were, respectively, initiated from the tips C and D of fissure ②, and the initiating direction was vertical to the pre-existing fissure.
- For  $\alpha_2$  smaller than or equal to  $90^\circ$ , the crack coalescence in the ligament region occurred after the peak strength, but for  $\alpha_2$  greater than  $90^\circ$ , the crack coalescence in the ligament region occurred before the peak strength or at the peak strength, which indicated that the stress interaction between two pre-existing fissures in the specimens for  $\alpha_2$  smaller than or equal to  $90^\circ$  was stronger and more difficult to break the bonds in the ligament region than for  $\alpha_2$  greater than  $90^\circ$ .
- For  $\alpha_2$  equal to or greater than  $90^\circ$ , the specimens had coalescence between the B tip of fissure ① and the D tip of fissure ②, whereas for  $\alpha_2$  smaller than or equal to  $45^\circ$ , the specimen had coalescence between the B tip of fissure ① and another crack initiated from the C tip of fissure ②. This reason may result from the high tension stress concentration between two fissures.

- At the tips of fissure ①, with increase of axial deformation, the tensile wing cracks were difficult to propagate along the direction of major principal stress in all the tested specimens except for  $\alpha_2 = 180^\circ$ . But, the length of tensile wing crack increased with the axial stress before the peak strength in the specimen for  $\alpha_2 = 180^\circ$ . However, at the tips of fissure ②, the first crack in specimens for  $\alpha_2$  greater than  $90^\circ$  had a large propagation with increase of axial deformation. It should be noted that in specimens for  $\alpha_2 = 135^\circ$  and  $180^\circ$ , the first crack was initiated from the D tip and the middle bottom part of the fissure, respectively.
- Secondary cracks were usually observed after the first crack in all the tested specimens. Sometimes, at the same fissure tips, several secondary cracks were emanated in order. In general, the propagating speed of secondary cracks was higher than the tensile wing crack. Far-field cracks were usually accompanied with the ultimate failure process. Anti-tensile crack was usually opposite to the tensile wing crack or some secondary tensile crack.

## 6.4 Stress Field in Red Sandstone Containing Two Unparallel Fissures

In order to explore deeply the fracture coalescence mechanism in the rock material, it is significant to analyze the stress field within the rock material (Zhang and Wong 2012), which is almost impossible to be obtained from the viewpoint of experiment. Therefore, in this section, we investigate mainly the effect of fissure angle  $\alpha_2$  on the stress field in red sandstone containing two unparallel fissures under uniaxial compression.

Figure 6.19 illustrated the plots of parallel bond forces in the red sandstone specimens containing two unparallel fissures when the axial stress was applied to 15 MPa, which corresponded to the stress level of “before crack initiation” shown in Fig. 6.11). It should be noted that at this stress level, the first cracks were not initiated from the tips of two fissures in the specimen. In Fig. 6.19, the parallel bond forces are represented by discrete straight line segments. Red stands for tensile force, while black stands for compressive force. Line thickness and orientation correspond to force magnitude and direction, respectively (color figure online).

For intact specimen, it was clear that the parallel bond force was uniformly distributed before crack initiation. But, for fissured specimens, the parallel bond force was not uniformly distributed before crack initiation, and the distribution form depended on the angle of fissure ② ( $\alpha_2$ ). When  $\alpha_2$  was  $0^\circ$  or  $180^\circ$ , the fissure tips were crowded by black segments, whereas the entire perimeter of fissure ② except for the tips was almost surrounded by red segments. The distribution of parallel bond forces indicated that part of the fissure perimeter was under tension, but the fissure tip regions were under compression. Furthermore in general, the magnitude of the forces at the position near the fissure perimeter was greater than that at the position far away the fissure perimeter, which was similar to the results for the

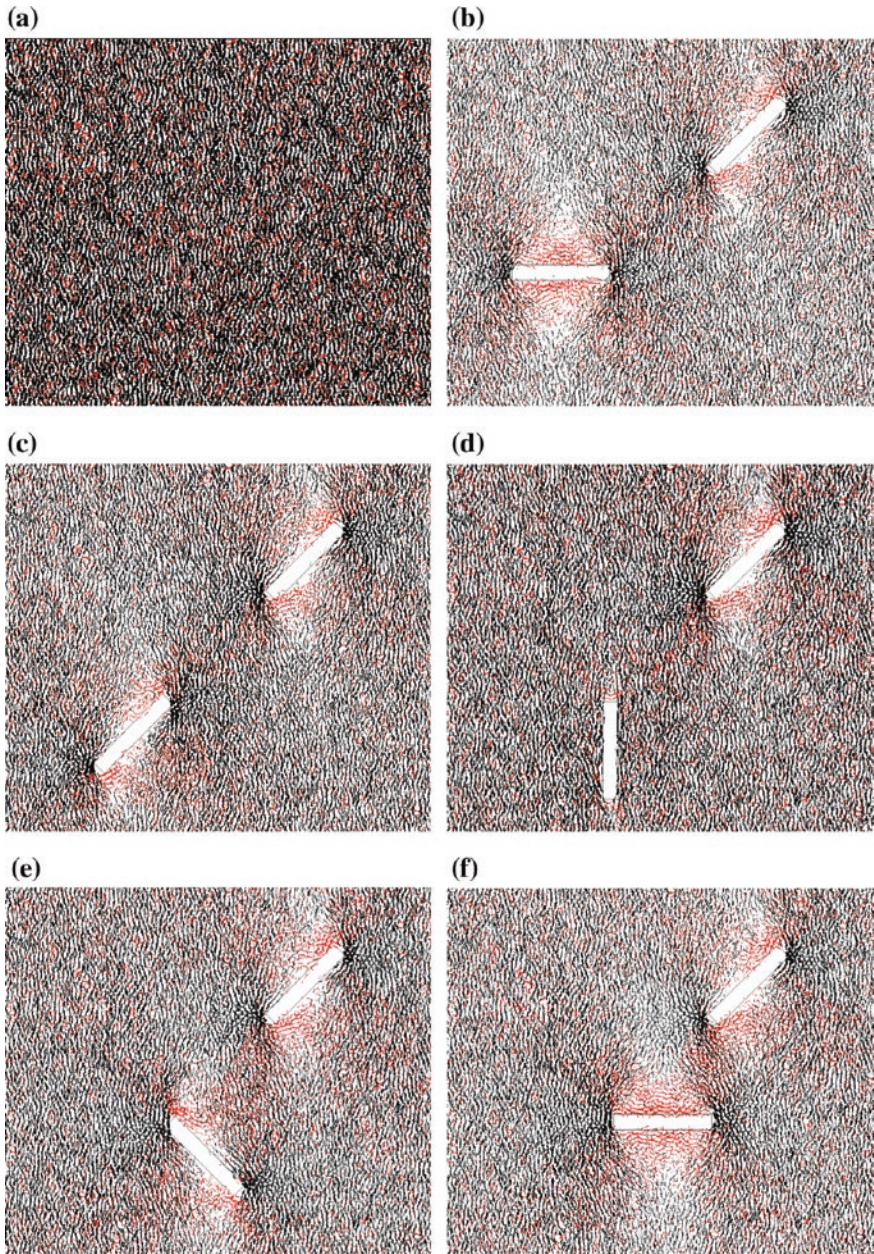


**Fig. 6.19** The distribution of parallel bond forces in the red sandstone containing two unparallel fissures just before the first crack initiation. **a** Intact specimen, **b**  $\alpha_2 = 0^\circ$ , **c**  $\alpha_2 = 45^\circ$ , **d**  $\alpha_2 = 90^\circ$ , **e**  $\alpha_2 = 135^\circ$ , **f**  $\alpha_2 = 180^\circ$  (with kind permission of Elsevier Publisher)

specimens containing a single fissure (Zhang and Wong 2012). When  $\alpha_2$  was  $45^\circ$  or  $135^\circ$ , compared to the distribution of fore field for  $\alpha_2 = 0^\circ$  or  $180^\circ$ , the extent of the red segments around the fissure perimeter decreased, while that of the black segments increased. The previous investigation for the rock-like material containing a single fissure also testified that when  $\alpha$  increased from  $0^\circ$  to  $75^\circ$ , the regions of black segments expanded gradually from the left tip toward the right tip along the top fissure surface, and from the right tip toward the left tip along the bottom fissure surface (Zhang and Wong 2012), which can also be seen from the comparison between Fig. 6.19b ( $\alpha_2 = 0^\circ$ ) and Fig. 6.19c ( $\alpha_2 = 45^\circ$ ). Therefore, when  $\alpha_2$  was  $45^\circ$  or  $135^\circ$ , only near the C tip along the top fissure surface and the D tip along the bottom fissure surface, the regions of red segments were observed, which indicates that there was an obvious tension stress concentration near the tips of fissure ②. However, when  $\alpha_2$  was  $90^\circ$  the entire perimeter of fissure ② except for the tips was almost surrounded by black segments, which meant the regions of the fissure perimeter were under compression; moreover, the direction of compression force was almost parallel to the major principal stress. But it should be noted that near the tips of fissure ②, the regions of red segments for  $\alpha_2 = 90^\circ$  were very less compared with that for  $\alpha_2 = 45^\circ$  or  $135^\circ$ , which indicated that it was difficult to initiate the tensile cracks from the tips. The regions of tensile stress concentration in the red sandstone specimens containing two unparallel fissures before the first crack initiation (Fig. 6.19) also revealed that the initiation of tensile wing cracks (first crack) in Figs. 6.12, 6.12, 6.13, 6.14, 6.15, 6.16, and 6.17 was reasonable.

Figure 6.20 illustrates the local magnification for the distribution of parallel bond forces in the ligament region of fissured specimens. In accordance with Fig. 6.20, we can make the following analysis. For  $\alpha_2 = 0^\circ$  and  $45^\circ$ , the extent of black color at the tips B and C were more obvious than that at the other positions of ligament regions, which indicated that the compressive force at the tips B and C was greater than that at the other positions of ligament regions. Compared with black segments, only less red segments were observed in the ligament regions, which meant that the tensile crack between B and C tip was difficult to form. Moreover, the orientations of compressive forces in the ligament region were similarly parallel to the major principal stress, but the orientations of tensile forces in the ligament region (see the red segments) were disordered. For  $\alpha_2 = 90^\circ$ , dense black color was observed at the B tip, while the dense black color was not observed at the C tip. Except for the above point, the distribution of forces at the other positions of ligament regions was similar to that for  $\alpha_2 = 0^\circ$  and  $45^\circ$ . However, for  $\alpha_2 = 135^\circ$  and  $180^\circ$  the red and black segments in the regions between the B and D tip (see the elliptical region shown in Fig. 6.20) were obviously more than those in the regions between the B and C tips, which also indicated that more tensile stress concentration in the regions between the B and D tips were easier to emanate crack coalescence. Generally, the distribution of parallel bond forces in the ligament region of fissured specimens (Fig. 6.20) also revealed that the coalescence of cracks in the ligament region was reasonable.

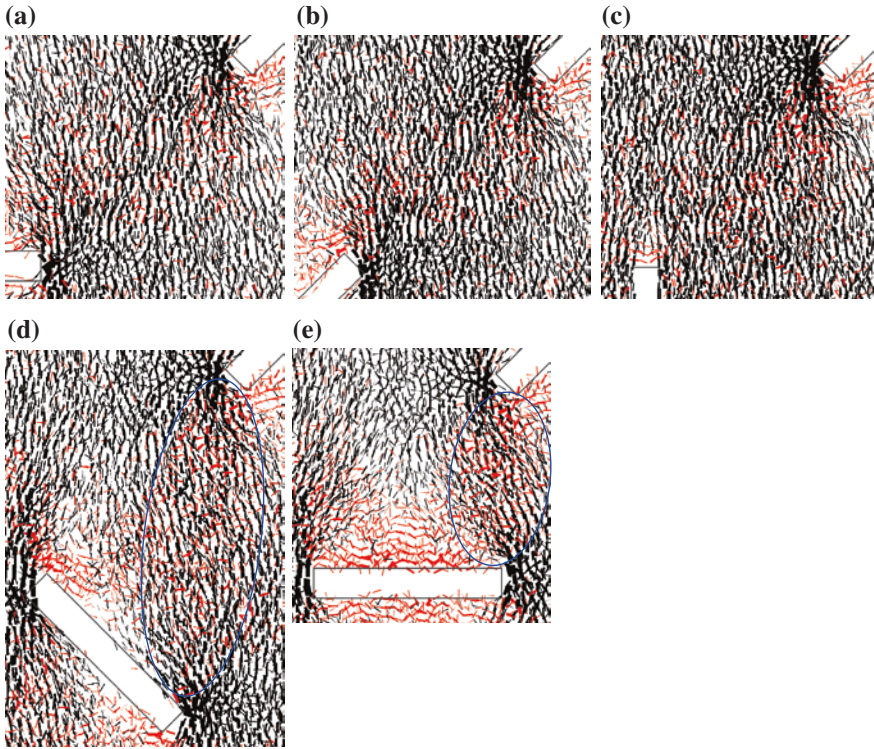


**Fig. 6.20** Local magnification for distribution of parallel bond forces in the red sandstone containing two unparallel fissures just before the first crack initiation. **a**  $\alpha_2 = 0^\circ$ , **b**  $\alpha_2 = 45^\circ$ , **c**  $\alpha_2 = 90^\circ$ , **d**  $\alpha_2 = 135^\circ$ , **e**  $\alpha_2 = 180^\circ$  (with kind permission of Elsevier Publisher)

Figure 6.21 shows the plots of parallel bond forces in the intact specimen obtained by PFC<sup>2D</sup>. In Fig. 6.21, the five plots correspond to the crack modes at point a (crack initiation stress), c (peak strength) to g (ultimate failure) in specimen NRS-1<sup>#</sup>. It is clear that the parallel bond forces in the specimens are not uniformly distributed after the specimen reaches the peak strength (see point C–F in Fig. 6.21). When the specimen produces some macroscopic cracks, the density of forces close to the macroscopic cracks decrease and some blank regions come into being, which indicates that the stress concentration is released and the parallel bonds are broken in tension.

But when there are two unparallel fissures in the specimens, in the deformation process in response to the axial stress, the evolution characteristics of stress field distribution at the tips of pre-existing fissures are different from that for the intact specimen. Two examples for  $\alpha_2 = 0^\circ$  and  $135^\circ$  are illustrated in Figs. 6.22 and 6.23, respectively.

For  $\alpha_2 = 0^\circ$ , as shown in Fig. 6.19b, the axial stress level was 15 MPa (before crack initiation, see Fig. 6.11b), the dense red color was crowded around the top and bottom sides of pre-existing fissure ②, indicating a region of tensile stress

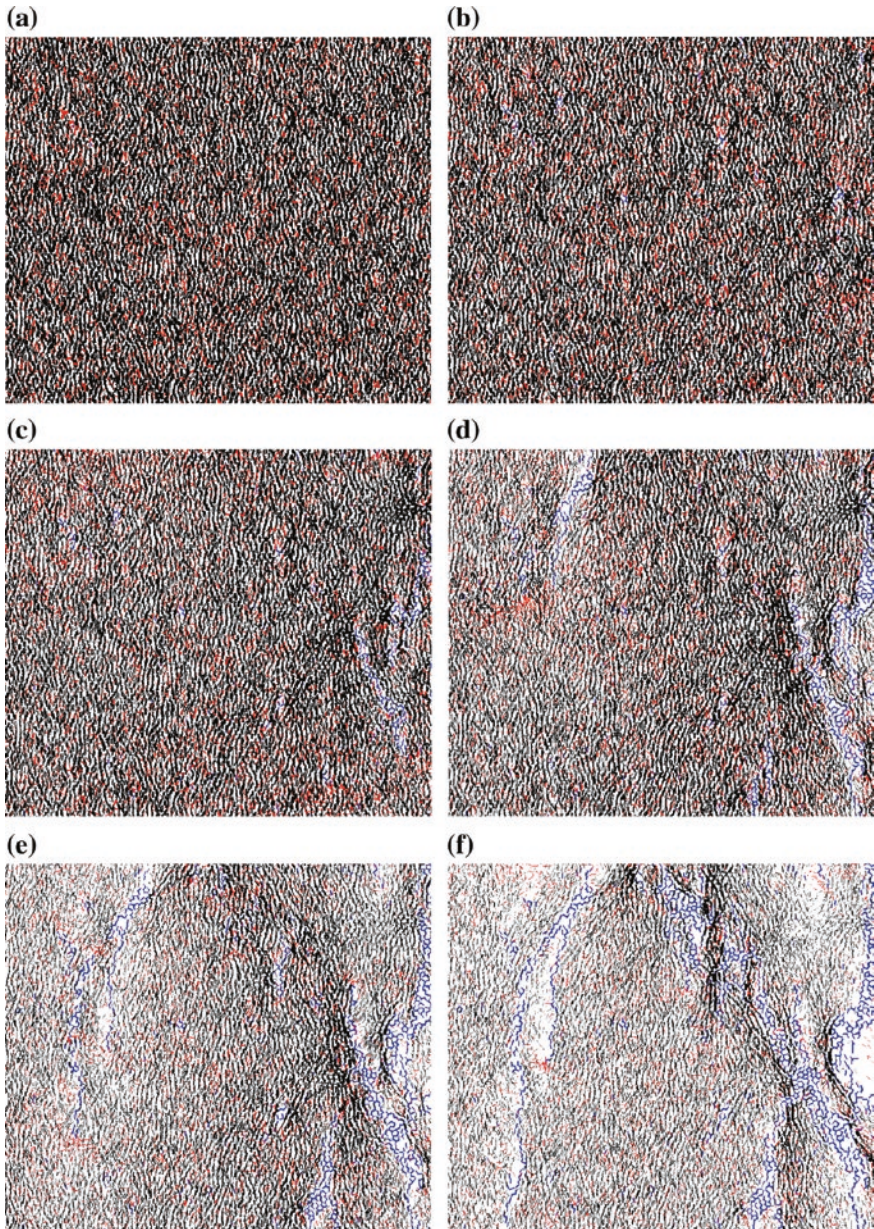


**Fig. 6.21** Force vector plots in the deformation process of intact specimen. *Blue color* segments stand for micro-cracks initiated in response to external loading (color figure online). The positions of these points in this figure correspond to those denoted in Fig. 6.11a. **a** Point a (37.13 MPa before peak strength), **b** point c (52.41 MPa at peak strength), **c** point d (49.77 MPa after peak strength), **d** point e (44.52 MPa after peak strength), **e** point f (36.70 MPa after peak strength), **f** point g (20.84 MPa after peak strength) (with kind permission of Elsevier Publisher)

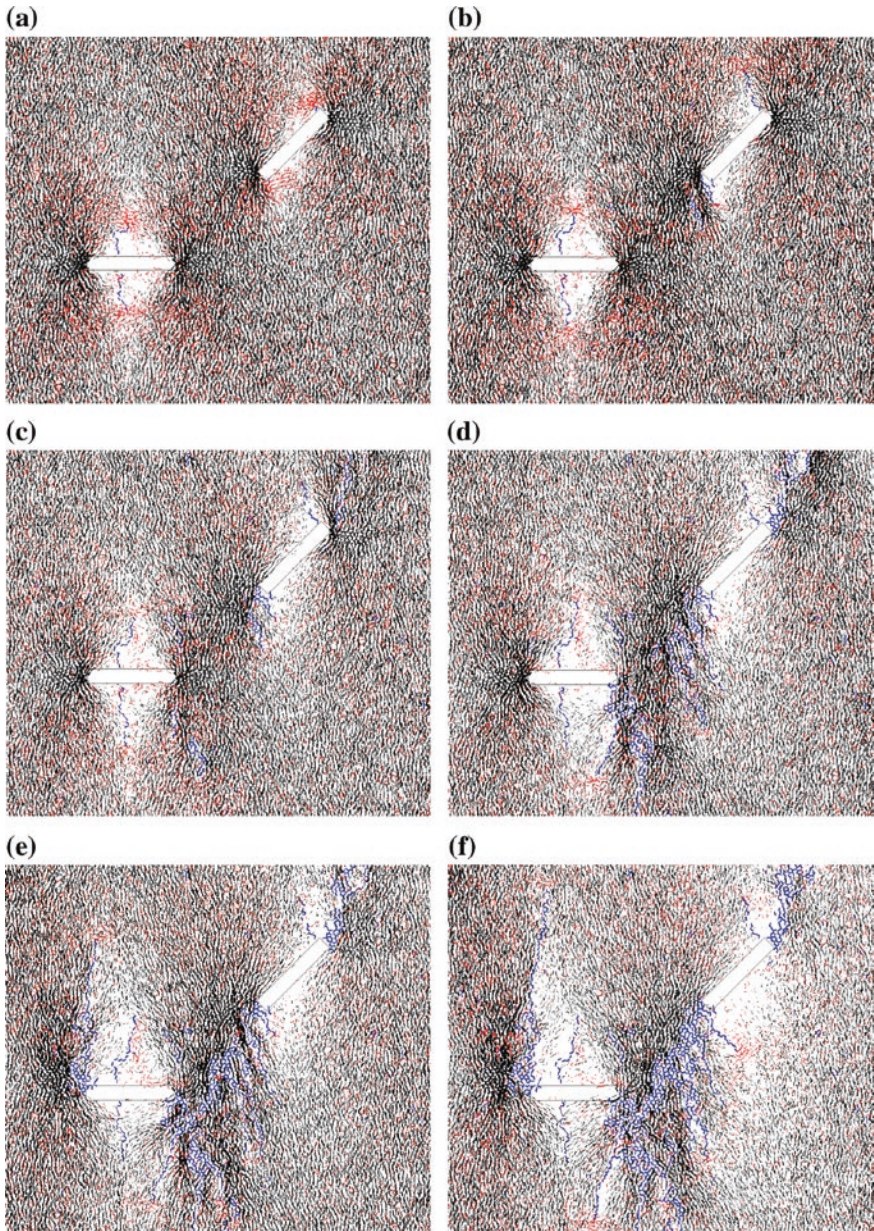


**Fig. 6.22** Force vector plots in the deformation process of fissured specimen for  $\alpha_2 = 0^\circ$ . Blue color segments stand for micro-cracks initiated in response to external loading (color figure online). The positions of these points in this figure correspond to those denoted in Fig. 6.11b. **a** Point a (25.7 MPa before peak strength), **b** point b (33.44 MPa before peak strength), **c** point c (37.16 MPa at peak strength), **d** point d (35.3 MPa after peak strength), **e** point e (31.57 MPa after peak strength), **f** point f (26.02 MPa after peak strength) (with kind permission of Elsevier Publisher)

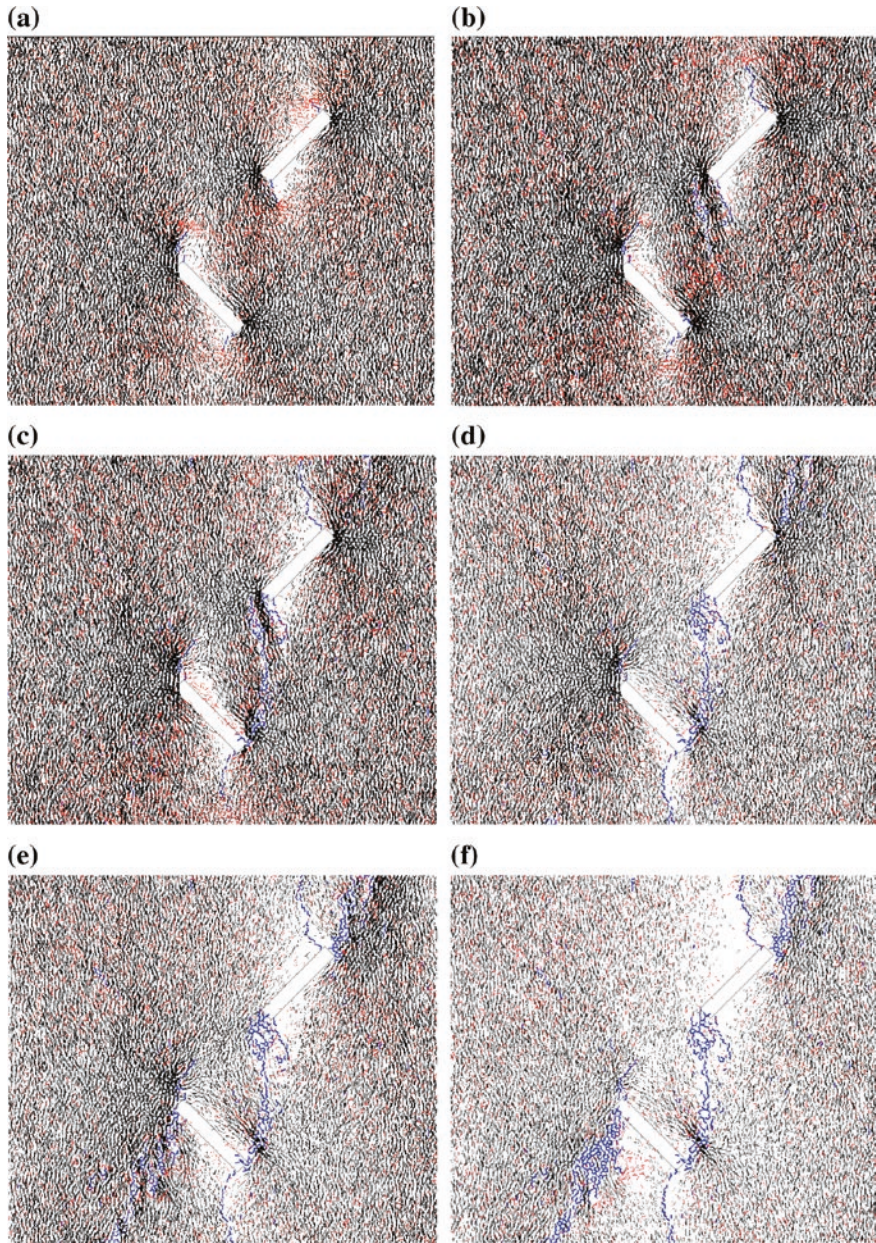


**Fig. 6.23** Force vector plots in the deformation process of fissured specimen for  $\alpha_2 = 135^\circ$ . *Blue color* segments stand for micro-cracks initiated in response to external loading (color figure online). The positions of these points in this figure correspond to those denoted in Fig. 6.11e. **a** Point a (24.92 MPa before peak strength), **b** Point b (36.01 MPa before peak strength), **c** Point c (36.97 MPa at peak strength), **d** Point d (36.41 MPa after peak strength), **e** Point e (34.69 MPa after peak strength), **f** Point f (25.51 MPa after peak strength) (with kind permission of Elsevier Publisher)

concentration. As the axial stress was increased to 25.7 MPa (Fig. 6.22a), two tensile cracks were initiated close to one-third of the D tip, from the top and bottom side of fissure ②. It should be noted that the red color around the top and bottom sides of fissure ② decreased a lot compared with that in Fig. 6.19b, which indicated that the tensile stress concentration in this region was released. But at the tips of newly developed cracks, the red color increased a lot, which meant that the newly developed crack tips would serve as the new tensile stress concentration region. However, the extent of the dense red color near the tips of fissure ① had no observable change compared with that in Fig. 6.19b, which resulted from the macro-tensile cracks at the tips of fissure ① not formed. When the axial stress was loaded to 33.44 MPa (Fig. 6.22b), the dense red color at the newly developed crack tips of fissure ② shifted outwards around the newly initiated micro-cracks, which indicated that new tensile stress concentration region would come into being at the newly developed crack tips. It should be noted that the propagation of two tensile cracks initiated from the top and bottom side of fissure ② was nonlinear, but the tensile stress concentration at the tips of fissure ① was released. The newly developed crack tips served as new tensile stress concentration region, which could be inferred from the increased red color segments at the newly developed crack tips of fissure ①. The further increase of axial deformation led to the specimen being loaded to the peak strength (point c, Fig. 6.22c). The tensile stress concentration was released at the A tip of fissure ① due to emanation of secondary crack, and the corresponding red color segments at this tip also decreased a lot. Two tensile cracks initiated from the top and bottom side of fissure ② propagated forward a little and the red color segments at the newly developed crack tips became less compared with Fig. 6.22b. At this region far away from the C tip, although some micro-cracks were observed, the red color segments nearby the C tip had no observable change compared with Fig. 6.22b, as the macro-cracks were not formed. After the peak strength, with increase of axial deformation, the red segments in the ligament region decreased gradually, and this indicated that the tensile stress concentration in this region was released due to crack coalescence from Fig. 6.22c–f. After crack coalescence, the density of black segments in the specimen decreased gradually with increase of deformation, which resulted from the adjustment of compressive stress field in this region. Furthermore, it should be noted that if the macro-tensile cracks stopped to propagate, the tensile stress concentration at the newly developed crack tips would also disappear, which could be obtained in accordance with the evolution process of tensile wing cracks from the top and bottom sides of fissure ② (Fig. 6.22c–f).

Figure 6.23 illustrates the evolution characteristics of stress field distribution at the pre-existing fissure tips in the specimens for  $\alpha_2 = 135^\circ$ . Despite the difference in crack coalescence process for  $\alpha_2 = 0^\circ$  and  $135^\circ$ , the evolution of the stress field distribution for  $\alpha_2 = 135^\circ$  is similar to that for  $\alpha_2 = 0^\circ$ , therefore, we do not make a detailed analysis on the evolution of stress field distribution around two pre-existing fissures during the cracking processes for  $\alpha_2 = 135^\circ$ . However, some

significant features for the evolution characteristics of stress field in the red sandstone containing two unparallel fissures can be summarized as follows.

- Once the tensile wing cracks (the first crack) were emanated from the fissure tips or close to the fissure tips, the tensile stress concentration in this region would be released. It should be noted that if the macro-tensile cracks at the fissure tips or close to the fissure tips were not formed, the extent of the dense red color near the fissure tips would have no observable change.
- With the propagation of the tensile wing crack, the tensile stress concentration region would transfer to the newly developed crack tips. But if the macro-tensile cracks stopped to propagate, the tensile stress concentration at the newly developed crack tips would also disappear.
- The red segments in the ligament region decreased with increasing axial deformation, which indicated that the tensile stress concentration in this region was released due to crack coalescence compared with Fig. 6.23a–c. After crack coalescence, the density of black segments in the ligament region decreased gradually with increase of deformation, which resulted from the adjustment of compressive stress field in this region.
- The emanation of secondary tensile and anti-tensile macro-cracks led to decrease of red and black color segments at the fissure tips (see Fig. 6.23d–f), which indicated the release of stress concentration. However, it should be noted that if micro-tensile cracks were not connected into the macro-tensile cracks, the dense red and black color segments would not have obvious change by comparing Fig. 6.23e, f.

## 6.5 Conclusions

On the basis of the previous experimental results for rectangular prismatic specimens ( $80 \times 160 \times 30$  mm) of red sandstone (Yang et al. 2013), a systematic numerical simulation by particle flow code (PFC<sup>2D</sup>) was performed to analyze deeply the strength, deformation, and fracture coalescence behavior of red sandstone containing two unparallel fissures under uniaxial compression. Through the simulated results, the following conclusions can be summarized.

1. In accordance with the experimental results of intact red sandstone, the numerical micro-parameters simulated for red sandstone were first confirmed, and then were further checked with the experimental results for red sandstone containing two unparallel fissures under uniaxial compression. Four key factors (i.e., the axial stress–axial strain curve, the peak strength and elastic modulus, the ultimate failure mode, and the crack coalescence process) were put forward to discriminate the rightness and reasonability of numerical simulated results. By comparing quantitatively the simulated results with the experimental

results, we found that the numerical simulated results (including the strength, deformability, and failure mode) were in good agreement with the experimental results.

2. Numerical simulated results showed that the peak strength and elastic modulus of red sandstone containing two unparallel fissures were increased at fissure angle  $\alpha_2 = 90^\circ$ , before decreasing up to our maximum fissure angle of  $180^\circ$ , which were similarly equal to the experiment. The ratio of lateral stiffness of intact red sandstone is only 0.123, which was distinctly lower than that of red sandstone containing two unparallel fissures (0.152 ~ 0.198). With the increase of fissure angle  $\alpha_2$ , the ratio of lateral stiffness of red sandstone containing two unparallel fissures first decreased and then increased, and had the lowest value at  $\alpha_2 = 90^\circ$ . In red sandstone, the tensile cracks in the intact specimen and fissured specimen were considerably greater in number than the shear cracks, and the differences became even more obvious with increase of axial deformation.
3. Through numerical simulation, we made a detailed summary for the crack initiation, propagation, and coalescence behavior in the entire deformation process of red sandstone, which was found to be dependent on fissure angle  $\alpha_2$ . The relationship between numerical axial stress–axial strain curve and the crack coalescence process, crack numbers evolution were constructed. In all the tested specimens, most of the cracks were observed after the peak strength. With increase of axial deformation, the tensile cracks increased exponentially. Moreover, the increasing rate of tensile cracks after the peak strength was obviously higher than that before the peak strength. Finally, in order to reveal in-depth the fracture coalescence mechanism of brittle red sandstone, the stress field in the specimens containing two unparallel fissures under uniaxial compression was also obtained and evaluated.

In this chapter, we only simulate the fracture coalescence behavior at laboratory scale, but due to obvious scale effect of rock material, the simulated results at laboratory scale are difficult for direct prediction of the strength of a real rock pillar (i.e., width/height = 10.0/20.0 m) at engineering scale, therefore in the future, the scale effect of rock containing intermittent fissures will be strengthened (Camones et al. 2013). At the same time, it should be pointed out that engineering rock mass is usually located in a triaxial stress state. Moreover, with the increase of rock mass engineering (i.e., rock slope engineering, underground rock engineering) height and depth, it will be more significant to investigate the crack coalescence behavior of fissured rock material under higher geo-stress from the experiment or numerical simulation. Therefore, in the eighth and ninth chapters, we will also strengthen the influence of confining pressure on the strength, deformability, and fracture coalescence behavior of rock material containing intermittent fissures in order to understand deeply the unstable failure mechanism of deep joint rock mass.

## References

- Camones LAM, Vargas Jr EDA, de Figueiredo RP, Velloso RQ (2013) Application of the discrete element method for modeling of rock crack propagation and coalescence in the step-path failure mechanism. *Eng Geol* 153:80–94
- Cho N, Martin CD, Sego DC (2007) A clumped particle model for rock. *Int J Rock Mech Min Sci* 44(7):997–1010
- Debecker B, Vervoort A (2013) Two-dimensional discrete element simulations of the fracture behavior of slate. *Int J Rock Mech Min Sci* 61:161–170
- Eberhardt E, Stead D, Stimpson B, Read RS (1998) Identifying crack initiation and propagation thresholds in brittle rock. *Can Geotech J* 35(2):222–233
- Lee H, Jeon S (2011) An experimental and numerical study of fracture coalescence in pre-cracked specimens under uniaxial compression. *Int J Solids Struct* 48(6):979–999
- Potyondy DO, Cundall PA (2004) A bonded-particle model for rock. *Int J Rock Mech Min Sci* 41(8):1329–1364
- Yang SQ, Jing HW, Wang SY (2012) Experimental investigation on the strength, deformability, failure behavior and acoustic emission locations of red sandstone under triaxial compression. *Rock Mech Rock Eng* 45(4):583–606
- Yang SQ, Liu XR, Jing HW (2013) Experimental investigation on fracture coalescence behavior of red sandstone containing two unparallel fissures under uniaxial compression. *Int J Rock Mech Min Sci* 63:82–92
- Yang SQ, Huang YH, Jing HW, Liu XR (2014) Discrete element modeling on fracture coalescence behavior of red sandstone containing two unparallel fissures under uniaxial compression. *Eng Geol* 178:28–48
- Zhang XP, Wong LNY (2012) Cracking processes in rock-like material containing a single flaw under uniaxial compression: a numerical study based on parallel bonded-particle model approach. *Rock Mech Rock Eng* 45:711–737
- Zhang XP, Wong LNY (2013) Loading rate effects on cracking behavior of flaw-contained specimens under uniaxial compression. *Int J Fract* 180:93–110

## Chapter 7

# Fracture Mechanical Behavior of Red Sandstone Containing a Single Fissure and Two Parallel Fissures After Exposure to Different High-Temperature Treatments

It is well known to us that the stability and safety of deep underground mining excavations and nuclear waste depositories rely on accurate knowledge of the physical and mechanical properties of representative rocks under the action of high temperature (Zhang et al. 2012). Many experimental investigations have demonstrated that high temperature significantly affects the physical properties of sandstones (Heuze 1983; Glover et al. 1995; Chopra 1997; Zhang et al. 2001; Tang et al. 2011; Zhao et al. 2012). Analytical and numerical modeling of thermomechanical processes in sandstones have shown that variations in rock physical properties (such as bulk density, porosity, compressional wave velocity, etc.) should not be expected between 100 and 200 °C, but become more significant above 400 or 500 °C (Tian et al. 2012). Indeed, thermal cracking experiments have shown that the greatest changes are likely to be achieved once the temperature has exceeded 573 °C, i.e., the  $\alpha/\beta$  transition of quartz (Glover et al. 1995). Li et al. (2011) investigated the change in the longitudinal wave velocity and mechanical behavior of sandstone after different high-temperature treatments using triaxial unloading experiments. Heap et al. (2009) studied the influence of temperature on the time-dependent behavior of sandstone. They found that rate of stress corrosion cracking was greatly increased at 75 °C, resulting in a faster creep strain rate and a shorter time-to-failure. Wu et al. (2000) and Ying et al. (2012) carried out static and dynamic experimental studies on thermally stressed sandstone specimens. They investigated the influence of high temperature on the failure mode, peak strength, and peak strain.

To date, no laboratory experiments have been performed on pre-fissured sandstone specimens that have been exposed to high temperatures. Therefore, the influence of temperature on fracture coalescence of sandstones containing pre-existing fissures remains unknown. We therefore performed a systematic study analyzing the strength, deformation behavior, crack initiation, and crack coalescence stress of red sandstone containing either a single fissure or two parallel fissures after exposure to different high temperatures (Yang et al. 2014). In this study, we investigated the fracture coalescence process using both photographic and AE monitoring techniques.

## 7.1 Rock Material and Testing Procedure

### 7.1.1 *The Experimental Material and Heating Procedure*

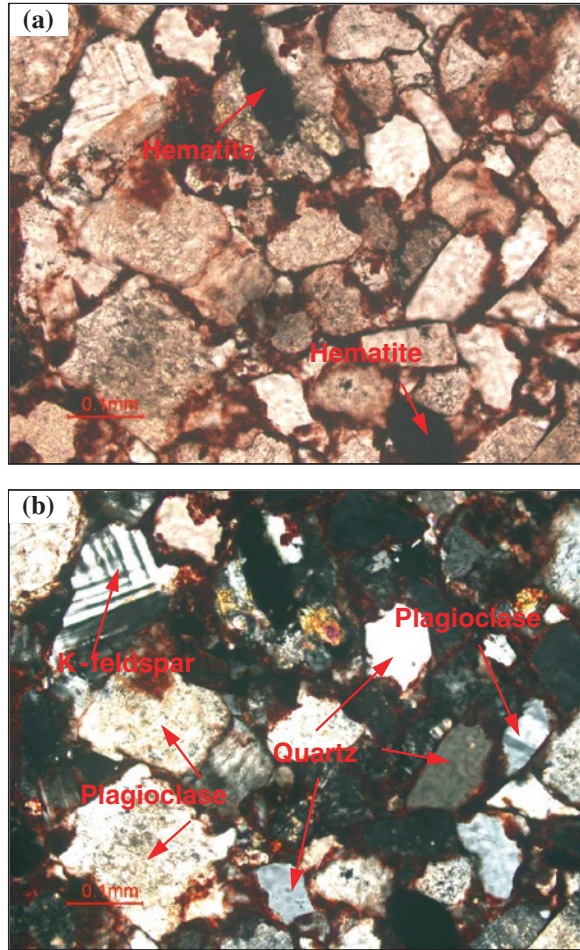
All of the experiments presented in this chapter were performed on red sandstone from Linyi City, Shandong province, China. The intact (i.e., no heating or deformation) red sandstone is a medium-grained heterogeneous sandstone with average density of  $2400 \text{ kg/m}^3$ . In this research, the high-temperature treatments were administered to the specimens using a high temperature furnace (model SGM.M10) in the following procedure. First, the specimens were heated to their target temperature (300, 600, or 900 °C) at a rate of 20 °C/min. They were then left at their target temperature for 2 h. Finally, the specimens were cooled naturally to room temperature (25 °C) in a confined space.

Thin section observations (Fig. 7.1) have revealed that the tested red sandstone consists of mainly plagioclase, K-feldspar, quartz detrital grains, volcanic rock fragments, and smectite, and very minor quantities of hematite and zeolite. Moreover, with the increase of temperature, the mineral composition did not change, but microscopic structures greatly changed, which can be testified by observation under both binocular microscope (Fig. 7.2) and a scanning electron microscope (SEM, Fig. 7.3) of red sandstone after different high-temperature treatments. From Figs. 7.2 and 7.3, it is clear that at room temperature (25 °C), red sandstone specimens show more texture flaws (including pores and original cracks in this research). When the temperature is increased from 25 to 300 °C, specimens show less surface area fraction of pores and original cracks, which results mainly from the thermal expansion of mineral grains and the resultant closure of some texture flaws. However, after 300 °C high-temperature exposure and above, some new microscopic cracks are generated in the specimen. Here, the number of newly formed microscopic cracks in the specimen after 600 °C high-temperature exposure is less than that after 900 °C high-temperature exposure. Moreover, the width of cracks at 900 °C is greater than that at 600 °C, which indicates that the 900 °C high-temperature treatment causes more serious damage to the tested red sandstone than the 600 °C high-temperature treatment.

### 7.1.2 *Specimen Preparation and Fissure Geometry*

Rectangular prismatic specimens of red sandstone, with dimensions of  $80 \times 160 \times 30 \text{ mm}$ , were prepared from the same set of blocks. All specimens had a height-to-width ratio of 2.0, to ensure a uniform stress state within the central part of the specimens. The geometries of the specimens containing a single fissure, and those containing two parallel fissures, are shown in detail in Fig. 7.4. The fissures were cut using a high-pressure water jet cutting device, and were approximately 2.0 mm wide.

**Fig. 7.1** Thin section observation of red sandstone before heat treatment. **a** plane polarization photo of microstructure, and **b** crossed polarization photo of microstructure (with kind permission of Elsevier Publisher)



In order to accurately investigate the effect of high temperatures on the strength, deformability, and fracture coalescence behavior of red sandstone containing a single fissure and two parallel fissures under uniaxial compression, the same fissure geometries were used from specimen to specimen. In Fig. 7.4,  $2a$  is fissure length,  $2b$  is ligament length (i.e., the distance between two inner fissure tips),  $\alpha$  is fissure angle (i.e., the angle of fissure with the horizontal direction), and  $\beta$  is ligament angle (i.e., the angle of the connecting line of two inner fissure tips with the horizontal direction). For the single fissure specimens,  $2a$  and  $\alpha$  were fixed at 16 mm and  $45^\circ$ , respectively. Whereas for the two parallel fissure specimens,  $2a$  and  $2b$  were fixed at 16 and 22 mm, respectively, and  $\alpha$  and  $\beta$  were fixed at  $45^\circ$  and  $90^\circ$ , respectively. A full description of the specimens used in this chapter is given in Table 7.1.

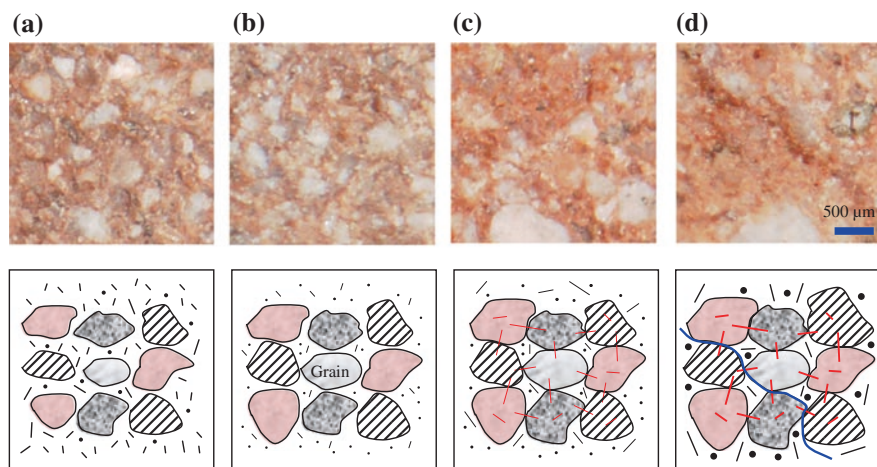


**Fig. 7.2** A binocular microscope observation of red sandstone after different high-temperature treatments. In the figure, the *black lines* represent the original fissures, and the *circle dots* represent the pores. The *red lines* represent newly formed microscopic cracks due to thermal treatment, whereas the *blue line* represents the macroscopic crack due to the connection of many microscopic cracks. **a**  $F = 25\text{ }^{\circ}\text{C}$ . **b**  $F = 300\text{ }^{\circ}\text{C}$ . **c**  $F = 600\text{ }^{\circ}\text{C}$ . **d**  $F = 900\text{ }^{\circ}\text{C}$  (with kind permission of Elsevier Publisher)

### 7.1.3 Testing Procedure and AE Monitoring

All of the uniaxial compression experiments in this chapter were conducted using a rock mechanics servo-controlled testing system. Tests were conducted under displacement-controlled conditions, with a strain rate of  $1.059 \times 10^{-5}/\text{s}$  until specimen failure. The load imposed on the specimen and the displacement of the specimen were recorded simultaneously and continuously. Two rigid steel blocks, with dimensions of  $33 \times 83 \times 15\text{ mm}$ , were placed between the loading frame and the rock specimen.

During experimentation, in order to investigate the fracture coalescence characteristics of the deforming specimens, the output of AEs was continuously monitored. AEs are transient elastic waves generated by the rapid release of energy within a material, such as the strain energy released during micro-crack propagation. Monitoring AE during deformation has become an increasingly important diagnostic tool in material science which has provided a wealth of information regarding the failure process in brittle materials (Fortin et al. 2006; Lockner et al. 1991; Benson et al. 2007; Brantut et al. 2011) and can be used in failure forecasting modeling (Bell et al. 2011a, b). AE counts were recorded by a DS2 full-information AE measuring system via two AE sensors that were attached to the back face of the specimen using hot bar as a coupling agent and fixed in place using tape, a similar method to that of Li et al. (2005). The coordinates of the two AE sensors were 40, 50, and 40, 110 mm, respectively. At the same time, a

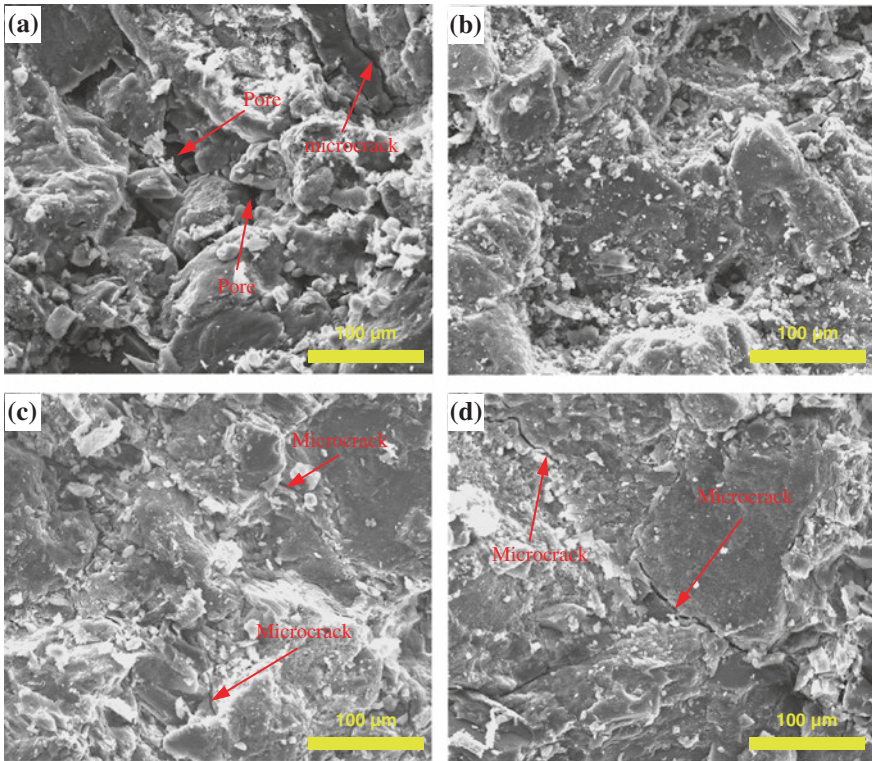


**Fig. 7.3** SEM observation of red sandstone after different high-temperature treatments. **a**  $F = 25$  °C. **b**  $F = 300$  °C. **c**  $F = 600$  °C. **d**  $F = 900$  °C (with kind permission of Elsevier Publisher)

photographic monitoring technique was used to capture images of the propagating cracks and the failure of the specimen.

## 7.2 Strength and Deformation Behavior

In the previous study (Yang et al. 2013), the experimental results demonstrated that the tested red sandstone deforms in a brittle manner (axial stress drops abruptly after the peak stress). On the basis of these experiments, we can confirm that the peak strength ( $\sigma_c$ ) and peak strain at failure ( $\varepsilon_{1c}$ ) of intact red sandstone specimens were 52.59 MPa and  $5.059 \times 10^{-3}$  at room temperature, respectively. Moreover, it can be seen that the failure mode of intact red sandstone specimens was axial splitting, which was also testified by the general absence of AE prior to the peak stress (Yang et al. 2013). It is clear that AEs of intact red sandstone specimens occur at moderate stresses and increase exponentially as the load approaches the peak strength.

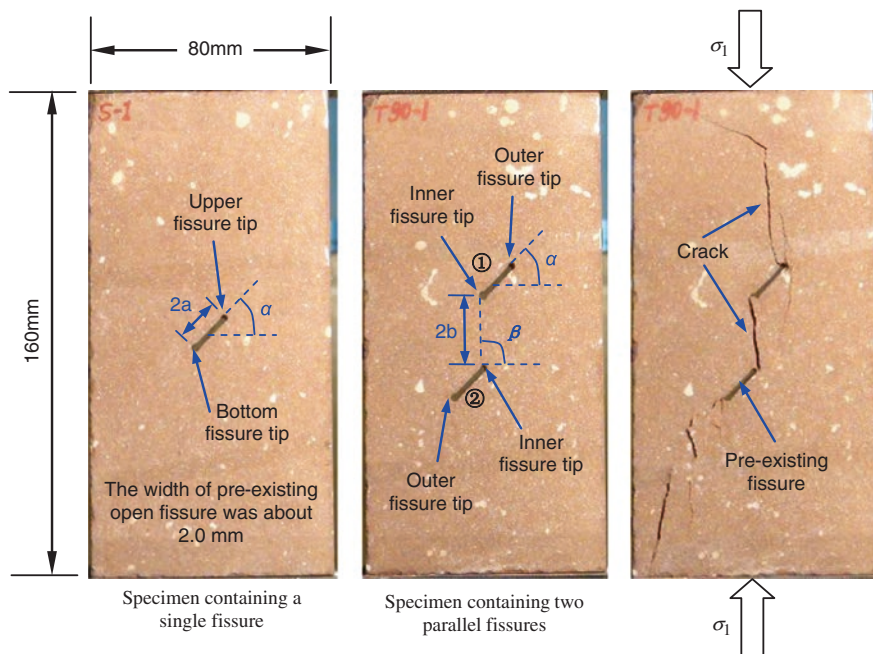


**Fig. 7.4** Geometry of the fissures in the red sandstone specimens, where  $\alpha$  is fissure angle,  $2a$  is fissure length,  $2b$  is ligament length,  $\beta$  is ligament angle (with kind permission of Elsevier Publisher)

**Table 7.1** Red sandstone specimens containing a single or two parallel fissures after different high-temperature treatments

Specimen	W/mm	H/mm	T/mm	$\alpha/^\circ$	$\beta/^\circ$	$2a/mm$	$2b/mm$	T/ $^\circ C$	Note
S-1 <sup>#</sup>	80.5	160.4	29.9	45		16		25	Specimen containing a single fissure
S-2 <sup>#</sup>	80.6	160.5	28.1	45		16		25	
S-4 <sup>#</sup>	80.7	160.3	29.7	45		16		300	
S-5 <sup>#</sup>	81.3	161.0	29.9	45		16		600	
S-6 <sup>#</sup>	81.2	161.6	29.9	45		16		600	
S-7 <sup>#</sup>	81.7	162.1	30.6	45		16		900	
S-8 <sup>#</sup>	81.4	162.0	30.2	45		16		900	
T90-1 <sup>#</sup>	80.6	160.5	29.5	45	90	16	22	25	
T90-3 <sup>#</sup>	80.6	160.7	29.7	45	90	16	22	300	
T90-4 <sup>#</sup>	80.7	161.6	29.7	45	90	16	22	300	
T90-5 <sup>#</sup>	81.4	161.0	29.9	45	90	16	22	600	
T90-6 <sup>#</sup>	81.3	161.0	30.0	45	90	16	22	600	
T90-7 <sup>#</sup>	82.1	161.1	30.5	45	90	16	22	600	
T90-8 <sup>#</sup>	82.1	161.1	30.5	45	90	16	22	900	

Note W Width; H Height; T Thickness; F Temperature

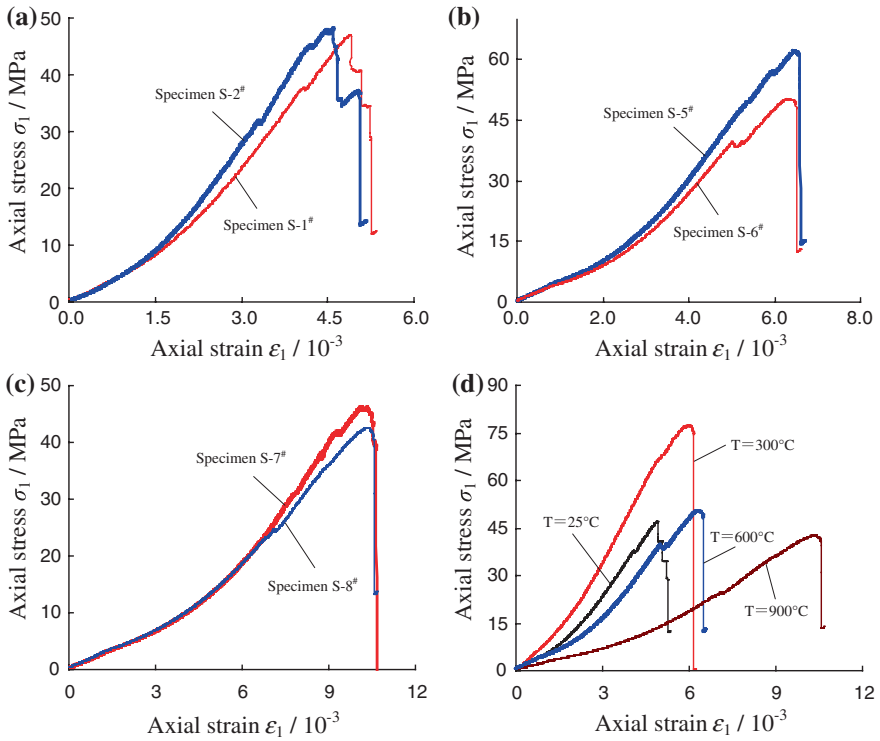


**Fig. 7.5** Axial stress–strain curves for red sandstone specimens containing a single fissure after different thermal treatments. **a**  $F = 25\text{ }^{\circ}\text{C}$ . **b**  $F = 300\text{ }^{\circ}\text{C}$ . **c**  $F = 600\text{ }^{\circ}\text{C}$ . **d** Different thermal treatment (with kind permission of Elsevier Publisher)

Figure 7.5 shows the axial stress-axial strain curves for red sandstone specimens containing a single fissure after different thermal treatments (the results of these experiments are listed in Table 7.2). To obtain the best possible results, we performed two experiments at each thermal treatment temperature. Figure 7.5 and Table 7.2 clearly show that temperature influences the strength and the deformation behavior of red sandstone containing a single fissure. It can also be seen that the effect of specimen variability is greater for the experiments performed on the heat-treated specimens (when compared with the experiments performed at room temperature). The average  $\sigma_c$  for the non-heat treated specimens containing a single fissure was 47.62 MPa, less than the 52.59 MPa for intact specimens (Yang et al. 2013).

Based on the experimental data for red sandstone specimens containing a single fissure listed in Table 7.2, Fig. 7.6 shows the evolution of peak stress and peak strain with increasing heat-treatment temperature for the specimens containing a single fissure. Figure 7.6a shows that, at a heat-treatment temperature of 300 °C, the specimen was much stronger (the  $\sigma_c$  was increased to 77.40 MPa). However, the  $\sigma_c$  decreased to 56.28 MPa (still higher than that for room temperature) at

**Table 7.2** Mechanical parameters of red sandstone specimens containing a single and two parallel fissures after thermal treatments

Specimen	$\varepsilon_{1c}/10^{-3}$	$\sigma_c/\text{MPa}$	$S_{50}/\text{GPa}$	$S_T/\text{GPa}$
S-1 <sup>#</sup>	4.896	47.04	7.82	9.61
S-2 <sup>#</sup>	4.593	48.19	8.75	10.49
S-4 <sup>#</sup>	5.942	77.40	11.81	13.03
S-5 <sup>#</sup>	6.460	62.20	7.71	9.63
S-6 <sup>#</sup>	6.294	50.36	6.55	8.00
S-7 <sup>#</sup>	10.13	46.25	3.44	4.57
S-8 <sup>#</sup>	10.37	42.56	3.29	4.10
T90-1 <sup>#</sup>	4.496	39.60	7.55	8.81
T90-3 <sup>#</sup>	5.458	61.14	10.09	11.20
T90-4 <sup>#</sup>	5.505	63.88	10.61	11.60
T90-5 <sup>#</sup>	6.233	51.74	7.78	8.30
T90-6 <sup>#</sup>	5.502	43.82	6.50	7.96
T90-8 <sup>#</sup>	10.63	30.50	2.09	2.87

600 °C and to 44.41 MPa (marginally lower than that for room temperature) at 900 °C. Therefore, although the uniaxial compressive strength first increased and then decreased, the ultimate change in peak stress from room temperature to 900 °C is very minimal. Figure 7.6b shows the change in peak strain with increasing heat-treatment temperature for the specimens containing a single fissure. It can be seen from Fig. 7.6b that, unlike the peak stress, the peak axial strain shows a progressive increase with increasing heat-treatment temperature. At room temperature, the peak axial strain was about  $4.745 \times 10^{-3}$ , which then increased further to  $6.377 \times 10^{-3}$  and  $10.25 \times 10^{-3}$  at 600 and 900 °C, respectively. Changes in peak axial strain were modest to 600 °C, but increased dramatically from 600 to 900 °C.

Figure 7.7 shows the axial stress–strain curves for red sandstone specimens containing two parallel fissures after different thermal treatments (these data are also listed in Table 7.2). In general, the reproducibility between the experiments performed under the same conditions was good. Similar to the experiments performed on specimens containing only one fissure, those containing two parallel fissures also displayed significant variation with increasing heat-treatment temperature. However, we observed more significant stress drops during the deformation prior to the peak stress. These are likely to be the result of the formation of smaller macro-cracks (i.e., those that do not completely rupture the specimen) within the specimen.

Based on the experimental data for red sandstone specimens containing two parallel fissures listed in Table 7.2, Fig. 7.6c, d further shows the influence of heat-treatment temperature on the peak stress and the peak axial strain of red sandstone containing two parallel fissures. From Fig. 7.6c, d, it can be seen that the influence of temperature on the peak stress and peak axial strain was similar to that in the experiments performed on specimens containing a single fissure (Fig. 7.6a, b). The peak stress first increased at 300 °C, before decreasing at both 600 and 900 °C (see Fig. 7.6c). At room temperature the peak stress was 39.60 MPa (less than

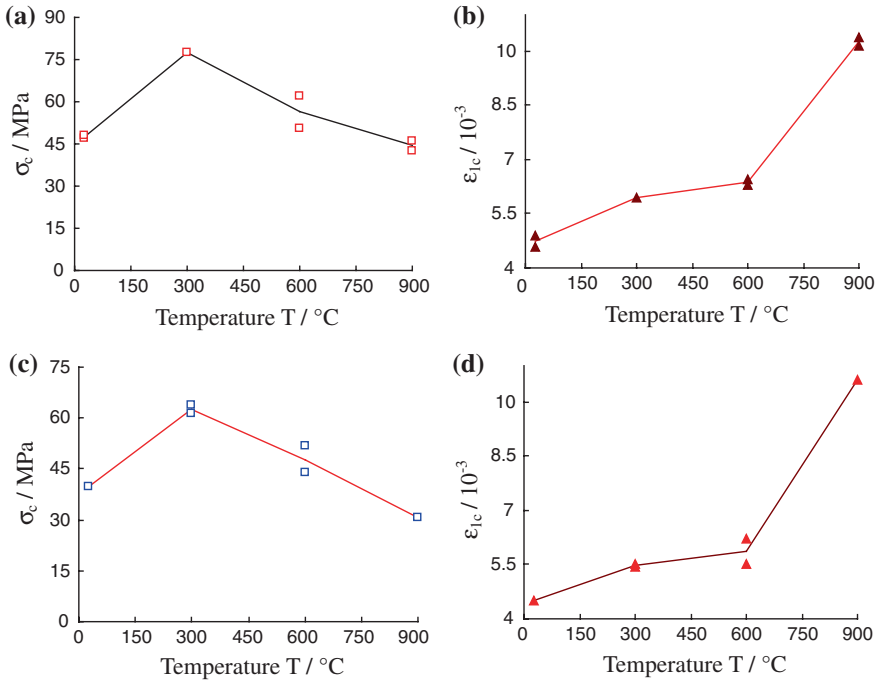
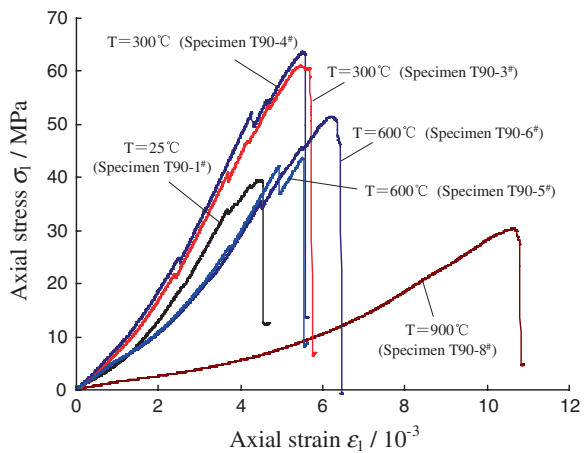


**Fig. 7.6** Influence of high-temperature treatments on the mechanical parameters of red sandstone containing a single fissure and two parallel fissures ( $\beta = 90^\circ$ ). **a** Uniaxial compressive strength of specimen containing a single fissure. **b** Peak axial strain of specimen containing a single fissure. **c** Uniaxial compressive strength of specimen containing two parallel fissures. **d** Peak axial strain of specimen containing two parallel fissures (with kind permission of Elsevier Publisher)

**Fig. 7.7** Axial stress–strain curves for red sandstone specimens containing two parallel fissures ( $\beta = 90^\circ$ ) after different thermal treatments (with kind permission of Elsevier Publisher)



that for one fissure, 47.62 MPa, and that for the specimen containing no fissures, 52.59 MPa). For the specimen with two fissures, the peak stress was increased to 62.51 at 300 °C, before decreasing to 47.78 MPa at 600 °C, and to 30.50 MPa at 900 °C (much lower than that for room temperature). Figure 7.6d shows the evolution of peak axial strain with increasing heat-treatment temperature for red sandstone containing two parallel fissures. At room temperature, the peak strain at failure was about  $4.496 \times 10^{-3}$ , and increased to  $5.868 \times 10^{-3}$  at 600 °C and  $10.63 \times 10^{-3}$  at 900 °C. As for the specimens containing one fissure, the greatest change in peak axial strain was seen from 600 to 900 °C.

In order to investigate the influence of high temperature on the stiffness of red sandstone containing a single fissure and two parallel fissures, both tangent stiffness (taken as the gradient of the stress–strain curve at 50 % of its uniaxial compressive strength,  $S_{50}$ ) and the secant stiffness (taken as the gradient of a line from zero stress to the peak stress,  $S_T$ ) were calculated for each experiment (the data are also listed in Table 7.2). Figure 7.8a, b, respectively, shows the influence of temperature on the tangent and secant stiffness of red sandstone containing a single fissure under uniaxial compression. From Fig. 7.8a, b, it can be seen that

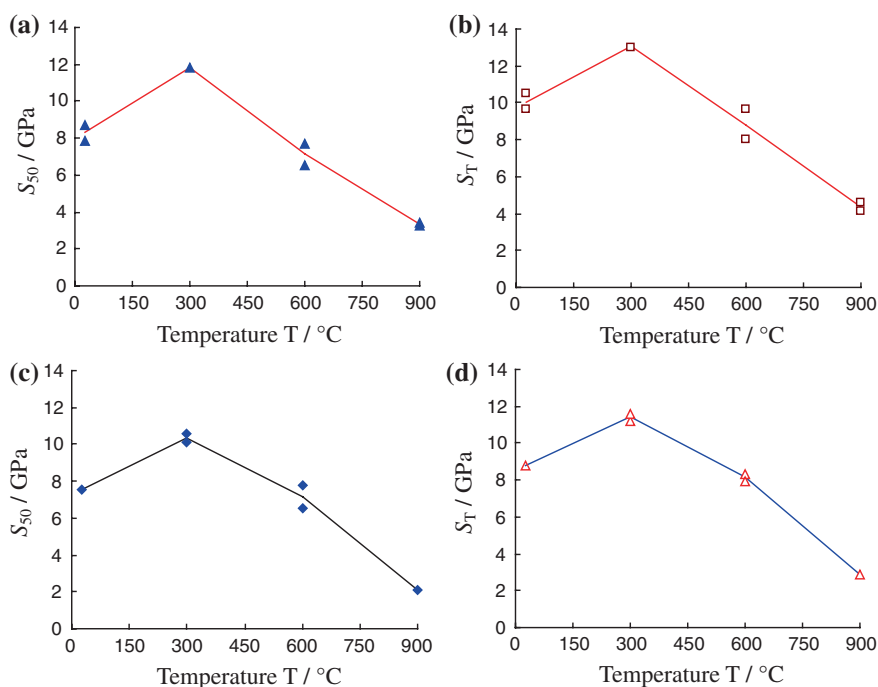


**Fig. 7.8** Influence of high-temperature treatment on the stiffness of red sandstone containing a single fissure and two parallel fissures ( $\beta = 90^\circ$ ). **a** Tangent stiffness of specimen containing a single fissure. **b** Secant stiffness of specimen containing a single fissure. **c** Tangent stiffness of specimen containing two parallel fissures. **d** Secant stiffness of specimen containing two parallel fissures (with kind permission of Elsevier Publisher)

temperature had a significant effect on both tangent and secant stiffness. Both increased at 300 °C, before decreasing at both 600 and 900 °C. For example, the  $S_{50}$  increased from 8.29 to 11.81 GPa from room temperature to 300 °C, and then decreased to 3.37 GPa at the maximum temperature of 900 °C. Figure 7.8c, d illustrates the influence of heat-treatment temperature on the tangent and secant stiffness of red sandstone containing two parallel fissures. The relationship is qualitatively similar to that for the specimens containing one fissure: both tangent and secant stiffness increased at 300 °C and then decreased up to 900 °C.

### 7.3 Fracture Evolution Behavior

In this section, the specimens containing two parallel fissures are chosen as an example to analyze the effect of high temperature on the fracture evolution behavior of fissured red sandstone. It should be noted that the AE and photographic monitoring techniques were simultaneously used to analyze the fracture coalescence characteristics during the entire deformation.

Figures 7.9, 7.10, 7.11 and 7.12 show the axial stress–time curves, the output of AEs, and the post-failure pictures for specimens of red sandstone containing two parallel fissures at room temperature, and 300, 600, and 900 °C, respectively. The stress–time curves and output of AE in Figs. 7.9, 7.10, 7.11 and 7.12 indicate that (1) all of the stress–time curves showed an initial nonlinear concave component at low stress levels (usually associated with the closure of original fissures and pores) and (2) very few AE events were recorded during this period. Therefore, during this initial stage, the output of AEs could be considered to be independent of the heat-treatment temperature. Following this initial stage of nonlinear deformation, the specimens entered a linear elastic deformation stage. Some AE events accompanied by axial stress drops were observed during this stage, and are likely due

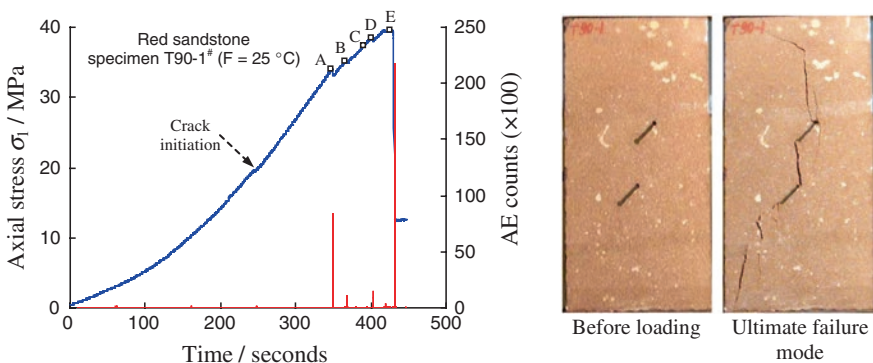


**Fig. 7.9** Axial stress and AE counts for red sandstone specimens containing two parallel fissures at  $F = 25\text{ °C}$  during the entire deformation process. The number in the brackets on the vertical axis indicates the multiplier of the coordinates (with kind permission of Elsevier Publisher)

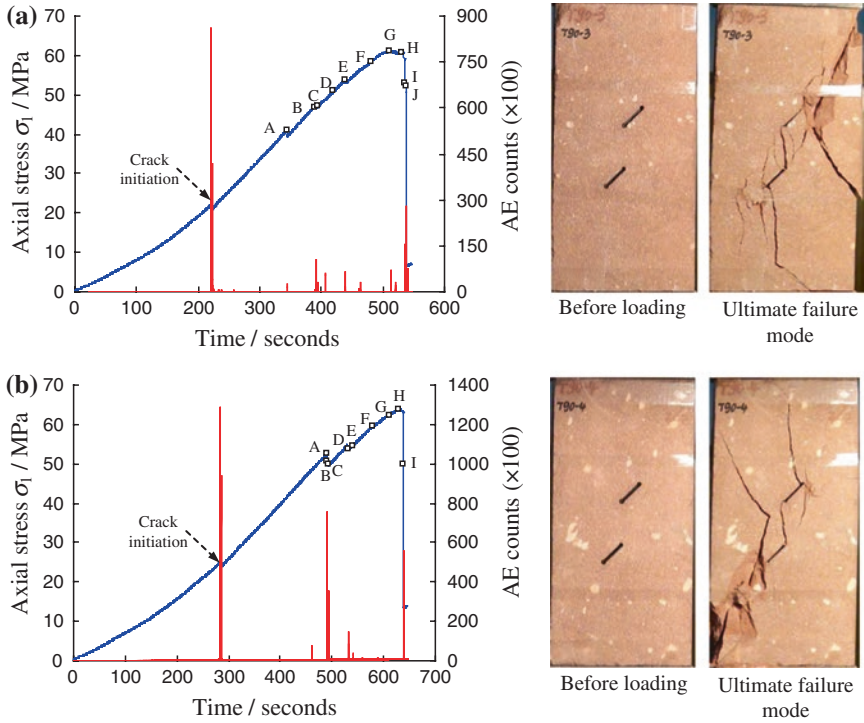


**Fig. 7.10** Axial stress and AE counts for red sandstone specimens containing two parallel fissures at  $F = 300\text{ }^{\circ}\text{C}$  during the entire deformation process. The number in brackets on the vertical axis indicates the multiplier of the coordinates. **a** Specimen T90-3#. **b** Specimen T90-4# (with kind permission of Elsevier Publisher)

to the formation of cracks. Finally, following the peak stress, there was a distinct stress drop and burst of AE, associated with the failure of the specimen. After the peak stress no further AEs were recorded. Note that at  $F = 900\text{ }^{\circ}\text{C}$ , the AE behavior of the red sandstone specimen containing two parallel fissures (Fig. 7.12) was different to that for any of the other temperatures (Figs. 7.9, 7.10 and 7.11). At  $900\text{ }^{\circ}\text{C}$ , no axial stress drops accompanying AE were seen in the axial stress–time curve, indicating that the crack evolution process had little influence on the axial stress–time curve of red sandstone at  $900\text{ }^{\circ}\text{C}$ .

Figure 7.13a, b shows the tensile wing crack initiation and propagation mode of red sandstone specimens containing two parallel fissures ( $\beta = 90^{\circ}$ ) after different high-temperature treatments under uniaxial compression. The effect of high temperature on the tensile wing crack initiation and propagation mode can be analyzed as follows. Except for specimen T90-5# ( $F = 600\text{ }^{\circ}\text{C}$ ), the tensile wing crack initiation mode for all other specimens was very similar, and independent of the temperature. Tensile wing cracks were initiated from both the inner and outer tips of fissures ① and ② (see Fig. 7.13), and propagated in the direction of

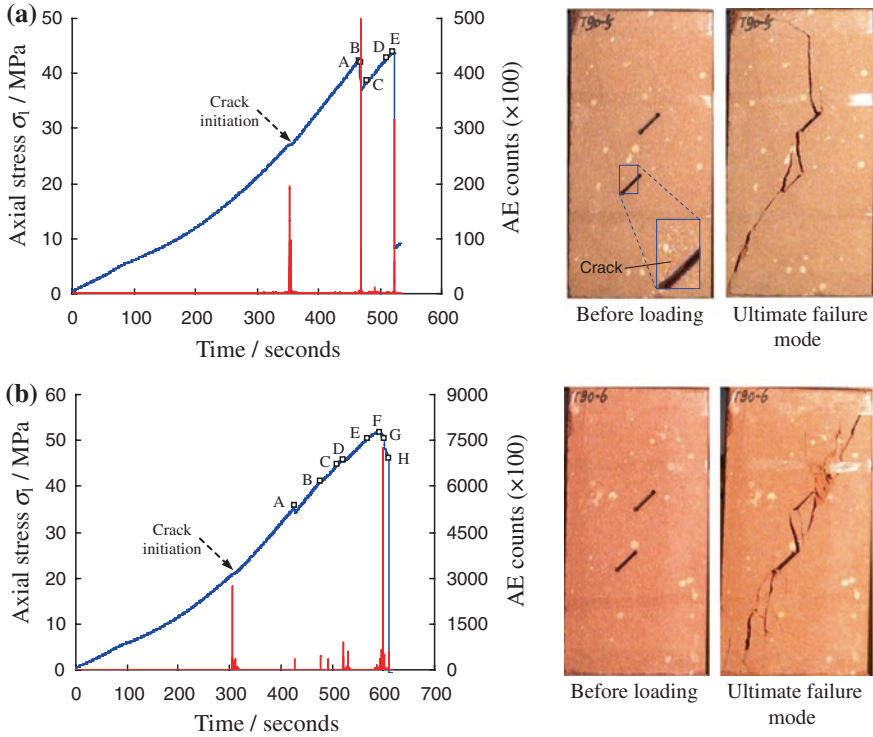


**Fig. 7.11** Axial stress and AE counts for red sandstone specimens containing two parallel fissures at  $F = 600\text{ }^{\circ}\text{C}$  during the entire deformation process. The number in brackets on the vertical axis indicates the multiplier of the coordinates. **a** Specimen T90-5#. **b** Specimen T90-6# (with kind permission of Elsevier Publisher)

the maximum principal stress. It should be noted that the propagation speed of the wing cracks emanating from the outer tips of the fissure was higher than that for those at the inner tips. This is likely the result of stress field interactions between the fissures limiting the crack propagation in the ligament region. However, for specimen T90-5# ( $F = 600\text{ }^{\circ}\text{C}$ ), an anti-tensile wing crack was initiated from the outer tip of fissure ② prior to loading (see crack in Fig. 7.11a). This is likely the result of a thermal crack that formed close to fissure ② during the thermal treatment of this particular specimen. As deformation progressed, a tensile wing crack was initiated from the inner and outer tip of fissure ① and the outer tip of fissure ②, while no tensile wing crack was initiated from the inner tip of fissure ②.

Figure 7.13c shows the crack coalescence process between fissures ① and ② in red sandstone containing two parallel fissures ( $\beta = 90^{\circ}$ ) after different high-temperature treatments under uniaxial compression. It is clear that all the specimens, except specimen T90-5# ( $F = 600\text{ }^{\circ}\text{C}$ ), coalescence occurred at the inner tips of fissures ① and ② as deformation progressed. This means that the mode of crack coalescence between fissures ① and ② was independent of the heat-treatment

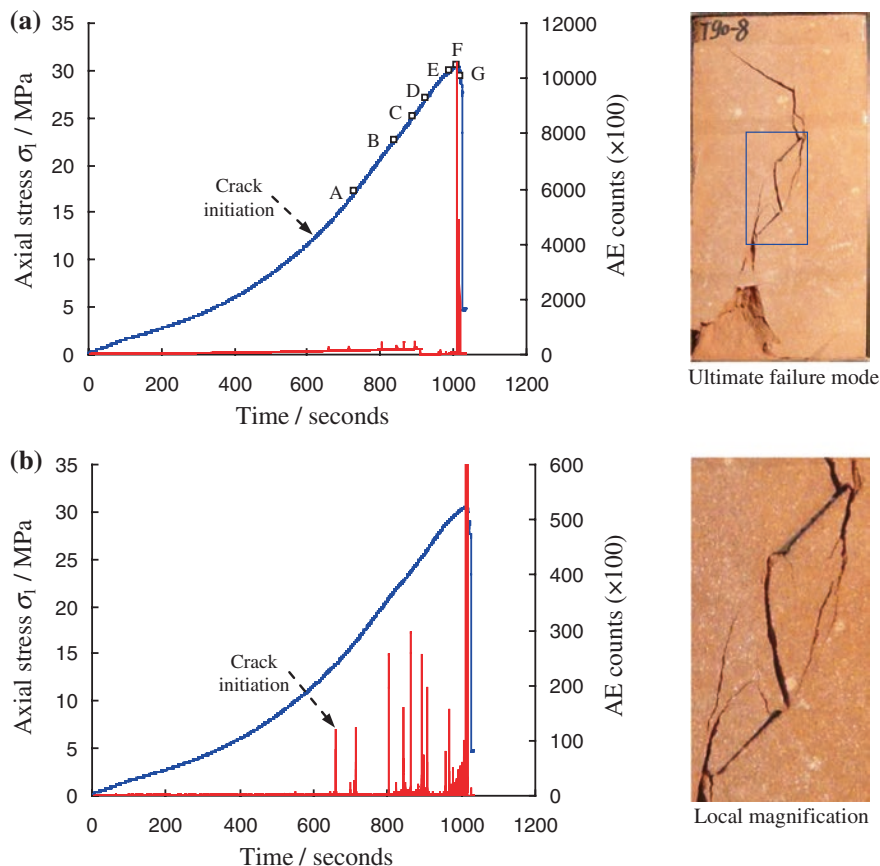
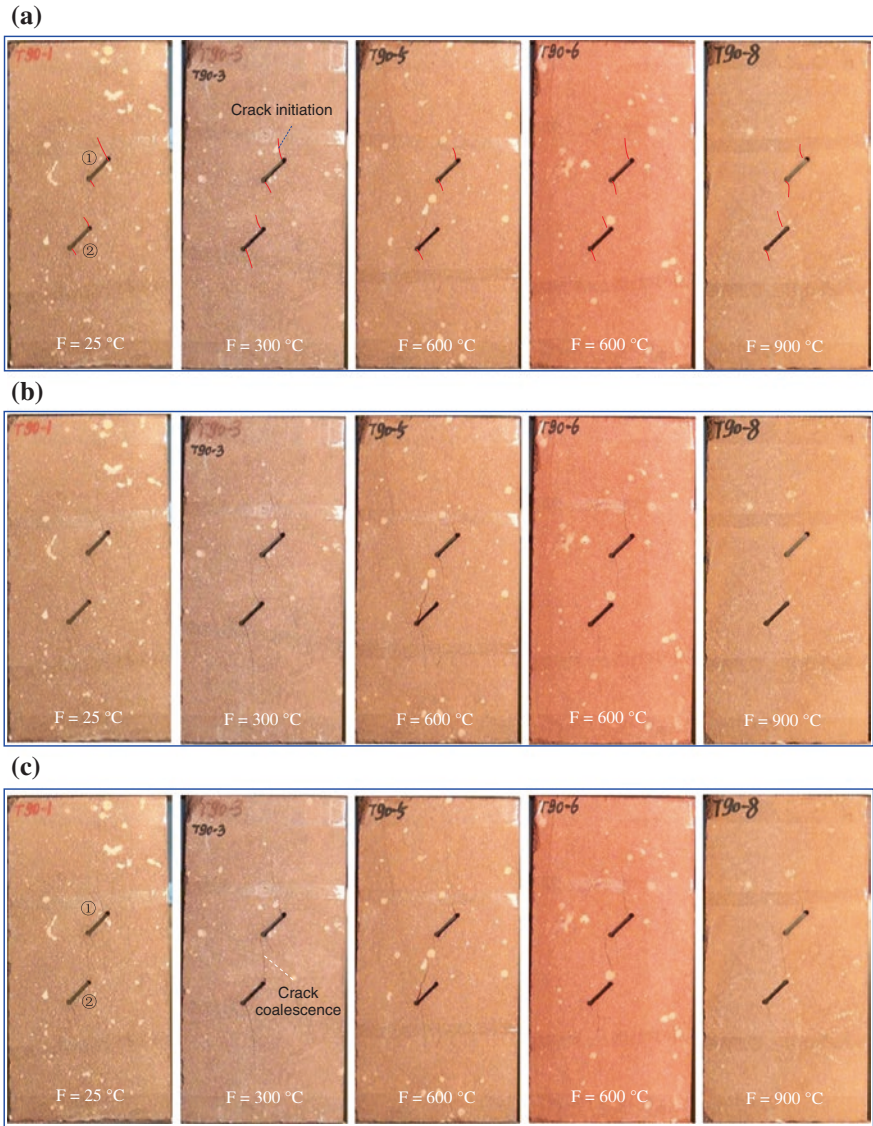


**Fig. 7.12** Axial stress and AE counts for red sandstone specimens containing two parallel fissures at  $F = 900\text{ }^{\circ}\text{C}$  during the entire deformation process. The number in brackets on the vertical axis indicates the multiplier of the coordinates. **a** Specimen T90-8<sup>#</sup> ( $F = 900\text{ }^{\circ}\text{C}$ ). **b** Local magnification (with kind permission of Elsevier Publisher)

temperature. The coalescence of fissures ① and ② also resulted in a clear axial stress drop in the axial stress–time curves. However, for specimen T90-8<sup>#</sup> ( $F = 900\text{ }^{\circ}\text{C}$ ), even though no clear axial stress drop in the axial stress–time curves was observed, the larger AE burst testified the coalescence of fissures ① and ②.

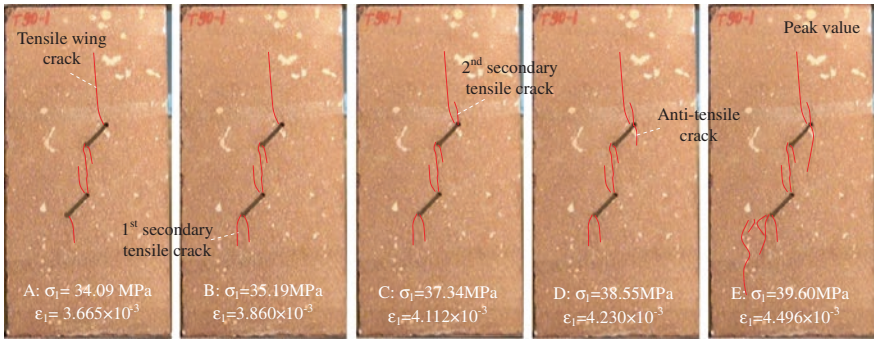
After the crack coalescence between fissures ① and ② in red sandstone specimens containing two parallel fissures, many secondary cracks emanated from the outer tips of the two fissures. However, no secondary cracks were seen to initiate from the inner tips of the fissures. We now consider the crack evolution process in more detail, using a time-lapse photographic monitoring technique.

Figure 7.14 shows the fracture evolution process for a specimen of red sandstone at room temperature ( $F = 25\text{ }^{\circ}\text{C}$ ). The letters in Fig. 7.14 correspond to those in Fig. 7.9. Figure 7.14 showed that, as axial deformation was increased,



**Fig. 7.13** Typical crack initiation, propagation, and coalescence modes in red sandstone containing two parallel fissures ( $\beta = 90^\circ$ ) after different high-temperature treatments under uniaxial compression. **a** Tensile wing crack initiation. **b** Tensile wing crack propagation. **c** Crack coalescence between fissure ① and ② (with kind permission of Elsevier Publisher)

two secondary tensile cracks were initiated from the outer tips of fissures ① and ②. Both propagated in the direction of the maximum principal stress. However, these secondary tensile cracks did not propagate as far as the original tensile wing cracks existed at the same fissure tips, suggesting that the secondary tensile cracks



**Fig. 7.14** Fracture evolution process of red sandstone specimen containing two parallel fissures ( $F = 25^\circ\text{C}$ ) after the crack coalescence between fissures ① and ② (with kind permission of Elsevier Publisher)

were harder to propagate. As deformation was increased further, an anti-tensile crack was observed to emanate from the outer tip of fissure ①. This anti-tensile crack was formed in the direction opposite to the secondary tensile crack initiated at the same position. Eventually, the peak stress was reached (point E in Fig. 7.14) and, at this moment, the anti-tensile crack had propagated significantly along the direction of the maximum principal stress, toward the bottom edge of the specimen. Contemporaneously, some far-field cracks were also observed at the left side of the specimen, resulting in the macroscopic rupture of the specimen.

The fracture evolution process of the two red sandstone specimens T90-3<sup>#</sup> and T90-4<sup>#</sup> ( $F = 300^\circ\text{C}$ ) is shown in Figs. 7.15 and 7.16, respectively. The letters in Figs. 7.15 and 7.16 correspond to those in Fig. 7.10. Figures 7.15 and 7.16 demonstrated that the fracture evolution process of the two specimens was very similar, and for this reason we discuss only specimen T90-3<sup>#</sup>. Following the coalescence of fissures ① and ②, an anti-tensile crack initiated from the outer tip of fissure ① (point C in Fig. 7.15), this was accompanied by a distinct burst of AE activity (Fig. 7.10a). When the specimen was loaded to point D, a secondary tensile crack was initiated from the outer tip of fissure ② which propagated along the direction of the maximum principal stress. As deformation progressed further, an anti-tensile crack was initiated from the outer tip of fissure ②, again propagating in the direction of the maximum principal stress.

At point F a secondary tensile crack was observed to emanate from the outer tip of fissure ①, while a far-field crack initiated close to fissure ②. When the specimen was loaded to the peak stress, the aperture of the secondary tensile crack and the anti-tensile crack initiated from the outer tip of fissure ① increased significantly. Note that this anti-tensile crack propagated toward the inner tip of fissure ②. Following the peak stress, the axial supporting capacity of the specimen was reduced as deformation was increased. Some surface spalling was observed close to the outer tip of fissure ① and some far-field cracks were also found at the top right and bottom left of the specimen (points I–J in Fig. 7.15).



**Fig. 7.15** Fracture evolution process of red sandstone specimen T90-3<sup>#</sup> containing two parallel fissures ( $F = 300\text{ }^{\circ}\text{C}$ ) after the crack coalescence between fissures ① and ② (with kind permission of Elsevier Publisher)

The fracture evolution process of the two red sandstone specimens T90-5<sup>#</sup> and T90-6<sup>#</sup> ( $F = 600\text{ }^{\circ}\text{C}$ ) is shown in Figs. 7.17 and 7.18, respectively. The letters in Figs. 7.17 and 7.18 correspond to those in Fig. 7.11. For specimen T90-5<sup>#</sup>, after the crack coalescence between fissures ① and ②, a shear crack was observed at the outer tip of fissure ② as axial deformation was increased. The propagation direction of this shear crack was first along the direction of fissure ②, but gradually curved along the direction of the maximum principal stress, toward the bottom edge of the specimen. This also led to a large stress drop (Fig. 7.11a). As deformation progressed from point A to point B, the aperture of the coalesced crack between the two fissures increased and the crack path became more distinct. Once the specimen had reached point C, a secondary tensile crack was initiated from the outer tip of fissure ①, and propagated toward the top edge of the specimen in the direction of the maximum principal stress. Between points C and E (the peak stress), no new cracks were observed. Following the peak stress, the specimen ruptured and a large stress drop was observed associated with a spike in AE activity (Fig. 7.11a).

However, the fracture evolution process for specimen T90-6<sup>#</sup> was different to that of specimen T90-5<sup>#</sup>. After the crack coalescence between fissures ① and



**Fig. 7.16** Fracture evolution process of red sandstone specimen T90-4<sup>#</sup> containing two parallel fissures ( $F = 300\text{ }^\circ\text{C}$ ) after the crack coalescence between fissures ① and ② (with kind permission of Elsevier Publisher)

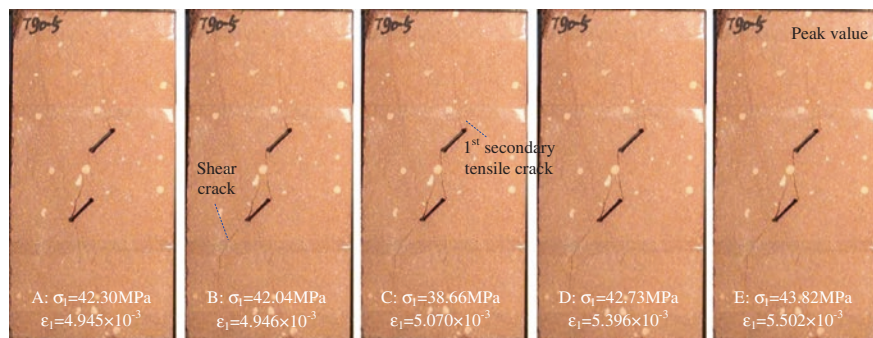


**Fig. 7.17** Fracture evolution process of red sandstone specimen T90-5<sup>#</sup> containing two parallel fissures ( $F = 600\text{ }^\circ\text{C}$ ) after the crack coalescence between fissures ① and ② (with kind permission of Elsevier Publisher)

②, a secondary tensile crack was observed at the outer tip of fissure ② (point B in Fig. 7.18). At point C, anti-tensile crack was initiated at the outer tip of fissure ①, and started to propagate toward the inner tip of fissure ②. As deformation



**Fig. 7.18** Fracture evolution process of red sandstone specimen T90-6# containing two parallel fissures ( $F = 600 \text{ }^\circ\text{C}$ ) after the crack coalescence between fissures ① and ② (with kind permission of Elsevier Publisher)

continued, two more secondary tensile cracks were seen to emanate from the outer tip of fissure ② (point D in Fig. 7.18) and the outer tip of fissure ① (point E in Fig. 7.18). At the peak stress (point E in Fig. 7.18), another anti-tensile crack was observed at the outer tip of fissure ②, and a far-field crack near the outer tip of fissure ①. After the peak stress, more far-field cracks were observed and the specimen failed, marked by a significant stress drop and a burst of AE activity (Fig. 7.11b). However, in Fig. 7.18, the anti-tensile crack at the outer tip of fissure ② was not so obvious. We have therefore taken high-zoom photographs to show the crack in more detail (Fig. 7.19). It can be seen from Fig. 7.19 that the aperture of the crack is very small, and that its propagation path, although roughly in the direction of the maximum principal stress, followed a tortuous path. This indicates that the larger grains again had an influence on crack coalescence and failure of these specimens.

The fracture evolution process of the red sandstone specimen T90-8# ( $F = 900 \text{ }^\circ\text{C}$ ) is shown in Fig. 7.20. The letters in Fig. 7.20 correspond to those in Fig. 7.12. At point B, a secondary tensile crack initiated from the outer tip of fissure ②, and propagated in the direction of the maximum principal stress. As axial stress was increased, an anti-tensile crack was observed at the outer tip of fissure ① (point C) and another anti-tensile crack at the outer tip of fissure ② (point D).

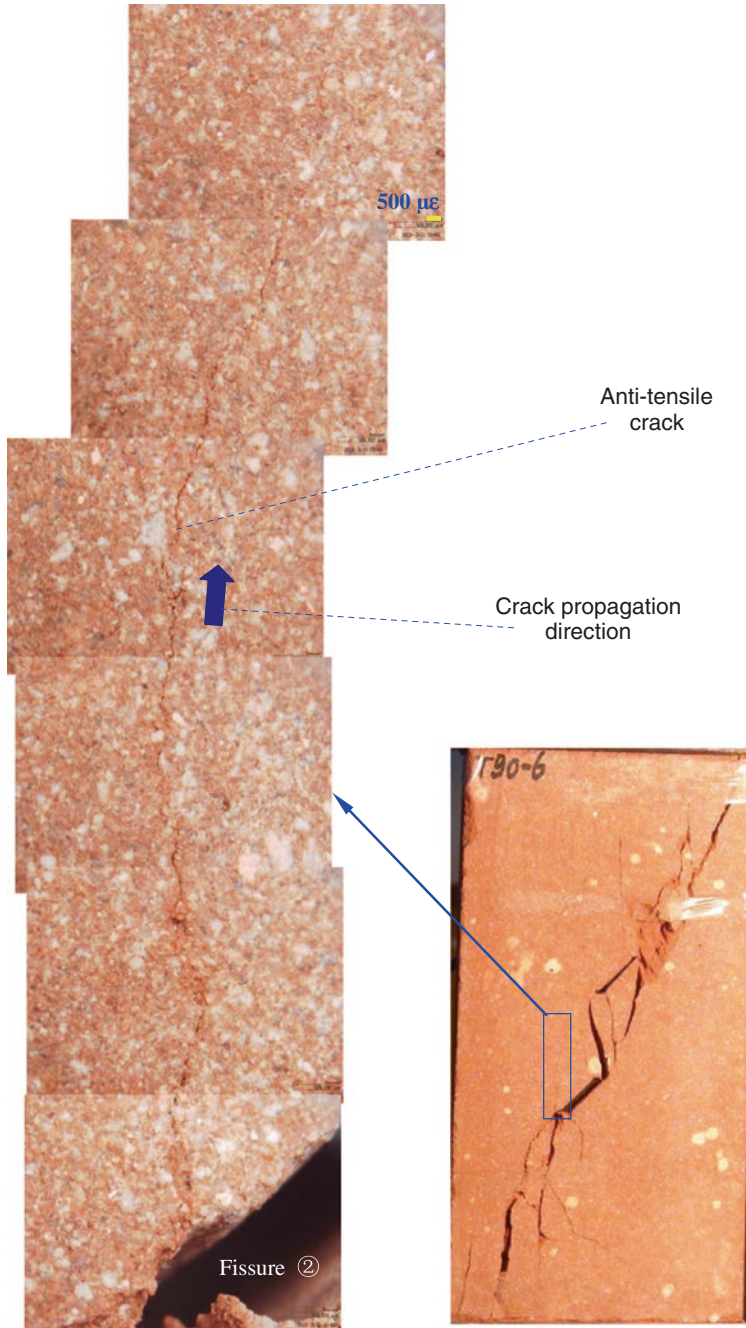


**Fig. 7.19** High-zoom photographs of an anti-tensile crack in red sandstone specimen T90-6# containing two parallel fissures at  $F = 600$  °C (with kind permission of Elsevier Publisher)

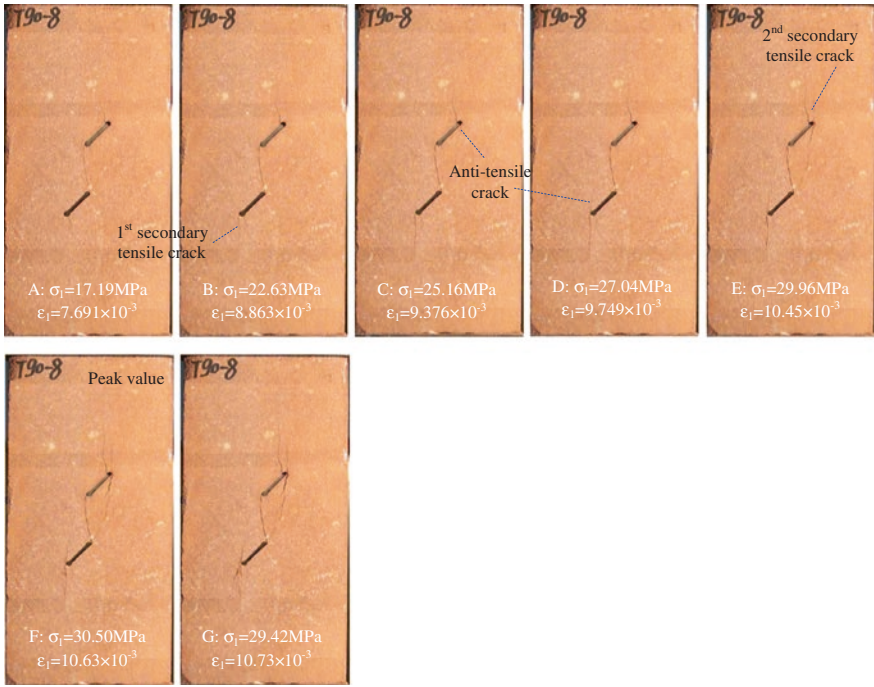


**Fig. 7.20** Fracture evolution process of red sandstone specimen containing two parallel fissures ( $F = 900\text{ }^\circ\text{C}$ ) after the crack coalescence between fissures ① and ② (with kind permission of Elsevier Publisher)

These two cracks started to propagate toward the inner tip of the two fissures. At point E, another secondary tensile crack emanated from the outer tip of fissure ①. As deformation was increased to point F, no new cracks were observed in the specimen. Following the peak stress, the specimen ruptured in a brittle manner and the apertures of the cracks increased, which was also evidenced by the AE events shown in Fig. 7.12. Surface spalling was also observed upon specimen failure.

Figure 7.21 shows the crack initiation stress and coalescence stress against temperature in red sandstone containing two parallel fissures ( $\beta = 90^\circ$ ). The peak strength is also given for comparison. In Fig. 7.21, the crack initiation stress is the stress at which the first tensile wing crack was initiated (as shown in Fig. 7.13a), and the crack coalescence stress corresponds to the stress at which fissures ① and ② coalesced (as shown in Fig. 7.13c). Figure 7.21 shows that the temperature influenced the crack initiation stress, the crack coalescence stress and the peak stress in a qualitatively similar manner. In detail, the temperature influenced the difference between the crack initiation stress and the peak stress.

As the temperature increased from 25 to 600  $^\circ\text{C}$ , the crack initiation stress increased from 19.58 to 24.11 MPa, whereas it decreased from 24.11 to

**Fig. 7.21** Crack initiation, coalescence, and peak stresses versus temperature in red sandstone containing two parallel fissures ( $\beta = 90^\circ$ ). Note that the lines of best-fit pass through the average values of the stresses for each temperature (with kind permission of Elsevier Publisher)

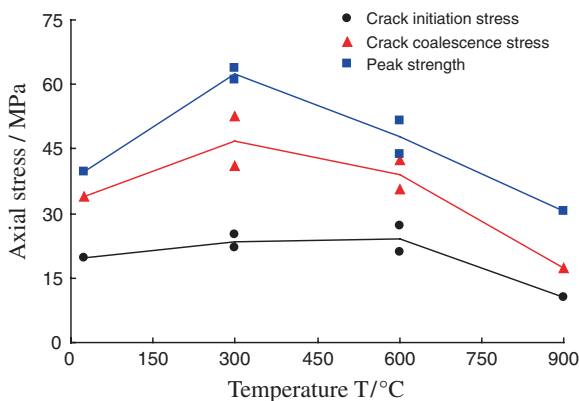
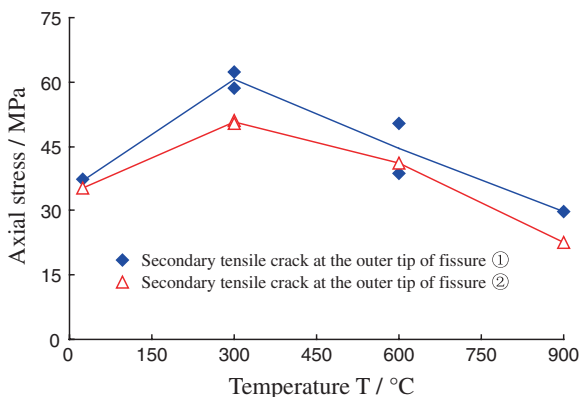


**Fig. 7.22** Initiated stresses of secondary tensile crack at the outer tips of two fissures versus temperature in red sandstone containing two parallel fissures ( $\beta = 90^\circ$ ). Note secondary tensile crack is the crack that initiated at the outer tip of fissure ① or ② (with kind permission of Elsevier Publisher)



10.45 MPa as the temperature was increased from 600 to 900 °C. However, the evolution of the crack coalescence stress followed the evolution of the peak stress more closely. As the temperature was increased from 25 to 300 °C, the crack coalescence stress increased from 34.09 to 46.81 MPa, whereas it decreased significantly from 46.81 to 17.19 MPa as the temperature was increased from 300 to 900 °C.

Figure 7.22 shows the stress at which a secondary tensile crack initiated at the outer tips of two fissures against heat-treatment temperature in red sandstone containing two parallel fissures ( $\beta = 90^\circ$ ). Here, we define a secondary tensile crack as a crack that initiated at the outer tips of either fissure ① or ②. As in Fig. 7.22, the axial stress required to initiate the secondary tensile crack depends on the heat-treatment temperature. The stress required to initiate the secondary tensile crack increased at 300 °C, before decreasing up to 900 °C.

## 7.4 Interpretation and Discussion

As mentioned previously, pre-existing fissures could result in the decrease of the strength of sandstone specimens. Further, those specimen containing two fissures were weaker than those containing only one fissure. This is an expected result, as cracks can form more easily from these macroscopic flaws than in the “intact” material. However, the relationship between the strength and material stiffness and the heat-treatment temperature has not been fully studied.

In the past, many investigations have been conducted on the effect of temperature during heat treatment (hereafter, temperature refers to this temperature) on the mechanical behavior of rock material. Furthermore, the critical temperature on reaching the maximum strength and elastic modulus is not constant, but depends on rock type. By carrying out uniaxial compression tests for limestone at heat-treatment temperatures from 25 to 800 °C, Mao et al. (2009) found that the strength and elastic modulus did not depend on the temperature at temperatures less than 700 °C, but decreased obviously with increasing temperature at temperatures higher than 700 °C. Zhang et al. (2009) performed uniaxial compression tests on marble at temperatures from 25 to 800 °C. They found that both the strength and elastic modulus of marble showed a general decrease with the increase of temperature. Based on the uniaxial compression experimental results for granite at temperatures between 25 and 1200 °C, Xu et al. (2008, 2009) found that both strength and elastic modulus of granite changed slightly with the increase of temperature in the range lower than 800 °C, whereas they decreased greatly at temperatures higher than 800 °C.

However, even for the same sandstone type (Yin et al. 2009; Ranjith et al. 2012; Brotóns et al. 2013), the critical temperature at reaching the maximum strength and elastic modulus is also not constant. In accordance with uniaxial compression test results of sandstone at temperatures between 25 and 600 °C, Wu et al. (2005) found that the strength at temperatures lower than 400 °C did not depend on the temperature, but decreased with the temperature at temperatures higher than 400 °C. Based on uniaxial compression experimental results on sandstone at temperatures between 25 and 300 °C, Rao et al. (2007) observed that both the strength and elastic modulus of sandstone increased at 250 °C, before decreasing up to their maximum temperature of 300 °C. By carrying out uniaxial compressive strength tests on sandstone at temperatures between 25 and 950 °C, Ranjith et al. (2012) demonstrated the dependence of mechanical properties on temperature where the strength and elastic modulus of sandstone increased with increasing temperature for temperatures less than 500 °C and decreased with increasing temperature for temperatures higher than 500 °C. Moreover, the critical temperature which affected the peak strength of sandstone is not equal to that which affected the elastic modulus.

It should be noted that in our research, both strength and stiffness of sandstone increased at 300 °C, before decreasing up to our maximum temperature of 900 °C. The above relationship in this research is similar to the effect of high-temperature

treatment on mechanical parameters of Jiaozuo sandstone (Yin et al. 2009). In the following section, for the mechanism of how the high-temperature treatment could have affected the mechanical parameters of red sandstone containing a single fissure and two parallel fissures under uniaxial compression, we make a detailed illustration.

The strengthening at 300 °C is perhaps surprising since red sandstone contains both clay mineral (smectite) and zeolites. First, clay minerals are well known to begin to dehydrate, which releases absorbed water between layers and in structural channels below 300 °C, generally resulting in a decrease in specimen strength (Somerton 1992; Mollo et al. 2011). Second, some zeolites are thermally unstable at low temperatures and can suffer irreversible changes to their structure, which also generally results in a decrease in specimen strength (Heap et al. 2012). However, even though the thermal expansion may cause the micro-cracks at 300 °C, it is not large enough to initiate any micro-cracks with the thermally induced strain (only locating at the elastic deformation stage). On the other hand, the closure of some texture flaws in red sandstone from 25 to 300 °C (Fig. 7.2a, b) strengthens the material and increases its stiffness. Based on the above descriptions, the high-temperature treatment could have made the specimens heat-treated at 300 °C stronger without producing any micro-cracks.

When the temperature was increased above 300 °C, it should be noted that differences in thermal expansion behaviors of mineral grains can also induce great thermal stresses within the rock material. Once the maximum thermal stress exceeds the tensile or shear strength limits of rock, new micro-cracks will initiate and develop (Fig. 7.2c; Yin et al. 2009). Furthermore, thermal stresses can also lead to the propagation of the original cracks, which may result in the structural damage of rocks. In addition, differences in thermal expansion along different crystallographic axes of the same mineral can also cause structural damage upon heating (Somerton 1992). Therefore, when the temperature was increased from 300 to 600 °C, the internal stresses built up as a result of the thermal-expansion mismatch between the minerals within red sandstone were sufficient to generate significant thermal microcracking (Fig. 7.2c). At 600 °C, the quartz will have passed the  $\alpha/\beta$  transition  $\sim 573$  °C (Somerton 1992), which results in a large increase in the volume of quartz; and therefore, a substantial amount of thermal microcracking (Glover et al. 1995).

As the temperature was increased to 900 °C, more and more thermal micro-cracks will have formed (Fig. 7.2d), again due to the stresses caused by mineral thermal expansion. Many thermal micro-cracks in the 900 °C specimens may have also encouraged crack interaction and coalescence. At the same time, we must note that in this research, the mineral composition of sandstone did not change with increasing temperature, but the porosity usually increases with the temperature especially above 300 °C (Tian et al. 2012, 2014), which can also reduce the strength and stiffness of the specimen.

Regardless of these changes in strength and material stiffness in the specimens, the peak strain at failure always increased as the temperature was increased, indicating that the specimens could support a larger axial strain before catastrophic

failure. The peak strain at failure increased slowly up to 600 °C, before increasing substantially at 900 °C. This is likely to be the result of a large increase in thermal micro-cracks, and their potential interaction and coalescence, from 600 to 900 °C.

## 7.5 Conclusions

In this chapter, a systematic experimental investigation was performed to explore the strength, deformation, and fracture evolution behavior of red sandstone specimens (with the dimensions of 80 × 160 × 30 mm) containing a single fissure and two parallel fissures ( $\beta = 90^\circ$ ) that underwent different high-temperature treatments. Based on our study, the conclusions can be summarized as follows:

1. Compared with intact specimen, the strength of red sandstone was reduced by the pre-existing fissures. Further, the strength of specimen containing two fissures ( $\beta = 90^\circ$ ) were weaker than those containing only one fissure. The uniaxial compressive strength and material stiffness of red sandstone containing a single fissure and two parallel fissures increased from 25 to 300 °C, before both decreasing up to the maximum temperature of 900 °C. However, the peak axial strain at failure always showed an increase with increasing heat-treatment temperature. The crack initiation, coalescence, and peak stresses depended on temperature. Furthermore, the crack coalescence stress between two pre-existing fissures is nonlinearly related to the temperature, which is similar to the effect of the heat-treatment temperature on peak strength.
2. Both photographic monitoring and AE monitoring techniques in the entire deformation process were employed to study the crack initiation, propagation, and coalescence in the pre-fissured specimens. For the specimens left at room temperature and those heat-treated to 300 °C, tensile wing cracks were usually initiated from the inner and outer tip of the fissure. However, at 600 and 900 °C, an anti-tensile wing crack was usually observed from the inner and outer tip of the fissure. Secondary tensile cracks were usually observed after tensile wing cracks had formed. Upon specimen failure, some surface spalling and far-field cracks were also observed. The crack initiation and coalescence modes between two fissures were independent of the heat-treatment temperature.
3. The relationship between the crack evolution process of red sandstone containing a single fissure and two parallel fissures was dependent on the temperature. Once the specimen contained thermally induced cracks at the fissure tips, the fracture evolution process could be obviously affected by these, which was different to those for the other specimens at the same temperature. Finally, a large number of AE events were usually associated with crack propagation and coalescence in the specimens containing a single fissure and two parallel fissures.
4. In accordance with SEM and thin section observation of red sandstone, the mechanism by which the high-temperature treatment affected the mechanical

parameters of the pre-fissured red sandstone was interpreted. At room temperature, red sandstone specimen showed more pores and cracks. When the temperature was increased to 300 °C, the closure of pores and cracks may be responsible for the increase of strength and stiffness. However, when the temperature was increased to 600 and 900 °C, the increase of volume of quartz due to  $\alpha/\beta$  transition, the interaction and coalescence of microcracks formed due to the stresses caused by mineral thermal expansion, and the increase of the porosity acted to reduce the strength and stiffness of the sandstone.

## References

- Bell AF, Greenough J, Heap MJ, Main IG (2011a) Challenges for forecasting based on accelerating rates of earthquakes at volcanoes and laboratory analogues. *Geophys J Int* 185:718–723
- Bell AF, Naylor M, Heap MJ, Main IG (2011b) Forecasting volcanic eruptions and other material failure phenomena: an evaluation of the failure forecast method. *Geophys Res Lett* 38: L15304. <http://dx.doi.org/10.1029/2011GL048155>
- Benson PM, Thompson AB, Meredith PG, Vinciguerra S, Young RP (2007) Imaging slow failure in triaxially deformed Etna basalt using 3D acoustic-emission location and X-ray computed tomography. *Geophys Res Lett* 34:L03303. doi:10.1029/2006GL028721
- Brantut N, Schubnel A, Guéguen Y (2011) Damage and rupture dynamics at the brittle-ductile transition: the case of gypsum. *J Geophys Res* 116: B01404 <http://dx.doi.org/10.1029/2010JB007675>
- Brotóns V, Tomás R, Alarcón SIJC (2013) Temperature influence on the physical and mechanical properties of a porous rock : san julian's calcarenite. *Eng Geol* 167:117–127
- Chopra PN (1997) High-temperature transient creep in olivine rocks. *Tectonophysics* 279:93–111
- Fortin J, Stanchits S, Dresen G, Gueguen Y (2006) Acoustic emission and velocities associated with the formation of compaction bands in sandstone. *J Geophys Res* 111:B10203. doi:10.1029/2005JB003854
- Glover PWJ, Baud P, Darot M, Meredith PG, Boon SA, LeRevelec M, Zoussi S, Reuschle T (1995) Phase transition in quartz monitored using acoustic emissions. *Geophys J Int* 120: 775–782
- Heap MJ, Baud P, Meredith PG (2009) The influence of temperature on brittle creep in sandstones. *Geophys Res Lett* 36:L19305. doi:10.1029/2009GL039373
- Heap MJ, Lavallée Y, Laumann A, Hess K-U, Meredith PG, Dingwell DB (2012) How tough is tuff in the event of fire? *Geology* 40:311–314
- Heuze FE (1983) High-temperature mechanical, physical and thermal properties of granitic rocks—a review. *Int J Rock Mech Min Sci Geomech Abstr* 20:3–10
- Li JL, Chen X, Dang L, Dong YH, Cheng Z, Guo J (2011) Triaxial unloading test of sandstone after high temperature. *Chin J Rock Mech Eng* 30: 1587–1595
- Li YP, Chen LZ, Wang YH (2005) Experimental research on pre-cracked marble under compression. *Int J Solids Struct* 42:2505–2516
- Lockner D, Byerlee J, Kuksenko V, Ponomarev A, Sidorin A (1991) Quasi-static fault growth and shear fracture energy in granite. *Nature* 350:39–42
- Mao XB, Zhang LY, Li TZ, Liu HS (2009) Properties of failure mode and thermal damage for limestone at high temperature. *Min Sci Technol* 19:290–294
- Mollo S, Vinciguerra S, Iezzi G, Iarocci A, Scarlato P, Heap MJ, Dingwell DB (2011) Volcanic edifice weakening via devolatilization reactions. *Geophys J Int* 186:1073–1077
- Ranjith PG, Viete DR, Chen BJ, Perera MSA (2012) Transformation plasticity and the effect of temperature on the mechanical behavior of hawkesbury sandstone at atmospheric pressure. *Eng Geol* 151:120–127

- Rao QH, Wang Z, Xie HF, Xie Q (2007) Experimental study of properties of sandstone at high temperature. *J Cent S Univ Technol (Engl Ed)* 14(s1):478–483
- Somerton WH (1992) Thermal properties and temperature-related behavior of rock/fluid systems. Elsevier, Amsterdam, pp 22–29
- Tang FR, Mao XB, Zhang LY, Yin HG, Li Y (2011) Effects of strain rates on mechanical properties of limestone under high temperature. *Min Sci Technol (China)* 21:857–861
- Tian H, Kempka T, Xu NX, Ziegler M (2012) Physical properties of sandstones after high temperature treatment. *Rock Mech Rock Eng* 45:1113–1117
- Tian H, Ziegler M, Kempka T (2014) Physical and mechanical behavior of claystone exposed to temperatures up to 1000 °C. *Int J Rock Mech Min Sci* 70:144–153
- Xu XL, Gao F, Shen XM, Xie HP (2008) Mechanical characteristics and microcosmic mechanisms of granite under temperature loads. *J China Univ Min Technol* 18: 413–417
- Xu XL, Kang ZX, Ji M, Ge WX, Chen J (2009) Research of microcosmic mechanism of brittle-plastic transition for granite under high temperature. *Procedia Earth Planet Sci* 1:432–437
- Wu XY, Baud P, Wong TF (2000) Micromechanics of compressive failure and spatial evolution of anisotropic damage in Darley Dale sandstone. *Int J Rock Mech Min Sci* 37: 143–160
- Wu Z, Qin BD, Chen LJ, Luo YJ (2005) Experimental study on mechanical character of sandstone of the upper plank of coal bed under high temperature. *Chin J Rock Mech Eng* 24: 1863–1867
- Yang SQ, Jing HW, Huang YH, Ranjith PG, Jiao YY (2014) Fracture mechanical behavior of red sandstone containing a single fissure and two parallel fissures after exposure to different high temperature treatments. *J Struct Geol* 69(Part A): 245–264
- Yang SQ, Liu XR, Jing HW (2013) Experimental investigation on fracture coalescence behavior of red sandstone containing two unparallel fissures under uniaxial compression. *Int J Rock Mech Min Sci* 63:82–92
- Ying TB, Li XB, Yin ZQ, Zhou ZL, Liu XL (2012) Study and comparison of mechanical properties of sandstone under static and dynamic loadings after high temperature. *Chin J Rock Mech Eng* 31: 273e279
- Yin GZ, Li XS, Zhao HB (2009) Experimental investigation on mechanical properties of coarse sandstone after high temperature under conventional triaxial compression. *Chin J Rock Mech Eng* 28(3): 598–604
- Zhang S, Leng W, Zhang F, Xiong Y (2012) A simple thermo-elastoplastic model for geomaterials. *Int J Plast* 34:93–113
- Zhang ZX, Yu J, Kou SQ, Lindqvist PA (2001) Effects of high temperature on dynamic rock fracture. *Int J Rock Mech Min Sci* 38:211–225
- Zhang LY, Mao XB, Lu AH (2009) Experimental study of on the mechanical properties of rocks at high temperature. *Sci China Ser E-Technol Sci* 52:641–646
- Zhao YS, Wan ZJ, Feng ZJ, Yang D, Zhang Y, Qu F (2012) Triaxial compression system for rock testing under high temperature and high pressure. *Int J Rock Mech Min Sci* 52:132–138

# Chapter 8

## Experimental Investigation on Strength and Failure Behavior of Pre-cracked Marble Under Conventional Triaxial Compression

In the preceding sections, physical experiments on pre-fissured rock materials under uniaxial compression have been performed. Engineering rock mass is usually located in a triaxial stress state. Up to now, the strength behaviors of pre-cracked rock materials under triaxial stress have not been fully investigated, and the fundamental mechanisms of crack coalescence in real rock materials with confining pressures are still not fully understood. Therefore, we have carried out the experimental investigation on real pre-cracked marble samples under conventional triaxial compression (Yang et al. 2008). The emphasis of this chapter is focused on to investigate the influence of the geometry of fissure on strength parameters of marble material, to put forward a new evaluation criterion of confirming the cohesion and internal friction angle of pre-cracked marble, to analyze the crack initiation, propagation, and coalescence in real marble material under different confining pressures.

### 8.1 Experimental Methodology

#### 8.1.1 Marble Material

In order to investigate the mechanical behavior of rock with two pre-existing closed cracks, the marble material located in the midland ground of China was chosen for the experimental study in this chapter. The marble has a crystalline and blocky structure, which is macroscopically very homogeneous with average unit weight about  $2704 \text{ kg/m}^3$ .

The minerals in the marble specimens are mainly calcite, dolomite, and magnesite, and the chemical components are mainly Ca and Mg. The tested marble samples are classified into two categories based on the crystal size, i.e., “medium marble” and “coarse marble.”

For the medium marble, the crystal size is in the range of 1.0–4.0 mm (1.5 mm in average), while for the coarse marble, the crystal size ranges 4.0–6.0 mm (5.0 mm in average). The average crystal size of the marble was determined by optical microscope and SEM. The crystal size of medium marble is very nonuniform, resulting in a greater hardness, compared to the coarse marble, which has been submitted to higher recrystallization in shorter time. As a consequence, the average velocity of P-wave of medium marble is about 5101 m/s, while coarse marble is only 4507 m/s (Yang et al. 2003).

### 8.1.2 Pre-cracked Sample Preparation

In this chapter, a total of seventy marble samples were prepared to carry out uniaxial and conventional triaxial compression tests (the confining pressure equaled to 0, 5, 10, 15, 20, 30, 35, and 40 MPa). The samples were drilled from six rectangular blocks. When drilling, we machined the marble samples along the same direction in order to avoid the influence of anisotropy on the experimental results of marble. At the same time, machined marble samples were observed and carefully selected to preserve samples suitable for testing. In order to obtain the exact results as well as the best comparison, all the experiments were carried out in natural and dry conditions.

In accordance with the method suggested by the ISRM (Fairhurst and Hudson 1999), the length to diameter ratio of tested sample should be in the range of 2.0–3.0, in order to minimize the influence of the end friction effects on the testing results. Therefore, the size of all tested marble samples is cylindrical with 50 mm in diameter and 100 mm in length. As a result, all tested samples with the length to diameter ratio of 2.0 ensure a uniform stress state within the samples. The strength behaviors of samples under conventional triaxial compression tests were also determined according to the method suggested by the ISRM. Some intact machined marble samples are shown in Fig. 8.1, in which the comparison on the crystal size between medium and coarse marble is also given.

The geometry of flawed sample is described in Figs. 8.2 and 8.3. The flaw length is  $2a$ , flaw angle (the angle of flaw with the direction of the maximum compressive

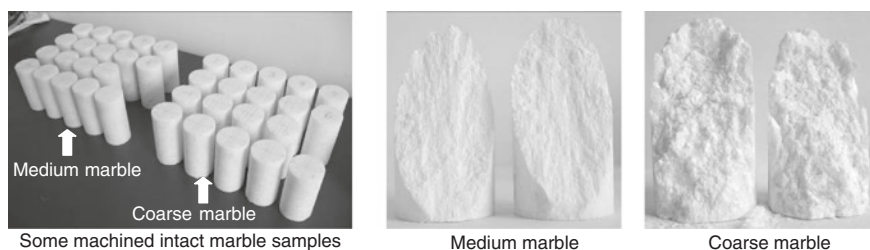


**Fig. 8.1** Some intact machined medium and coarse marble samples and respective fracture surfaces (with kind permission of Elsevier Publisher)

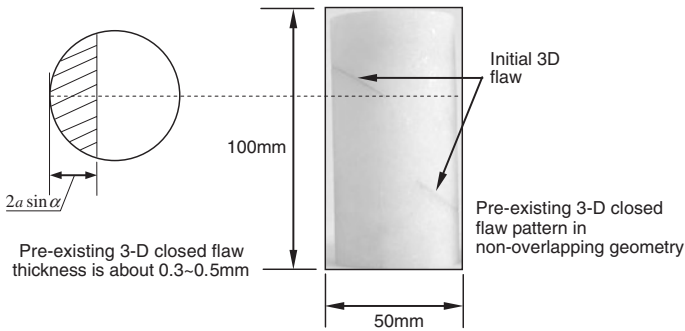


**Fig. 8.2** Flawed marble sample in nonoverlapping geometry (with kind permission of Elsevier Publisher)

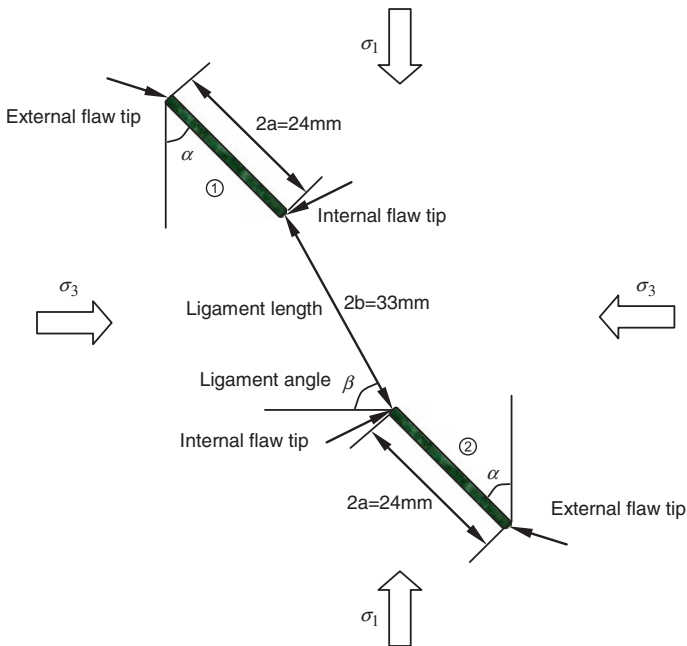


**Fig. 8.3** Geometry of flaws in the flawed sample (with kind permission of Elsevier Publisher)

stress) is  $\alpha$ , ligament angle (the angle of the line connected between two internal flaw tips with the direction of the confining pressure) is  $\beta$ , and ligament length (the distance between two internal flaw tips) is  $2b$ . To simplify the present analysis, the flaw length  $2a$  and ligament length  $2b$  are fixed at 24 and 33 mm, respectively.

A high-speed electric cutting machine was used to cut 3D flaws in the intact samples. Machined flaw thickness is about 0.3–0.5 mm. At the same time, the gypsum was chosen to fill into the flaw of samples in order to form the closed flaws

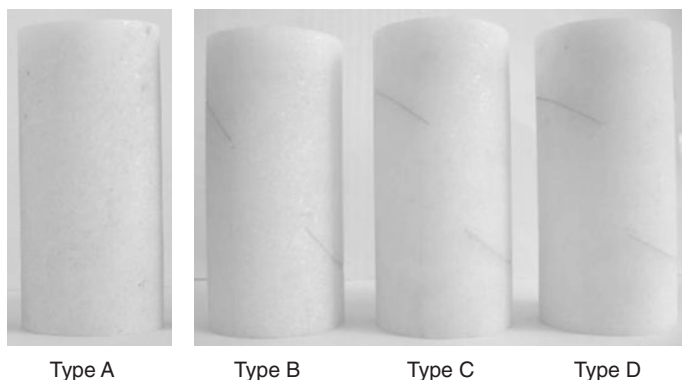


**Fig. 8.4** Four types of geometries of flaws of marble, in which Type A is intact sample; however, Types B, C, and D are all flawed sample with different pre-existing flaws (with kind permission of Elsevier Publisher)

**Table 8.1** Pre-existing crack geometries of flawed marble samples

Marble type	Flaw geometry	$\alpha$	$\beta$	$2a$ (mm)	$2b$ (mm)	$\sigma_3$ (MPa)
Coarse marble	Type A	N/A	N/A	N/A	N/A	0–30
	Type B	30	38	24	33	0–30
	Type C	45	61	24	33	0–30
	Type D	60	75	24	33	0–30
Medium marble	Type A	N/A	N/A	N/A	N/A	0–40
	Type B	30	38	24	33	0–30
	Type C	45	61	24	33	0–30
	Type D	60	75	24	33	0–30

(Dai 2006), which resulted from that the gypsum could be regarded as a weak material (Bobet and Einstein 1998). The mechanical parameters of this gypsum in this chapter are as follows: elastic modulus is  $\sim 1.2$  GPa, uniaxial compressive strength (UCS)  $\sim 6$  MPa, and Poisson's ratio  $\sim 0.31$ .

In order to investigate the effect of pre-existing crack geometry on the strength and deformation behavior of marble under different confining pressures, four types of geometries of flaws (Fig. 8.4) were chosen in this chapter. Detailed description for marble samples with different flaw geometries was listed in Table 8.1.

### 8.1.3 Experimental Procedure

Uniaxial and conventional triaxial compression experiments for intact and flaw marble samples were carried out on a rock servo-controlled system with the maximum loading capacity of 2000 kN and the maximum displacement capacity of

25 mm. This servo-controlled system can test samples in load or displacement control while the data from Linear Variable Displacement Transducer (LVDT) are recorded and analyzed in real time. Before applying the axial loads, the confining pressure was first applied to the sample at a constant rate of 0.5 MPa/s, which ensured that the sample was under uniform hydrostatic stresses. And then, the axial deviatoric stress began to impose the surface of rock sample at the 0.002 mm/s displacement control rate until the failure took place.

In this research, we measured the axial force with the loading capacity of 1000 KN and the axial deformation with the displacement capacity of 5 mm. During the whole uniaxial and triaxial compression experiments, loads and deformations of the tested marble samples were recorded simultaneously. Moreover, two rigid steel cylinders (50 mm in diameter and 20 mm in length) were placed between the loading frame and rock sample, which decreased distinctly the influence of the end friction effects on the testing results of marble samples with the length to diameter ratio ~2.0 (Yang et al. 2005a).

## 8.2 Triaxial Experimental Results of Pre-cracked Marble

### 8.2.1 Brittle-Ductile Transition Mechanism of Intact Marble

Typical axial stress-axial strain curves for intact coarse and medium marbles (Type A) are shown in Figs. 8.5 and 8.6, respectively, in which the denoted number is the confining stress, MPa. In accordance with Figs. 8.5 and 8.6, we can conclude that the yielding stress (the stress value that begins to depart the linear elastic phase in the axial stress–strain curve) and triaxial compressive strength (TCS) of intact sample increase gradually with the confining pressure.

**Fig. 8.5** Typical triaxial stress–strain curves of intact coarse marble (Type A) (with kind permission of Elsevier Publisher)

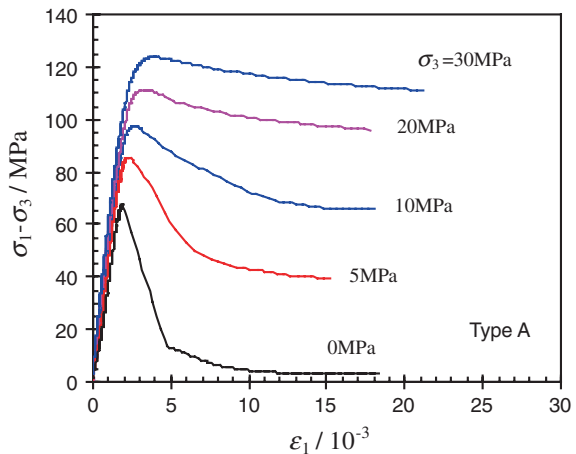
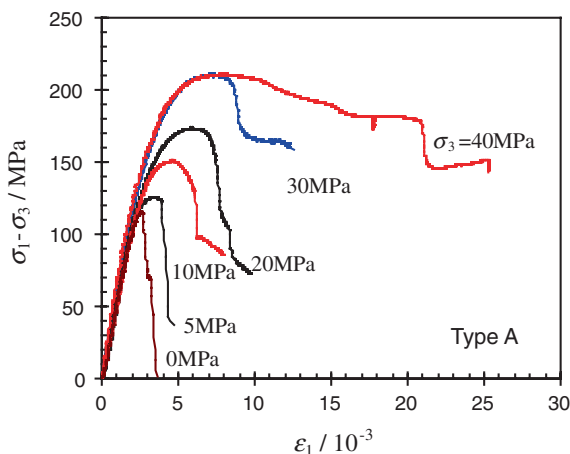


**Fig. 8.6** Typical triaxial stress–strain curves of intact medium marble (Type A) (with kind permission of Elsevier Publisher)



For intact coarse marble shown in Fig. 8.5, the post-peak deformation changes gradually from softening to hardening. When  $\sigma_3$  equals, approximately, to  $\sim 30$  MPa, the deformation of the sample comes out distinct yielding platform and the plastic flow takes place, i.e., the post-peak deformation behavior of the sample changes into an ideal plasticity. At this time, the corresponding  $\sigma_3 = 30$  MPa can be called transition confining pressure (TCP). However, when  $\sigma_3$  is lower than  $\sim$ TCP, the stress–strain curve displays a point of TCS. This brittle-ductile transition (BDT)  $\sigma_3$  of intact coarse marble happens at about 30 MPa. The ratio of TCP to the average value of UCS is  $\sim 0.43$ .

For intact medium marble shown in Fig. 8.6, triaxial experimental curves have some similarity and some differences as shown in Fig. 8.5. Even though no distinct yielding platform under tested maximum  $\sigma_3 = 40$  MPa, the samples that showed brittleness under lower  $\sim\sigma_3$  changes into plasticity and ductility under higher  $\sim\sigma_3$ . Moreover, we can find that the mechanical parameters of intact medium marble are higher than that of intact coarse marble at the same confining pressure. Besides, in accordance with Fig. 8.5, it can be seen that the Young's modulus of intact coarse marble increases with the confining pressure, while the Young's modulus of intact medium marble according to Fig. 8.8 appears to be independent of the confining pressure. However, intact medium marble shows more nonlinear deformation before peak stress and more brittleness after peak stress than intact coarse marble.

The mechanism on the BDT of intact marble sample shown in Figs. 8.5 and 8.6 can be made a qualitative discussion as follows. For intact marble material, it is homogeneous from the macroscopic view, but strongly heterogeneous at the mesoscopic scale. Macroscopic fracture phenomenon may be regarded as the average effect of much mesoscopic failure and heterogeneous mesoscopic failure can be described by probability and statistics theory such as Weibull distribution, etc. (Xie and Gao 2000; Wong et al. 2006). Thus, we can believe that mesoscopic element material can be regarded as a random variable and distributes randomly in the rock sample. Moreover, the mesoscopic element material may be thought as the synthetical result of many factors such as the ratio of mineral constituent, size of

grain, behavior of agglutinate, distribution of flaw in the rock, etc. (Zhu and Tang 2004; Yuan and Harrison 2006). Therefore, the strength and stiffness of mesoscopic element material in the sample varies strongly from one element to another.

Under lower confining pressures, with the increase of loading, many mesoscopic material elements with low strength and stiffness reach first its maximum supporting capacity, yield softening and produce plastic deformation during the yielding of sample. But after the macroscopic stress–strain response of tested marble sample reaches the peak stress, the mesoscopic material elements with high strength and stiffness will unload due to not reaching its maximum supporting limit, for the moment, the plastic deformation in the sample does not tend to uniform. Therefore, with the decreasing macroscopic axial deviatoric stress, the plastic deformation initiated further will concentrate on those failed mesoscopic material elements with low strength and stiffness, which results in a localized deformation. As a result, the samples under lower confining pressures show a softening behavior.

Under higher confining pressures, the mesoscopic material elements with low strength and stiffness reach first its maximum supporting capacity, yield softening and produce the plastic deformation. Afterward, if we want to make the sample to fail macroscopically, the axial stress must be increased continuously. Thus when the macroscopic stress–strain response of tested marble sample reaches the peak stress, the mesoscopic material elements with higher strength and stiffness in the sample will also reach its maximum supporting limit, yielding failure and initiating plastic deformation. Therefore, the total deformation in the sample will tend to uniform and then plastic deformation of the sample will also increase, which results in distinct yielding platform in the macroscopic stress–strain curves nearby the peak stress. However, when the confining pressure reaches to  $\sim$ TCP, the yielding failure takes place in all the mesoscopic material elements in the sample while the macroscopic stress–strain response of the sample reaches the peak stress, which results in that the intact sample initiates the plastic flow.

### 8.2.2 Triaxial Stress–Strain Curves of Pre-cracked Marble

Figure 8.7 shows typical triaxial stress–strain curves for pre-cracked coarse marble with different geometries of flaws (Types B, C, and D), and Fig. 8.8 for pre-cracked medium marble with different geometries of flaws (Types B, C, and D). From Figs. 8.7 and 8.8, it is very clear that the yielding stress and TCS of flawed sample increase gradually with the confining pressure but existing the strength difference compared with intact sample, which will be analyzed in detail in the next section. Besides, the stress–strain curve of flawed samples shows an abrupt change of slope (see Figs. 8.7 and 8.8) under lower confining pressures, coincident with the propagation of wing cracks at the internal tips of two flaws.

Tables 8.2 and 8.3 list the strength  $\sim\sigma_S$  (the maximum axial supporting capacity, i.e., the maximum compressive stress), elastic modulus  $\sim E_S$  (the slope of approximation linear part in the stress–strain curve), and failure strain  $\sim\varepsilon_c$  (the strain value at rupture in terms of the stress–strain curve) of coarse and medium marbles with different

**Fig. 8.7** Typical triaxial stress–strain curves of pre-cracked coarse marble samples with different flaw geometries (Types B, C, and D) (with kind permission of Elsevier Publisher)

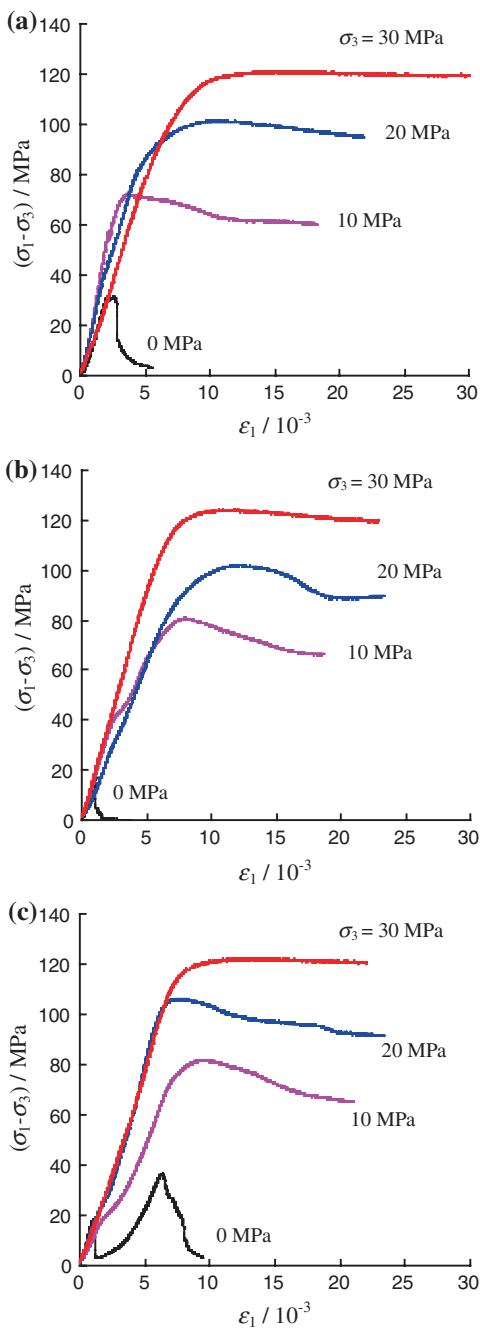


**Fig. 8.8** Typical triaxial stress–strain curves of pre-cracked medium marble samples with different flaw geometries (Types B, C, and D) (with kind permission of Elsevier Publisher)

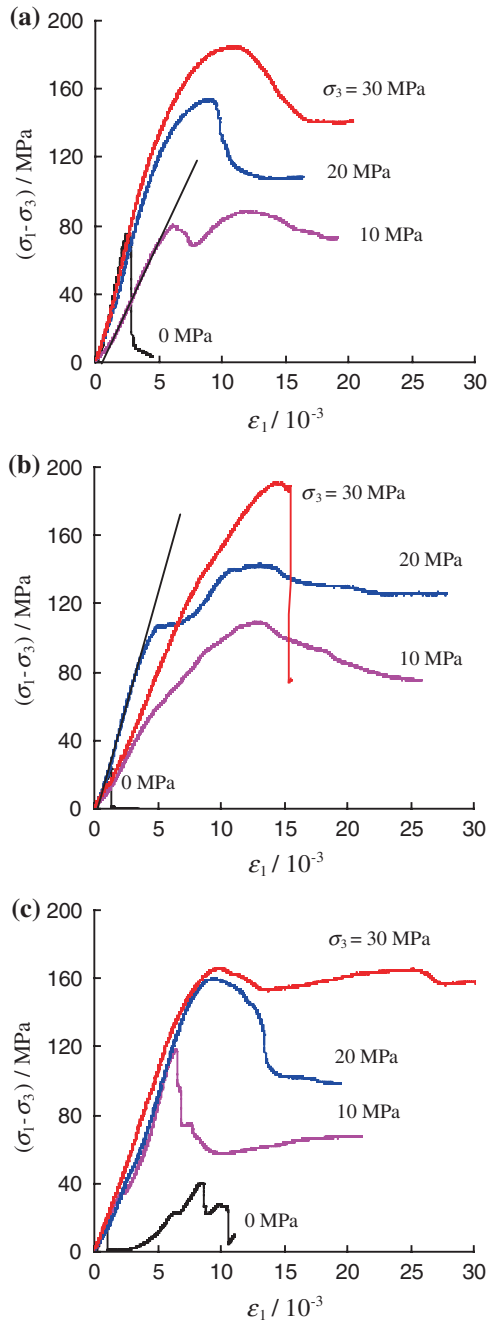


**Table 8.2** Strength, elastic modulus, and failure strain of coarse marble with different geometries of flaws and confining stresses

Geometry of flaw	$\sigma_3$ (MPa)	$E_S$ (GPa)	$\varepsilon_c$ ( $10^{-3}$ )	$\sigma_S$ (MPa)
Type A	0	45.54	2.082	69.83
	10	49.34	2.602	109.4
	20	50.64	3.071	129.3
	30	53.61	3.917	154.4
Type B	0	18.26	2.066	31.2
	10	29.41	3.568	82.2
	20	17.48	10.33	121.6
	30	16.38	14.00	150.7
Type C	0	19.78	1.050	17.2
	10	16.07	7.546	90.4
	20	13.06	12.22	122.3
	30	18.43	10.94	154.5
Type D	0	20.29	6.320	36.6
	10	12.98	9.428	91.8
	20	18.92	7.325	126.4
	30	16.78	12.73	155.3

**Table 8.3** Strength, elastic modulus, and failure strain of medium marble with different geometries of flaws and confining stresses

Geometry of flaw	$\sigma_3$ (MPa)	$E_S$ (GPa)	$\varepsilon_c$ ( $10^{-3}$ )	$\sigma_S$ (MPa)
Type A	0	49.90	2.711	119.3
	10	51.25	4.497	161.2
	20	50.39	5.992	193.6
	30	50.51	7.951	235.9
Type B	0	37.20	2.550	75.1
	10	16.66	11.75	98.5
	20	27.10	9.013	173.8
	30	31.42	11.16	214.6
Type C	0	21.70	1.325	23.8
	10	13.56	13.01	119.3
	20	26.19	13.21	163.3
	30	18.01	14.38	221.2
Type D	0	21.01	8.460	39.9
	10	28.27	6.458	128.7
	20	23.96	9.470	180.2
	30	22.17	9.879	196.2

flaw geometries and confining stresses. The mechanical parameters are the average value of tested samples for each same confining pressure. For the stress–strain curves of flawed sample with an abrupt change of slope, the linear phase before abrupt point were adopted to calculate the elastic modulus as shown in Fig. 8.8a, b.

The intact coarse marble samples failed at a strain of approximately 0.2–0.4 % under different confining pressure, while the intact medium marble samples failed at a strain of approximately 0.3–0.8 %, which were greater than that of the intact

coarse marble samples. Moreover, we found that  $\varepsilon_c$  of intact sample increased linearly with increasing  $\sigma_3$ , which had been proved in previous research on intact marble material by Yang et al. (2005b). However for flawed marble, the failure strain usually ranged from 0.2 to 1.4 % and increased nonlinearly with increasing  $\sigma_3$  for the same geometry of flaw, which was significantly dependent to pre-cracked coalescence in the flawed sample under different confining pressures.

In uniaxial compression, for Type C, the flaw angle  $\alpha = 45^\circ$  and ligament angle  $\beta = 61^\circ$  made the sample easier for a failure surface through the ligament to produce the shear failure mode. The only two flawed samples (Type C for coarse and medium marbles, respectively) failed at small strains (only 0.11–0.13 % lesser than 0.2 %) and was usually brittle (Figs. 8.7b and 8.8b). However, the two flawed samples (Type B for coarse and medium marbles at  $\sigma_3 = 0$  MPa, respectively) failed at a strain of about 0.21 and 0.26 %, which is approximately equal to that of intact sample. Except the above four flawed samples, the failure strains of other flawed samples were all greater than that of intact samples at the same confining pressure. Under the confining pressure, the only flawed sample (Type C for medium marble at  $\sigma_3 = 30$  MPa) underwent brittle failure at a strain of approximately 1.4 % (Fig. 8.8b).

From Tables 8.2 and 8.3, it can also be concluded that the elastic moduli of flawed sample are all smaller than that of intact sample, which can be explained as follows. Due to the heterogeneity of rock material, the existence of flaws in the sample results in the increase of slipping interface; therefore, the slippage of flawed sample will also increase in the process of axial compression, which reduces the elastic modulus of rock. Moreover, because the crack coalescence in the flawed sample with different geometries of flaws vary greatly with the confining pressure, the elastic modulus of flawed sample has no quantitative relation with the geometry of flaw and confining pressure.

In accordance with the tested data listed in Tables 8.2 and 8.3, generally, the strength and deformation behaviors of marble sample are found depending not only on the flaw geometry, but also on the confining pressure. Compared with the intact sample, the flawed sample failed with lower strengths, smaller elastic moduli, and larger failure strains, which is a better agreement with the findings for model material with nonpersistent joints by Prudencio and Van Sint Jan (2007). In the fifth section, we will make a detailed analysis for the mechanism of crack coalescence on the axial supporting capacity and deformation property with different confined stresses.

## 8.3 Strength Behavior of Pre-cracked Marble

### 8.3.1 *Strength Behavior in Accordance with Mohr-Coulomb Criterion*

The Mohr-Coulomb criterion is the simplest among numerous strength criteria that have been developed, which has been extensively applied in rock engineering practice (Mohr 1914; Jaeger and Cook 1979; Brady and Brown 1993; Zhao 2000; Palchik 2006; Al-Ajmi and Zimmerman 2006). This strength criterion states that

the shear failure occurs when the shear stress on a failure plane overcomes both the cohesion and the internal friction force that opposes motion along the failure plane, as shown in Fig. 8.9. It predicts that shear stress  $\tau$  increases linearly with the normal stress  $\sigma_n$ , which can be expressed in the following forms.

$$\begin{cases} \tau = C + \mu\sigma_n \\ \sigma_n = 0.5(\sigma_1 + \sigma_3) + 0.5(\sigma_1 - \sigma_3) \cos 2\alpha \\ \tau = 0.5(\sigma_1 - \sigma_3) \sin 2\alpha \end{cases} \quad (8.1)$$

where  $C$  is the cohesion of rock,  $\mu$  is the internal friction coefficient ( $\mu = \tan\varphi$ ), and  $\varphi$  is the internal friction angle of rock.

The linear Mohr-Coulomb criterion Eq. (8.1) can also be expressed in terms of the maximum axial supporting capability  $\sigma_S$  and the minimum principal stress  $\sigma_3$  (i.e., confining pressure):

$$\sigma_S = \sigma_0 + q\sigma_3 \quad (8.2)$$

where  $\sigma_0$  is usually regarded as UCS;  $\sigma_0$  and  $q$  are related to the cohesion  $C$  and the internal friction angle  $\varphi$ , which can be expressed in the following forms, respectively.

$$\sigma_0 = 2C \cos \varphi / (1 - \sin \varphi) \quad (8.3)$$

$$q = (1 + \sin \varphi) / (1 - \sin \varphi) \quad (8.4)$$

In accordance with Mohr-Coulomb criterion Eq. (8.2), the influence of confining pressure on the maximum supporting capability for intact marble sample is presented in Fig. 8.9. It is very clear that there are good linear regression coefficients of  $R = 0.990$  and  $0.985$ , respectively, for intact medium and coarse marble. From Fig. 8.9, we can see that the intact coarse and medium marbles all takes on typical shear failure mode even though in uniaxial compression (see the failure mode as shown in Fig. 8.9). Therefore, it can be believed that experimental results of intact sample have a smaller deviation from the linear Mohr-Coulomb criterion, which testifies that linear Mohr-Coulomb criterion is suitable for intact sample in this research. However, for flawed marble samples, in accordance with Mohr-Coulomb criterion the influence of  $\sigma_3$  on  $\sigma_S$  are presented in Figs. 8.10 and 8.11, respectively, for coarse and medium marbles. Even though with higher linear regression coefficient ( $R = 0.954$ – $0.990$ ) using the linear least square method, it is very clear that there is an obvious nonlinear relation between  $\sigma_S$  of flawed sample and  $\sigma_3$ , and this will be analyzed in detail in the next section. Here only strength behavior is analyzed in terms of Mohr-Coulomb criterion.

In accordance with Figs. 8.10 and 8.11, it is clear that  $\sigma_0$  ranges from 29.53 to 43.92 MPa for flaw coarse marble, while from 36.51 to 66.43 for flawed medium marble. However,  $q$  is between 3.91 and 4.44 for flaw coarse marble, but between 4.94 and 6.36 for flawed medium marble. The values of cohesion ( $C$ ) and internal friction angle ( $\varphi$ ) calculated according to Eqs. (8.3) and (8.4) for marble samples

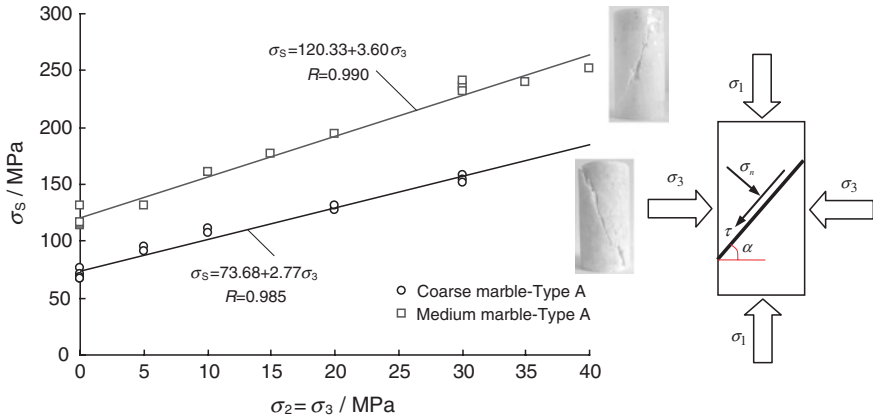


**Fig. 8.9** Strength behavior of intact coarse and medium marbles in accordance with Mohr-Coulomb criterion. *Open circle* and *open square* represent the experimental results. *R* is the correlation coefficient of determination of the linear regression (with kind permission of Elsevier Publisher)

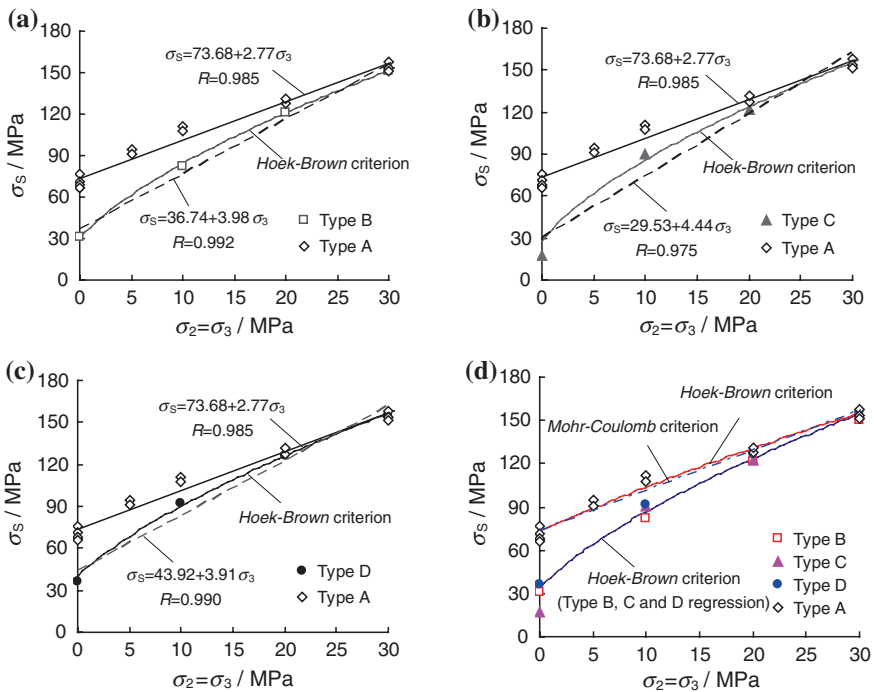


**Fig. 8.10** Strength analysis of coarse marble with pre-existing cracks. All the *symbols* represent the experimental results and the *lines* represent the theoretical values in accordance with Mohr-Coulomb or Hoek-Brown criterion. *R* is the correlation coefficient of determination of the regression (with kind permission of Elsevier Publisher)

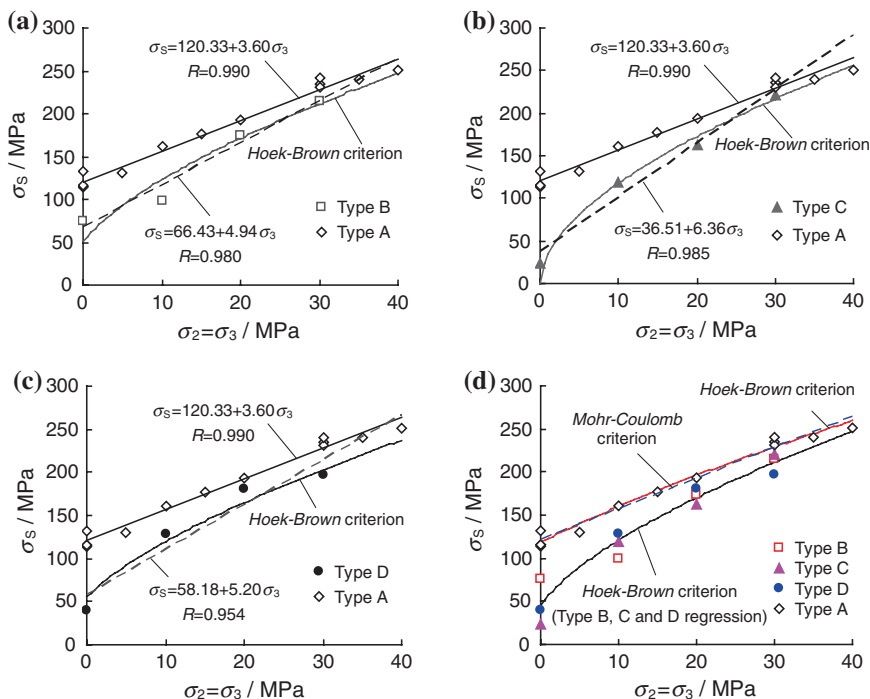


**Fig. 8.11** Strength analysis of medium marble with pre-existing cracks. All the *symbols* represent the experimental results and the *lines* represent the theoretical values in accordance with Mohr-Coulomb or Hoek-Brown criterion. *R* is the correlation coefficient of determination of the regression (with kind permission of Elsevier Publisher)

**Table 8.4** Strength parameters of intact and flawed marbles in accordance with linear Mohr-Coulomb criterion

Marble type	Geometry of flaw	UCS (MPa)	$\sigma_0$ (MPa)	$q$	$C$ (MPa)	$\varphi$ ( $^\circ$ )	$R$
Coarse marble	Type A	69.83	73.68	2.77	22.14	28.0	0.985
	Type B	31.20	36.74	3.98	9.21	36.8	0.992
	Type C	17.20	29.53	4.44	7.01	39.2	0.975
	Type D	36.60	43.92	3.91	11.11	36.3	0.990
Medium marble	Type A	119.3	120.33	3.60	31.71	34.4	0.990
	Type B	75.01	66.43	4.94	14.94	41.6	0.980
	Type C	23.83	36.51	6.36	7.24	46.7	0.985
	Type D	39.87	58.18	5.20	12.76	42.6	0.954

with four types of geometries of flaws (Type A, B, C and D) are presented in Table 8.4. From Table 8.4, it can be seen that the values of  $C$  range from 7.01 to 31.71 MPa, while the values of  $\varphi$  are between 28.0 and 46.7°. The above analysis shows that the values of  $C$  and  $\varphi$  are significantly dependent to the geometry of

flaw in the sample. Generally, for marble with the same crystal size, the value of  $C$  of flawed sample (Types B, C and D) is lower than that of intact sample (Type A), while the value of  $\varphi$  is higher than that of intact sample. The value of  $C$  of flawed sample with Type C is lower than that with Type B or D, but the value of  $\varphi$  of flawed sample with Type C is higher than that with Type B or D. Moreover from Figs. 8.10 and 8.11, we can predict that there must be a limiting value of  $\sigma_3$ , beyond this limiting value, the strength of coarse and medium marble sample may be independent of the geometry of flaw.

### 8.3.2 Strength Behavior in Accordance with Hoek-Brown Criterion

The Hoek-Brown criterion is an empirical strength criterion, which was originally derived from a lot of test data. Up to now, the Hoek-Brown criterion has been applied widely to rock mechanics and engineering practice. The basic equation describing the peak TCS of a wide range of isotropic rock materials can be written as Hoek and Brown (1980, 1997).

$$\sigma_S = \sigma_3 + (m\sigma_c\sigma_3 + s\sigma_c^2)^{0.5} \quad (8.5)$$

where  $\sigma_c$  is UCS of intact rock material,  $m$  and  $s$  are all material parameters, which vary with rock type. The parameter  $m$  reflects the soft and hard extent. When the parameter  $m$  is larger, the rock is harder. However, the parameter  $s$  reflects the fractured extent ranging from 0 to 1. When the parameter  $s$  is closer to zero, the rock is more broken.

Figures 8.10 and 8.11 show the Hoek-Brown strength envelope for coarse and medium marbles, respectively. At the same time, linear Mohr-Coulomb criterion is also plotted in Figs. 8.10 and 8.11 in order to compare. It is very clear for intact sample that there are almost no difference between Hoek-Brown criterion and Mohr-Coulomb criterion, which can be seen from Figs. 8.10d and 8.11d. However, the strength of flawed sample (Types B, C, and D) possesses distinct nonlinear behavior with increasing confining pressure, which shows that nonlinear Hoek-Brown criterion reflects better the strength properties of flawed sample than linear Mohr-Coulomb criterion. Therefore, for flawed sample, linear Mohr-Coulomb criterion predicts the rock strength higher than its actual value at lower confining pressure or higher confining pressure, but predicts the rock strength lower than its actual value at intermediate confining pressure.

The Hoek-Brown strength parameters of coarse and medium marbles with four types of geometries of flaws are listed in Table 8.5. Here,  $\sigma_c$  is the experimental average value of UCS of intact samples. As expected, it can be found that the value of  $s$  for intact sample is approximately 1.0. But the values of  $m$  for intact sample are 4.926 and 7.164, respectively, for coarse marble and medium marble. However, the value of  $s$  for flawed sample ranges from 0 to 0.329 which is

**Table 8.5** Strength parameters of intact and flawed marbles in accordance with nonlinear Hoek-Brown criterion

Marble type	Geometry of flaw	$\sigma_c$ (MPa)	$m$	$s$	$a$	$R$
Coarse marble	Type A	69.83	4.926	1.097	0.5	0.983
	Type B	69.83	6.631	0.182	0.5	0.999
	Type C	69.83	7.168	0.152	0.5	0.996
	Type D	69.83	6.893	0.329	0.5	0.999
Medium marble	Type A	119.3	7.164	0.986	0.5	0.983
	Type B	119.3	8.474	0.185	0.5	0.967
	Type C	119.3	9.743	0.000	0.5	0.992
	Type D	119.3	7.513	0.216	0.5	0.963

significantly lower than that of intact sample, but the value of  $m$  for flawed sample ranging from 6.631 to 9.734 is slightly higher than that of intact sample.

From Eqs. (8.2) and (8.5), it can be seen that there is no direct correlation between linear Mohr-Coulomb criterion and nonlinear Hoek-Brown criterion. In most of the geotechnical software, the strength parameters ( $C$  and  $\varphi$ ) of rock often need to be provided when carrying out the numerical analysis, but determination of the values of  $C$  and  $\varphi$  for a kind of rock that has been evaluated as a Hoek-Brown material is a difficult problem (Hoek and Brown 1997). The tangent method theory, which was put forward by Hoek and Brown (1997), Hoek (1990) can be used to confirm approximately the equivalent  $C$  and  $\varphi$  of rock.

For a given confining pressure  $\sigma_3$ , the tangent line of Eq. (8.5) is actually linear Mohr-Coulomb criterion Eq. (8.2). If Eq. (8.5) is differentiated with respect to  $\sigma_3$ , the following equation can be obtained.

$$\frac{\partial \sigma_S}{\partial \sigma_3} = 1 + \frac{m\sigma_c}{2\sqrt{m\sigma_c\sigma_3 + s\sigma_c^2}} \quad (8.6)$$

Thus in accordance with Eq. (8.4), Eq. (8.7) can be obtained.

$$q = \frac{1 + \sin \varphi}{1 - \sin \varphi} = \frac{\partial \sigma_S}{\partial \sigma_3} = 1 + \frac{m\sigma_c}{2\sqrt{m\sigma_c\sigma_3 + s\sigma_c^2}} \quad (8.7)$$

According to Eq. (8.7), the internal friction angle can be expressed in Hoek-Brown parameters  $m$  and  $s$ , i.e.,

$$\varphi = 2 \arctan \sqrt{1 + \frac{m\sigma_c}{2\sqrt{m\sigma_c\sigma_3 + s\sigma_c^2}}} - 90^\circ \quad (8.8)$$

If Eq. (8.5) is substituted into Eq. (8.2), Eq. (8.9) can be obtained.

$$\sigma_0 = \frac{2C \cos \varphi}{1 - \sin \varphi} = (1 - q)\sigma_3 + \sqrt{m\sigma_c\sigma_3 + s\sigma_c^2} \quad (8.9)$$

Therefore in accordance with Eqs. (8.7) and (8.9), the cohesion can be expressed in the following form.

$$C = \frac{\frac{m\sigma_c\sigma_3 + 2s\sigma_c^2}{\sqrt{m\sigma_c\sigma_3 + s\sigma_c^2}}}{4\sqrt{1 + \frac{m\sigma_c}{2\sqrt{m\sigma_c\sigma_3 + s\sigma_c^2}}}} \quad (8.10)$$

According to Eqs. (8.8) and (8.10),  $C$  and  $\varphi$  for a kind of rock that has been evaluated as a Hoek-Brown material can be confirmed. It can be seen that the values of  $C$  and  $\varphi$  are very sensitive to the range of values of  $\sigma_3$  used to generate the simulated full-scale triaxial test results. On basis of trial and error method, Hoek and Brown (1997) found that the most consistent results can be approximately obtained in the range  $0 < \sigma_3 < 0.25\sigma_c$ . Therefore, Eqs. (8.8) and (8.10) can be transferred into the following forms by denoting  $\sigma_3 = k\sigma_c$  ( $k = 0-0.25$ ).

$$\varphi = 2 \arctan \sqrt{1 + \frac{m}{2\sqrt{km + s}}} - 90^\circ \quad (8.11)$$

$$C = \frac{\frac{(km + 2s)\sigma_c}{\sqrt{km + s}}}{4\sqrt{1 + \frac{m}{2\sqrt{km + s}}}} \quad (8.12)$$

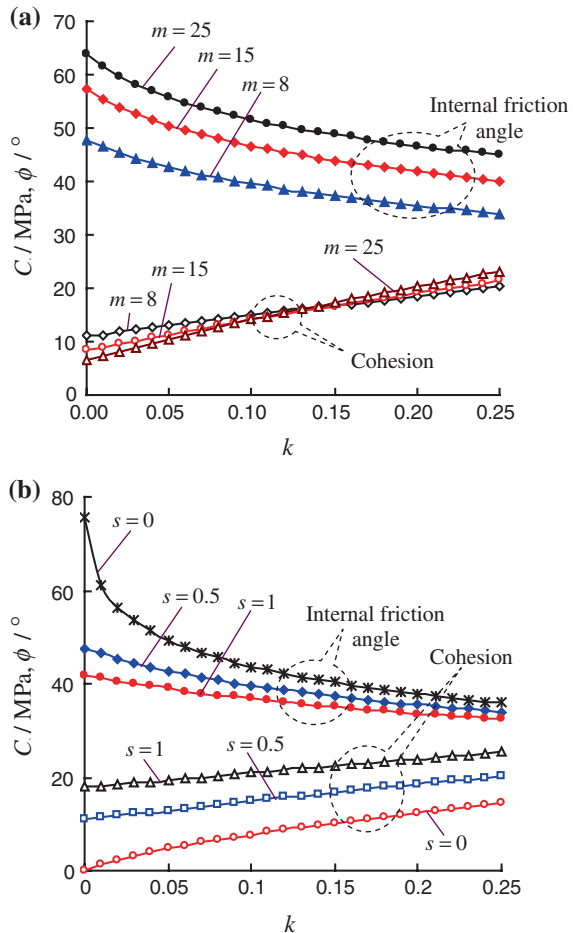
Figure 8.12 shows the effect law of  $m$  and  $s$  values on the relation between  $C$ ,  $\varphi$  and confining pressure  $\sigma_3 = k\sigma_c$ . From Fig. 8.12, we can conclude that the  $C$  and  $\varphi$  of rock are actually the function of  $\sigma_3$ , in which, the  $C$  values increase with increasing  $\sigma_3$ , but the  $\varphi$  values decrease with increasing  $\sigma_3$ .

The effect of parameter  $m$  on the relation between the strength parameters and confining pressure is shown in Fig. 8.12a when  $s$  and  $\sigma_c$  equal to 0.5 and 80 MPa, respectively. From Fig. 8.12a, it can be seen that, at the same confining pressure, the  $\varphi$  values increase with the increasing of parameter  $m$ . Moreover,  $\varphi$ - $k$  curve becomes steeper with increasing parameter  $m$ . But after  $k$  increases to a certain critical value, the  $\varphi$ - $k$  curve has a tendency to converge. With a greater parameter  $m$ , the  $C$  values are more sensitive to  $k$ .

The effect of parameter  $s$  on the relation between the strength parameters and confining pressure is shown in Fig. 8.12b when  $m$  and  $\sigma_c$  equal to 8 and 80 MPa, respectively. From Fig. 8.12b, it can be seen that, at the same confining pressure, the  $\varphi$  values increase with the decreasing of parameter  $s$ . Moreover,  $\varphi$ - $k$  curve becomes steeper with decreasing parameter  $s$ . But after  $k$  increases to a certain critical value, the  $\varphi$ - $k$  curve has a tendency to converge. However at the same confining pressure, the  $C$  values increase with increasing values of the parameter  $s$ ; moreover, the  $C$ - $k$  curve becomes slower with increasing parameter  $s$ .

Table 8.6 lists the cohesion and internal friction angle ( $k = 0.06, 0.08, 0.10, 0.12, 0.14, \text{ and } 0.16$ ) of coarse and medium marbles, which are calculated based on the tangent method theory by Eqs. (8.11) and (8.12). Compared with the

**Fig. 8.12** The effect of the parameter  $m$  and  $s$  on the relation between the strength parameters and confining pressure (with kind permission of Elsevier Publisher)



strength parameters listed in Table 8.4, it can be seen in Table 8.6, the friction angle ( $k = 0.16$ , i.e.,  $\sigma_3 = 11.2$  MPa) of coarse marble and the friction angle ( $k = 0.10$ , i.e.,  $\sigma_3 = 11.9$  MPa) of medium marble are approximately the same for both the tangent and the line determined by linear Mohr-Coulomb regression analysis. The maximum discreteness of friction angle is only  $\sim 4\%$ . For intact sample, the cohesion calculated by tangent method theory has almost no any difference with that by linear Mohr-Coulomb regression analysis of triaxial test data, for example,  $\sim 22.89$  MPa compared with  $\sim 22.14$  MPa for coarse marble and  $\sim 31.75$  MPa compared with  $\sim 31.71$  MPa for medium marble. However for flawed coarse marble sample, the cohesion intercept for the tangent is  $C = 11.01$  MPa (Type C,  $k = 0.16$ ) which is approximately 57% higher than that obtained by linear regression analysis of triaxial test data. For flawed medium marble sample, the cohesion intercept for the tangent is  $C = 9.28$  MPa (Type B,  $k = 0.10$ ) which is approximately 61% lower than that obtained by linear regression analysis of triaxial test data.

**Table 8.6** The cohesion and internal friction angle of intact and flawed marbles based on the tangent method theory in accordance with Hoek-Brown parameters (Table 8.5)

Marble type	Geometry of flaw	k = 0.06		k = 0.08		k = 0.10		k = 0.12		k = 0.14		k = 0.16	
		C (MPa)	$\varphi$ (°)										
Coarse marble	Type A	21.15	30.7	21.49	30.1	21.84	29.6	22.19	29.1	22.54	28.7	22.89	28.2
	Type B	7.62	43.3	8.41	41.5	9.17	40.0	9.90	38.8	10.61	37.7	11.29	36.7
	Type C	7.10	44.5	7.95	42.7	8.76	41.1	9.54	39.8	10.29	38.7	11.01	37.7
	Type D	9.80	41.8	10.50	40.4	11.19	39.1	11.86	38.0	12.52	37.0	13.16	36.2
Medium marble	Type A	30.06	36.9	30.91	36.1	31.75	35.3	32.60	34.7	33.44	34.0	34.27	33.4
	Type B	7.53	45.9	8.43	44.0	9.28	42.5	10.10	41.2	10.89	40.1	11.66	39.1
	Type C	4.96	49.6	6.09	47.2	7.14	45.4	8.12	43.8	9.05	42.5	9.93	41.4
	Type D	8.05	44.2	8.86	42.5	9.65	41.0	10.41	39.8	11.15	38.7	11.86	37.7

### 8.3.3 A New Evaluation Criterion Based on Optimal Approximation Polynomial Theory

Based on the above tangent method theory, many cohesions and internal friction angles for a kind of rock that has been evaluated as a Hoek-Brown material can be obtained by different  $\sigma_3$  values. Therefore, when adopting the tangent method theory to confirm  $C$  and  $\varphi$  values, the most critical step is the selection of the range of  $\sigma_3$  values, but up to now there are no theoretically correct methods for choosing the range (Hoek and Brown 1997). Moreover, the tangent method theory (See Fig. 8.13) is actually to approximate Hoek-Brown criterion by many polygonal lines. Even though the approximate order is very high, it is impossible to reduce the whole approximation error by tangent method theory. Therefore, in this section, a new evaluation criterion for a kind of rock that has been evaluated as a Hoek-Brown material is put forward by adopting optimal approximation polynomial theory in functional analysis, which can be used to confirm more precisely the strength parameters (cohesion and internal friction angle) of flawed sample, and to avoid effectively the shortcoming of good approximation in a certain testing point but bad approximation on the whole.

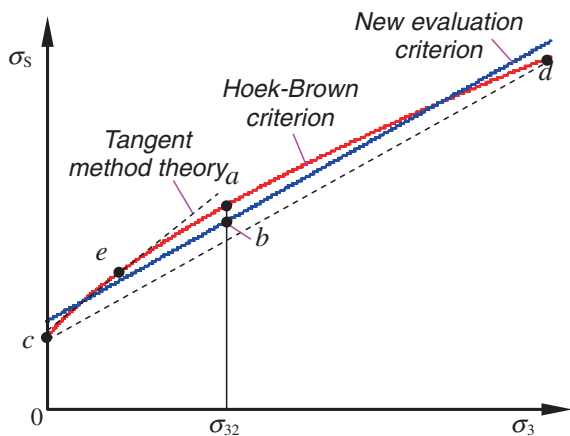
Optimal approximation polynomial theory is described as follows (Rivlin 1974, 1987). Let  $C_{[a, b]}$  be the space of real-valued continuous functions on the real interval  $[a, b]$ . We denote by  $H_n$  ( $H_n \subset C_{[a, b]}$ ) the space of algebraic polynomials of degree at most  $n$ , i.e.,  $H_n = \text{span} \{1, x, \dots, x^n\}$ .  $1, x, \dots, x^n$  are a group of function set without linear correction. Element  $P_n(x)$  on  $H_n$  space can be denoted as follows.

$$P_n(x) = a_0 + a_1x + \dots + a_nx^n, a_0, a_1, \dots, a_n \text{ are arbitrary real number.}$$

We set

$$\|f\|_\infty = \max_{x \in [a, b]} |f(x)|, \quad \forall f \in C_{[a, b]} \tag{8.13}$$

**Fig. 8.13** Tangent method theory, new evaluation criterion and Hoek-Brown criterion (with kind permission of Elsevier Publisher)



$P_n^*(x) \in H_n$  is called a best approximation polynomial to  $f$  on the real interval  $[a, b]$ , which makes  $P_n^*(x)$  satisfies the following equation.

$$\Delta(f, P_n) = \max_{a \leq x \leq b} |f(x) - P_n^*(x)| = \min_{p_n \in H_n} \|f(x) - P_n(x)\| \tag{8.14}$$

In Eq. (8.14), such an  $P_n^*(x)$  always exists, and is, indeed, unique. When  $n = 1$ ,  $P_1(x) = a_0 + a_1x$  is called as optimal approximation first equation. We can now state the famous Chebyshev Theorem (Rivlin 1974).  $P_n^*(x) \in H_n$  is a best approximation polynomial to  $f \in C_{[a,b]}$  if, and only if, there exist  $n + 2$  distinct points,  $a \leq x_1 < x_2 < \dots < x_{n+2} \leq b$ , for which

$$P(x_k) - f(x_k) = (-1)^k \lambda \|P(x) - f(x)\|_\infty, \quad \lambda = \pm 1 \quad k = 1, 2, 3, \dots, n + 2 \tag{8.15}$$

The main themes of the Chebyshevian approach are existence, uniqueness, and characterization of best approximations.

Based on the optimal approximation polynomial theory, a new evaluation criterion for a kind of rock that has been evaluated as a Hoek-Brown material is obtained to confirm the cohesion and internal friction angle. That is to say, on the basis of Hoek-Brown criterion [Eq. (8.5)], we need to calculate the optimal approximation first equation  $P_1(\sigma_3) = \sigma_0 + q\sigma_3$  on the real interval  $[0, 30 \text{ MPa}]$ . Here,  $\sigma_0$  and  $q$  are given in Eqs. (8.3) and (8.4), respectively.

In accordance with Chebyshev Theorem [Eq. (8.15)], there exists three distinct points at least,  $0 \leq \sigma_{31} < \sigma_{32} < \sigma_{33} \leq 30 \text{ MPa}$  when  $n = 1$ , for which

$$P_1(\sigma_{3k}) - f(\sigma_{3k}) = (-1)^k \lambda \|P(\sigma_3) - f(\sigma_3)\|_\infty, \quad \lambda = \pm 1 \quad k = 1, 2, 3 \tag{8.16}$$

According to Eq. (8.5), i.e.,  $f(\sigma_3) = \sigma_3 + (m\sigma_c\sigma_3 + s\sigma_c^2)^{0.5}$ , we can get

$$f'(\sigma_3) = 1 + \frac{m\sigma_c}{2\sqrt{m\sigma_3\sigma_c + s\sigma_c^2}} \tag{8.17}$$

From Eq. (8.17), it can be seen that the function  $f'(\sigma_3)$  is a monotonic function. Therefore, the function  $f'(\sigma_3) - q$  only has single zero point on the open interval  $(0, 30 \text{ MPa})$ , which this zero point is denoted as  $\sigma_{32}$ . Thus  $P_1(\sigma_{32}) - f'(\sigma_{32}) = q - f'(\sigma_{32}) = 0$ , i.e.,  $f'(\sigma_{32}) = q$ . Another two distinct points must be at the endpoint of the interval  $[0, 30 \text{ MPa}]$ , i.e.,  $\sigma_{31} = 0$  and  $\sigma_{33} = 30 \text{ MPa}$ . Moreover, the following equation can be satisfied.

$$P_1(0) - f(0) = P_1(30) - f(30) = -[P_1(\sigma_{32}) - f(\sigma_{32})] \tag{8.18}$$

According to Eq. (8.18), we can obtain.

$$\begin{cases} \sigma_0 + q \times 0 - f(0) = \sigma_0 + q \times 30 - f(30) \\ \sigma_0 + q \times 0 - f(0) = f(\sigma_{32}) - (\sigma_0 + q\sigma_{32}) \end{cases} \tag{8.19}$$

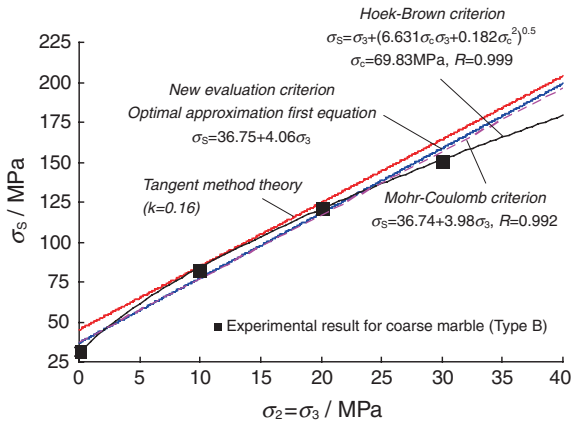
Solving Eq. (8.19), Eq. (8.20) can be obtained.

$$\begin{cases} q = \frac{f(30) - f(0)}{30} = f'(\sigma_{32}) \\ \sigma_0 = \frac{f(0) + f(\sigma_{32})}{2} - \frac{f(30) - f(0)}{30} \frac{\sigma_{32}}{2} \end{cases} \tag{8.20}$$

**Table 8.7** The cohesion and internal friction angle of intact and flawed marbles based on optimal approximation polynomial theory in accordance with Hoek-Brown criterion (Table 8.5)

Marble type	Geometry of flaw	Optimal approximation first equation	$\sigma_{32}$ (MPa)	Maximum deviation (MPa)	C (MPa)	$\varphi$ (°)
Coarse marble	Type A	$74.85 + 2.73\sigma_3$	13.03	1.707	22.65	27.7
	Type B	$36.75 + 4.06\sigma_3$	10.45	6.956	9.12	37.2
	Type C	$35.13 + 4.28\sigma_3$	10.17	7.908	8.49	38.4
	Type D	$45.68 + 3.89\sigma_3$	11.10	5.625	11.58	36.2
Medium marble	Type A	$121.03 + 3.69\sigma_3$	13.09	2.564	31.50	35.0
	Type B	$60.42 + 5.34\sigma_3$	10.81	9.105	13.07	43.2
	Type C	$23.34 + 7.22\sigma_3$	7.50	23.34	4.34	49.2
	Type D	$63.02 + 4.92\sigma_3$	11.14	7.571	14.20	41.5

**Fig. 8.14** A new evaluation criterion to confirm the cohesion and internal friction angle (with kind permission of Elsevier Publisher)



Thus we get the optimal approximation, first equation  $P_1(\sigma_3)$  in accordance with Eq. (8.20), and then by Eqs. (8.3) and (8.4), the  $C$  and  $\varphi$  values of rock can be confirmed. The special geometrical significance is shown in Fig. 8.13, in which the new evaluation criterion line is parallel to the straight line  $cd$ . The maximum deviation equals to the length of line segment  $ab$ .

According to the Hoek-Brown strength parameters listed in Table 8.5, the cohesion and internal friction angle of intact and flawed marbles are confirmed in Table 8.7 based on the above optimal approximation polynomial theory. Figure 8.14 shows a typical comparison between experimental result and several evaluation criteria. From Fig. 8.14, we can see that the cohesion given by tangent method theory ( $k = 0.16$ ) is obviously higher than that by other two kinds of linear envelopes. However, the cohesion and internal friction angle confirmed by new evaluation criterion has a slight difference with that by best fit Mohr-Coulomb envelope for triaxial test data (i.e., equivalent Mohr-Coulomb envelope, Sofianos and Nomikos 2006). Therefore, the strength parameters given by the new

evaluation criterion in this research are more precise than that by tangent method theory, which avoid the shortcoming of the tangent method theory, i.e., good approximation in a certain testing point but bad approximation on the whole.

### 8.4 Failure Mode of Pre-cracked Marble

In this research, all the tests were carried out at a strain rate of  $2 \times 10^{-5}/s$ . For intact sample, the coarse and medium marbles under different confining pressures all lead to typical shear failure mode with a single fracture surface (Fig. 8.15) and the fracture surface is very smooth, which results from the friction of macroscopic crack surfaces.

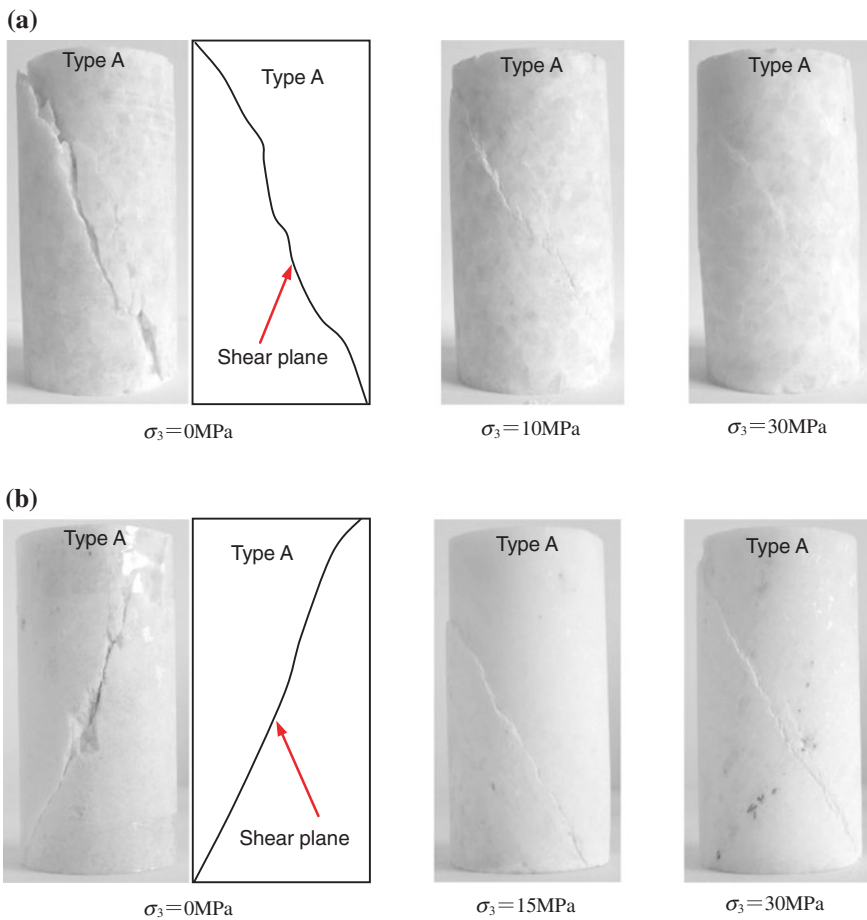


**Fig. 8.15** Failure modes of intact coarse and medium marble samples (Type A) under different confining pressures. **a** Coarse marble. **b** Medium marble (with kind permission of Elsevier Publisher)

For flawed samples (Types B, C, and D), under uniaxial compression, we observed three typical failure modes (Fig. 8.16) of coarse and medium marbles in the test program: tensile mode, shear mode, and mixed mode (tensile and shear) with wing and secondary cracks, which are analyzed in detail as follows. (a) *Tensile mode* (Type B): Wing crack initiates simultaneously from internal tips of two flaws ① and ②, but crack coalescence does not occur between flaws ① and ②. The wing crack initiates along the direction of the maximum principal stress, afterward with the increase of axial deformation, the crack coalescence indicates deviation and failure of crystalline grains in marble. In the end, the propagation and coalescence of cracks result in unstable failure of a sample. However after the wing crack initiated from internal tip of flaw ② propagates to the end surface of sample, the reverse secondary crack at the internal tip of flaw ② is also observed. (b) *Shear mode* (Type C): Wing crack initiates simultaneously from internal tips of two flaws ① and ②, and the crack coalescence only occurs between flaws ① and ②. The wing cracks initiated

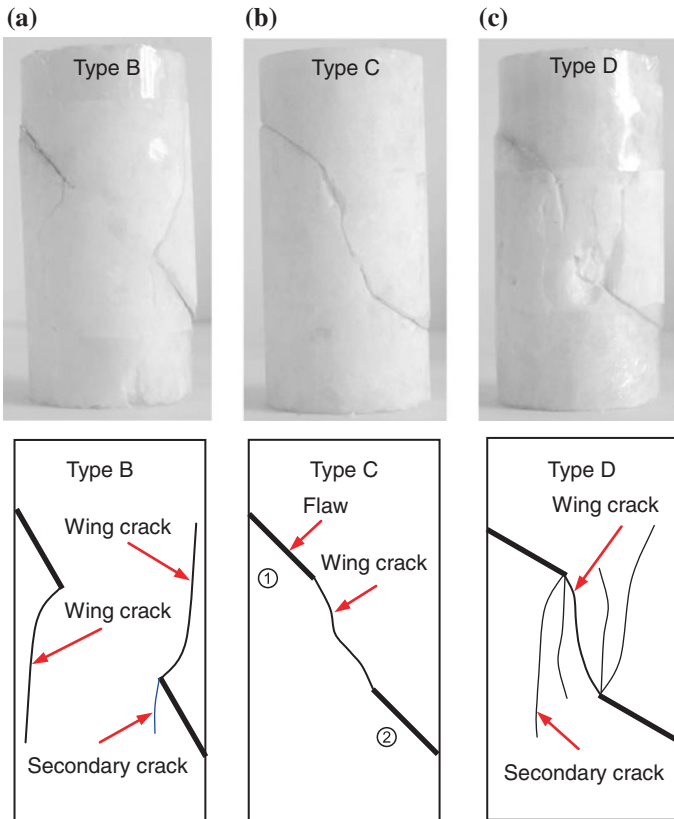
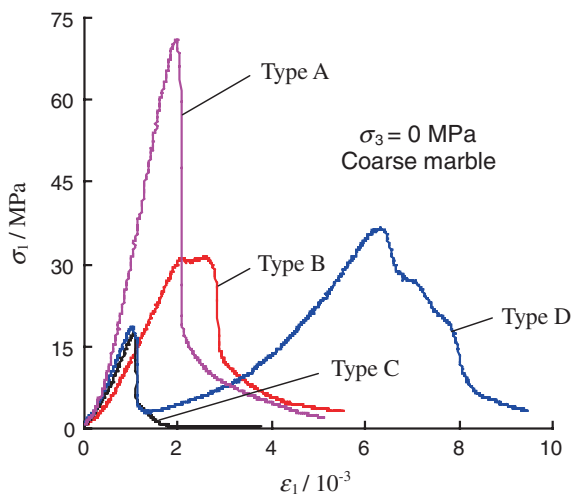


**Fig. 8.16** Typical failure modes of flawed samples with three types of geometries (Types B, C, and D) under uniaxial compression. **a** Tensile mode. **b** Shear mode. **c** Mixed mode (with kind permission of Elsevier Publisher)

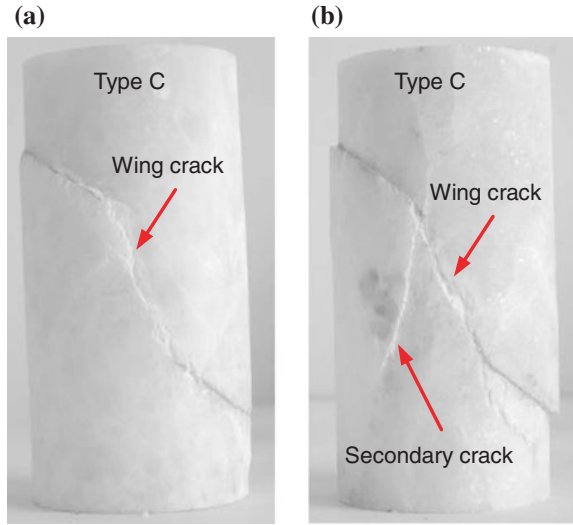
from internal tips of two flaws ① and ② occur toward the middle part between two flaws; however, this does not lead to a wider crack. When the two wing cracks coalescence and merge at the ligament part between two flaws, the macroscopic failure takes place in the sample; moreover the crack coalescence path is very smooth. (c) *Mixed mode* (Type D): The sample fails by a combination of tensile and shear mode. Two kinds of cracks, wing cracks and secondary cracks, are all observed in the sample. After the sample first initiates shear mode as the same as shown in Fig. 8.16b, with the increase of axial deformation, the sample begins to initiate secondary cracks at internal tips of two flaws ① and ② along the direction of the maximum principal compression stress. The coalescence path of secondary cracks is very rough due to the influence of crystal grains in marble. As mentioned above, the failure mode of samples is found to depend obviously on the geometry of flaw.

Figure 8.17 shows the effect of the geometry of flaw on the axial deviatoric stress of marble in uniaxial compression and the failure mode corresponds to Fig. 8.16. For Type B, the sample comes out as a small phase of yielding platform nearby peak stress, which results from the following explanation. The wing crack at internal tips of flaws initiates and propagates along the maximum principal stress when the sample is loaded to  $\sim 0.7\sigma_S$ . Marble is a kind of typically crystalline material. The transmission speed of crystal grains on the force and their deformation are different in the sample, which results in a zigzag path of crack coalescence. When the sample is loaded to up to  $\sigma_S$ , the slippage of pre-existing flaws and the propagation of wing cracks lead to the process that inhomogeneous stress field in the sample comes to adjust gradually. The macroscopic manifestation of adjusting is to initiate the plastic flow nearby peak stress. For Type C, the sample comes into being the shear mode (Fig. 8.16b). The sample cannot support completely when axial supporting capacity of the sample drops rapidly to zero after peak strength of 17.2 MPa. However for type D (Fig. 8.16c), the difference compared with Type C, the axial supporting capacity of the sample does not drop

**Fig. 8.17** Effect of geometry of flaw on the axial principal stress of marble in uniaxial compression (with kind permission of Elsevier Publisher)



**Fig. 8.18** Typical failure modes of flaw samples (Type C) under lower confining pressure of 10 MPa. **a** Coarse marble. **b** Medium marble (with kind permission of Elsevier Publisher)



to zero after the first larger strength of 18.7 MPa. For the moment, the axial supporting capacity of the sample is about 3.0 MPa and corresponding axial strain is  $\sim 1.34 \times 10^{-3}$ , rock sample is located on the self-locking state. Afterward, with the increase of axial deformation, the wing crack surface takes place the occlusion and the axial supporting capacity begins to increase slowly. Due to obvious damage of inner supporting structure in the sample, the reloading elastic modulus (10.54 GPa) is distinctly lower than first elastic modulus ( $\sim 20.29$  GPa); however, the sample can support higher axial stress (i.e., 36.6 MPa), which is 1.96 time of the first larger strength ( $\sim 18.7$  MPa). Therefore in uniaxial compression, the peak strength of rock sample has a close relation with the geometry of flaw, which is significantly dependent on the crack coalescence at internal tips of two flaws.

The failure modes of flawed marble samples at lower confining pressures ( $\sigma_3 = 10$  MPa) are approximately the same as those shown in Fig. 8.16. Figure 8.18 gives the failure mode of flawed sample (Type C) under lower confining pressure of 10 MPa. The sample takes also on typical shear mode, which is similar to that shown in Fig. 8.16b. The wing crack initiates from internal tips of two flaws ① and ②, and the crack coalescence only occurs through the ligament part between flaws ① and ②. The secondary crack is also observed at internal tip of flaw ① in the medium marble. Compared with the failure mode at  $\sigma_3 = 0$  MPa, the wing crack at  $\sigma_3 = 10$  MPa is closer due to the role of confining stress; moreover, the crack coalescence path is rougher. The initiation and propagation of wing cracks at internal tips of flaws result in an abrupt change of slope in stress–strain curve (Fig. 8.7b).

For coarse marble with different flaw geometries (Types B, C, and D), the wing cracks and secondary cracks initiate at the internal tips of flaws for uniaxial or lower confining pressures but disappear under higher confining pressure (Fig. 8.19). Figure 8.19a shows the failure mode of the sample at  $\sigma_3 = 20$  MPa. The sample exhibits typical shear mode penetrating directly pre-existing flaw ①. Figure 8.19b

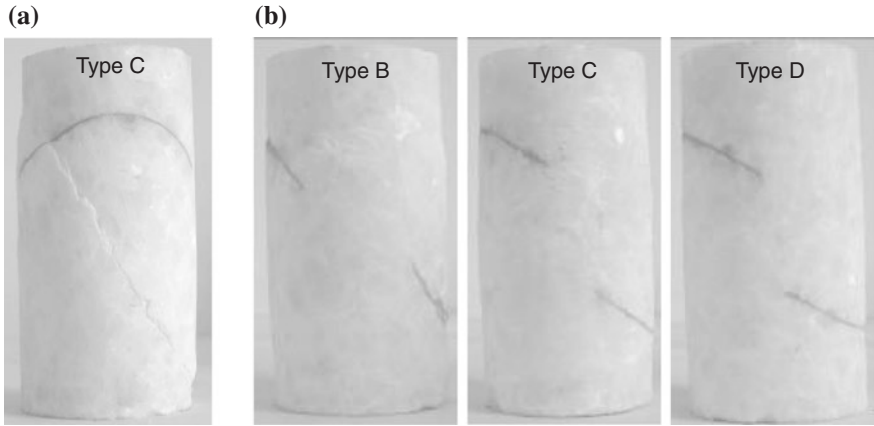
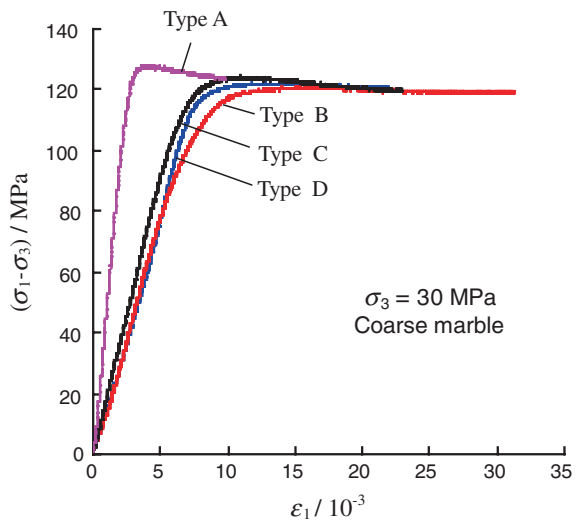


**Fig. 8.19** Failure modes of coarse marble samples with three kinds of flaw geometries (Types B, C, and D) under higher confining pressure of **a**  $\sigma_3 = 20$  MPa and **b**  $\sigma_3 = 30$  MPa (with kind permission of Elsevier Publisher)

**Fig. 8.20** Effect of the geometry of flaw on the axial deviatoric stress of coarse marble under higher confining pressure (with kind permission of Elsevier Publisher)



shows failure modes of the sample at  $\sigma_3 = 30$  MPa. The sample takes on the drum shape. Although no obvious wing cracks and secondary cracks are observed between flaws ① and ②, some slippage traces can be seen from the surface of sample.

Figure 8.20 shows the effect of flaw geometry on the axial deviatoric stress of coarse marble under higher confining pressure of 30 MPa and the failure mode corresponds to Fig. 8.19b. Under uniform hydrostatic pressure, pre-existing flaws in the sample close completely and do not occur to slip with the increase of loading. Thus less stress concentration fields is initiated at internal tips of

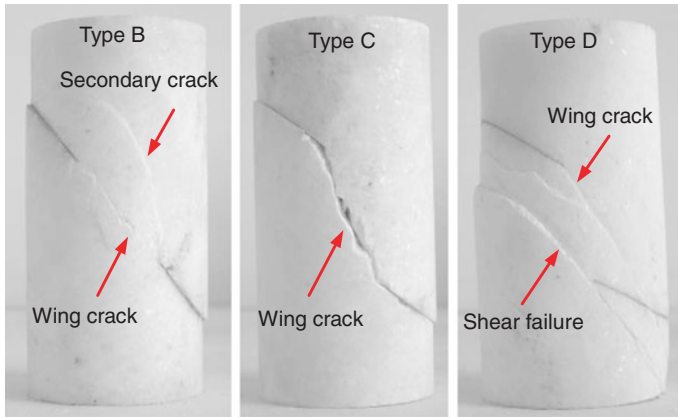


**Fig. 8.21** Failure modes of medium marble samples with three types of flaw geometries (Types B, C, and D) at  $\sigma_3 = 30$  MPa (with kind permission of Elsevier Publisher)

two flaws, which results in no obvious wing cracks and secondary cracks. From Fig. 8.20, we can see out that the elastic modulus of flawed samples with three types of geometries of flaws has a small difference, which the maximum deviation is only  $\sim 2$  GPa. After the sample goes into the yielding flow, the difference of axial supporting capacity between intact sample and flawed sample is approximately same, which shows that the supporting capacity of coarse marble sample is only related to the confining pressure but almost no relation with flaw geometry at  $\sigma_3 = 30$  MPa. The supporting capacity by friction among crystal grains determines the strength behavior of coarse marble under higher confining pressure. The coarse marble sample can support higher axial stress macroscopically by friction, and the deformation of sample tends to uniform, which leads to the ductile and plastic behavior of coarse marble under higher confining pressure.

For medium marble with different geometries of flaws (Types B, C, and D), the wing cracks and secondary cracks were also observed under higher confining pressure ( $\sigma_3 = 30$  MPa) (Fig. 8.21), but they are different compared with those under uniaxial compression shown in Fig. 8.16. For Type B, the wing crack initiates from internal tips of two flaws ① and ②. At the same time, the secondary crack is also observed at internal tip of flaw ② in the medium marble, which propagates first along the direction of axial stress and then deviates toward flaw ①. Moreover from the coalescence path of wing crack, we can conclude that the interaction between flaws ① and ② is very intensive due to the effect of confining pressure. For Type C, the sample takes on typical shear failure mode, which is the same as that in uniaxial compression. But the crack coalescence path is a zigzag. During the test of the sample, a loud sound can be heard and the sample takes place the brittle rupture. However for Type D, the sample takes on the drum and double-layered failure surface. The wing crack is only observed at the internal tip of flaw ①.

**Fig. 8.22** Effect of geometry of flaw on the axial deviatoric stress of medium marble under higher confining pressure (with kind permission of Elsevier Publisher)

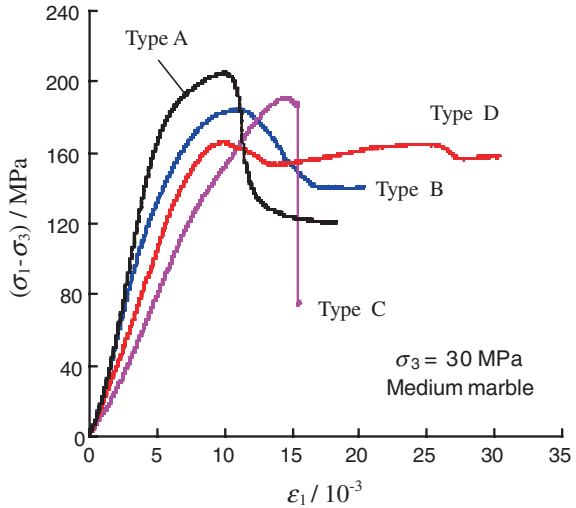


Figure 8.22 shows the effect of geometry of flaw on the axial deviatoric stress of medium marble at  $\sigma_3 = 30$  MPa and the failure mode corresponds to Fig. 8.21. The elastic modulus of flawed samples with three kinds of geometries of flaws differs greatly from one to another. From Figs. 8.21 and 8.22, the failure mode and deformation behavior of medium marble are dependent to the crack coalescence in the sample even though at  $\sigma_3 = 30$  MPa. The stable coalescence of cracks in the sample (Type B) leads to the slow reduction of stress–strain curve after peak stress, but a zigzag failure of the sample (Type C) leads to the abrupt drop of stress–strain curve after peak stress. However, final double-layered failure surface in the sample (Type D) shows the process that the internal material yields and softens gradually during the axial loading, which results in the two slight stress-drop behaviors of stress–strain curve after the peak stress.

In accordance with the effect of the geometry of flaw on the axial deviatoric stress of coarse marble at  $\sigma_3 = 30$  MPa in Fig. 8.20, we can believe that for the confining pressure larger than 30 MPa, the strength of the samples of coarse marble does not change with the presence of flaws. Thus it is quite possible that for  $\sigma_3$  larger than a certain critical value, the axial stress–axial strain behavior of medium marble with different types of geometries of flaws (Types B, C, and D) will be similar to that of coarse marble in Fig. 8.20. Moreover, this certain critical  $\sigma_3$  value may depend on the geometry of flaw. Beyond the certain critical  $\sigma_3$  value, the wing cracks and secondary cracks may not be observed at the internal tips of two flaws, which will be able to result in that the cohesion and internal friction angle of marble sample is independent of the flaw geometry. However, because the maximum confining pressure of testing system is limited and only 40 MPa, we cannot carry out triaxial tests for medium marble sample under the confining pressures larger than 40 MPa, which will be further investigated for pre-cracked medium marble in the future.

## 8.5 Conclusions

An experimental investigation on the strength behavior, propagation, and coalescence of fractures in coarse and medium marbles under conventional triaxial compression was performed. On the basis of the experimental results of pre-cracked marble samples in this paper, the following conclusions can be drawn.

Compared with intact sample, the flawed sample fails with lower strengths, smaller elastic moduli, and larger failure strains. The stress–strain curve of flawed sample shows an abrupt change of slope under lower confining pressures, coincident with the propagation of wing cracks at the internal flaw tips. Peak strain of intact sample without flaw increases linearly with the increase of confining pressure. But for flawed samples, the failure strain usually ranges from 0.2 to 1.4 % and increases nonlinearly with increasing  $\sigma_3$  for the same geometry of flaw. The failure strain is significantly influenced by pre-cracked coalescence in the flawed sample under different confining pressures.

The peak strength is found depending not only on the geometry of flaw, but also on the confining pressure. The applicability of linear Mohr-Coulomb and nonlinear Hoek-Brown criterion is evaluated for intact and flawed samples. For intact sample, there is almost no difference between nonlinear Hoek-Brown criterion and linear Mohr-Coulomb criterion. However, the strength of flawed sample shows distinct nonlinear behavior, which is in a better agreement with Hoek-Brown criterion than Mohr-Coulomb criterion. Moreover for flawed sample, linear Mohr-Coulomb criterion predicts a higher strength than its actual value at lower confining pressure and higher confining pressure, but a lower strength than its actual value at intermediate confining pressure.

In the range of tested confining pressure (0–30 MPa) for flawed samples, the values of cohesion and internal friction angle are significantly dependent to the geometry of flaw in the sample. For the marble with the same crystal size, the value of cohesion of flawed sample is lower than that of intact sample, while the value of internal friction angle is higher than that of intact sample. In order to confirm more precisely the strength parameters (cohesion and internal friction angle), a new evaluation criterion for a kind of rock that has been evaluated as a Hoek-Brown material is put forward by adopting optimal approximation polynomial theory, which can avoid the shortage of tangent method theory that has good approximation in a certain testing point but bad approximation on the whole.

For intact marble sample (Type A), typical shear failure mode with a single fracture surface under different confining pressures is observed, while for flawed sample (Types B, C, and D), under uniaxial compression and lower confining pressures ( $\sigma_3 = 10$  MPa), tests for coarse and medium marbles exhibit three basic failure modes, i.e., tensile mode, shear mode, and mixed mode. Shear mode is associated with lower strength behavior. However under higher confining pressures ( $\sigma_3 = 30$  MPa), for coarse marble, the axial supporting capacity is not related to the geometry of flaw and the friction among crystal grains determines the strength behavior of coarse marble, and no obvious wing cracks and secondary

cracks are observed between two flaws; for medium marble, the failure mode and deformation behavior are dependent on the crack coalescence in the sample, and the coalescence of wing cracks and secondary cracks are all observed.

In this chapter, the marble with four different types of geometries of flaws are carried out conventional triaxial compression experiment by fixing the flaw length and ligament length in the sample and pre-existing only two flaws. Nevertheless, the lengths and the numbers of flaws in a sample will all affect the strength behaviors and crack coalescence modes. Therefore, further experimental verification of the above presented conclusions will still be reinforced for other kinds of rocks and other types of geometries of flaws. Laboratory tests are being conducted to investigate the effects of rock type with other types of geometries of flaws. Finally, it is useful to notice that the time-dependency (creep) behavior of rock is quite important according to relation stages included under conventional triaxial experiments (Xie and Shao 2006; Yang et al. 2006). Therefore, taking into account the long-term stability of jointed rock engineering, triaxial compression creep tests for pre-cracked rock will be investigated in the future.

## References

- Al-Ajmi AM, Zimmerman RW (2006) Stability analysis of vertical boreholes using the Mogi-Coulomb failure criterion. *Int J Rock Mech Min Sci* 43:1200–1211
- Bobet A, Einstein HH (1998) Fracture coalescence in rock-type materials under uniaxial and biaxial compression. *Int J Rock Mech Min Sci* 35:863–889
- Brady BHG, Brown ET (1993) *Rock mechanics for underground mining*, 2nd edn. Chapman & Hall, London
- Dai Y (2006) Testing analysis and constitutive model study of unsaturated slates. Doctoral thesis (in Chinese), Institute of Rock and Soil Mechanics, Chinese Academy of Sciences, Wuhan, China (in Chinese)
- Fairhurst CE, Hudson JA (1999) Draft ISRM suggested method for the complete stress-strain curve for the intact rock in uniaxial compression. *Int J Rock Mech Min Sci* 36(3):279–289
- Hoek E (1990) Estimating Mohr-Coulomb friction and cohesion values from the Hoek-Brown failure criterion. *Int J Rock Mech Min Sci Geomech Abstr* 12:227–229
- Hoek E, Brown ET (1980) *Underground excavation in rock*. Institution of Mining and Metallurgy, London
- Hoek E, Brown ET (1997) Practical estimates of rock mass strength. *Int J Rock Mech Min Sci* 34:1165–1186
- Jaeger JC, Cook NGW (1979) *Fundamentals of rock mechanics*, 3rd edn. Chapman & Hall, New York
- Mohr O (1914) *Abhandlungen aus dem Gebiete der Technischen Mechanik*, 2nd edn. Ernst, Berlin
- Palchik V (2006) Application of Mohr-Coulomb failure theory to very porous sandy shales. *Int J Rock Mech Min Sci* 43:1153–1162
- Prudencio M, Van Sint Jan M (2007) Strength and failure modes of rock mass models with non-persistent joints. *Int J Rock Mech Min Sci* 34:1165–1186
- Rivlin TJ (1974) *The chebyshev polynomials*. Wiley, New York
- Rivlin TJ (1987) A view of approximation theory. *IBM J Res Dev* 31:162–168
- Sofianos AI, Nomikos PP (2006) Equivalent Mohr-Coulomb and generalized Hoek-Brown strength parameters for supported axisymmetric tunnels in plastic or brittle rock. *Int J Rock Mech Min Sci* 43:683–704

- Wong T-F, Wong RHC, Chau KT, Tang CA (2006) Microcrack statistics, Weibull distribution and micromechanical modeling of compressive failure in rock. *Mech Mater* 38(7):664–681
- Xie HP, Gao F (2000) The mechanics of cracks and a statistical strength theory for rocks. *Int J Rock Mech Min Sci* 37:477–488
- Xie SY, Shao JF (2006) Elastoplastic deformation of a porous rock and water interaction. *Int J Plast* 22:2195–2225
- Yang SQ, Zhang XM, Su CD (2003) Testing study on acoustic property of marble block. *J Liaoning Tech Univ* 22(6):772–775 (in Chinese)
- Yang SQ, Su CD, Xu WY (2005a) Experimental and theoretical study of size effect of rock material. *Eng Mech* 22(4):112–118 (in Chinese)
- Yang SQ, Su CD, Xu WY (2005b) Experimental investigation on strength and deformation properties of marble under conventional triaxial compression. *Rock Soil Mech* 26(3):475–478 (in Chinese)
- Yang SQ, Xu WY, Xie SY, Shao JF (2006) Studies on triaxial rheological deformation and failure mechanism of hard rock in saturated state. *Chin J Geotech Eng* 28(8):962–969 (in Chinese)
- Yang SQ, Jiang YZ, Xu WY, Chen XQ (2008) Experimental investigation on strength and failure behavior of pre-cracked marble under conventional triaxial compression. *Int J Solids Struct* 45:4796–4819
- Yuan SC, Harrison JP (2006) A review of the state of the art in modelling progressive mechanical breakdown and associated fluid flow in intact heterogeneous rocks. *Int J Rock Mech Min Sci* 43:1001–1022
- Zhao J (2000) Applicability of Mohr-Coulomb and Hoek-Brown strength criteria to the dynamic strength of brittle rock. *Int J Rock Mech Min Sci* 37:1115–1121
- Zhu WC, Tang CA (2004) Micromechanical model for simulating the fracture process of rock. *Rock Mech Rock Eng* 37(1):25–56

# Chapter 9

## Numerical Investigation on the Failure Mechanical Behavior of Red Sandstone Containing Two Coplanar Fissures Under Conventional Triaxial Compression

Deep underground engineering rock masses are usually located within triaxial stress state; therefore, it is more relevant to investigate the failure mechanical behavior of rock material containing pre-existing fissures under triaxial compression. However, only few experimental or numerical investigations are carried out for failure mechanical behavior of pre-cracked rock material under triaxial compression. Therefore, in this chapter, to better understand the strength failure crack coalescence phenomena in fractured rock mass under triaxial stress state, two-dimensional discrete element simulation was conducted for red sandstone specimens containing two coplanar fissures under triaxial stress state. The emphasis of this chapter is focused on to investigate the influence of coplanar fissure angle on deformation strength parameters of red sandstone material under triaxial compression to analyze the crack initiation propagation coalescence processes in red sandstone material under different confining pressures.

### 9.1 Discrete Element Model and Micro-Parameters

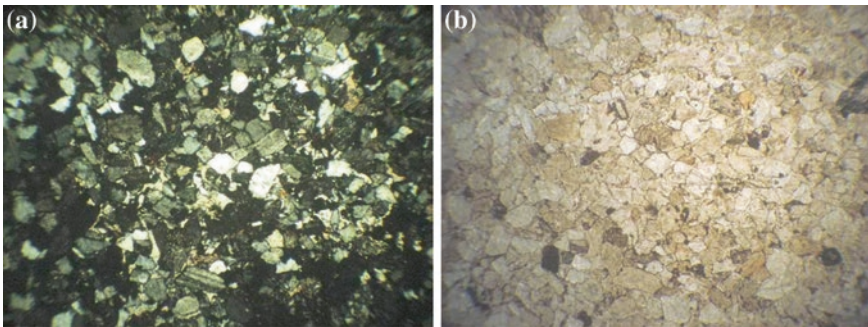
Rock behaves like a cemented granular material with complex-shaped grains, in which both the grains and the cement are deformable (Potyondy and Cundall 2004). The DEM-based PFC<sup>2D</sup> commercial tool can be used for simulating the mechanical behavior of rocks by the interaction between an assembly of circular particles with specified statistical size distributions and bounded with four rigid walls for triaxial compression. These particles are generated by an automatic particle generator with radii being distributed either uniformly or according to a Gaussian distribution. In this chapter, we also chose the parallel bond model to carry out the numerical simulation (Cho et al. 2007).

### 9.1.1 Intact Red Sandstone Material and Micro-Parameters

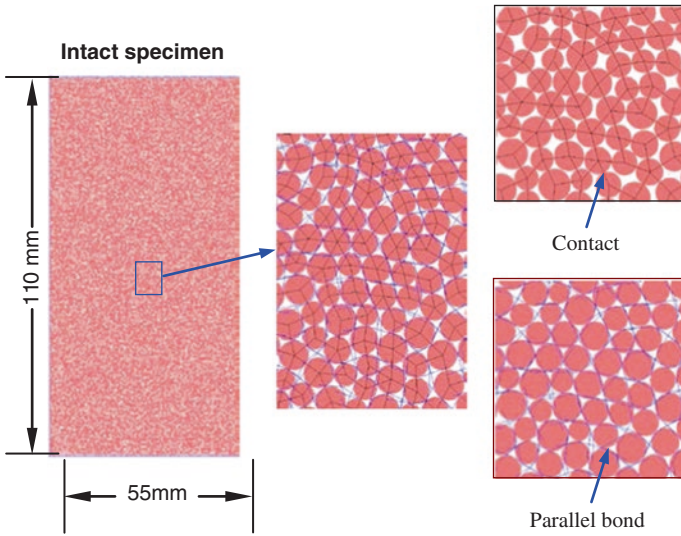
The rock material in this chapter was red sandstone, which was collected from Shandong province of China. The mineral components of red sandstone material were feldspar, quartz, debris, and agglutinate according to optical microscopy and SEM results (Fig. 9.1) (Yang and Jing 2013). The mass content of agglutinate in red sandstone material consisted of gypsum, barite, and iron integument. Red sandstone is a fine- to medium grained feldspathic sandstone with a connected porosity of 8.9 %. The triaxial experiments were carried out on cylindrical specimens with 55 mm in diameter and 110 mm in length. The specimens were all cored from the same large rectangular block and in the same orientation. The experiments were all carried out on dry specimens at room temperature. The average dry density of tested red sandstone was approximately  $2375 \text{ kg/m}^3$ .

Figure 9.2 shows one numerical intact specimen generated by PFC<sup>2D</sup>, and the scale of numerical specimen is approximately equal to that of experimental specimen, i.e., the dimensions of 55 mm in diameter (D) and 110 mm in length (L). All specimens had a height-to-diameter ratio of 2.0 to ensure a uniform stress state within the central part of the specimens. Each numerical intact specimen was discretized into 16,609 particles with 43,125 contacts and 33,175 parallel bonds. The rock specimen is prepared as a random dense packing of sphere particles with different radii distributed according to a uniform distribution, in which the ratio of smallest radius over the largest radius is chosen as 1.5 in this chapter. The minimum radius of particle is 0.26 mm. The average unit weight of simulated red sandstone was about  $2375 \text{ kg/m}^3$ , which is the same as the experimental red sandstone.

An external displacement was applied on the top of the rock specimens in the axial direction. To ensure that the specimen remained in a quasi-static equilibrium throughout the test, a sufficiently low displacement loading rate 0.05 m/s was applied. For our simulation, all the specimens were all loaded to the stage of residual strength during triaxial compression. The microparameters in this chapter were confirmed by the following method. First, we established a quantitative correction



**Fig. 9.1** Microscopic structure of red sandstone (Yang and Jing 2013), **a** orthogonal light ( $\times 40$ ), **b** plane-polarized light ( $\times 40$ )



**Fig. 9.2** Numerical intact specimen generated in PFC<sup>2D</sup> in this chapter

between the macroparameters and microparameters of red sandstone by carrying out the sensitivity analysis of microparameters. And then, the microparameters were confirmed using the trial and error method. The macroscopic behavior of intact red sandstone obtained by experiment was used in this chapter to calibrate the micro-parameters. The macroscopic results obtained by numerical simulation after each trial was used to check the microparameters. This process was repeated until the numerical results achieved a good agreement with the experimental results.

In accordance with the above method, we obtained the micro-parameters used in the PFC<sup>2D</sup> model for red sandstone specimens in this chapter, as listed in Table 9.1. The Young's modulus of the particle and the parallel bond are all 14.6 GPa, and the ratio of normal to shear stiffness of the particle and the parallel bond is 3.3. The particle friction coefficient is 1.6. The mean value of parallel-bond normal strength ( $\sigma_n$ ) and the mean value of parallel-bond shear strength ( $\tau_n$ ) are, respectively, 62.5 MPa and 550 MPa.

### 9.1.2 Comparison of Triaxial Experimental and Numerical Results of Intact Specimen

In accordance with the micro-parameters listed in Table 9.1, we can carry out particle flow simulation for intact red sandstone under triaxial compression. Figure 9.3 shows the axial deviatoric stress-axial strain curves of intact red sandstone under different confining pressures obtained by numerical simulation.

**Table 9.1** The microparameters used in the PFC<sup>2D</sup> model for red sandstone specimens in this chapter

Micro-parameters	Values	Remarks
Young's modulus of the particle, $E_c$ (GPa)	14.6	
Young's modulus of the parallel bond, $\bar{E}_c$ (GPa)	14.6	
Parallel-bond radius multiplier	1.0	
Ratio of normal to shear stiffness of the particle, $k_n/k_s$	3.3	
Ratio of normal to shear stiffness of the parallel bond, $\bar{k}_n/\bar{k}_s$	3.3	
Particle friction coefficient, $\mu$	1.6	
Parallel-bond normal strength, mean (MPa)	62.5	Normal distribution
Parallel-bond normal strength, standard deviation (MPa)	18.75	
Parallel-bond shear strength, mean (MPa)	550	Normal distribution
Parallel-bond shear strength, standard deviation (MPa)	165	

In order to compare the analysis, the experimental axial deviatoric stress-axial strain curves of intact red sandstone (Yang and Jing 2013) are also presented in Fig. 9.3. From Fig. 9.3, it can be seen that, generally, the numerically simulated axial deviatoric stress-axial strain curves of intact red sandstone specimen under different confining pressures have agreed very well with the experimental curves, not only the pre-peak region but also the post-peak region. The experimental and simulated post-peak behavior of red sandstone all appears brittle even at the highest confining pressure of 35 MPa.

In accordance with Fig. 9.3, it can be seen that the numerical stress-strain curves of intact red sandstone specimen at the lower confining pressures do not show a initial nonlinear deformation; whereas, the experimental stress-strain curves at the lower confining pressures show initially a nonlinear (concave) deformation, which usually results from the closure of pre-existing micro-cracks (Yang and Jing 2013). After the stage of micro-crack closure, the stage of elastic deformation dominates the linear portions of the stress-strain curves. With continuous increase of axial deformation, the stress-strain curves begin to depart from the linear behavior, which marks the yielding of the specimens. At this time, the specimens enter a phase of strain hardening. However, when the peak strength is reached, there is a stage of strain softening. Finally, the specimens enter the stage of residual strength.

Besides, from Fig. 9.3, it is very clear that the numerically simulated elastic deformation and post-peak softening behavior of intact red sandstone are all in a good agreement with the experimental results. Figure 9.4 further presents the comparison of elastic modulus of intact red sandstone specimen obtained by experiment and simulation. From Fig. 9.4, it can be seen that the elastic modulus of red sandstone increases nonlinearly with increasing confining pressure (Yang and Jing 2013). Moreover, the experimental elastic modulus of intact specimen is approximately equal to the numerical value at the same confining pressure.

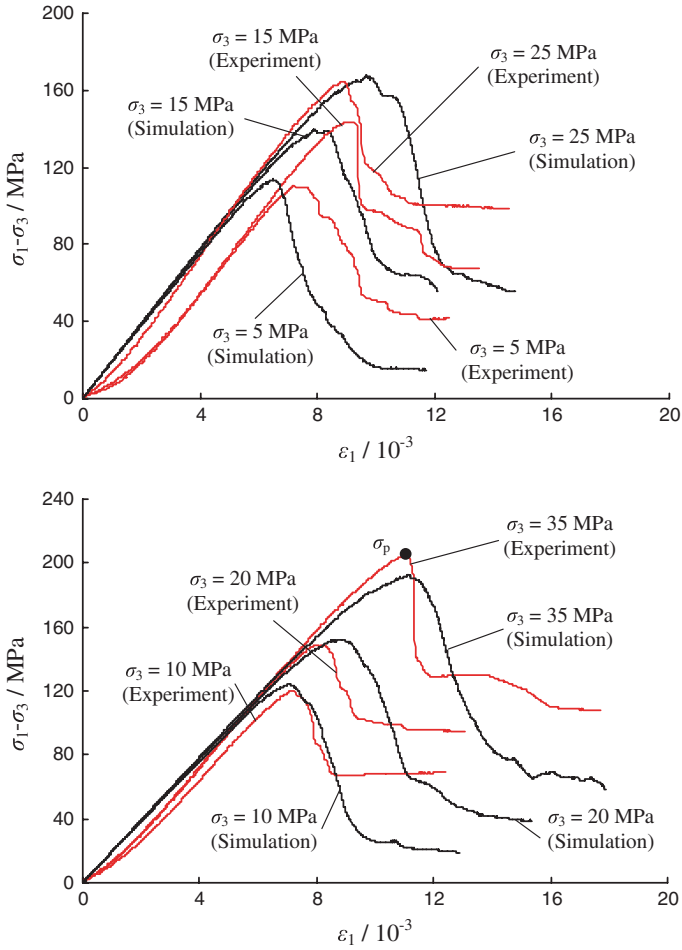


**Fig. 9.3** Comparison of axial deviatoric stress-axial strain curves of intact red sandstone under different confining pressures obtained by experiment and simulation

Based on the compared results by experiment and simulation, Figs. 9.3 and 9.5 further presents the comparison of peak strength of intact red sandstone under different confining pressures obtained by experiment and simulation. In Fig. 9.5, all hollow symbols represent the experimental results and the line represents the theoretical value in accordance with Mohr-Coulomb criterion.

From Fig. 9.5, we can see that the numerically simulated peak strength of intact red sandstone specimens under different confining pressures are all quantitatively approximate to those obtained by experiment. The maximum difference of peak strength between experiment and simulation is that at the confining pressure of 35 MPa. At  $\sigma_3 = 35$  MPa, the average peak strength of intact red sandstone by experiment is 239.7 MPa, while the numerical peak strength is 227.97 MPa, which

**Fig. 9.4** Comparison of elastic modulus of intact red sandstone specimen by experiment and simulation

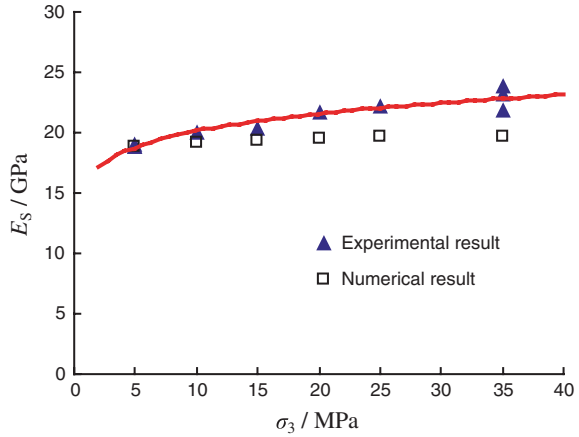
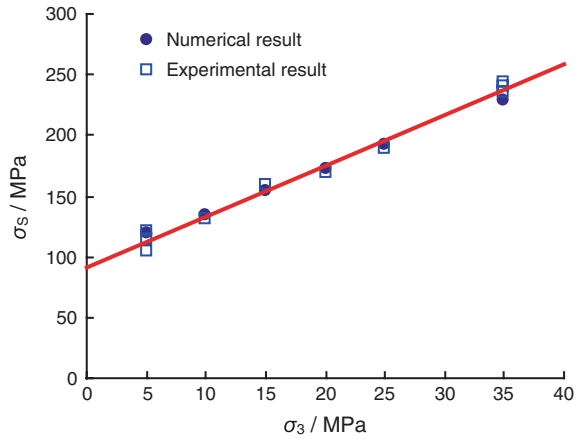


**Fig. 9.5** Comparison of peak strength of intact red sandstone under different confining pressures obtained by experiment and simulation. The line represents the theoretical value in accordance with Mohr-Coulomb criterion



has a difference of 11.73 MPa. The maximum dispersion extent between experiment and simulation (the dispersion extent is defined as the percentage ratio of the absolute difference between experimental and simulated value and the average value) is about 5.02 %.

Figure 9.6 presents the comparison of ultimate failure mode of intact red sandstone specimen obtained by experiment and simulation. From Fig. 9.6, it is very clear that with the increase of confining pressure, the failure mode of intact red sandstone specimens changes from single tension fracture to mixed tension and shear fracture, and then to single shear fracture (Yang and Jing 2013), which has been validated according to experimental observation for tested confining pressure from 5 to 35 MPa. Whereas, from the numerical observation of intact specimen under different confining pressures, we can see that with the increase of confining pressure, the failure mode of intact red sandstone specimens changes from single

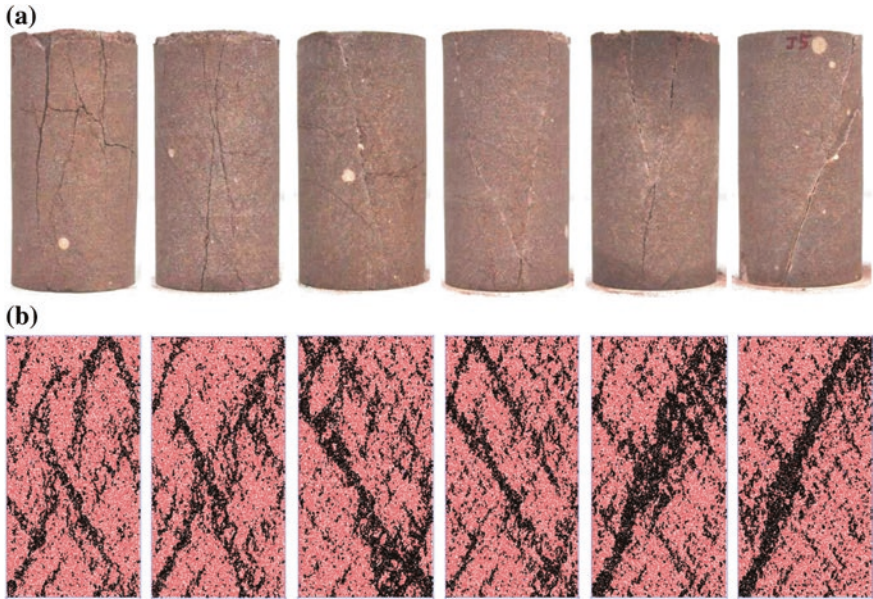


**Fig. 9.6** Comparison of ultimate failure mode of intact red sandstone specimen obtained by experiment and simulation, **a** experimental failure modes ( $\sigma_3 = 5, 10, 15, 20, 25$  and  $35$  MPa from left to right, respectively), **b** numerical failure modes ( $\sigma_3 = 5, 10, 15, 20, 25$  and  $35$  MPa from left to right, respectively)

tension fracture to single shear fracture. In general, the numerical failure modes of intact red sandstone specimens under different confining pressures are very similar to the experimental failure modes.

## 9.2 Macroscopic Strength and Deformation Behavior

In order to investigate the triaxial mechanical behavior of red sandstone containing two coplanar fissures, two coplanar fissures are pre-fabricated by deleting particles in the intact red sandstone. The geometry of red sandstone specimens containing two coplanar fissures is described in Fig. 9.7. The geometry of two coplanar fissures is defined by four geometrical parameters—fissure length  $2a$ , ligament length  $2b$ , fissure angle (the angle of fissure with the horizontal direction)  $\alpha$ , and ligament angle  $\beta$  as shown in Fig. 9.7.

In this chapter, open fissure width in flawed specimens was about 2.0 mm. To investigate the effect of pre-existing coplanar fissure geometry on the mechanical behavior of red sandstone subject to triaxial compression stress, different geometries of two coplanar fissures by varying inclination angle ( $\alpha = \beta$ ) while keeping two constants ( $2a = 12$  mm and  $2b = 18$  mm) were chosen. Detailed description

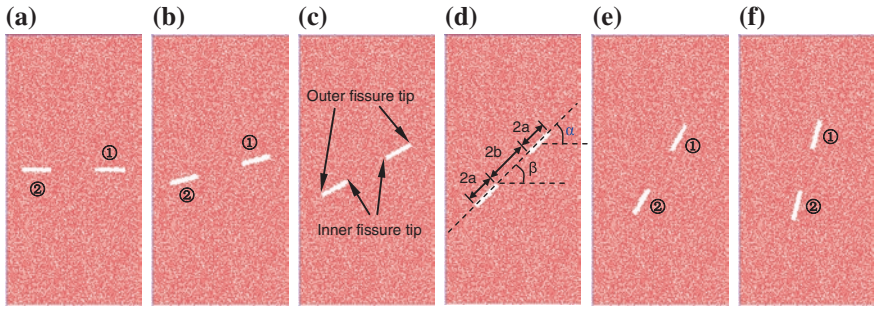


**Fig. 9.7** Numerical specimens containing two coplanar fissures. Where,  $\alpha$  is fissure angle,  $\beta$  is ligament angle,  $2a$  is fissure length ( $2a = 12$  mm), and  $2b$  is ligament length ( $2b = 18$  mm), **a**  $\alpha = \beta = 0^\circ$ , **b**  $\alpha = \beta = 15^\circ$ , **c**  $\alpha = \beta = 30^\circ$ , **d**  $\alpha = \beta = 45^\circ$ , **e**  $\alpha = \beta = 60^\circ$ , **f**  $\alpha = \beta = 75^\circ$

**Table 9.2** Red sandstone specimens containing two coplanar fissures under different confining pressures

$\alpha = \beta$ ( $^\circ$ )	D (mm)	L (mm)	2a (mm)	2b (mm)	$\sigma_3$ (MPa)
0	55	110	12	18	5, 10, 15, 20, 25 and 35
15	55	110	12	18	5, 10, 15, 20, 25 and 35
30	55	110	12	18	5, 10, 15, 20, 25 and 35
45	55	110	12	18	5, 10, 15, 20, 25 and 35
60	55	110	12	18	5, 10, 15, 20, 25 and 35
75	55	110	12	18	5, 10, 15, 20, 25 and 35

for red sandstone specimens containing two coplanar fissures under triaxial compression is listed in Table 9.2. A series of conventional triaxial simulations are carried out for red sandstone specimens containing two coplanar fissures with different confining pressures, namely 5, 10, 15, 20, 25, and 35 MPa.

### 9.2.1 Triaxial Deformation Behavior of Red Sandstone Containing Two Coplanar Fissures

Axial deviatoric stress-axial strain curves of red sandstone containing two coplanar fissures under different confining pressures are shown in Fig. 9.8, in which the denoted number is the confining stress, MPa. In accordance with Fig. 9.8, we can conclude that the yielding stress (the stress value that begins to depart the linear elastic phase in the axial deviatoric stress-axial strain curve) and TCS (triaxial compressive strength,  $\sigma_p$ ) of red sandstone containing two coplanar fissures increase gradually with the confining pressure, but existing the strength difference compared with intact specimen, which will be analyzed in detail in the next section.

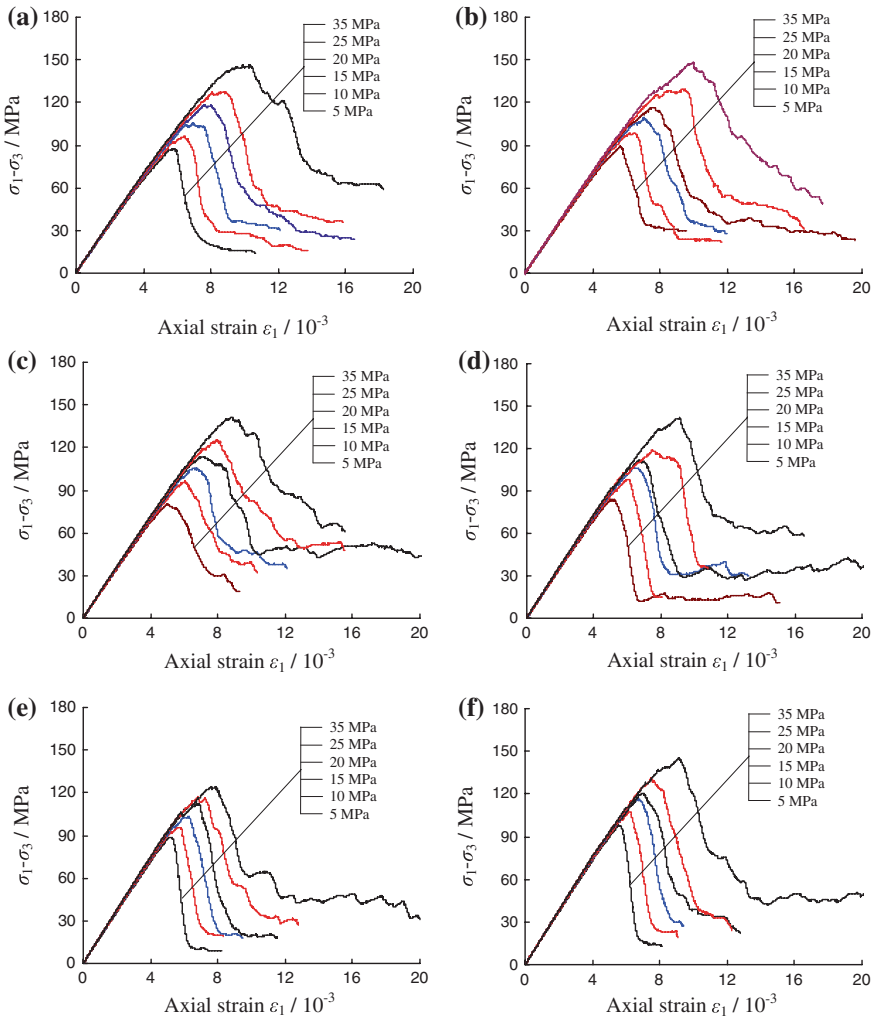


**Fig. 9.8** Axial deviatoric stress-axial strain curves of red sandstone specimens containing two coplanar fissures under different confining pressures, **a**  $\alpha = \beta = 0^\circ$ , **b**  $\alpha = \beta = 15^\circ$ , **c**  $\alpha = \beta = 30^\circ$ , **d**  $\alpha = \beta = 45^\circ$ , **e**  $\alpha = \beta = 60^\circ$ , **f**  $\alpha = \beta = 75^\circ$

Tables 9.3, 9.4, and 9.5 list the peak strength  $\sim\sigma_S$ , the elastic modulus  $\sim E_S$ , and peak axial strain  $\sim\varepsilon_{1C}$  of red sandstone with different coplanar fissure geometries and confining stresses, respectively. In accordance with the numerical results listed in Tables 9.3, 9.4, and 9.5, generally, the strength and deformation behaviors of red sandstone are found depending not only the coplanar fissure geometry, but also on the confining pressure. Compared with the intact specimen, the flawed specimen containing two coplanar fissures failed with lower strengths, smaller elastic moduli, and peak axial strains.

**Table 9.3** Peak strength ( $\sigma_S$ ) of red sandstone containing two coplanar fissures under triaxial compression (*unit* MPa)

$\sigma_3$ (MPa)	Intact specimen	$\alpha = \beta = 0^\circ$	$\alpha = \beta = 15^\circ$	$\alpha = \beta = 30^\circ$	$\alpha = \beta = 45^\circ$	$\alpha = \beta = 60^\circ$	$\alpha = \beta = 75^\circ$
5	118.96	92.84	94.03	85.21	88.98	94.00	103.01
10	134.95	106.73	108.76	106.09	108.41	105.90	117.63
15	154.90	120.12	124.04	120.72	121.74	118.22	132.06
20	172.53	138.06	136.66	133.52	131.87	132.42	140.81
25	192.85	152.40	154.62	150.24	143.96	142.06	155.90
35	227.97	180.95	183.25	176.59	176.83	159.37	180.32

Note  $\sigma_S = \sigma_p + \sigma_3$

**Table 9.4** Elastic modulus of red sandstone containing two coplanar fissures under different confining pressures (*unit* GPa)

$\sigma_3$ (MPa)	Intact specimen	$\alpha = \beta = 0^\circ$	$\alpha = \beta = 15^\circ$	$\alpha = \beta = 30^\circ$	$\alpha = \beta = 45^\circ$	$\alpha = \beta = 60^\circ$	$\alpha = \beta = 75^\circ$
5	18.79	16.98	17.12	17.23	17.67	18.12	18.47
10	19.10	17.25	17.42	17.44	17.94	18.37	18.67
15	19.32	17.36	17.61	17.66	18.13	18.54	18.81
20	19.48	17.37	17.72	17.78	18.24	18.65	18.92
25	19.59	17.41	17.78	17.84	18.36	18.77	19.01
35	19.73	17.63	17.92	17.99	18.51	18.90	19.10

**Table 9.5** Peak axial strain of red sandstone containing two coplanar fissures under different confining pressures (*unit*  $10^{-3}$ )

$\sigma_3$ (MPa)	Intact specimen	$\alpha = \beta = 0^\circ$	$\alpha = \beta = 15^\circ$	$\alpha = \beta = 30^\circ$	$\alpha = \beta = 45^\circ$	$\alpha = \beta = 60^\circ$	$\alpha = \beta = 75^\circ$
5	6.504	5.834	5.652	5.004	4.963	5.151	5.562
10	7.055	6.407	6.447	6.028	6.055	5.594	6.204
15	7.906	6.918	7.063	6.561	6.386	6.237	6.715
20	8.801	7.608	7.591	7.075	6.733	6.427	7.013
25	9.691	8.681	9.352	7.942	7.506	6.792	7.493
35	11.15	10.30	9.954	8.871	9.116	7.856	9.143

From Table 9.4, it can be seen that the elastic moduli of intact red sandstone specimen are higher than that of red sandstone containing two coplanar fissures at the same confining pressure, which can be explained as follows. Due to the heterogeneity of rock material, the existence of two coplanar fissures in the specimen results in the increase of slipping interface; therefore, the slippage of flawed specimen will also increase axial compression, which reduces the elastic modulus of rock.

Figure 9.9a shows the influence of confining pressure on the elastic modulus of red sandstone containing two coplanar fissures. From Fig. 9.9a, it can be seen that for the same coplanar fissure angle, with the increase of confining pressure, the elastic modulus of red sandstone containing two coplanar fissures all increases

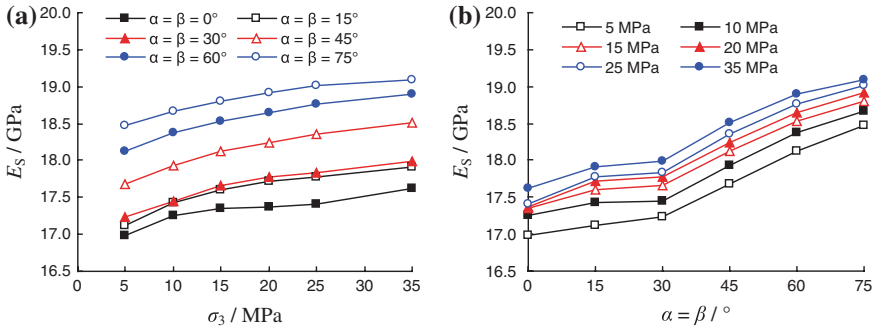


**Fig. 9.9** Influence of confining pressure and coplanar fissure angle on the elastic modulus of red sandstone specimens containing two coplanar fissures

nonlinearly. Take  $\alpha = \beta = 45^\circ$  as an example, the elastic modulus of flawed red sandstone specimen increases from 17.67–18.51 GPa as the confining pressure increases from 5 to 35 MPa.

Figure 9.9b shows the influence of coplanar fissure angle on the elastic modulus of red sandstone containing two coplanar fissures. From Fig. 9.9b, we can conclude that for the same confining pressure, the elastic modulus of red sandstone containing two coplanar fissures all increases nonlinearly with increasing coplanar fissure angle. But it should be noted that for  $\alpha = \beta$  smaller than  $30^\circ$ , the elastic modulus of flawed specimen has a slight increasing as the coplanar fissure angle; whereas for  $\alpha = \beta$  greater than  $30^\circ$ , the elastic modulus of flawed specimen increases rapidly with the coplanar fissure angle. For example for  $\sigma_3 = 10$  MPa, the elastic modulus of flawed specimen only increases from 17.25 to 17.44 GPa as  $\alpha = \beta$  increases from  $0^\circ$  to  $30^\circ$ , but from 17.44 to 18.67 GPa as  $\alpha = \beta$  from  $30^\circ$  to  $75^\circ$ .

The intact red sandstone specimens failed at a strain of approximately 0.65–1.1 % under different confining pressure, but for flawed red sandstone, the failure strain usually ranged from 0.50 to 1.0 %. With the increase of confining pressure, the peak axial strain of red sandstone increased linearly for the same geometry of coplanar fissure, as shown in Fig. 9.10a.

Figure 9.10b shows the influence of coplanar fissure angle on the peak axial strain of red sandstone specimens containing two coplanar fissures. As the coplanar fissure angle increases, the peak axial strain of flawed specimen takes on a nonlinear variance, which depends on the confining pressure. At  $\sigma_3 = 5$  MPa, the peak axial strain first decreases from  $5.834 \times 10^{-3}$  to  $4.963 \times 10^{-3}$  and then increases from  $4.963 \times 10^{-3}$  to  $5.562 \times 10^{-3}$  with increasing coplanar fissure angle, which has a lowest value for  $\alpha = \beta = 45^\circ$ . When  $\sigma_3$  ranges from 10 to 20 MPa, even though the peak axial strain also first decreases and then increases, the lowest value is for  $\alpha = \beta = 60^\circ$ , which is different to that at  $\sigma_3 = 5$  MPa. However, when  $\sigma_3$  is increased to 25 and 35 MPa, the lowest peak axial strain at the same confining pressure is still for  $\alpha = \beta = 60^\circ$ , but the variance of peak axial strain as the coplanar fissure angle for  $\alpha = \beta$  smaller than  $45^\circ$  is very complex, which may be result from the difference of crack coalescence process.

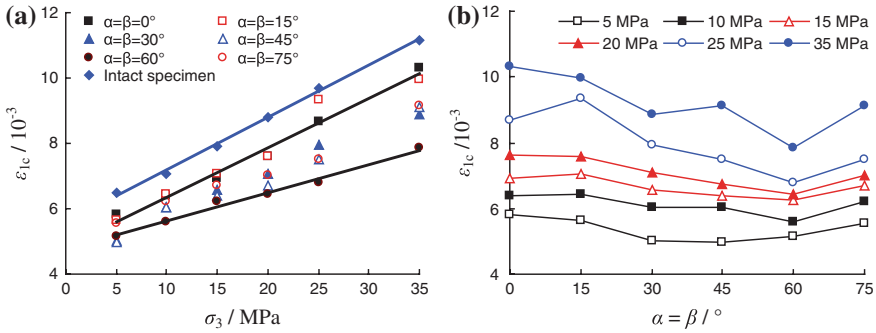


**Fig. 9.10** Influence of confining pressure and coplanar fissure angle on the peak axial strain of red sandstone specimens containing two coplanar fissures

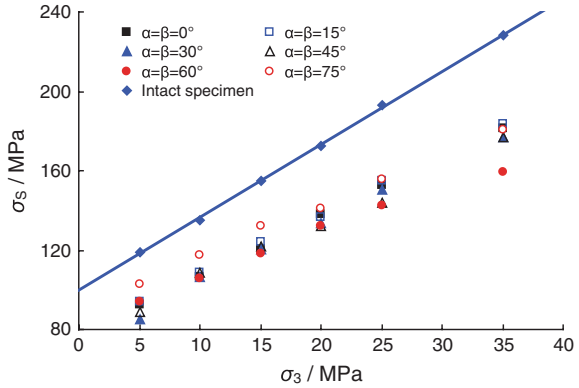
### 9.2.2 Triaxial Strength Behavior of Red Sandstone Containing Two Coplanar Fissures

Based on the peak strength data listed in Table 9.3, the influence of confining pressure on the maximum supporting capacity for red sandstone specimen with different flaw geometries is presented in Fig. 9.11. From Fig. 9.11, it is very clear that there is an obvious linear relation between the peak strength of red sandstone with different flaw geometries and the confining pressure, which can be expressed by the linear Mohr-Coulomb criterion. Table 9.6 lists the peak strength parameters of red sandstone containing two coplanar fissures in accordance with linear Mohr-Coulomb criterion.

In accordance with Table 9.6, for intact red sandstone,  $\sigma_0$  and  $q$  are 99.59 MPa and 3.68, respectively. However, for flawed red sandstone containing two coplanar fissures,  $\sigma_0$  ranges from 73.90 to 91.60 MPa, but  $q$  from 2.22 to 2.99. Generally, the values of  $\sigma_0$  and  $q$  for flawed specimens are lower than those for intact specimens. From Table 9.6, it can be seen that the cohesion and internal friction angle are, respectively, 25.96 MPa and  $34.9^\circ$  for intact specimen. Whereas for flawed specimens, the values of  $C$  range from 21.37 to 28.68 MPa, and the values of  $\varphi$  are between  $22.3$  and  $29.9^\circ$ . It is very clear that the internal friction angles of flawed specimens are all lower than that of intact specimen. But for  $\alpha = \beta$  smaller than  $60^\circ$ , the cohesions of flawed specimens are lower than that of intact specimen; whereas for  $\alpha = \beta$  greater than  $60^\circ$ , the cohesions of flawed specimens are higher than that of intact specimen.

The values of  $C$  and  $\Phi$  are significantly dependent to the coplanar fissure angle, which can be concluded from Fig. 9.12. From Fig. 9.12, it can be seen that the value of  $C$  keeps a constant basically as the coplanar fissure angle increases from 0 to  $15^\circ$ , and then the value of  $C$  decreases from 22.85 to 21.37 MPa as  $\alpha = \beta$  increases from 15 to  $30^\circ$ . When  $\alpha = \beta$  increases from 30 to  $60^\circ$ , the value of  $C$  increases rapidly from 21.37 to 28.41 MPa, while, the value of  $C$  keeps a constant

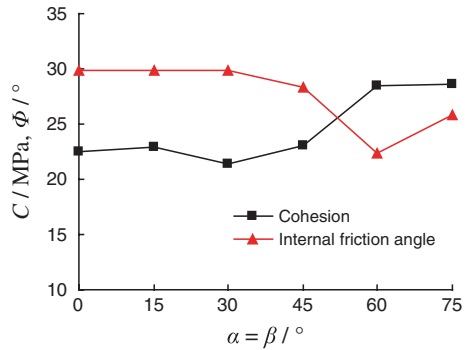
**Fig. 9.11** Relationship between peak strength and the confining pressure of red sandstone with different flaw geometries. The line represents the theoretical value in accordance with Mohr-Coulomb criterion



**Table 9.6** Peak strength parameters of red sandstone containing two coplanar fissures obtained in accordance with linear Mohr-Coulomb criterion

Fissure geometry	$\sigma_0$ (MPa)	$q$	$C$ (MPa)	$\varphi$	$R$
Intact specimen	99.59	3.68	25.96	34.9	1.000
$\alpha = \beta = 0^\circ$	77.35	2.97	22.44	29.8	1.000
$\alpha = \beta = 15^\circ$	78.90	2.98	22.85	29.8	1.000
$\alpha = \beta = 30^\circ$	73.90	2.99	21.37	29.9	0.995
$\alpha = \beta = 45^\circ$	77.37	2.80	23.12	28.3	0.995
$\alpha = \beta = 60^\circ$	84.66	2.22	28.41	22.3	0.995
$\alpha = \beta = 75^\circ$	91.60	2.55	28.68	25.9	1.000

**Fig. 9.12** Influence of coplanar fissure angle on the peak strength parameters of red sandstone specimens containing two coplanar fissures



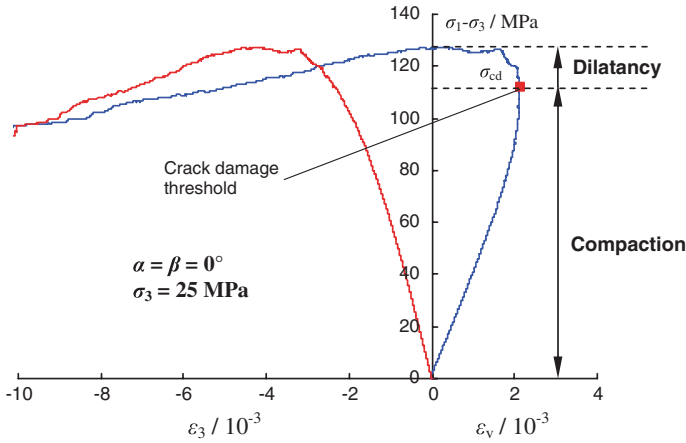
basically as  $\alpha = \beta$  increases from 60 to 75°. However, the variance of internal friction angle as the coplanar fissure angle is different from the cohesion. The value of  $\Phi$  keeps a constant  $\sim 29.8^\circ$  basically as the coplanar fissure angle increases from 0 to 30°. Afterward with the increase of coplanar fissure angle from 30 to 75°, the value of  $\Phi$  decreases first from 29.9 to 22.3° and then increases from 22.3 to 25.9°, which has a lowest value (22.3°) at  $\alpha = \beta = 60^\circ$ .

Table 9.7 lists the crack damage threshold of red sandstone containing two coplanar fissures under different confining pressures. The  $\sigma_{cd}$  is the crack damage threshold (Wong et al. 1997; Fairhurst and Hudson 1999; Heap et al. 2009), i.e.,

**Table 9.7** Crack damage threshold ( $\sigma_{sd}$ ) of red sandstone containing two coplanar fissures under different confining pressures

$\sigma_3$ /MPa	$\alpha = \beta = 0^\circ$	$\alpha = \beta = 15^\circ$	$\alpha = \beta = 30^\circ$	$\alpha = \beta = 45^\circ$	$\alpha = \beta = 60^\circ$	$\alpha = \beta = 75^\circ$
5	74.26	79.67	72.94	72.15	85.93	88.83
10	87.42	96.41	92.84	99.00	101.80	110.65
15	104.13	102.47	113.16	108.76	111.16	127.48
20	118.58	122.00	125.64	125.89	128.15	134.38
25	137.02	131.20	135.10	131.16	134.22	150.32
35	156.13	157.01	160.11	165.25	157.32	171.65

Note  $\sigma_{sd} = \sigma_{cd} + \sigma_3$ ; and the unit is MPa.

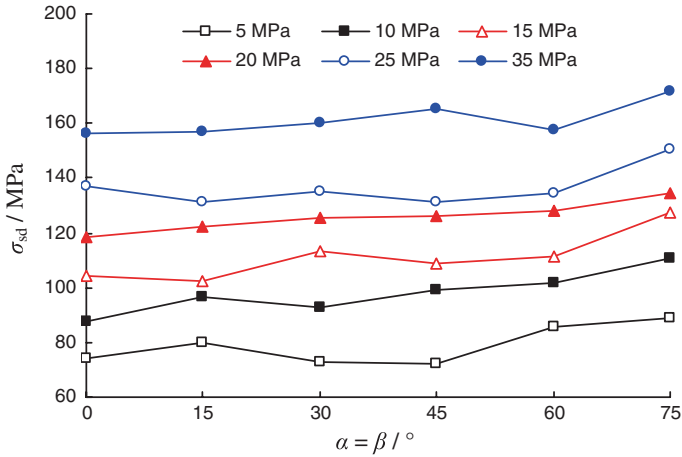


**Fig. 9.13** Confirm on crack damage threshold of red sandstone.  $\epsilon_3$  represents the circumferential strain.  $\epsilon_v$  refers to the volumetric strain, which is calculated from the sum of the axial strain and twice the circumferential strain (i.e.,  $\epsilon_v = \epsilon_1 + 2\epsilon_3$ )

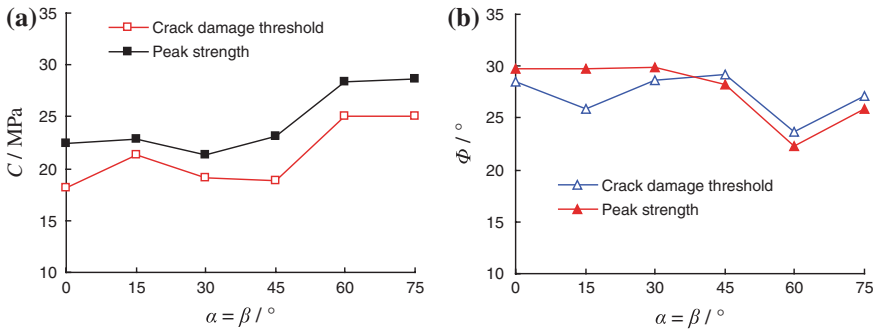
the corresponding axial deviatoric stress where the volumetric deformation of the specimen switches from compaction-dominated to dilatancy-dominated, as shown in Fig. 9.13.

Figure 9.14 presents the influence of coplanar fissure angle on the crack damage threshold of red sandstone containing two coplanar fissures under different confining pressures. From Fig. 9.14, we can conclude that at the same confining pressure, the crack damage threshold of red sandstone containing two coplanar fissures is dependent to the coplanar fissure angle, especially for  $\alpha = \beta$  greater than  $45^\circ$ .

From Fig. 9.15a, it is very clear that the value of  $C$  of red sandstone calculated using the regression analysis for the crack damage threshold are lower than the value of  $C$  calculated using the regression analysis for the peak strength. Moreover in general, the influence of coplanar fissure angle on the cohesion calculated using the regression analysis for  $\sigma_{sd}$  is similar to that for  $\sigma_S$ , except for a little difference at  $\alpha = \beta = 0^\circ$ . However from Fig. 9.15b, the value of  $\Phi$  using the regression analysis for  $\sigma_{sd}$  is approximately equal to that for  $\sigma_S$  except for  $\alpha = \beta = 15^\circ$ . At



**Fig. 9.14** Influence of coplanar fissure angle on the crack damage threshold of red sandstone containing two coplanar fissures under different confining pressures



**Fig. 9.15** Influence of coplanar fissure angle on the strength parameters of red sandstone specimens containing two coplanar fissures by using crack damage threshold

$\alpha = \beta = 15^\circ$ , the value of  $\Phi$  using the regression analysis for  $\sigma_{sd}$  is lower  $\sim 3.9^\circ$  than that for  $\sigma_s$ , which may be result from the difference of crack coalescence process for this coplanar fissure angle.

### 9.3 Fracture Evolution Behavior

In this research, the crack initiation, propagation, and coalescence are all observed in red sandstone specimens containing two coplanar fissures under triaxial compression, which the fracture coalescence behavior are obviously dependent to

confining pressure and coplanar fissure angle. Therefore, in this section, a systematic evaluation will be presented on the fracture coalescence behavior in red sandstone specimens containing two coplanar fissures.

### 9.3.1 Fracture Evolution Process of Intact Specimen

Figure 9.16 presents the crack propagation mode in the deforming process of intact red sandstone specimens under different confining pressures. The letters shown in Fig. 9.16a correspond to the time slices of Fig. 9.16b, c.

Using Fig. 9.16, we can analyze the evolution process of cracks in intact specimen during triaxial compression. When the axial deviatoric stress is loaded to points A and B, the micro-cracks in the specimen are very rare, and they results from small micro-failure occurrences during the elastic deformation. Moreover, it can be concluded that the micro-cracks are randomly distributed through the specimen. After point B, with the increase of axial deformation, the micro-cracks continue to increase, propagate and coalesce at the local positions, and when the axial deviatoric stress reaches point C (peak strength, i.e.,  $\sigma_1 - \sigma_3 = 100\% \sigma_p$ ), a number of micro-cracks are observed and some micro-cracks begin to concentrate and interact. Notice, before the peak strength, the evolution behavior of micro-cracks in the intact specimen seems to be independent to the confining pressure, as the crack evolution mode shown at points A–C in Fig. 9.16b, c. But after the peak strength, from the accumulated micro-cracks plot in Fig. 9.16b, c, it can be seen that the micro-cracks increase sharply, propagate and coalesce (see points C–F in Fig. 9.16b, c, which forms the main fracture surface and result in the final collapse of intact specimen. It should be noted that the crack evolution process in the intact specimen after the peak strength depends on the confining pressure. When the confining pressure is lower (e.g., 5 MPa), the failure mode of the intact specimen is mainly axial splitting failure. Whereas when the confining pressure is higher (e.g., 25 MPa), the failure mode of the intact specimen is mainly shear failure, as the crack evolution mode shown at point F in Fig. 9.16c.

In accordance with the variance of numbers of accumulated micro-cracks, we can also analyze the damage evolution behavior in the intact specimen. From Fig. 9.16a, it is very clear that the variance of numbers of accumulated micro-cracks with the axial deformation is very approximate at  $\sigma_3 = 5$  and 25 MPa. Herein we take  $\sigma_3 = 5$  MPa as an example to analyze. The micro-cracks numbers at point A ( $\sigma_1 - \sigma_3 = 75.17$  MPa = 66%  $\sigma_p$ ) are 189, which means that the specimen contains a small amount of internal damage. When the axial deviatoric stress reaches point B ( $\sigma_1 - \sigma_3 = 100.69$  MPa = 88.4%  $\sigma_p$ ), the micro-cracks numbers reach 675, indicating that more damage takes place within the specimen, which also leads to that the axial deviatoric stress-axial strain curve begins to depart the linearity. When reaching the peak strength (point C), the micro-cracks numbers in the specimen total 1991. The micro-cracks are now accumulating throughout the entire specimen. However, the specimen is still macroscopically coherent, even

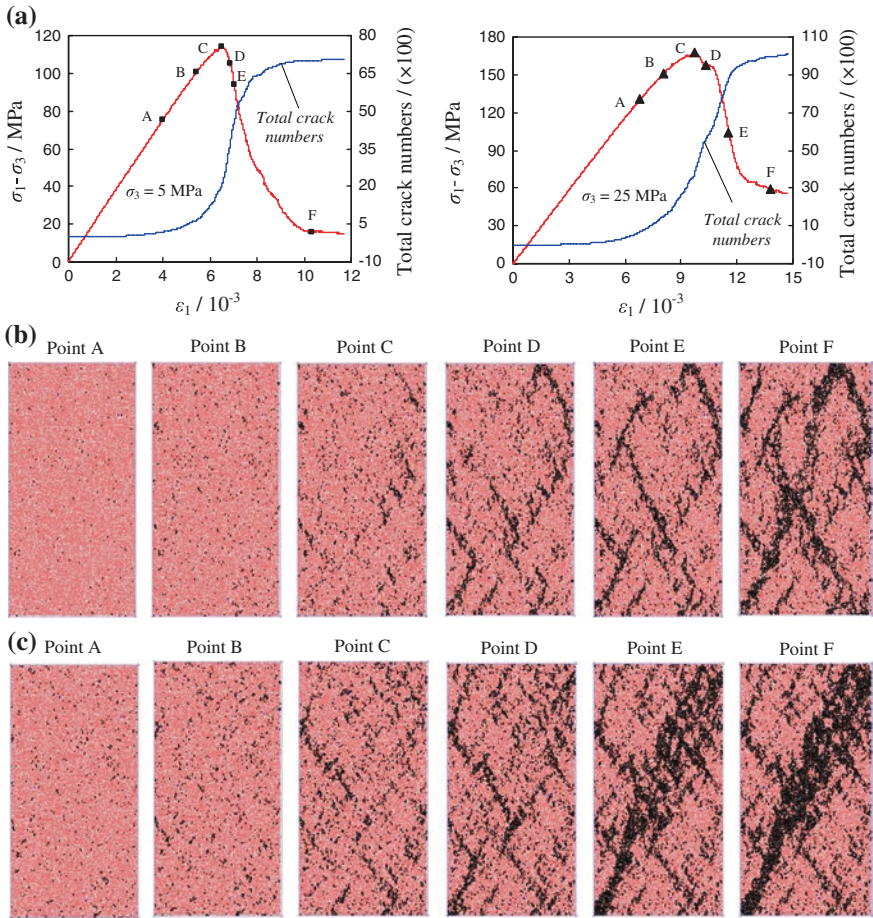


**Fig. 9.16** Crack propagation mode in the deforming process of intact red sandstone specimens under different confining pressures. **a** Relation between axial stress-axial strain curve and total crack numbers in intact specimens, **b** crack propagation process in intact specimen (point C refers to the peak value) ( $\sigma_3 = 5 \text{ MPa}$ ), **c** crack propagation process in intact specimen (point C refers to the peak value) ( $\sigma_3 = 25 \text{ MPa}$ )

though it has some internal damage failure. After the peak strength, from point C–F, the micro-cracks numbers increase rapidly from 1991 to 7011 and more micro-cracks are observed throughout the specimen, which means that most fracturing takes place at the post-peak stage. At this moment, the main mode with axial splitting failure plane can be seen from Fig. 9.16b. Moreover, it should be noted that point F has been located at the stage of residual strength. Therefore, after point F, the micro-cracks numbers will not increase with the axial deformation any longer, which can be validated from Fig. 9.16a.

### 9.3.2 Fracture Evolution Process of Flawed Specimen

Figures 9.17, 9.18, and 9.19 present the influence of coplanar fissure angle on crack propagation mode in the deforming process of red sandstone specimens containing two coplanar fissures, respectively. Taking into account very good similarity of crack propagation mode of flawed red sandstone with the same coplanar fissure angle but different confining pressure, in this section, we only analyze the crack propagation behavior of red sandstone containing two coplanar fissures at  $\sigma_3 = 5$  MPa.

From Figs. 9.17, 9.18, and 9.19, it is very clear that these cracks in the specimens were not simultaneously initiated with the increase of axial deformation, but

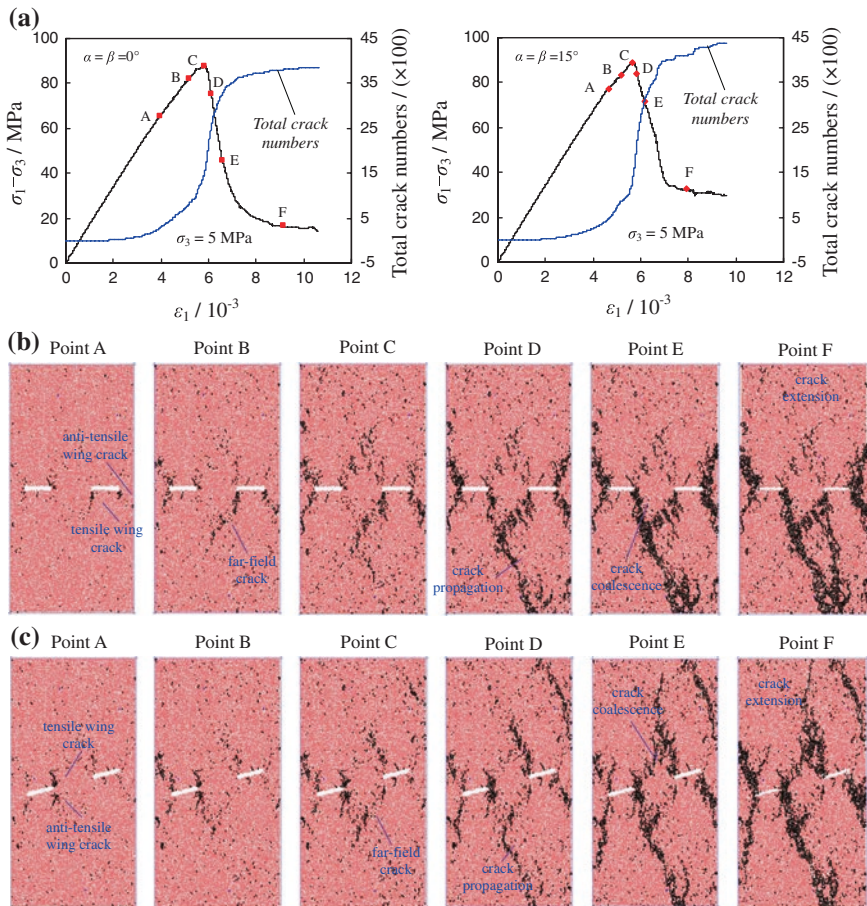


**Fig. 9.17** Crack propagation mode in the deforming process of red sandstone containing two coplanar fissures for  $\alpha = \beta = 0^\circ$  and  $15^\circ$ . **a** Relation between axial stress-axial strain curve and total crack numbers in flawed specimens ( $\alpha = \beta = 0^\circ$  and  $15^\circ$ ), **b** crack propagation process in flawed specimen (point C refers to the peak value) ( $\alpha = \beta = 0^\circ$ ), **c** crack propagation process in flawed specimen (point C refers to the peak value) ( $\alpha = \beta = 15^\circ$ )

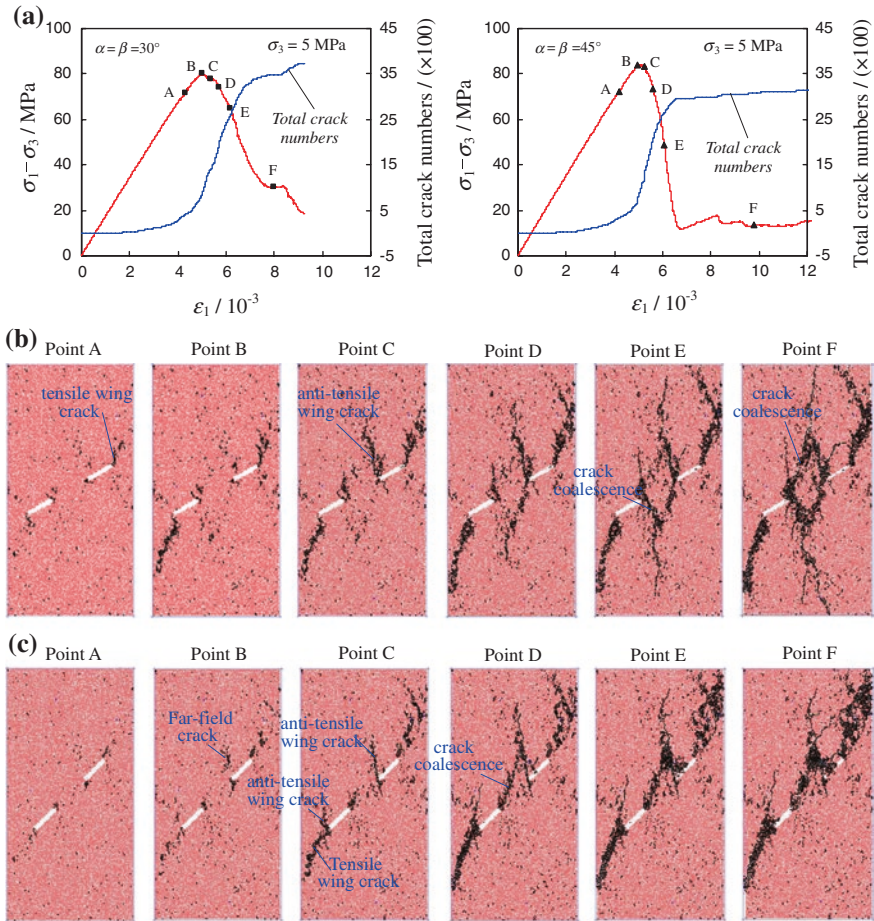


**Fig. 9.18** Crack propagation mode in the deforming process of red sandstone containing two coplanar fissures for  $\alpha = \beta = 30^\circ$  and  $45^\circ$ . **a** Relation between axial stress-axial strain curve and total crack numbers in flawed specimens ( $\alpha = \beta = 30^\circ$  and  $45^\circ$ ), **b** crack propagation process in flawed specimen (point B refers to the peak value) ( $\alpha = \beta = 30^\circ$ ), **c** crack propagation process in flawed specimen (point B refers to the peak value) ( $\alpha = \beta = 45^\circ$ )

as a gradual evolution process. Moreover, the crack evolution process of red sandstone containing two coplanar fissures depends obviously on the coplanar fissure angle. In accordance with Figs. 9.17, 9.18, and 9.19, the crack evolution process can be analyzed detailed as follows.

For  $\alpha = \beta = 0^\circ$  (see Fig. 9.17b), when the specimen was loaded to point A, tensile wing cracks (the first cracks) emanate from the inner tips of two pre-existing fissures, and one anti-tensile wing crack (the first crack) is observed from the outer tip of fissure ①. The unsymmetrical crack initiation processes in two pre-existing fissures result from the heterogeneity related to the arbitrarily generated particle

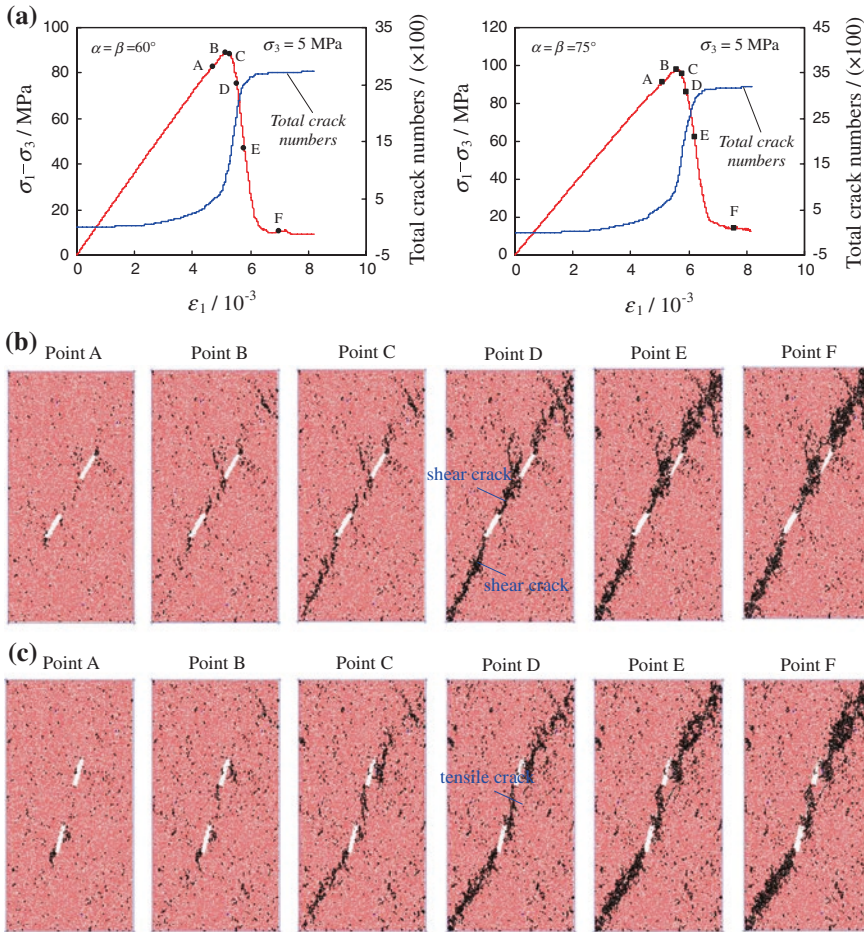


**Fig. 9.19** Crack propagation mode in the deforming process of red sandstone containing two coplanar fissures for  $\alpha = \beta = 60^\circ$  and  $75^\circ$ . **a** Relation between axial stress-axial strain curve and total crack numbers in flawed specimens ( $\alpha = \beta = 60^\circ$  and  $75^\circ$ ), **b** crack propagation process in flawed specimen (point B refers to the peak value) ( $\alpha = \beta = 60^\circ$ ), **c** crack propagation process in flawed specimen (point B refers to the peak value) ( $\alpha = \beta = 75^\circ$ )

assembly. As the axial deformation increases, the axial deviatoric stress is loaded to point B, at the outer tip of fissure ②, two tensile cracks initiate and propagate in the upward and downward directions. At the same time, far-field crack is also observed at this stress level. When the specimen is loaded to the peak strength (point C), the previous cracks take place the propagation (e.g., tensile wing cracks initiated at the outer tip of fissure ②) and new tensile crack initiates from the outer tip of fissure ①. After the peak strength, with the increase of axial deformation, the axial deviatoric stress begins to decrease rapidly, which also leads to the crack propagation and

coalescence. At point D, in the below of ligament region, far-field crack occurs in the propagation and further links with tensile wing crack at the inner tip of fissure ①. At the same time, one anti-tensile wing crack initiates from the inner tip of fissure ②. As the axial deformation increases, even though the axial deviatoric stress continues to decrease, coalescence occurs due to the linkage of two cracks (see point E shown in Fig. 9.17b). Further extension of the macro-cracks leads to the failure of the specimen, which can be validated from point F shown in Fig. 9.17b. It should be noted that at the middle portion of two pre-existing fissures, some micro-cracks are connected into one macro-crack (see Point B shown in Fig. 9.17b), but the macro-crack does not propagate as the other cracks with the increase of axial deformation.

For  $\alpha = \beta = 15^\circ$  (see Fig. 9.17c), in general, the crack propagation process is very similar to that for  $\alpha = \beta = 0^\circ$ . Some minor differences can be described as follows. Even though the order of crack initiation in the specimen for  $\alpha = \beta = 15^\circ$  is different to that for  $\alpha = \beta = 0^\circ$ , the initiating cracks at the inner and outer tips of fissure ② is very approximate, which can be validated from the comparison of point D shown in Fig. 9.17b, c. Whereas at the inner and outer of fissure ①, the initiating cracks are different. For  $\alpha = \beta = 15^\circ$ , two anti-tensile wing cracks are observed from the inner and outer tips of fissure ①, respectively, but for  $\alpha = \beta = 0^\circ$ , no anti-tensile wing crack initiates from the inner tip of fissure ①. Moreover for  $\alpha = \beta = 15^\circ$ , coalescence occurs due to the linkage between one anti-tensile wing crack and one tensile wing crack (see point E shown in Fig. 9.17c). The coalescence position for  $\alpha = \beta = 15^\circ$  is located in the top area of ligament region, but only in the bottom area of ligament region for  $\alpha = \beta = 0^\circ$ . No any coalescence is observed from the inner tip of fissure ① to the anti-tensile wing crack at the inner tip of fissure ②.

For  $\alpha = \beta = 30^\circ$  (see Fig. 9.18b), with the increase of axial deformation, tensile wing cracks (the first crack) initiate from the inner and outer tips of two pre-existing fissures, but the propagating speed of tensile wing cracks initiated from the outer tips of two fissures is greater than that from the inner tips, which can be validated from point B (the peak strength) shown in Fig. 9.18b. At the same time, one anti-tensile wing crack emanates from the inner tip of fissure ①, and one secondary tensile wing crack from the inner tip of fissure ②. After the peak strength, with the increase of axial deformation, the axial deviatoric stress begins to decrease. When the axial deviatoric stress drops to point C shown in Fig. 9.18b, the anti-tensile wing crack at the inner tip of fissure ① takes place the propagation in the upward direction toward the boundary of the specimen. As the axial deviatoric stress further drops to point D, one secondary tensile crack emanates from the inner tip of fissure ① and propagates in the downward direction with a steep angle. With the increase of axial deformation, the axial deviatoric stress further drops, the first coalescence occurs due to the linkage between the inner tip of fissure ② and secondary tensile crack from the inner tip of fissure ① (see point E in Fig. 9.18b), and then the second coalescence between the inner tip of fissure ② and anti-tensile wing crack from the inner tip of fissure ① (see point F in Fig. 9.18b). It should be noted, in the process of crack coalescence, original cracks in the ligament region become progressively wider and the length of some cracks increases (from points D–F in Fig. 9.18b).

Generally, for  $\alpha = \beta$  smaller than or equal to  $30^\circ$ , the width of two pre-existing fissures decreases with the increase of axial deformation. But for  $\alpha = \beta$  greater than  $30^\circ$ , the width of two pre-existing fissures does not occur in the variance with the increase of axial deformation.

For  $\alpha = \beta = 45^\circ$  (see Fig. 9.18c), when the specimen is loaded to point A, tensile wing cracks (the first cracks) emanate from the tips of two pre-existing fissures. As the axial deformation increases, the axial deviatoric stress is loaded to point B (i.e., peak strength), several far-field cracks formed due to the linkage of some micro-cracks are observed nearby the fissure ①. The continuous increase of axial deformation leads that the specimen is loaded to post-peak value, and the axial deviatoric stress begins to decrease. When the axial deviatoric stress drops to point C, tensile wing crack from the outer tip of fissure ② extend and develop until the left bottom position of the specimen. At the same time, one anti-tensile wing crack is also observed from the outer tip of fissure ②. Besides, one anti-tensile wing crack initiates from the inner tip of fissure ① and links with the far-field crack. Several secondary tensile cracks are also observed from the outer tip of fissure ① and propagate in the upward direction along the axial stress. As the axial deformation increases, the specimen drops to point D, coalescence occurs due to the linkage between the inner tip of fissure ② and the anti-tensile wing crack from the inner tip of fissure ①. Moreover, the anti-tensile wing crack from the inner tip of fissure ① also propagates in the upward direction along the axial stress. The crack type of coalescence is actually shear crack (Yang 2011). Further extension of the macro-cracks leads to the failure of the specimen, which can be validated from points E–F shown in Fig. 9.18c.

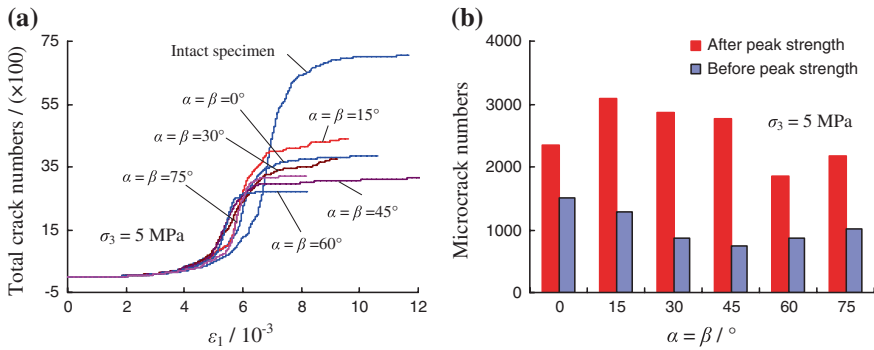
For  $\alpha = \beta = 60$  and  $75^\circ$  (see Fig. 9.19b, c), the crack propagation mode of red sandstone containing two coplanar fissures is different from those for  $\alpha = \beta$  smaller than  $60^\circ$ , but the crack propagation mode of specimen for  $\alpha = \beta = 60^\circ$  is very approximate to that for  $\alpha = \beta = 75^\circ$ . Before the peak strength, tensile cracks initiate from the tips or periphery of pre-existing fissures. After the peak strength, the crack coalescence occurs between the inner tips of two pre-existing fissures in the ligament region, which can be validated from point D. For  $\alpha = \beta = 60^\circ$ ; the macroscopic failure mode of the specimen is mainly the shear crack, which emanates from the tips of pre-existing fissures. But at the inner tip of fissure ①, one anti-tensile wing crack is observed in the upward direction. However, for  $\alpha = \beta = 75^\circ$ , in the ligament region, the type of coalesced crack is tensile crack, not shear crack. But nearby the outer tips of two pre-existing fissures, the type of crack is mainly shear crack. Moreover, it should be noted that with the increase of axial deformation, the cracks become progressively wider and wider.

### 9.3.3 *Effect of Confining Pressure and Coplanar Fissure Angle*

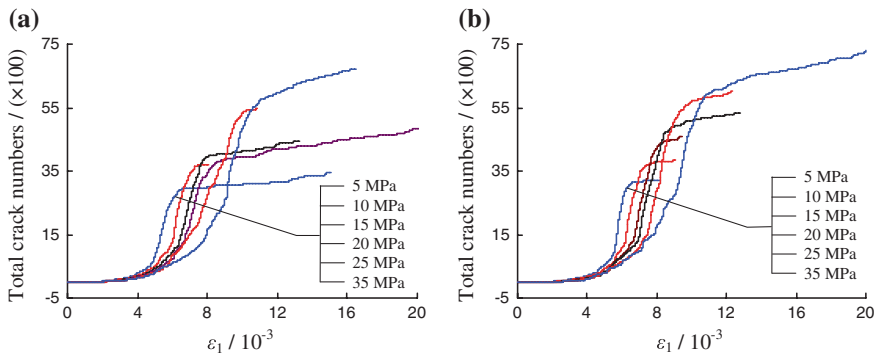
Figure 9.20a presents the effect of coplanar fissure angle on the crack evolution curve of red sandstone containing two coplanar fissures at  $\sigma_3 = 5$  MPa. From

Fig. 9.20a, it can be seen that generally, the total crack numbers in the specimens for  $\alpha = \beta$  smaller than  $45^\circ$  are greater than that for  $\alpha = \beta$  greater than  $45^\circ$ , but no clear relation between the crack numbers and coplanar fissure angle. Figure 9.20b shows the comparison of crack numbers between before and after peak strength for different coplanar fissure angles. From Fig. 9.20b, we can conclude that more total crack numbers occur after peak strength. When reaching the peak strength, total crack numbers decrease first and then increase with the coplanar fissure angle, and has a smallest value at  $\alpha = \beta = 45^\circ$ . But after the peak strength, total crack numbers have no a clear relation with the coplanar fissure angle.

Figure 9.21 presents the typical effect of confining pressure on the crack evolution curve of red sandstone containing two coplanar fissures for  $\alpha = \beta = 30$  and  $75^\circ$ . From Fig. 9.21, it can be seen that at the same confining pressure, the total micro-cracks numbers in the specimen are not active when the axial deviatoric



**Fig. 9.20** Effect of coplanar fissure angle on the crack evolution curve, micro-crack numbers before and after peak strength of red sandstone containing two coplanar fissures at  $\sigma_3 = 5$  MPa



**Fig. 9.21** Typical effect of confining pressure on the crack evolution curve of red sandstone containing two coplanar fissures. **a**  $\alpha = \beta = 45^\circ$ , **b**  $\alpha = \beta = 75^\circ$

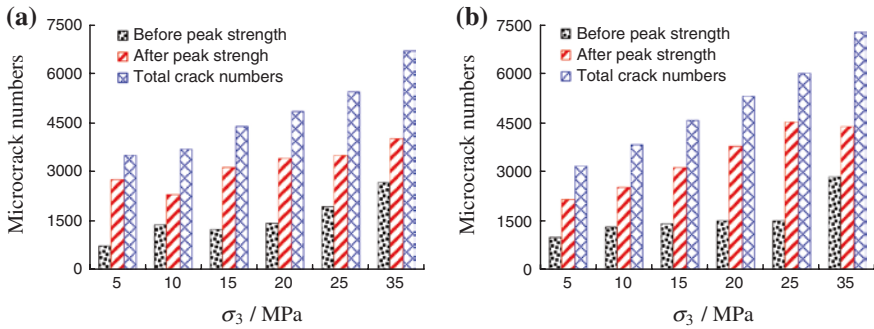


**Fig. 9.22** Typical effect of confining pressure on the micro-crack numbers of red sandstone containing two coplanar fissures

stress before peak strength is smaller and has a slow increasing tendency with the increase of applied axial strain. Whereas, after the elastic yielding stress, the total micro-cracks numbers in the specimen become more active and has a rapid increasing tendency with the increase of axial deformation, which indicates that the specimen begins to initiate the macroscopic crack from the fissure tips. In the deforming process from the peak strength to the residual strength, the total micro-cracks numbers in the specimen increase linearly with the applied axial strain as the macroscopic cracks propagate and coalesce. Finally, when the specimen enters the stage of the residual strength, the total micro-cracks numbers in the specimen keep basically a constant with the increase of axial strain.

But the crack evolution behavior of red sandstone containing two coplanar fissures is dependent to the confining pressure, which can be validated from Fig. 9.22. When the applied deformation is smaller, the confining pressure has almost no influence on the relation between total crack numbers and applied strain of flawed red sandstone, but when the applied deformation is larger, the confining pressure has a significant effect on the relation between total crack numbers and applied strain of flawed red sandstone. At the same axial deformation, if the confining pressure is higher, the total crack numbers of flawed red sandstone before the stage of residual strength will also be less due to the limitation of high confining pressure. The evolution of total crack numbers of flawed red sandstone under lower confining pressures is faster after peak strength than that under higher confining pressures, which can be seen from Fig. 9.21. From Fig. 9.22, it can be concluded that in general, micro-cracks numbers in the specimen increase with increasing confining pressure; moreover, more total crack numbers occur after peak strength than before peak strength.

### 9.3.4 Stress and Displacement Field

In order to explore deeply the fracture coalescence mechanism in red sandstone containing two coplanar fissures, it is significant to analyze the stress and displacement

field internal the rock material, which is very difficult to be obtained in the experimental process. Therefore, in this section, we will investigate the stress and displacement field in red sandstone containing two coplanar fissures under triaxial compression. Here, we only take  $\alpha = \beta = 45^\circ$  ( $\sigma_3 = 5$  MPa) as an example to analyze.

Figure 9.23 illustrates force vector plots in the deformation process of red sandstone specimen containing two coplanar fissures for  $\alpha = \beta = 45^\circ$  at  $\sigma_3 = 5$  MPa. In Fig. 9.23, the parallel bond forces are represented by the discrete straight line segments. Red colour stands for tensile force, while black colour stands for compressive force. Line thickness and orientation correspond to force magnitude and direction, respectively (color figure online). Figure 9.24 shows the evolution process of displacement field plots, which corresponds to those figures shown in Fig. 9.23.

It should be noted that for intact specimen, the parallel bond force was uniformly distributed before crack initiation; whereas for flawed specimens, the parallel bond force was not uniformly distributed before crack initiation, which could be seen from the plot shown in Fig. 9.23a. From Fig. 9.23a, it can be seen that some regions nearby the tips of two pre-existing fissures are crowded by red segments, which indicates that the regions were under tension, but some regions nearby the tips of two pre-existing fissures are crowded by black segments, which indicates that the regions were under compression. When the axial deviatoric stress is loaded to 72.07 MPa, the macro-crack begins to initiate from the tension stress concentration region at the fissure tips, as shown in Fig. 9.23b. At the same time, the red segments will decrease due to the initiation of macro-crack at the fissure tips. When the specimen is loaded to the peak strength (i.e., 83.98 MPa) shown in Fig. 9.23c, one far-field crack is observed nearby the fissure ①. After the peak strength, with the increase of axial deformation, one longer macro-crack initiates due to the linkage between far-field crack and the inner tip of fissure ① (see Fig. 9.23d), which also indicates that the parallel bond force in this region is broken. During the deformation from point d to f in Fig. 9.23, we can see that the coalescence occurs in the ligament region due to the break of parallel bond force. The red segments in the ligament region will decrease with the increasing axial deformation, which indicates that the tensile stress concentration in this region is released due to the crack coalescence.

Besides, the evolution process of this anti-tensile crack initiated from the outer tip of fissure ②, it can be concluded that with the propagation of the tensile crack, the tensile stress concentration region will transfer to the newly developed crack tips, which can be validated from the transformation of red segments shown in the elliptical region of Fig. 9.23d–f. But if the macro-tensile cracks stop to propagate, the tensile stress concentration at the newly developed crack tips will also disappear.

From Fig. 9.24, some significant features for the evolution characteristics of displacement field in the red sandstone containing two coplanar fissures for  $\alpha = \beta = 45^\circ$  at  $\sigma_3 = 5$  MPa can be summarized as follows.

- Before the macro-crack initiation, the displacement field is symmetrically distributed in the specimen for intact specimen and flawed specimen even though with small micro-cracks shown in Fig. 9.24a. But compared with intact

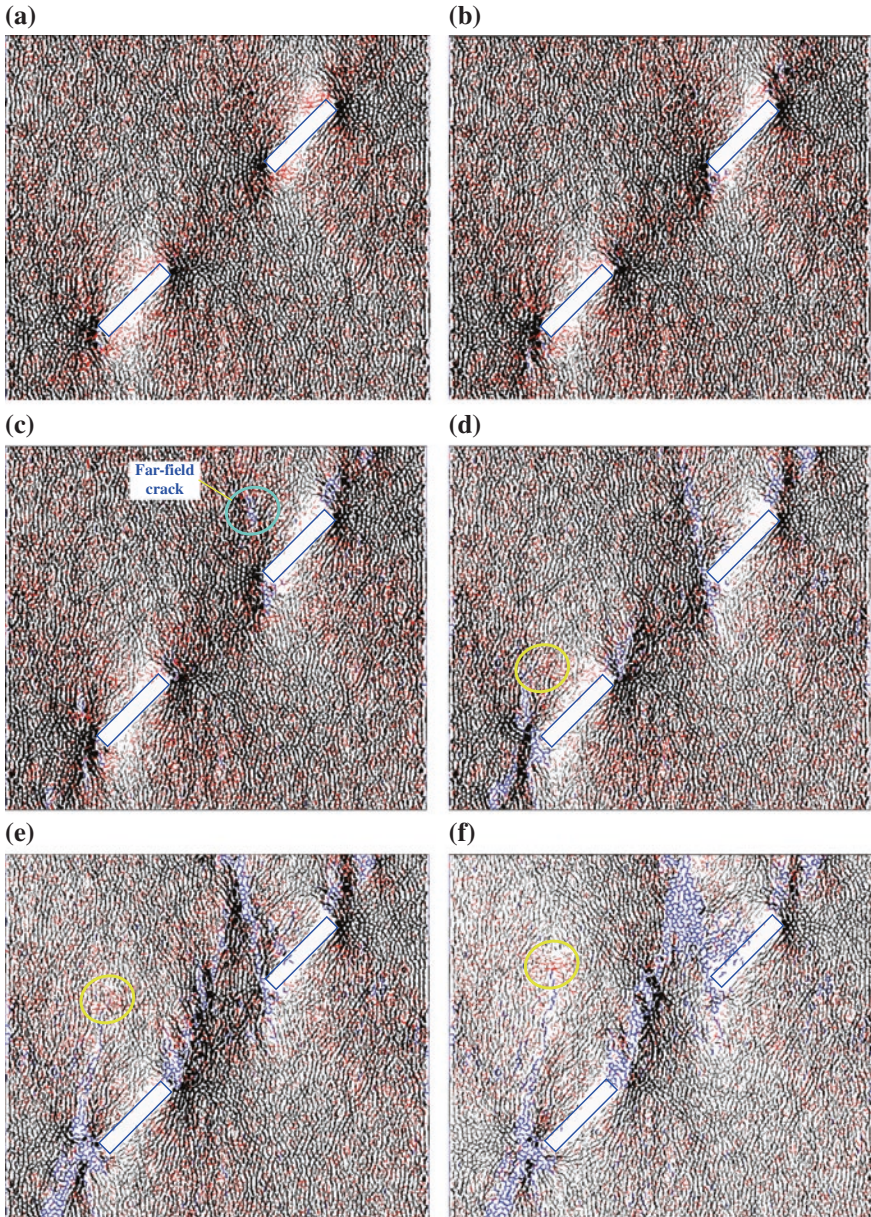


**Fig. 9.23** Force vector plots in the deformation process of red sandstone specimen containing two coplanar fissures for  $\alpha = \beta = 45^\circ$  at  $\sigma_3 = 5$  MPa. Blue colour segments stand for micro-cracks initiated in response to external loading. **a**  $\varepsilon_1 = 3.172 \times 10^{-3}$ ,  $\sigma_1 - \sigma_3 = 55.56$  MPa = 66.2 %  $\sigma_p$ , **b**  $\varepsilon_1 = 4.167 \times 10^{-3}$ ,  $\sigma_1 - \sigma_3 = 72.07$  MPa = 85.8 %  $\sigma_p$ , **c**  $\varepsilon_1 = 4.963 \times 10^{-3}$ ,  $\sigma_1 - \sigma_3 = 83.98$  MPa = 100 %  $\sigma_p$ , **d**  $\varepsilon_1 = 5.262 \times 10^{-3}$ ,  $\sigma_1 - \sigma_3 = 83.20$  MPa = 99.1 %  $\sigma_p$ , **e**  $\varepsilon_1 = 5.606 \times 10^{-3}$ ,  $\sigma_1 - \sigma_3 = 73.71$  MPa = 87.8 %  $\sigma_p$ , **f**  $\varepsilon_1 = 6.077 \times 10^{-3}$ ,  $\sigma_1 - \sigma_3 = 48.47$  MPa = 57.7 %  $\sigma_p$

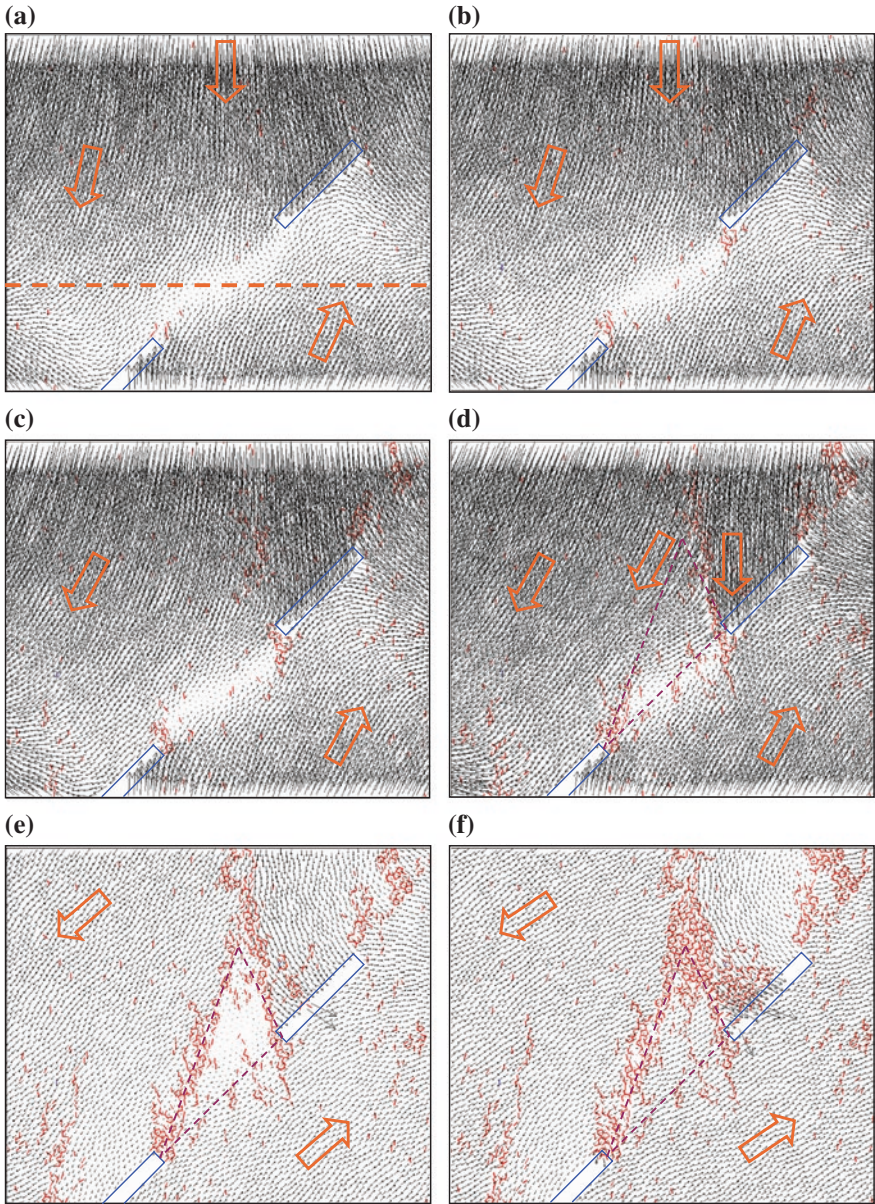


**Fig. 9.24** Displacement field plots in the deformation process of red sandstone specimen containing two coplanar fissures for  $\alpha = \beta = 45^\circ$  at  $\sigma_3 = 5$  MPa. Red colors stand for micro-cracks initiated in response to external loading. **a**  $\epsilon_1 = 3.172 \times 10^{-3}$ ,  $\sigma_1 - \sigma_3 = 55.56$  MPa = 66.2 % $\sigma_p$ , **b**  $\epsilon_1 = 4.167 \times 10^{-3}$ ,  $\sigma_1 - \sigma_3 = 72.07$  MPa = 85.8 % $\sigma_p$ , **c**  $\epsilon_1 = 4.963 \times 10^{-3}$ ,  $\sigma_1 - \sigma_3 = 83.98$  MPa = 100 % $\sigma_p$ , **d**  $\epsilon_1 = 5.262 \times 10^{-3}$ ,  $\sigma_1 - \sigma_3 = 83.20$  MPa = 99.1 % $\sigma_p$ , **e**  $\epsilon_1 = 5.606 \times 10^{-3}$ ,  $\sigma_1 - \sigma_3 = 73.71$  MPa = 87.8 % $\sigma_p$ , **f**  $\epsilon_1 = 6.077 \times 10^{-3}$ ,  $\sigma_1 - \sigma_3 = 48.47$  MPa = 57.7 % $\sigma_p$

specimen, pre-existing fissures have a great influence on the displacement field in the specimen. In the ligament region, the displacement value was smallest in the specimen. For fissure ①, the displacement value nearby the top surface is higher than that nearby the bottom surface. Nearby the top part of central line of the specimen, the left particles move in the downward direction, but the trend direction of the displacement of has a minor deviation toward the left boundary of the specimen. But the right particles first move in the upward direction and twist toward the right boundary of the specimen due to the existence of fissure ①. But the displacement variance of particles nearby fissure ② was reverse to that nearby fissure ① due to the symmetry.

- Due to the propagation of macro-crack, the particles in the specimen moved originally toward a direction will move toward two different directions, which can be seen from Fig. 9.24d. The particles between two different directions will have an acute angle, which increases with the increase of axial deformation, as shown in Fig. 9.24d–f.
- Due to the coalescence of macro-crack, not only the displacement values of the particles but also the displacement directions of the particles change with the increase of axial deformation. Sometimes, the directions of displacement vector plots are completely reverse to that before the macro-crack coalescence. For example, in Fig. 9.24d, we can conclude that the particles in the triangle region moves in the downward direction along a parallel direction to the pre-existing fissures; whereas in Fig. 9.24f, the particles in the triangle region moves in the upward direction along a parallel direction to the pre-existing fissures.
- Once no new macro-crack initiation, the directions of displacement vector plots will not take place the variance any more. From Fig. 9.24, it is very clear that with the increase of axial deformation, the displacement direction of the particles below the pre-existing fissures deviates toward the bottom boundary of the specimen.

## 9.4 Conclusions

In this chapter, a systematic numerical simulation by particle flow code (PFC<sup>2D</sup>) was performed to analyze deeply the strength, deformation, and fracture coalescence behavior of red sandstone containing two coplanar fissures under triaxial compression. Through the simulated results, the following conclusions can be summarized.

1. On basis of the experimental results of intact red sandstone specimens without any pre-existing fissures under conventional triaxial compression, the microparameters used in this chapter were first confirmed. The validation of the simulated models was cross-checked with the experimental results of intact red sandstone under different confining pressures. By comparing quantitatively the

simulated results of intact red sandstone with triaxial experimental results, we found that the numerical simulated results (including the axial deviatoric stress-axial strain curve, the peak strength, the elastic modulus and the ultimate failure mode) were in good agreement with triaxial experimental results.

2. By adopting the same microparameters as the intact specimen, the strength and deformation behavior of red sandstone containing two coplanar fissures under different confining pressures were simulated successfully. The simulated results show that the strength and deformation behavior of red sandstone is dependent not only on the confining pressure, but also the coplanar fissure angle. The elastic modulus of flawed red sandstone increases nonlinearly but the peak axial strain increases linearly with increasing confining pressure. But even though the elastic modulus of flawed red sandstone increases with the coplanar fissure angle, the peak axial strain is not a monotonic function as the coplanar fissure angle. Compared with intact specimen, the specimen containing two coplanar fissures fails with lower strengths, smaller elastic moduli, and peak strains.
3. The peak strength of red sandstone containing two coplanar fissures increases with the confining pressure, which are in good agreement with linear Mohr-Coulomb criterion. The cohesion and internal friction angle of red sandstone obtained by using the peak strength are distinctly dependent to the coplanar fissure angle. The cohesion ( $C$ ) and internal friction angle ( $\Phi$ ) are, respectively, 25.96 MPa and 34.9° for intact specimen. Whereas for flawed specimens, the values of  $C$  range from 21.37 to 28.68 MPa, and the values of  $\Phi$  are between 22.3 and 29.9°. Generally, the internal friction angles of flawed specimens are lower than that of intact specimen. But for  $\alpha = \beta$  smaller than 60°, the cohesions of flawed specimens are lower than that of intact specimen; whereas for  $\alpha = \beta$  greater than 60°, the cohesions of flawed specimens are higher than that of intact specimen.
4. The crack damage threshold of red sandstone containing two coplanar fissures increases with the confining pressure, which can be expressed in accordance with linear Mohr-Coulomb criterion. The value of  $C$  of red sandstone calculated using the regression analysis for the crack damage threshold are lower than the value of  $C$  calculated using the regression analysis for the peak strength. In general, the influence of coplanar fissure angle on the cohesion calculated using the regression analysis for the crack damage threshold is similar to that for the peak strength. However, the value of  $\Phi$  using the regression analysis for crack damage threshold is approximately equal to that for peak strength.
5. Finally, the relationship between the real-time crack evolution process and the axial stress-axial strain curve of red sandstone containing two coplanar fissures is constructed, and the evolution process of the force and displacement field is analyzed in detail, which reveals deeply the micromechanical mechanism of flawed red sandstone under triaxial compression. These investigated conclusions are very important for ensuring the stability and safety of deep joint rock mass engineering.

## References

- Cho N, Martin CD, Sego DC (2007) A clumped particle model for rock. *Int J Rock Mech Min Sci* 44(7):997–1010
- Fairhurst CE, Hudson JA (1999) Draft ISRM suggested method for the complete stress—strain curve for the intact rock in uniaxial compression. *Int J Rock Mech Min Sci* 36(3):279–289
- Heap MJ, Baud P, Meredith PG, Bell AF, Main IG (2009) Time-dependent brittle creep in Darley Dale sandstone. *J Geophys Res* 114:B07203. doi:[10.1029/2008JB006212](https://doi.org/10.1029/2008JB006212)
- Potyondy DO, Cundall PA (2004) A bonded-particle model for rock. *Int J Rock Mech Min Sci* 41(8):1329–1364
- Wong TF, David C, Zhu W (1997) The transition from brittle faulting to cataclastic flow in porous sandstones: mechanical deformation. *J Geophys Res* 102(B2):3009–3025
- Yang SQ (2011) Crack coalescence behavior of brittle sandstone samples containing two coplanar fissures in the process of deformation failure. *Eng Fract Mech* 78:3059–3081
- Yang SQ, Jing HW (2013) Evaluation on strength and deformation failure behavior of red sandstone under simple and complex loading paths. *Eng Geol* 164:1–17